UNIVERSITAT DE BARCELONA

Growth and characterization of new multiferroic materials

Emerson Coy

UNIVERSITAT DE BARCELONA

Departament de Física Aplicada i Òptica,
Facultat de Física

GROWTH AND CHARACTERIZATION OF NEW MULTIFERROIC MATERIALS Emerson Coy

GROWTH AND CHARACTERIZATION OF NEW MULTIFERROIC MATERIALS

PhD dissertation
Emerson Coy

UNIVERSITAT DE BARCELONA

GROWTH AND CHARACTERIZATION OF NEW MULTIFERROIC MATERIALS

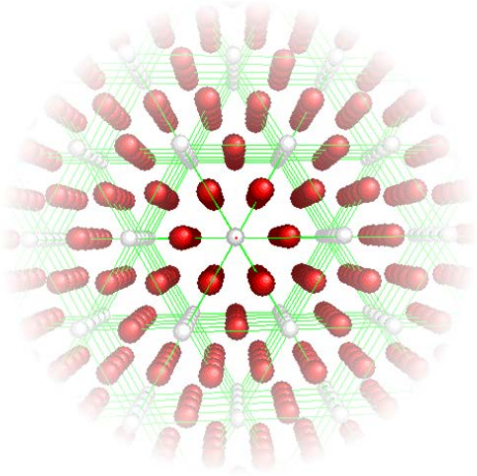

Emerson Coy

PhD thesis

Director:

Dr. Manuel Varela Fernández

Departament de Física Aplicada i Òptica,
Facultat de Física
Universitat de Barcelona

2015

GROWTH AND CHARACTERIZATION OF NEW MULTIFERROIC MATERIALS

Emerson Coy

Thesis submitted for the degree of Doctor of Philosophy at University of Barcelona

PhD Program: Nanoscience

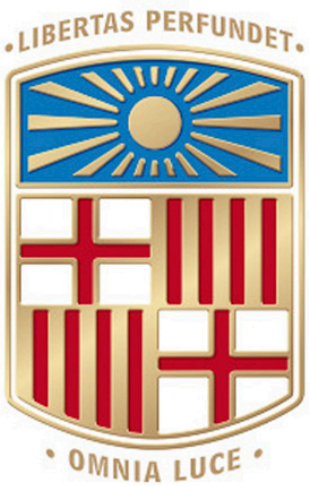

Departament de Física Aplicada i Òptica,
Facultat de Física
Universitat de Barcelona
2015

A mi madre……
mi padre…..
y mi zuzel .

ABSTRACT

Multiferroic materials, in which two or more ferroic ordering take place in the same phase, have driven major interest in the last few years, not only due to the possibility of exploring novel physical properties in those materials, but also the implications that such properties show in novel technological applications. From those materials, the especially interesting are those in which the ferromagnetic (FM) and ferroelectric (FE) ordering take place, due to their direct application in magnetodielectric devices. In the field of multiferroic materials such materials could play an important role in a new generation of none volatile magnetic random access memories (MRAM), in which a sufficiently strong magnetodielectric coupling could allow for the modification of the magnetic state, not only with a magnetic field, but with an electric field. This fact would allow for a dramatic reduction in energy consumption and would promote the further technological integration (the major commercial drawback of MRAMs), due to the fact that an electric field, contrary to the magnetic field, can be applied locally. Additionally, such multiferroic materials could prove useful in magnetic tunnel junctions, in which the ferroelectric and ferromagnetic nature would allow them to codify four resistive states, instead of the traditional two states of ferroelectric or ferromagnetic junctions, allowing for the implementation of a generation of four state memories.

The materials with perovskite structure, $ABB'O_3$ (A=Rare Earth, Bismuth, Lead and Yttrium), bring a broad spectrum of possibilities when it comes to design of multifunctional materials. This is due to the wide variety of A, B, B´ cations that are

compatible with such structure. However, in the case of $R(NiMn)O_3$, such oxides have been poorly studied and many detailed studies, both in bulk and thin films are needed. The cation selection of B and B' seems to transform the paramagnetic ordering (PM) into FM below room temperature. The multiferroicity of these materials is typically provided by the A cation of the perovskite formula, which can be Bi or Pd, in order to create a Type 1 multiferroic. In this type of materials, i.e: Bi_2NiMnO_6, the ferroelectricity and ferromagnetism arose by separate mechanisms, the FE is provided by the A cation, with so called long pair electrons, which are free electrons in the valence band that do not participate in any chemical reaction in the compound, while the Ni^{2+}(d8) and (Mn^{4+}) (d3) provides the FM. However, even though the materials are multiferroic, their magnetodielectric coupling, crucial for future industrial applications, is weak, due to the different mechanisms that provide their FM and FE ordering.

On the other hand, the FE induction by geometrical distortion of the perovskite lattice, for example in $YMnO_3$, is an interesting case since rotations of the MnO_6 octahedrons promote an important structural change, in which the oxygen atoms move closer to the Y and, due to a large dipole interaction, generate a stable FE state. Moreover, the deformation of the unit cell generates a weak spin canting on the Mn cations, that can be promoted by Li doping or lattice distortions. This behavior could prove useful in the $R(NiMn)O_6$ family, which shows strong FM.

This thesis is devoted to the study of $R(Ni_{0.5}Mn_{0.5})O_3$ (Y,Sm, Nd and Pr) and $Bi(Fe_{0.5}Mn_{0.5})O_6$ grown in thin films by pulsed laser deposition technique.

Firstly, this thesis focuses on the growth and characterization of thin films of $Y(Ni_{0.5}Mn_{0.5})O_3$ (YNMO) on strontium titanate substrates $SrTiO_3$(001) (STO). The influence of the deposition parameters, such as temperature, fluence and ablation frequency, on the morphology and crystalline quality of the films is investigated. The study reveals that the YNMO films grown on STO(001,011 and 111) substrates are epitaxial and that their crystalline quality and epitaxial relationship are similar to those of the YMO compound. In particular, it is observed that a single out of plane domain is the norm for all the substrate orientations, while there are various in-plane domains. Moreover, chemical composition studies reveal Ti diffusion from the substrate to the YNMO film when STO(111) substrates are used.

Once the growth conditions of YNMO are optimized, the magnetic and dielectric properties are studied. All the films show a paramagnetic to ferromagnetic transition at a

temperature around 95K, with a magnetic moment of YNMO(001) = 4.35μ_B/f.u, YNMO(100) = 4,4 μ_B/f.u and YNMO(101) = 3,7μ_B/f.u, confirming the ferromagnetic nature of the samples. The dielectric characterization reveal a FE ordering on the YNMO films, and what is more, the existence of a dielectric anisotropy on the films, that is characterized by the absence of ferroelectric response on YNMO samples deposited on STO(001), while YNMO samples on STO(111) show a strong FE response. This anisotropy could be explained, according to recent theoretical studies, in the improper origin of the observed ferroelectriciy. The coexistence of FM and FE response shows in a conclusive manner the multiferroic nature of the YNMO compound.

Secondly, studies similar to those previously presented are performed for thin films of $R(Ni_{0.5}Mn_{0.5})O_3$ (Sm, Nd and Pr) compounds grown on STO(001). In this case the deposition temperature turns out to play a crucial role on the epitaxial growth of all the studied compounds. It is shown that the ratio between the b/a lattice parameters influences the epitaxial growth of the films, being the decisive factor between single or multi domain films. All the samples show a PM to FM transition at temperatures around 190K

Finally, films of $Bi(Fe_{0.5}Mn_{0.5})O_6$ have been grown on STO(001) substrates. The films are epitaxial and grow under epitaxial strain. Samples show a FM behavior at room temperature with a weak signal of 7,42 emu/cm^3 and 0,4 μ_B/f.u(Fe-Mn). The dielectrical characterization shows the influence of external magnetic fields on the dielectric properties of the film above room temperature.

RESUMEN

Los materiales multiferroicos, en los que dos o más ordenes ferroicos tienen lugar en la misma fase, ha despertado gran interés en los últimos años debido, no solo al hecho de explorar nuevas propiedades físicas en los materiales, sino también a las implicaciones de las nuevas propiedades funcionales en las aplicaciones tecnológicas. De dichos materiales resultan especialmente interesantes aquellos que presentan un orden ferroeléctrico (FE) y ferromagnético (FM) debido a su aplicación directa en dispositivos magnetoelectrónicos. En este ámbito los materiales multiferroicos podrían tener una gran relevancia en una nueva generación de memorias magnéticas RAM (MRAM) de control eléctrico, no volátiles, en las que, si el acoplamiento magnetoeléctrico es suficientemente grande, se podría modificar el estado magnético no con un campo magnético sino con un campo eléctrico. Este hecho permitiría una reducción radical en el consumo de potencia y favorecería a su vez una mayor integración (la principal desventaja de las MRAMs para competir en el mercado), ya que el campo eléctrico, a diferencia del campo magnético, puede aplicarse de forma muy localizada. Por otro lado, dichos materiales multiferroicos podrían emplearse en una nueva generación de uniones túnel, en las que el carácter ferroeléctrico y ferromagnético permitiría codificar información en cuatro estados resistivos en lugar de en dos, como viene siendo hasta ahora en las convencionales uniones túnel magnéticas o ferroeléctricas, dando lugar a una nueva generación de memorias de cuatro estados.

Los materiales con estructura perovskita, $ABB´O_3$, (A=Tierra Rara, Bismuto, Plomo e Ytrio) ofrecen una gran versatilidad a la hora de diseñar materiales funcionales

debido a la gran variedad de cationes A, B y B´ compatibles con tal estructura. Sin embargo en el caso de $R(NiMn)O_3$, estos óxidos han sido poco estudiados y muchos carecen de estudios detallados tanto en forma másica como en capa fina. Esta selección de cationes en la posición B y B´ parece transformar la estructura perovskita la cual típicamente presenta un ordenamiento paramagnético (PM) en FM a temperaturas inferiores a la ambiente. El carácter multiferroico de estos materiales es típicamente aportado por el catión A en la formula perovskita, el cual puede ser un átomo de Bi, o Pb, para crear un multiferroico tipo 1. En los materiales de este tipo, por ejemplo el Bi_2NiMnO_6, la ferroelectricidad y el ferromagnetismo provienen de fuentes diferentes, el carácter FE es aportado por el catión A con -*lone pairs electrons*-, los cuales son electrones libres en la banda de valencia que no participan en las reacciones químicas del compuesto, mientras la combinación Ni^{2+} (d8) and Mn^{4+} (d3) aporta el FM. Pese al carácter multiferroico de estos materiales su acoplamiento magnetoelectrico, indispensable para sus aplicaciones industriales futuras, es débil, puesto que su FE y FM provienen de efectos independientes.

Por otra parte la inducción de FE por distorsiones geométricas de la celda perovskitas, como es el caso de $YMnO_3$ (YMO), es un caso interesante de considerar ya que la rotación de los octaedros MnO_5 genera un cambio estructural importante, en el cual los oxígenos se desplazan a una posición más cercana al Y, esto sumado a una larga interacción de los dipolos conduce al material a un estado FE estable. Además la deformación de la celda genera un débil FM en este material, el cual proviene un pequeño giro en los espines del Mn ya sea debido a un dopaje con Li o por la deformación de la celda. Este comportamiento podría resultar interesante en la familia de perovskitas $R(NiMn)O_3$ las cuales presentan un fuerte FM.

Esta tesis está dedicada al estudio de la perovskitas $R(Ni_{0.5}Mn_{0.5})O_3$ (Y, Sm, Nd y Pr) y $Bi(Fe_{0.5}Mn_{0.5})O_6$ crecidas en capa fina usando la técnica de depósito mediante ablación por láser pulsado.

En primer lugar, esta tesis se centra en el crecimiento y caracterización de capas finas del compuesto $Y(Ni_{0.5}Mn_{0.5})O_3$ (YNMO) sobre substratos de titanato de estroncio, $SrTiO_3$(001) (STO). Se estudia la influencia de los parámetros de depósito tales como temperatura, fluencia y frecuencia de ablación sobre la morfologia y la calidad cristalina de las capas obtenidas. El estudio pone de manifiesto que las capas de YNMO crecidas sobre substratos de STO(001,011 y 111) son epitaxiales de YNMO y que la calidad

cristalina y las relaciones epitaxiales entre la capa y el subtrato son semejantes a las obtenidas en el compuesto YMO. En particular se observa un único dominio cristalino fuera del plano independientemente de la orientación del sustrato, mientras que dentro del plano se presentan varios dominios cristalinos. Por otra parte, los estudios de composición química revelan una difusión de Ti desde el sustrato hacía la capa de YMNO cuando se utilizan substratos STO(111)..

Una vez optimizadas las condiciones de crecimiento del compuesto YNMO, se estudian sus propiedades magnéticas y dieléctricas. Todas las capas presentan una transición de fase paramagnetica a ferromagnética a una temperatura alrededor de 95K con un momento magnético de YNMO(001)= 4.35μB/f.u, YNMO(100) = 4,4 μB/f.u and YNMO(101) = 3,7μB/f.u, confirmando el carácter ferromagnético de las muestras. La caracterización dieléctrica revela el carácter FE de las capas de YNMO y lo que es más interesante, la existencia de anisotropía dieléctrica en las capas, ésta se pone de manifiesto en la ausencia de respuesta FE en capas YNMO sobre STO(001) que contrasta con la fuerte respuesta de las capas de YNMO sobre STO(111). Esta anisotropía puede tener su origen, a la luz de los recientes estudios teóricos, en el carácter impropio de la ferroelectricidad observada, a la luz de recientes estudios teóricos. La coexistencia de FM y FE muestra de manera conclusiva el carácter multiferroico del compuesto YNMO.

En segundo lugar se han realizado estudios similares a los anteriores para el caso de capas finas de los compuestos del tipo $R(Ni_{0.5}Mn_{0.5})O_3$ (Sm, Nd y Pr) crecidas en STO(001). En este caso la influencia de la temperatura de depósito resulta ser un factor importante para la obtención, en todos los compuestos estudiados, de crecimiento epitaxial. Se observa que el cociente b/a entre las constantes red juega un factor importante en la epitaxia de las capas, siendo este cociente un factor determinante en el crecimiento mono-dominio o multi-dominio de las capas. Todas las muestras presentan transiciones PM a FM a temperaturas alrededor de 190K.

Por último, se han crecido y estudiado capas finas del compuesto $Bi(Fe_{0.5}Mn_{0.5})O_6$ depositadas sobre STO(001). Las capas obtenidas son epitaxiales y crecen sometidas a estres inducido por el substrato. Presentan comportamiento FM a temperatura ambiente pero con una débil señal de 7,42 emu/cm^3 y 0,4 μB/f.u(Fe-Mn). La caracterización dieléctrica pone de manifiesto la influencia, a temperaturas superiores a la ambiente, de la presencia de campo magnético sobre las propiedades dieléctricas.

Table of contents

CHAPTER 1

Introduction

In the following chapter several aspects of this work will be mentioned, among the most important will be a brief description of the motivation for this work, a view of the general objective of the thesis and finally an outline of the presented work.

1.1. Motivation

One of the most interesting features of oxide materials is the multifunctional properties that these exhibit. Such wide range of properties allow them to be applied in many electronic applications, regarding their intrinsic properties, such as conductivity (in the case of superconductor and insulators) and ferroic orders (ferroelectric, ferroelastic and ferromagnetic). Additionally, and increasing their market appeal, the combination of such properties are very desirable and effects such as magnetoresistance and the most wanted magnetocapacitance are still driving much attention to these materials.

The combination of ferromagnetism and dielectric properties have gave birth to the encouraging field of spintronics. This field has consolidated further with the application of giant magnetoresistance on solid state memories and information storage. Moreover, the intrinsic applications of spintronics in quantum computing, has boosted the investigation on the fundamental and applied physics making it a very attractive and far reaching field.

In similar fashion, materials in which more than one ferroic ordering take place are called multiferroic materials, in specific, the ferroelectric and ferromagnetic

ordering are the ones more desired for electronic applications. By combining both ferroic ordering in the same crystalline phase, several novel electronics applications can take place, the two most promising will be, first, the possibility of writing both magnetic and electric bits of information, increasing the density of information in solid state devices, and second, having both ferroic orderings interdependent in the materials, would allow the control of the electric properties of the film by magnetic fields and vice versa. However, ferroelectricity and ferromagnetism in matter tend to be independent phenomena that are rarely found together. In fact, at the fundamental level, both effects arise from different mechanisms; the ferroelectricity arises from the electric dipole ordering, while the ferromagnetism arises due to the spin ordering. Thus, research in the fundamental mechanism leading to the coexistence of both ferroic orderings in complex oxides is promising and most welcome in order to expand the comprehension of such interdependency.

The most common structure for multiferroic materials is the perovskite, with a ABO_3 formula, where A and B are cations. In this structure, the B site is in the center of an oxygen octahedron (BO_6) while the A atom is in the center of the unit cell. Most of this perovskites follow the cubic symmetry, although some of them show a distorted crystallinity to a lower symmetry such in the case of orthorhombic $TbMnO_3$[**1**–**4**]. Multiferroic perovskites are “tailored” by setting a B magnetic atom, while the ferroelectric response comes from the A cation, usually Bi and Pd atoms with long range unpaired electrons[**1**,**5**–**8**].

Double perovskite materials ($A_2BB^*O_6$) have received a growing attention during the past few years, mainly due to the variety of A and B site atoms compatible with this structure and the consequent variability of their functional properties. The wide variety of elements and the formula complexity was rewarded with many compatible elements such as Co, Fe, Ni, Mn, Mo, Nb, Bi, Pb, Y and virtually all rare-earth elements. The existence of such a broad range of elements, friendly with the perovskite formula, added to the promising results given by the multiferroic material Bi_2NiMnO_6, [**9**–**12**] and the ferromagnetic La_2NiMnO_6 **[13–16]** suggested that the A_2NiMnO_6 composition offered interesting research possibilities in the functional oxide and multiferroic materials field.

Additionally, the Goodenough–Kanamori's rule states that the superexchange magnetic interaction between two transition metals, B and B* (Ni and Mn in the present case), when one of them possesses half-filled e_g orbital and the other one empty e_g orbital, is ferromagnetic. Therefore, a long set of double perovskites with A_2NiMnO_6

formula had shown, experimentally, its ferromagnetic nature in multiple studies [**5**,**17**–**19**]. However, many of these materials had not been studied in thin film form, and there was a lack of morphological, crystalline and functional characterizations. These studies were required for any further development or industrial application.

Furthermore, the hexagonal $YMnO_3$ (YMO), a well-studied multiferroic material that exhibits a very high ferroelectric temperature of 900K and an antiferromagnetic ordering around 80K was carefully studied by X. Marti [**20**]. Additionally, the magnetoelectric coupling in this material had been discussed in the literature [**21**] and its orthorhombic structure on thin films had been also carefully studied [**22**,**23**]. On the other hand, $YNiO_3$ (YNO) had been reported as a monoclinic $P2_1/n$ structure with an antiferromagnetic ordering above 150K and a metal-insulator transition at around 580K in bulk [**24**]. However, to our best knowledge, there were not much studies performed on thin films of $YNiO_3$ (YNO).

A few studies on thin films and powders of Y_2NiMnO_6 had established that partial substitution of Ni had a strong influence on the magnetic properties of [**25**–**27**]. Although these studies have shown that the structure of the $YMnO_3$ thin film, changed from a multi domain film, to a single in-plane domain, findings that seems to defy the heteroepitaxial in plane strain, previously reported and carefully studied on YMO thin films [**23**].

The effect of Ni partial substitution on the magnetic and dielectric properties of the $YMnO_3$ perovskite (Y_2NiMnO_6) was then stablished as the central topic of this thesis. In order to follow a slightly different approach than the one used by X. Marti in his doctoral thesis, where he started with a ferroelectric/antiferromagnetic material and showed the ferromagnetic ordering due to epitaxial strain. In this case, the starting point will be a ferromagnetic material Y_2NiMnO_6 that, although theorized as multiferroic, lacked of experimental evidence supporting this fact.

Additionally to this, R= Sm (Samarium), Nd (Neodymium) and Pr (Praseodymium) ions were used in the $RNi_{0.5}Mn_{0.5}O_3$ formula and also grown in thin films on $SrTiO_3$ (STO) substrates. Such materials have not been stabilized in thin films and lacked of many morphological, crystalline and functional characterizations.

Finally, $Bi(FeMn)O_3$ was also included in this thesis, based on the promising results reported in thin films [**15**,**28**] and the relative similarity to the work developed in our research group by E. Lamgenberg [**9**] in relation to the compound Bi_2NiMnO_6.

This thesis was, stablished as a cross link between the work of X. Marti and E. Langenberg and a continuation on the study of epitaxial thin films and multiferroic novel perovskites grown by pulsed laser deposition.

1.2. Introduction to $R(Ni_{0.5}Mn_{0.5})O_3$ perovskites

The simple perovskite structure, as mentioned before is given by the ABO_3 chemical formula (where *A* and *B* are cations). In the simple cubic form, oxigen atoms are placed in the middle of the cube edges, surrounding the B cation in an octahedron (BO_6) while the A cation is surrounded by 12 oxygen atoms AO_{12}, as shown in **Figure 1.1**

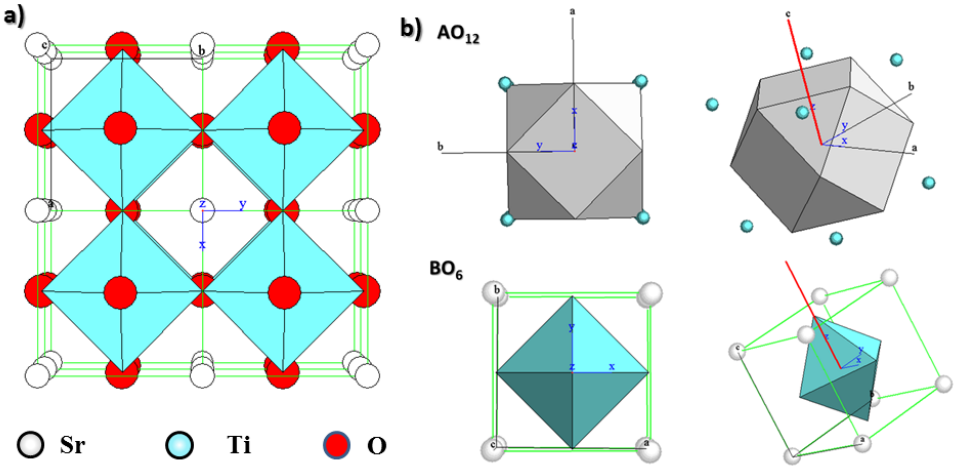

Figure 1.1: *Schematic depicting a) ABO_3 perovskite of $SrTiO_3$ and b) the AO_{12} polygons surrounding the Sr atom and the BO_6 octahedrons around the Ti atom.*

In the ideal case, such is $BaTiO_3$, the octahedrons are aligned. This case arouses when the A cation fits perfectly in the center of the cubic structure, without deforming it. When the A atom is smaller, the whole unit cells twists in order to reach minimum energy, this leads to the so called octahedron tilting and changes the lattice symmetry. **Figure 1.2** shows an example of this transformation from a simple cubic perovskite into an orthorhombic one due to the tilting of the octahedrons.

The structural stability of the unit cell is determined by the Goldschmidt tolerance factor, this factor is useful to identify the compatibility of an ion with a given crystalline structure, since it considers all ionic radii and gives a qualitative results of the compatibility of the atoms.

The Goldschmidt tolerance factor (t) is a dimensionless number that is obtained from the following formula[**29**]:

$$t = \frac{r_A + r_0}{\sqrt{2(r_B + r_0)}} \quad \text{Equation 1.1}$$

Where r_A, r_B and r_0 are the ionic radii of A, B and oxygen atoms. The result of this calculation equation is t=1, for a perfect cubic perovskite, **Figure 1.2 (left)** and t<1 for an orthorhombic or rhombohedral due to the tilting of the octahedron, **Figure 1.2 (right)**.

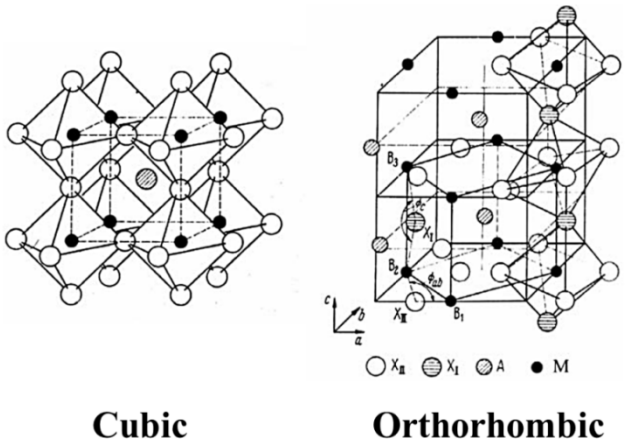

Figure 1.2: *Schematic depicting the lowering of symmetry of the ABO_3 perovskite by the tilting of BO_6 octahedrons* [**30**].

In double perovskites the Goldschmidt tolerance factor slightly changes, due to the nature of the mixed atoms, the modified formula is described as follows[**19**]:

$$t = \frac{r_A + r_0}{\sqrt{2(\langle r_B \rangle + r_0)}} \quad \text{Equation 1.1}$$

Where the $< r_B >$ stands for the average of the B and $B`$ bounding lenghts. According to D. Serrate et al [**19**] for double perovskites the tolerance factor works in a rather different way, for $t > 1.05$ an hexagonal structure is adopted, for $1.05 > t > 1.00$ the compound becomes cubic within the Fm3m space group, for $1.00 > t > 0.97$ the most likely structure corresponds to the $I4/m$ tetragonal space group, and finally, if $t < 0.97$ the compound becomes either monoclinic ($P2_1/n$) or orthorhombic, being this last case the most common for $R_2(MnNi)O_6$ family.

Double perovskites proposed in this study have been synthesized in the literature and their bulk parameters have been also reported. **Table 1.1** shows several important crystallographic parameters including the average bounding angle between Ni-O-Mn atoms in the structure [**17**].

Crystalline distortions play an important role on the functional properties of different perovskites, in general, centrosymmetric unit cells exclude the possibility of ferroelectricity, but allow the appearance of ferromagnetic ordering, In general, one of the advantages of double perovskites is the possibility of tailoring or tuning certain properties, due to the wide variety of cations available. One of these properties is the ferromagnetic ordering.

1.3. Magnetic order in $R(Ni_{0.5}Mn_{0.5})O_3$ perovskites

In order to understand the origin of the magnetism in the $R(Ni_{0.5}Mn_{0.5})O_3$ it is important to discuss the Goodenough-Kanamori rule, first formulated by Goodenough in 1955 [**31**–**33**] and subsequently provided more rigorous mathematical underpinning by Kanamori in 1959 [**34**]. It is applied to interatomic spin-spin interactions between two atoms that are mediated by virtual electron transfers, in this case the formalism is applied for Ni^{2+}-O-Mn^{4+} interactions [**35**,**36**].

LATICCE CONSTANTS

R_2NiMnO_6	**Lattice parameters**	**Ave(°). Ni-O-Mn**
Pr_2NiMnO_6	a = 5.4453(8) Å, b = 5.4701(7) Å, c = 7.6966(1) Å,β = 90.030(3)°, V = 229.257(7) Å^3	158,65
Nd_2NiMnO_6	a = 5.4145(9) Å, b = 5.4842(1) Å, c = 7.6742(1) Å,β = 90.011(2)°, V = 227.883(9) Å^3	157,95
Sm_2NiMnO_6	a = 5.3524(9) Å, b = 5.5119(1) Å, c = 7.6103(1) Å,β = 90.034(3)°, V = 224.522(1) Å^3	152,3
Y_2NiMnO_6	a = 5.2285(1) Å, b = 5.5518(1) Å, c = 7.4872(2) Å,β = 89.744(1)°, V = 217.337(1) Å^3	145,9

Table 1.1: *Lattice constants of RNMO bulk materials and their average angle(Ave(°) Ni-O-Mn) for R=Pr, Nd, Sm & Y*

An easy example is observed in La_2NiMnO_6 double perovskite, where the ferromagnetic interactions are provided by the half-filled e^2 and filled t^6 orbitals on Ni^{2+} and the empty e^0 and half-filled t^3 orbitals in the Mn^{4+} ions [**5**,**37**,**38**]. In this type of perovskites the super exchange is mediated/interrupted by oxygen anions, thus the

direct exchange is weakened, but as compensation the interaction shows ferromagnetic ordering.

In an ideal perovskite, the bounding angle between B-O-B atoms are 180^{O}, in this case interactions are more easily achieved. However, due to the presence of the same e_g orbital filling, such interactions are commonly antiferromagnetic (AFM), as shown **Figure 1.3**. In this case, the $R_2BB`O_6$ perovskites, the ferromagnetic (FM) ordering can be promoted, by choosing the appropriate set of ions, with the conditions aforementioned, B(empty $e_g$ orbital) – O – B`(half-filled e_g orbitals), however it is important to notice that the total magnetization of the system, will be strongly influenced by the tilting of the octahedrons in the unit cell, thus deviating the Ni-O-Mn angle from its maximum ferromagnetic contribution.

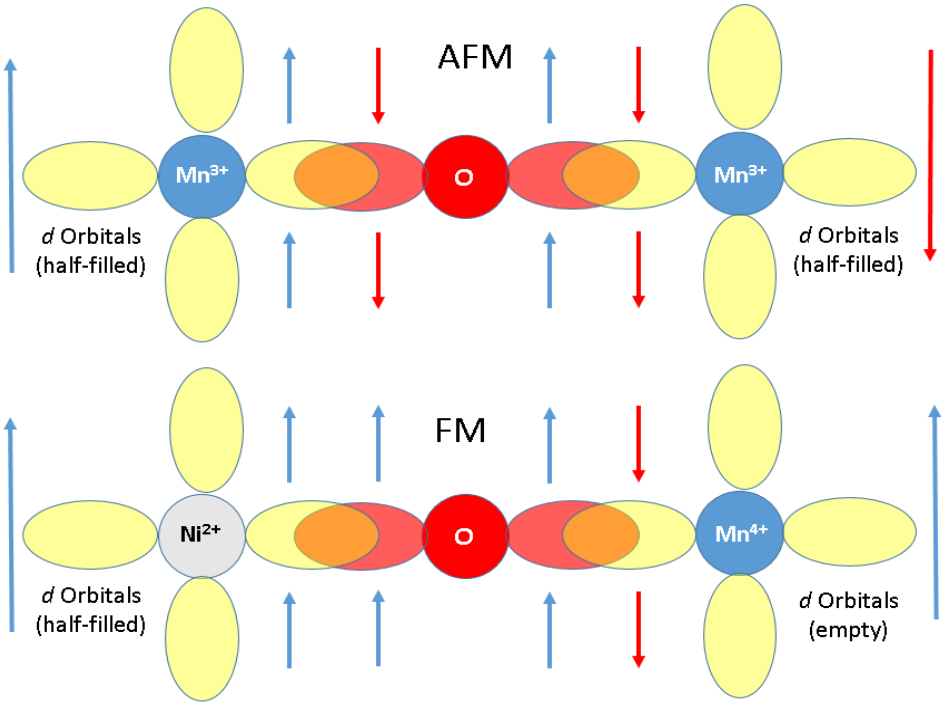

Figure 1.3: *Schematic representation of the superexchange interaction between Mn^{3+} -O- Mn^{3+} (AFM) and Ni^{2+}- O – Mn^{4+} (FM).*

It is worth mentioning that in $RNiMnO_6$ perovskites a second scenario can take place, the Ni^{3+}-O-Mn^{3+}, however in this case the interaction would be more likely antiferromagnetic, similar to the case shown in **Figure 1.3**, due to the half-filled –O-half-filled interactions. Thus, the existence of ferromagnetic response shows some level of the so called B-site ordering, with Ni atoms which only second neighbours is a Mn

atom therefore allowing the superexchange interaction and promoting the ferromagnetic ordering.

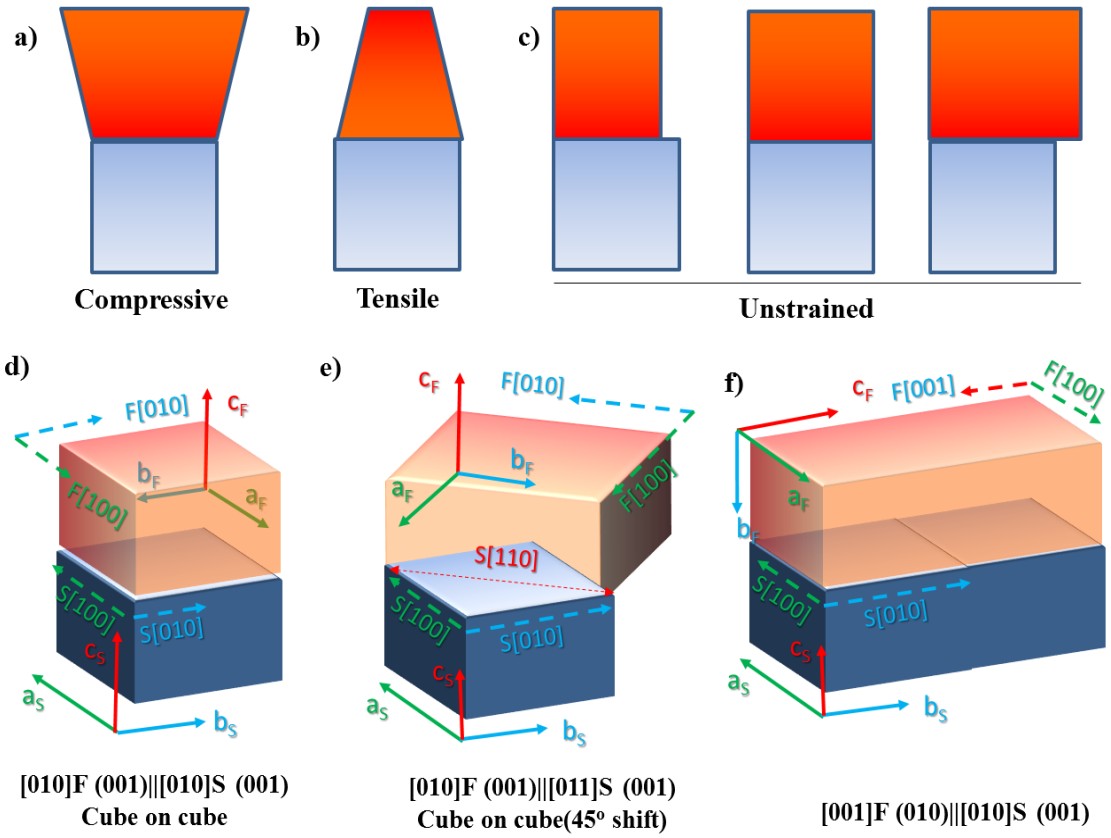

Figure 1.4: *Schematics showing different types of strain a) compressive, b) tensile, c) unstrained, and 3 types of epitaxial relationships, brakets [] show the directions for each crystals in the case of d) cube on cube, e) 45^{O} shifted cube on cube and f) F(010)/S(001) single domain, while parenthesis () refer to the out of plane direction.*

1.4. Epitaxial strain in thin films

Single and double perovskites can be further "tuned" by the so call "epitaxial engineering", this is due to the intrinsic stress that the materials undertake when grown in thin films. The unit cells of the substrate, acts as a grid in which atoms should allocate. When materials are forced to grown on a specific substrate, especially in the case of highly energetic processes such as pulsed laser deposition or sputtering, the growing material adapts its crystalline structure to the one from the substrate. In general, materials with larger unit cell parameters would suffer compressive strains while materials with smaller parameters will elongate. This is not true for all the cases,

since the symmetry of the material being grown would be strongly influenced by a given substrate.

The strain induced by the substrate, strongly depends on the epitaxial relationship of the film respect to the substrate. Epitaxy plays a major role in the tuning of the functional properties of thin films, since they can be enabled (or enhanced). Epitaxy is a term used to address ordinated layers that are grown on crystalline substrates and retain a well-defined crystalline relationship with the substrate. Epitaxial growth can be classified in two types, i) homoepitaxial growth: defined as the growth of similar materials on top of each other, i.e: Si on Si, or Ag on Ag, or ii) heteroepitaxial growth: defined as the growth of two different materials in chemical composition, that may or may not have the same crystalline structure. i.e: GaAs on Si substrate. It is important to mention that epitaxial relationships on thin films can be directly investigated by high resolution transmission electron microscopy (HR-TEM) and indirectly by X-ray diffraction.

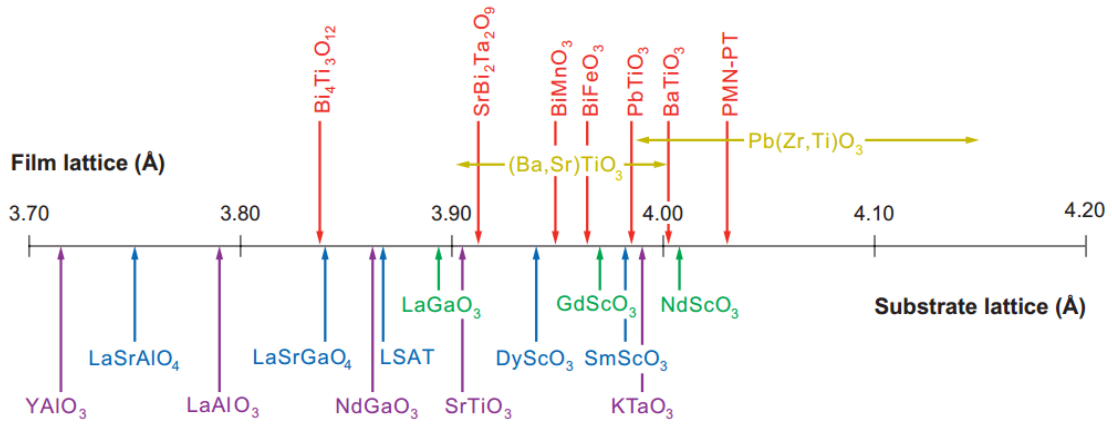

Figure 1.5: *List of some of the perovskite and perovskite-related substrates that are available commercially (below the horizontal line). Red and yellow lines show the materials that can be tuned by the epitaxial strain* [**39**]

As previously mentioned, when a material is grown on top of a crystalline substrate, this will be subjected to compressive or tensile strain. This effect can be appreciated in **Figure 1.4 a,b),** also, depending on the chemistry of the materials and differences of the unit cells, films may present little or no strain, as shown **Figure 1.4 c)**. The unstrained (or relaxed) materials can comprehend several unit cells, in this way after a given number of substrate crystalline units a matching dimensions can be found.

Moreover, there are several cases in which materials will show more complex epitaxial relationships, some of this relationships can be appreciated in **Figure 1.4 d,e,f)**. It is important to remark that some epitaxial relationships can comprehend several unit cells, as in the case of unstrained films, and homoepitaxial thin films that are classified here as unstrained films. Epitaxial relationships are typically presented in the form of [hkl]*film*(hkl)|| [hkl]*Substrate*(hkl), where the index in "[]" refers to the directions, in-plane, that are parallel to each other, while the index in"()" refer to the out of plane direction of both materials.

As shown previously, some functional properties such as ferroelectricity and ferromagnetism, are strongly tightened to the crystalline structure of the material, here is where epitaxial engineering brings an extra tuning possibility, by carefully choosing the substrate (chemistry and lattice parameters) the strain to which the material being grown in thin films can be selected and therefore its functional properties. In **Figure 1.5**, a list of substrates, discriminated by lattice constant, are presented. All the presented substrates are compatible with the perovskite formula and suitable to grow the R_2NiMnO_6 structure.

Epitaxial engineering plays a major role in the tuning of functional properties of different oxides, for this reason is very important to identify the strain that affects a film. In this case strain ε and deformation f, **Equation 1.2 and 1.3** are useful parameters that allow the evaluation of stress in the material.

$$\varepsilon = \frac{a_{film} - a_{substrate}}{a_{bulk}} \qquad \textbf{Equation 1.2}$$

$$f = \frac{l_{film} - l_{bulk}}{l_{bulk}} \qquad \textbf{Equation 1.3}$$

Where a_{film} and $a_{substrate}$ stand for the lattice parameter of both film and subtrate whereas l_{film} and l_{bulk} are related to the lattice parameters of the film respect of is bulk dimensions.

Strain, though, leads to stress in the material, with an energy cost which increases with the increment of thickness, mainly due to the increment of material under stress of the on growing film, with respect to the incoming matter. Due to this, there is a point where it becomes energetically more favorable to release the strain (by means of the formation of dislocations[**40**], crystallographic domains [**41**] or even changing sample

stoichiometry [**42**]). This results in a relaxation of the film, i.e. recovering the bulk lattice parameter. A film is said to be fully relaxed when its structure is identical to that of the bulk. For some applications and materials, especially those exhibiting properties not observed in bulk material, this point is an important parameter to consider.

1.5. Single phase multiferroic perovskites

Multiferroic materials can be classified in some subgroups according to the origin of the ferroelectric ordering in them.

Type I multiferroics: This group is the most numerous; the materials exhibit both ferromagnetism and ferroelectricity usually with a rather large polarization; however both ferroic orderings have distinctive temperature and origin mechanisms. Due to this fact, the magneto electric coupling between ferroic orders is very weak. This group can be further divided in three small sub-groups according to the origin of the ferroelectricity.

i) *Ferroelectric polarization due to long paired electrons*: This group of perovskites takes advantage of the ABO_3 (also in ABB`O3) formula to promote the ferroelectric polarization. As mentioned before, the B site of the perovskite formula is responsible for the magnetic ordering of the structure, while the A site, in this type of multiferroics, is selected to promote the ferroelectricity. The selected atoms are cations with of long pair electrons (i.e. Bi^{3+}, Pb^{3+},…), these are electrons that don't take part in any chemical bound and are responsible for the electric polarization on these materials. Examples of this group are $BiFeO_3$, $BiMnO_3$, $PbMnO_3$ & Bi_2NiMnO_6 [**13**,**15**,**43**]

ii) *Ferroelectricity due to charge ordering*: Charge ordering can occur when cations in the same structural site have difference valence. This mechanism relies on the simultaneous presence of inequivalent sites and bonds. However, how strong the magnetoelectric coupling in this case will be is still an open question. This mechanisms works in $RNiO_3$ and in $TbMn_2O_5$ [**3**,**44**] compounds.

iii) *"Geometric" Ferroelectricity*: Those are materials known as hexagonal manganites, such YMnO3, LuMnO3 & …, in these compounds the tilting of the MnO_5 polyhedrons generates a closer packaging in the perovskite.

As a result, there is a displacement of the oxygen ions to a closer position towards the A ions, thus, promoting the dielectric dipole [**45**].

Type II multiferroics: This group of materials is one of the most promising due to the origin of the multiferroicicity. In this group, the magnetism causes the ferroelectric polarization, thus, implying a strong magnetoelectric coupling. However, the ferroelectric polarization has always low values and appears at rather lower temperature than the magnetic ordering (typically antiferromagnetic).It can be organize in two subgroups:

i) *Spiral magnets*: Ferroelectricity appears in conjunction with a spiraling magnetic phase, mostly of the cycloid type. In this case, ferroelectricity arises in the plane in which the cycloid resides and is perpendicular to the propagation vector of it. This is due to the so-called inverse Dzyloshinsky-Moriya interaction, $P=A\sum r_{ij} \times (S_i \times S_j)$, where r_{ij} is the connecting vector between S_i and S_j spins and A is spin-orbit interaction[**1**].

ii) *Collinear magnets:* In this group all the magnetic moments are aligned along a particular axis in up-up-down-down arrangement (↑↑↓↓). Due to an exchange striction the distortion of ferro and antiferro bounds (↑↑ and ↑↓) is different, and thus the material becomes ferroelectric, due to the ordered dipoles. This case is observed in perovskite compounds such as $HoMnO_3$ [**46**] and pseudo perovskites with octahedral rotations[**47**] such as Ca_3CoMnO_6 [**48**]

1.6. $R(Ni_{0.5}Mn_{0.5})O_3$ (R=Y, Sm, Nd & Pr) perovskites

The magnetic properties of $R(Ni_{0.5}Mn_{0.5})O_3$ (R=Y, Sm, Nd & Pr) have been widely studied in bulk. Kichizo Asai et al [**49**], reported on the magnetic properties of solid solutions of several rare earth (RE) pervoskites, showing that the magnetic ordering of the solutions was ferromagnetic. Their studies also shown a progressive reduction of the Curie temperature (Tc), with the increment of RE atomic radius from La=295K down to Lu=50K, **Figure 1.6 a).** This effect was attributed to the bounding angle (θ) dependence of the superexchange interactions between Me^{2+} and Mn^{4+} through O^{2-}. The dependency turned out to be roughly linear, following $\cos^2 \theta$, with a small deviation for the heavier RE elements **Figure 1.6b).**

Further studies, by C.L Bulle et al [**50**], on the octahedral tilting and distortion of the $R(Ni_{0.5}Mn_{0.5})O_3$ family by Raman spectroscopy demonstrated that the variation on RE atomic radius have no significant influence on the octahedral distortions. However, it is strongly influenced by the octahedral tilting angle in order to maintain the total orbital overlap between the RE^{3+} ions. These results provide insightful information, since the electrical resistivity and the associated band gap are primarily governed by the B-O sublattice. Therefore there is an increase in resistivity and band gap with the decrement of the RE atom due to the higher octahedral tilting.

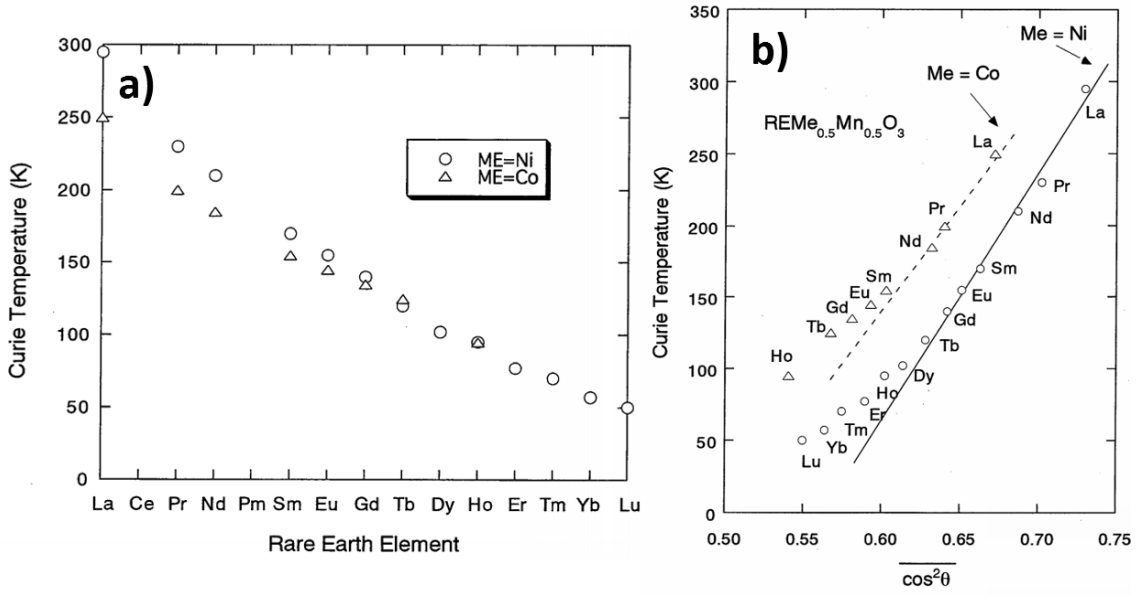

Figure 1.6: *Magnetic characterization of $ReNi_{0.5}Mn_{0.5}O_3$ perovskites a) Re dependence of the Curie temperature an f b) Curie temperature vs cos2 θ* [**50**]

Nevertheless, further experiments performed by R.J. Booth et al [**17**], shown a comprehensive analysis of the unit cell parameters and bound angles Ni-O-Mn for $R(Ni_{0.5}Mn_{0.5})O_3$ compounds, **Table 1.1**. Moreover, in their work, the dielectric constant ε and the loss tan δ was reported, **Table 1.2**, showing a detriment of the dielectric constant as function of the atomic radii. The low values of ε, the loss tan δ and high resistivity of the samples, ~10^7 Ω -cm at 300 K, were attributed to the B-site ordering of the Ni and Mn atoms.

Although promising, very few studies had been done on the stabilization of this perovskites on thin films. One of the studies was performed at the University of Barcelona by E. Langenberg [**51**] in the frame of his PhD thesis [**9**], in which the epitaxial stabilization of Bi_2NiMnO_6 compound, although very difficult, allowed to

conclusively prove the coexistence of ferroelectricity and ferromagnetism in the same crystalline phase in thin films [**12**,**52**]. In the case of the proposed RE elements (plus Y), no epitaxial stabilization was reported for Sm, Pr, and Nd.

Thin films of $YNi_{0.5}Mn_{0.5}O_3$ have been reported previously the literature in two studies. Y. Ma. et al [**53**,**54**], reported the epitaxial stabilization of the compound on STO(001) substrates with a short description of the ferromagnetic response. The studies of thin film properties were further expanded in both morphology and ferromagnetic response two years later[**55**]. The reports showed a cube on cube epitaxial relationship with a 45^0 shift in plane with a T_c similar to the bulk materials. According to their results, the partial substitution of Ni in the $YMnO_3$ structure influenced a different kind of growth than the one observed for un-doped $YMnO_3$. According with results of X. Marti [**21**,**23**], the $YMnO_3$ thin films showed multiple in-plane domains, making it plausible to study epitaxial strain effects. Moreover, the lattice constant values reported for $YNi_{0.5}Mn_{0.5}O_3$ the unit cell showed some variations, but the changes where not so drastic to suggest major differences between the $YMnO_3$ and $YNi_{0.5}Mn_{0.5}O_3$ films.

Microwave dielectric properties of R_2MnNiO_6

R_2NiMnO_6	ε	tan δ
Pr_2NiMnO_6	*23*	0.013
Nd_2NiMnO_6	*22*	0.0073
Sm_2NiMnO_6	*18*	0.0036
Y_2NiMnO_6	*15*	0.004

Table 1.2: *Dielectric constants reported by R.J. Booth et al [**17**] for RNMO bulk*

As it was shown, at the time of this thesis, studies on R_2NiMnO_6 thin films where scare and had left unaddressed some questions.

In an attempt to clarify some of the open issues presented above, the objectives of this thesis can be summarized as follows.

1.7. Objectives of the thesis

This thesis is aimed to understand the following issues:

- ***The effect of Ni partial substitution on the crystalline and functional properties of $YMnO_3$.***
  - To growth thin films of Y_2NiMnO_6 on Strontium Titanate ($SrTiO_3$ -STO) single crystalline substrates with different orientations STO(001),(011) and (111) by Pulsed Laser Deposition.
  - To investigate Ni doped $YMnO_3$ perovskite and its effect on the structure, crystallinity and chemical properties of the films.
  - To determine and investigate the magnetic and dielectric properties of YNMO films deposited on STO(001),(011) and (111)
- ***Synthesis and characterization of $R(Ni_{0.5}Mn_{0.5})O_3$ R=Nd, Pr & Sm, thin films.***
  - To synthesize and stabilize the RNMO perovskites in thin film form by PLD on $SrTiO_3$ substrates.
  - To investigate the effect of deposition temperature on the morphological and crystalline properties of the films is presented and discussed.
  - Determination of the magnetic properties of single crystalline perovskites thin films.
  - To discuss the role of *R* atom on the morphological and crystalline properties of the thin films.
- ***Synthesis and characterization of highly strained of $Bi(Fe_{0.5}Mn_{0.5})O_3$ thin films***
  - To growth highly strained $Bi(Fe_{0.5}Mn_{0.5})O_3$ thin films on $SrTiO_3$(001) substrates by PLD.
  - To study and discuss of the morphological, crystalline and chemical properties of the films.
  - To investigate and discuss the magnetic and dielectric properties of the films.

1.8. Outline of the thesis

Chapter 1. This chapter shows the motivation of this thesis, and then introduces the reader to important concepts such: the perovskite materials, ferroelectric and ferromagnetic orderings, epitaxy and the state of art the field at the starting point of this thesis. At this point the objectives and outline of the thesis are presented.

Chapter 2 introduces the experimental techniques used throughout the thesis; the techniques are introduced with a detailed description of the generalities of the each one

of the techniques, followed by the equipment layout and the protocol used in each technique. Target synthesis is addressed first, then the main thin film growth technique, pulsed laser deposition (PLD) is described and then by the sputtering technique. Then the structural, microstructural, chemical and morphological characterización techniques used are introduced, i.e. X-ray Diffraction, Transmission Electron Microscopy (TEM & HR-TEM), Atomic Force Microscopy (AFM), X-ray Photoelectron Spectroscopy (XPS), Electron Energy Loss Spectroscopy (EELS) and Secondary Ion Mass Spectrometry (SIMS). Finally, functional characterization techniques are presented, Superconducting quantum interference device (SQUID), Vector Network Analyzer Ferromagnetic Resonance (VNA-FMR), Ferroelectric response and Temperature dependent complex Impedance Spectroscopy (IS).

Chapter 3 is devoted to the growth and characterization of YNMO thin films. Films are deposited sweeping a wide variety of parameters such, substrate temperature, laser ablation frequency and oxygen pressure. Then the structural, microstructural, chemical and morphological characterization techniques are used to investigate the crystallinity, epitaxial relationship, growth mechanism, surface morphology and proper stoichiometry for each set of samples. Evidence of a small magnetic anisotropy is observed. Results are discussed and correlated to their growing conditions. Finally, functional characterization investigates the magnetic and dielectric properties of the YNMO thin films with different orientation.

Chapter 4 studies different thin films of $R(Ni_{0.5}Mn_{0.5})O_3$ R=Nd, Pr & Sm grown by PLD on $SrTiO_3(001)$. The effect of deposition temperature on the crystalline properties of the films is studied and their epitaxial relationships determined. Results are discussed focusing on the lattice deformation and epitaxial relationship of the as a function of their cationic compositions. Finally, the magnetic nature of the films is investigated and compared with the bulk counterparts.

Chapter 5 compiles studies performed on $Bi(Fe_{0.5}Mn_{0.5})O_3$ thin films, optimal growth conditions and epitaxial relationship are studied, followed by a XPS analysis of film. Ferromagnetic characterization and VNA analysis addressed the ferromagnetic nature of the film, while impedance spectroscopy aims to characterize the dielectric behaviour of the films.

Finally, a summary of the main conclusions and scientific contributions resulting of this thesis is presented.

Appendixes included are: Target dimensions, lattice parameter determination using XRD data and subtraction of the SrTiO3 diamagnetism from the substrates.

References

[1] Eerenstein, W., Mathur, N.D. and Scott, J.F. (2006) **Multiferroic and magnetoelectric materials.** *Nature*, **442**, 759–65. http://dx.doi.org/10.1038/nature05023

[2] Raghavan, C.M., Kim, J.W., Kim, H.J., Kim, W.J. and Kim, S.S. (2012) **Preparation and properties of rare earth (Eu, Tb, Ho) and transition metal (Co) co-doped BiFeO3 thin films**. *Journal of Sol-Gel Science and Technology*, **64**, 178–83. http://dx.doi.org/10.1007/s10971-012-2845-0

[3] Xiang, H., Wei, S.-H., Whangbo, M.-H. and Da Silva, J. (2008) **Spin-Orbit Coupling and Ion Displacements in Multiferroic TbMnO3**. *Physical Review Letters*, **101**, 037209. http://dx.doi.org/10.1103/PhysRevLett.101.037209

[4] Jehanathan, N., Lebedev, O., Gélard, I., Dubourdieu, C. and Van Tendeloo, G. (2010) **Structure and defect characterization of multiferroic ReMnO(3) films and multilayers by TEM.** *Nanotechnology*, **21**, 75705. http://dx.doi.org/10.1088/0957-4484/21/7/075705

[5] Khomskii, D.I. (2006) **Multiferroics: Different ways to combine magnetism and ferroelectricity**. *Journal of Magnetism and Magnetic Materials*, **306**, 1–8. http://dx.doi.org/10.1016/j.jmmm.2006.01.238

[6] Catalan, G. and Scott, J.F. (2009) **Physics and Applications of Bismuth Ferrite**. *Advanced Materials*, **21**, 2463–85. http://dx.doi.org/10.1002/adma.200802849

[7] Spaldin, N.A. and Fiebig, M. (2005) **Materials science. The renaissance of magnetoelectric multiferroics.** *Science (New York, NY)*, **309**, 391–2. http://dx.doi.org/10.1126/science.1113357

[8] Fiebig, M. (2005) **Revival of the magnetoelectric effect**. *Journal of Physics D: Applied Physics*, **38**, R123–52. http://dx.doi.org/10.1088/0022-3727/38/8/R01

[9] Langenberg Pérez, E. **Growth and characterisation of Bi-based multiferroic thin films** [Internet]. Universitat de Barcelona.

[10] Schmidt, R., Ventura, J. and Langenberg, E. (2012) **Magnetoimpedance spectroscopy of epitaxial multiferroic thin films**. *Physical Review B*, **86**, 035113. http://dx.doi.org/10.1103/PhysRevB.86.035113

[11] Langenberg, E., Fina, I., Ventura, J., Noheda, B., Varela, M. and Fontcuberta, J. (2012) **Dielectric properties of (Bi_{0.9}La_{0.1})_{2}NiMnO_{6} thin films: Determining the intrinsic electric and magnetoelectric response**. *Physical Review B*, **86**, 085108. http://dx.doi.org/10.1103/PhysRevB.86.085108

[12] Langenberg, E., Fina, I., Gemeiner, P., Dkhil, B., Fàbrega, L., Varela, M. et al. (2012) **Ferroelectric phase transition in strained multiferroic (Bi0.9La0.1)2NiMnO6 thin films**. *Applied Physics Letters*, **100**, 022902. http://dx.doi.org/10.1063/1.3675869

[13] Singh, M., Truong, K., Jandl, S. and Fournier, P. (2009) **Long-range Ni/Mn structural order in**

epitaxial double perovskite La2NiMnO6 thin films. *Physical Review B*, **79**, 224421. http://dx.doi.org/10.1103/PhysRevB.79.224421

[14] Hashisaka, M., Kan, D., Masuno, A., Takano, M., Shimakawa, Y., Terashima, T. et al. (2006) **Epitaxial growth of ferromagnetic La[sub 2]NiMnO[sub 6] with ordered double-perovskite structure**. *Applied Physics Letters*, **89**, 032504. http://dx.doi.org/10.1063/1.2226997

[15] Langenberg, E., Rebled, J., Estradé, S., Daumont, C.J.M., Ventura, J., Coy, L.E. et al. (2010) **Long-range order of Ni[sup 2+] and Mn[sup 4+] and ferromagnetism in multiferroic (Bi[sub 0.9]La[sub 0.1])[sub 2]NiMnO[sub 6] thin films**. *Journal of Applied Physics*, **108**, 123907. http://dx.doi.org/10.1063/1.3524278

[16] Lin, Y.Q., Chen, X.M. and Liu, X.Q. (2009) **Relaxor-like dielectric behavior in La2NiMnO6 double perovskite ceramics**. *Solid State Communications*, **149**, 784–7. http://dx.doi.org/10.1016/j.ssc.2009.02.028

[17] Booth, R.J., Fillman, R., Whitaker, H., Nag, A., Tiwari, R.M., Ramanujachary, K.V. et al. (2009) **An investigation of structural, magnetic and dielectric properties of R2NiMnO6 (R=rare earth, Y)**. *Materials Research Bulletin*, **44**, 1559–64. http://dx.doi.org/10.1016/j.materresbull.2009.02.003

[18] Vasala, S. and Karppinen, M. (2014) **A2B′B″O6 perovskites: A review**. *Progress in Solid State Chemistry*,. http://dx.doi.org/10.1016/j.progsolidstchem.2014.08.001

[19] Serrate, D., Teresa, J.M. De and Ibarra, M.R. (2006) **Double perovskites with ferromagnetism above room temperature**. *Journal of Physics: Condensed Matter*, **19**, 023201. http://dx.doi.org/10.1088/0953-8984/19/2/023201

[20] Marti, X. (2009) **Growth and characterization of magnetoelectric YMnO 3 epitaxial thin films**. Autonomus University of Barcelona.

[21] Fina Martínez, I. **Ferroelectricity and magnetoelectric coupling in magnetic ferroelectrics and artificial multiferroic heterostructures** [Internet]. Universitat de Barcelona.

[22] Salvador, P.A., Doan, T.D., Mercey, B. and Raveau, B. (1998) **Stabilization of YMnO3 in a Perovskite Structure as a Thin Film**. *Chemistry of Materials*, **10**, 2592–5.

[23] Martí, X., Sánchez, F., Skumryev, V., Laukhin, V., Ferrater, C., García-Cuenca, M.V. et al. (2008) **Crystal texture selection in epitaxies of orthorhombic antiferromagnetic YMnO3 films**. *Thin Solid Films*, **516**, 4899–907. http://dx.doi.org/10.1016/j.tsf.2007.09.023

[24] Prokhorov, V.G., Kaminsky, G.G., Kim, J.M., Yoo, Y.J., Lee, Y.P., Svetchnikov, V.L. et al. (2012) **Evidence of the Griffiths phase in multiferroic BiMnO3 and BiFe0.5Mn0.5O3 films**. *Low Temperature Physics*, **38**, 413. http://dx.doi.org/10.1063/1.4709440

[25] Mouallem-Bahout, M., Roisnel, T., André, G., Gutierrez, D., Moure, C. and Peña, O. (2004) **Nuclear and magnetic order in Y(Ni,Mn)O3 manganites by neutron powder diffraction**. *Solid State Communications*, **129**, 255–60. http://dx.doi.org/10.1016/j.ssc.2003.09.039

[26] Macedo Filho, R.B., Pedro Ayala, A. and William de Araujo Paschoal, C. (2013) **Spin-phonon**

coupling in Y2NiMnO6 double perovskite probed by Raman spectroscopy. *Applied Physics Letters*, **102**, 192902. http://dx.doi.org/10.1063/1.4804988

[27] Kakarla, D.C., Jyothinagaram, K.M., Das, A.K. and Adyam, V. (2014) **Dielectric and Magnetodielectric Properties of R 2 NiMnO 6 (R = Nd,Eu,Gd,Dy, and Y)**. Viehland D, editor. *Journal of the American Ceramic Society*, Blackwell Publishing Inc. **97**, 2858–66. http://dx.doi.org/10.1111/jace.13039

[28] Cortie, D.L., Stampfl, a. P.J., Klose, F., Du, Y., Wang, X.L., Zhao, H.Y. et al. (2012) **The magnetic structure of an epitaxial BiMn[sub 0.5]Fe[sub 0.5]O[sub 3] thin film on SrTiO[sub 3] (001) studied with neutron diffraction**. *Applied Physics Letters*, **101**, 172404. http://dx.doi.org/10.1063/1.4762818

[29] Buttner, R.H. and Maslen, E.N. (1992) **Structural parameters and electron difference density in BaTiO3**. *Acta Crystallographica Section B Structural Science*, International Union of Crystallography. **48**, 764–9. http://dx.doi.org/10.1107/S010876819200510X

[30] Goodenough, J.B. and Zhou, J.-S. (2007) **Orbital ordering in orthorhombic perovskites**. *Journal of Materials Chemistry*, **17**, 2394. http://dx.doi.org/10.1039/b701805c

[31] Goodenough, J.B. (1955) **Theory of the Role of Covalence in the Perovskite-Type Manganites [La , M (II)] Mn O 3**. *Physical Review*, **100**, 564–73. http://dx.doi.org/10.1103/PhysRev.100.564

[32] Goodenough, J.B. (1997) **Electronic structure of CMR manganites (invited)**. *Journal of Applied Physics*, **81**, 5330. http://dx.doi.org/10.1063/1.364536

[33] Goodenough, J.B. (2004) **Electronic and ionic transport properties and other physical aspects of perovskites**. *Reports on Progress in Physics*, **67**, 1915–93. http://dx.doi.org/10.1088/0034-4885/67/11/R01

[34] Kanamori, J. (1959) **Superexchange interaction and symmetry properties of electron orbitals**. *Journal of Physics and Chemistry of Solids*, **10**, 87–98.

[35] Peña, O., Barahona, P., Gil, V., Tartaj, J. and Moure, C. (2008) **Magnetic behavior of solid solutions REMe0.50 Mn0.50 O3 (RE = Y, La, Pr, Nd, Eu, Gd, Er; Me = Ni,Co)**. *Boletin de La Sociedad Espanola de Ceramica Y Vidrio*, **47**, 138–42.

[36] Sharma, G., Tripathi, T.S., Saha, J. and Patnaik, S. (2014) **Magnetic entropy change and critical exponents in double perovskite Y2NiMnO6**. *Journal of Magnetism and Magnetic Materials*, Elsevier. **368**, 318–23. http://dx.doi.org/10.1016/j.jmmm.2014.05.035

[37] Belik, A. a. (2013) **Origin of magnetization reversal and exchange bias phenomena in solid solutions of BiFeO3-BiMnO3: intrinsic or extrinsic?** *Inorganic Chemistry*, **52**, 2015–21. http://dx.doi.org/10.1021/ic302384j

[38] Bi, L., Taussig, A., Kim, H.-S., Wang, L., Dionne, G., Bono, D. et al. (2008) **Structural, magnetic, and optical properties of BiFeO3 and Bi2FeMnO6 epitaxial thin films: An experimental and first-principles study**. *Physical Review B*, **78**, 104106. http://dx.doi.org/10.1103/PhysRevB.78.104106

[39] Schlom, D.G., Chen, L.-Q., Eom, C., Rabe, K.M., Streiffer, S.K. and Triscone, J. (2007) **Strain tuning of ferroelectric thin films**. *Annual Review of Materials Research*, **37**, 589–626. http://dx.doi.org/10.1146/annurev.matsci.37.061206.113016

[40] Matthews, J.W. and Blakeslee, A.E. (1974) **Defects in epitaxial multilayers**. *Journal of Crystal Growth*, **27**, 118–25. http://dx.doi.org/10.1016/S0022-0248(74)80055-2

[41] Pompe, W., Gong, X., Suo, Z. and Speck, J.S. (1993) **Elastic energy release due to domain formation in the strained epitaxy of ferroelectric and ferroelastic films**. *Journal of Applied Physics*, **74**, 6012. http://dx.doi.org/10.1063/1.355215

[42] Estradé, S., Arbiol, J., Peiró, F., Abad, L., Laukhin, V., Balcells, L. et al. (2007) **Cationic diffusion in La[sub 2⁄3]Ca[sub 1⁄3]MnO[sub 3] thin films grown on LaAlO[sub 3] (001) substrates**. *Applied Physics Letters*, **91**, 252503. http://dx.doi.org/10.1063/1.2799740

[43] Sakai, M., Masuno, A., Kan, D., Hashisaka, M., Takata, K., Azuma, M. et al. (2007) **Multiferroic thin film of Bi[sub 2]NiMnO[sub 6] with ordered double-perovskite structure**. *Applied Physics Letters*, **90**, 072903. http://dx.doi.org/10.1063/1.2539575

[44] Hur, N., Park, S., Sharma, P. a, Ahn, J.S., Guha, S. and Cheong, S.-W. (2004) **Electric polarization reversal and memory in a multiferroic material induced by magnetic fields.** *Nature*, **429**, 392–5. http://dx.doi.org/10.1038/nature02572

[45] Van Aken, B.B., Palstra, T.T.M., Filippetti, A. and Spaldin, N. a. (2004) **The origin of ferroelectricity in magnetoelectric YMnO3.** *Nature Materials*, **3**, 164–70. http://dx.doi.org/10.1038/nmat1080

[46] Lee, N., Choi, Y.J., Ramazanoglu, M., Ratcliff, W., Kiryukhin, V. and Cheong, S.W. (2011) **Mechanism of exchange striction of ferroelectricity in multiferroic orthorhombic HoMnO 3 single crystals**. *Physical Review B - Condensed Matter and Materials Physics*, **84**, 3–6. http://dx.doi.org/10.1103/PhysRevB.84.020101

[47] Islam, M. a, Rondinelli, J.M. and Spanier, J.E. (2013) **Normal mode determination of perovskite crystal structures with octahedral rotations: theory and applications**. *Journal of Physics: Condensed Matter*, **25**, 175902. http://dx.doi.org/10.1088/0953-8984/25/17/175902

[48] Choi, Y.J., Yi, H.T., Lee, S., Huang, Q., Kiryukhin, V. and Cheong, S.W. (2008) **Ferroelectricity in an ising chain magnet**. *Physical Review Letters*, **100**, 6–9. http://dx.doi.org/10.1103/PhysRevLett.100.047601

[49] Asai, K., Fujiyoshi, K., Nishimori, N., Satoh, Y., Kobayashi, Y. and Mizoguchi, M. (1998) **Magnetic Properties of REMe 0.5Mn 0.5O 3 (RE = Rare Earth Element, Me = Ni, Co)**. *Journal of the Physical Society of Japan*, The Physical Society of Japan. **67**, 4218–28. http://dx.doi.org/10.1143/JPSJ.67.4218

[50] Bull, C.L. and McMillan, P.F. (2004) **Raman scattering study and electrical properties characterization of elpasolite perovskites Ln2(BB′)O6 (Ln=La, Sm...Gd and B,B′=Ni, Co, Mn)**. *Journal of Solid State Chemistry*, **177**, 2323–8. http://dx.doi.org/10.1016/j.jssc.2004.02.022

[51] Langenberg, E., Varela, M., García-Cuenca, M. V., Ferrater, C., Polo, M.C., Fina, I. et al. (2009) **Epitaxial thin films of (Bi0.9La0.1)2NiMnO6 obtained by pulsed laser deposition**. *Journal of*

Magnetism and Magnetic Materials, **321**, 1748–53. http://dx.doi.org/10.1016/j.jmmm.2009.02.005

[52] Langenberg, E., Fina, I., Ventura, J. and Noheda, B. (2012) **Dielectric properties of (Bi 0.9 La 0.1) 2 NiMnO 6 thin films: Determining the intrinsic electric and magnetoelectric response**. *Physical Review B*, **86**, 085108. http://dx.doi.org/10.1103/PhysRevB.86.085108

[53] Ma, Y., Guilloux-Viry, M., Pena, O. and Moure, C. (2004) **Y(Ni, Mn)O3 epitaxial thin films prepared by pulsed laser deposition**. *Physica Status Solidi (a)*, **201**, 2385–9. http://dx.doi.org/10.1002/pssa.200304911

[54] Ma, Y., Guilloux-Viry, M., Barahona, P., Peña, O., Moure, C., Ghilane, J. et al. (2006) **YNixMn1−xO3 thin films by pulsed laser deposition: Structure and magnetic properties**. *Thin Solid Films*, **510**, 275–9. http://dx.doi.org/10.1016/j.tsf.2005.12.159

[55] Ma, Y., Guilloux-Viry, M., Barahona, P., Peña, O. and Moure, C. (2005) **Annealing effects on the microstructure and properties of Y(Ni,Mn)O3 thin films**. *Journal of the European Ceramic Society*, **25**, 2147–50. http://dx.doi.org/10.1016/j.jeurceramsoc.2005.03.061

CHAPTER 2

Experimental Techniques

The following chapter focuses on the experimental techniques used in the development of this thesis. The thin film technology used on the production of the samples would be addressed first, and then the characterization techniques employed throughout this work would be presented. Finally the functional characterization techniques used and some techniques that have assisted specific studies will be mentioned.

2.1 Target Synthesis

Target synthesis was carried out in the Chemistry Faculty/ Department of Material Science at University of Barcelona by Dr. Elena Xurriguera. A solid state reaction of a stoichiometric mixture of commercially available oxides was used for the whole $R(Ni_{0.5}Mn_{0.5})O_3$ (R=Y, Pr, Nd &Sm) family of materials. In the case of $Bi(Fe_{0.5}Mn_{0.5})O_3$ an extra 10% of bismuth is added to the mixture in order to compensate from loses during preparation. Dimensions are shown in **Appendix 1**.

2.1.1 Synthesis Protocol

- For a given material, a stoichiometric mixture of commercially available pure oxides is prepared.
- Material is mixed manually in a mortar for up to 10 minutes.
- Material is placed in a commercially available silica pellet (each target composition would use an especially dedicated pellet to avoid contamination).

- Material is gently compressed to promote interactions.
- Pellet is calcined at 900°C for 12 hours in air.
- Pulverization process takes place using mortar.
- Thoroughly mixing is carried out, for 5 to 10 minutes.
- Second thermal treatment take place, this time the temperature is 1000°C for 8 hours in air.
- Second pulverization and mixing is carried out.
- A hydraulic piston is used in order slowly compress the target (at a maximum pressure of 37 MPa).
- Finally thermal treatment takes place at a temperature of 1200°C for 6 hours in air.
- Target stoichiometry is controlled by XPS analysis, technique that is later described in this text.
- Integrity of the target is tested in the PLD equipment by shooting 300-500 pulses at room temperature and gas base pressure of $9*10^{-4}$ mbar.
- Extra treatment at 900°C for 12 hours in air is used if the target is broken after the whole process. This extra thermal process is also used to re solidify any broken targets after carefully wearing exposed surfaces.

2.2 Growth Techniques

In this section the pulsed laser deposition (PLD) technique and the specific apparatus used to growth $R(Ni_{0.5}Mn_{0.5})O_3$ (R=Y, Pr, Nd & Sm) and $Bi(Fe_{0.5}Mn_{0.5})O_3$ thin films would be described. Later on, the RF sputtering used to growth top metallic electrodes will be also described. Films were growth within the group`s laboratory at Department of Applied Physics and Optics, University of Barcelona.

2.2.1 Pulsed Laser Deposition (PLD)

2.2.1.1 Technique description

Pulsed Laser Deposition is a wide used and well known deposition technique used in thin films growth of wide variety of materials for nearly 60 years. In this technique the material is emitted from the target in the form of plasma or plume by an incident pulsed laser beam. The material is then deposited in a substrate that is commonly placed parallel to the target in a vacuum chamber[**1**]. Excimer lasers are typically the ones used in pulsed laser ablation, this comes from the mid-seventies when it was discovered that a combination of two identical atoms (Dimers) like Ar^*, Kr^* or F^* could generate a strong ultraviolet (UV) pulsed beam under electric excitation. Due to the UV nature of the beam, the energy from the laser is absorbed by the materials generating a well-

known plume [**2**,**3**]**.** The wavelength of these laser beams depends on the elements that are being excited in the system coming from 126 nm for Ar_2^* to and 337 nm for N_2. **(Table 2.1).**

EXCIMER LASERS WAVELENGHT

Gasses	Wavelength
Ar_2*	126 nm
Kr_2*	146 nm
ArF	193 nm
KrF	248 nm
XeBr	282 nm
XeCl	308 nm
N_2	337 nm

Table 2.1: *Different wavelengths in various excimer atomic configurations.*

It has been shown that the wavelength of the incident beam can affect the properties of the deposited film [**4**–**6**] and has also has an intrinsic relation with the ablation threshold in metals and dielectrics [**7**]. Moreover it is very clear is that the wavelength is determining in the ablation process where smaller ones would lead to a better absorption of the beam and less thermal diffusion on the target. PLD systems based on KrF lasers are widely used due to the fulfillment of these characteristics; its beam has the perfect wavelength, which is big enough to prevent excessive interactions with the O_2 in the atmosphere and is small enough to show a good absorption on the ablated materials and a low thermal dispersion. In addition, PLD has two more important characteristics that grant it special properties: the elevate kinetic energy of the produced species during the ablation process and the also high deposition rate.

The **Table 2.2**, compare the typical values of PLD with other known values from other physical techniques, such thermal evaporation and sputtering. As it can be observed, the kinetic energy of the ablated species is approximately one order of magnitude higher for PLD than from cathode pulverization and two orders in the case of thermal evaporation. High energetic particles contribute to film quality by different means; these highly energetic particles are the result of a quick transformation between solid state to plasmatic, which for oxide films is very important due to their role in the stoichiometric growth and crystalline properties of the film. Moreover the quick growth

rate would imply the rapid crystallization or "solidification" of the plasmatic material arriving to the substrate, leading to a wide range of potential metastable phases and materials [**7**–**9**].

COMPARATION OF TECHNIQUES

Technique	Kinetic Energy (eV)	Growth Rate ($nm*s^{-1}$)
Thermal Evaporation	<1	0.01 to 0.1
Cathode Pulverization	5-10	0.1 to 1.0
PLD	10-100	10^3 to10^4

Table 2.2: *Data of the kinetic energy of particles arriving to the substrate and their growth rate on the vapor phase*[**10**]**.**

Deposition process can be explained in three main steps [**2**,**3**,**11**], **i)** Laser parameters, some of the parameters that are strongly related with this step are the photon energy and fluence; this can be described by the formula: F= J/cm^2 where F represents the fluence in terms of the laser beam energy over the spot area; fluence is a very important parameter that allows to generate a correct ablation regime, higher fluencies lead to a higher number of energetic particles and some undesirable effects whereas, in contrast, lower fluencies lead to thermal evaporation and poor stoichiometry, moreover multiple properties and characteristics of the materials are strongly related to the fluence used on the deposition process[**12**,**13**]. **ii)** Ejection of material is the step when the plume is generated and after the interaction laser-matter, at this stage some parameters such as plume shape and flying distance are important to take into account; metallic materials would have a strong tendency to present melting areas due to their high diffusion and energetic transport, even though some deflection of the energy has been observed. These effects demand a meticulous selection of parameters since very high fluence values have been known to increase the droplet ejections in metals whereas lower energy favors the thermal evaporation of the materials. Furthermore, flying times and the energetic value of the extracted ions, which are strongly related to the energetic fluence, are determining in the appearance of dislocation and imperfections on the deposited film [**14**,**15**]. The final stage of the process is the arriving material from the target to complete the **iii)** Film deposition, when the material arrive to the surface of the substrate in the form of energetic particles the adhesion process takes place. Depending on the chemistry, temperature and

crystallographic orientation of the substrate different features such as epitaxy, adhesion and dislocations can be controlled and ultimately used to obtain materials with specific properties and characteristics.

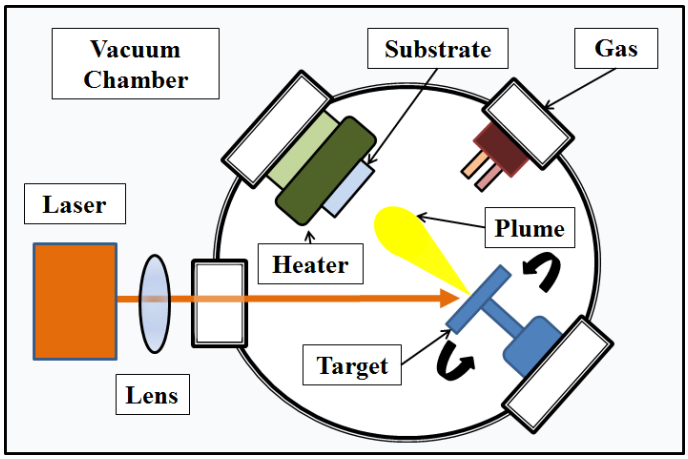

Figure 2.1: *Schematic representation of a typical Pulsed Laser Deposition (PLD) system.*

Once the ejected material arrives to the substrate the nucleation process takes place. The properties of a thin film of a given material would be affected not only by its chemistry but also many parameters such substrate temperature [**16**,**17**]and ablation rate [**9**] play an important role in this technique and crucial on the film growth process. These parameters would couple with the so called epitaxial engineering, described in the previous chapter, where the carefully selection of substrates and materials allow to the appearance of new properties, mainly due to the epitaxial strain involved.

Films grown by PLD take advantage of the multiple tunable parameters in order to obtain different materials and metastable phases. The highly energetic particles provided by the intense laser beam, would receive extra kinetic energy from the substrate that is usually heated above 500 C^{O}, this extra energy allows surface diffusion and couples with the add atom energy to promote nucleation substrate surface making this technique very suitable for growing complex materials where excellent stoichiometric is crucial and high quality films are desirable. The typical schematics of a PLD the deposition chamber are shown in **Figure 2.1**.

2.2.1.2 PLD Apparatus

The films in this thesis were grown in a PLD system on the Department of Applied Physics and Optics at University of Barcelona, in the GECFE group (Thin films for Spintronics Applications) under the direction and supervision of Prof. Manuel Varela.

The PLD system works with a KrF excimer laser from Lambda Physik LPX205i, working with a wavelength of $\lambda = 248$ nm and pulse duration of 34 ns. The laser has an optical pathway of around 4 meters. A rectangular mask is used at a distance of around 1.5 meters before the PLD`s vacuum chamber in order to reshape the laser beam and get rid of its near-Gaussian borders and keep the homogeneous plateau with the aim of guarantee the uniform ablation and energy distribution of the incident laser beam. The laser beam is focused by commercially available AR-coated convex lens, mounted on a platform with three degrees of freedom, manually controlled by micrometric screws, lens are placed at about 5 cm outside the vacuum chamber. **Figure 2.2 (a)** shows the actual equipment used to growth the samples.

All targets used in the system have cylindrical shape; circumferences ranging from 2.5 to 1.5 cm are the norm, with variable thickness, no bigger than 0.8 cm. Targets are placed on an automatic spinning carrousel with 4 slots for multilayered samples. The laser path inside the chamber is described by the **Figure 2.2 (b)**, where the way to the carrousel is described by the strapped lines; the path length is of about 20 cm with an approximately angle of 30^{O} [1], all the targets are manually polished between deposits in order to guarantee the material stoichiometry and the linear ejection of material. Once the ablation process takes place, the plume travels a constant distance for each experiment **Figure 2.2 (c)**, this parameter can be tuned by the micrometric screws that are attached to the heater, these screws provide three degrees of freedom, allowing to the pertinent correction on aim of the plume ejection.

The heater system is controlled by a standard thermocouple attach to a PID system in order to maintain a constant temperature during the ablation process, temperatures range from few tens of Celsius to a maximum of $900^{O}C$. The vacuum

[1] This angle may vary depending on previous users; since it is not as a tunable parameter, it is considered as an unintentional displacement between users during use. However, since the plume follows the targets surface's normal vector, and this is a constant whenever the inflection angle changes or not, also the fluency is calculated with the projected spot, this changes are considered as neglectable.

chamber works with a turbo molecular pump, coupled to a mechanical pump, fully automatized reaching a maximum vacuum of $5*10^{-5}$ mbar. Gas pressure is controlled with electronic mass flow equipment and assisted manually by the turbo molecular by-pass, this is done in order to help the oxygen pressure build inside the chamber. Finally the oxigen gas used has a purity of 99.99995% and the working pressure is in the range of $1*10^{-1}$ and $9*10^{-1}$.

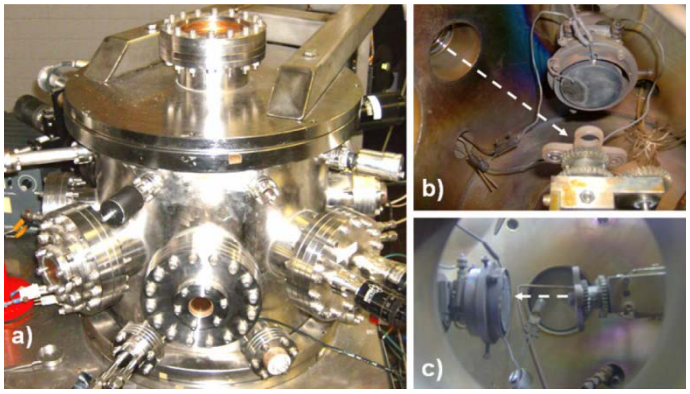

Figure 2.2: *Pulsed Laser Deposition. a) Vacuum chamber. b) Internal set up and laser interaction with the ablation target. C) Flight distance from the target to the substrate holder.*

2.2.1.3 PLD Deposit Protocol

- Laser chamber must be refilled after 60.000 pulses.
- If volatile atoms were deposited before, a pre vacuum process is needed to clean the chamber.
- Path way mask is checked before any set of experiments.
- Values of the micrometric screws on the lens are replicated and spot size tested by thermal fax paper.
- Heater is placed in the approximately plume center.
- Target is manually polished.
- Few hundred pulses are shooting in the same vacuum conditions as the first experiment schedule in order to determine the plume center. (No substrate is used at this point).
- After determining the ablation center, the substrate is place in the respective ablation spot.
- The target is manually polished, with the shutter closed, in order to avoid deposit on the substrate 300 pulses are shoot to clean any residual of sand paper on the target or poor stoichiometric material.
- Vacuum pumps are activated and allowed to reach the maximum vacuum possible in the system in order to clean the chamber. a value under $9*10^{-5}$ is standard.

- Mass flow is partially set to reach any pressure close to the working pressure. Typically $5*10^{-1}$ mbar.
- Once the pressure inside the chamber is stable, the heater and current source are activated and set to the working temperature.
- Final adjustments of oxygen pressure and mass flow take place.
- Deposition phase.
- Temperature is turn down.
- After the temperature reaches $400^{O}C$ the vacuum pump by pass is closed and the pumps turned off.
- Oxygen by pass is completely open till temperature is below $60^{O}C$ (for sample removal).
- Chamber is left in vacuum between deposits.

2.2.2 RF Sputtering deposition

2.2.2.1 Technique description

This physical technique is shortly described in this work due to its single and specific in this thesis, also because of is common use in the field and in our group. RF sputtering is applied in this thesis in order to growth platinum top electrodes used in the dielectric characterization of multiple samples [**18**].

RF sputtering is a widely used technique for long area deposition of material; the process is carried out due to the impact of highly energetic particles on the targets surface **Figure 2.3**. In this process, ions are extracted from a glow discharge (plasma). Through momentum transfer from the incident ions on the material, atoms are ejected or sputtered from the target upon impact with the cathode. These atoms travel from the target to the substrate, acting as anode, assisted by the plasma, typically Argon (Ar^{+}) is used for metallic films such as platinum, in order to condensate onto the substrate. Also it is important to note that this technique is effective in the case of conductive and none conductive targets, the contrary of DC sputtering which is technologically simpler, but allows only conductive targets to be used [**8**].

RF voltage is applied to the electrodes in order to promote the glow of the argon gas in the chamber. At lower voltages the collisions are insufficient to ignite the plasmatic state of the argon gas, it is only when high enough voltages and a high enough gas pressure is applied that the secondary electrons and sputtered atoms from the targets surface start ionizing the argon gas in Ar^{+}, the so called mean free path of the sputtered electrons and ions has to be large enough to allow the plasmatic state to take place,

energy exchange, and sufficiently short to prevent excessive collisions that can frustrate the glow of the plasma. When the self-sustained plasmatic state is achieved and a visible light emission is observed the material transfer is taking place. Also, as it can be expected, one of the main parameters in this technique is the applied voltage, it is direct responsible of the energy of Ar+ ions and homogeneous area of ablation on the cathode.

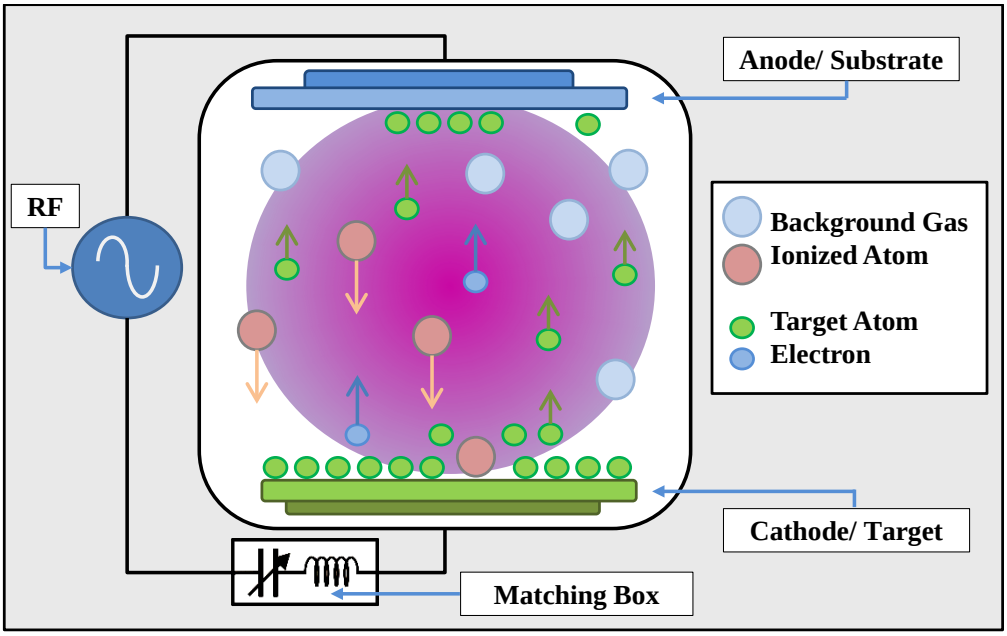

Figure 2.3: *Schematic representation of a typical r.f. sputtering system.*

It is common protocol to start the plasma with a shutter acting as anode in order to control the deposition time that in our case will be used to control the electrode thickness by a given voltage.

2.2.2.2 RF Sputtering apparatus

Top electrodes were grown on the Department of Applied Physics and Optics at University of Barcelona, in the GECFE group (Thin Films for Spintronics Applications) under the direction and supervision of Prof. Manuel Varela by a simple shadow mask technique.

The actual RF sputtering system used in this thesis is shown in **Figure 2.4**, it counts with 2" circular magnetron sputter source from Kurt J. Lesker Coimpany with a KJLC RF Generator, Automatic Matching Network, and Controller power source attached to it. The target used was a commercially available platinum disc 1/8" thick,

diameter 2" and of 99.9995% purity, kept in the maximum vacuum, between deposits. The vacuum chamber is pumped by a turbo molecular pump backed by a mechanical pump, reaching a maximum vacuum of $4\text{-}6*10^{-7}$ mbar.

The system can be used also for PLD deposits[2] it counts with rectangular mask at the beam`s output from the laser equipment and a second mask at around 50 cm before the vacuum chamber in order to reshape the laser beam and get rid of its near-Gaussian borders and keep the homogeneous plateau. The laser beam is focused by commercially available AR-coated convex lens, mounted on a platform with three degrees of freedom, manually controlled by micrometric screws, and lens are placed at about 5 cm outside the vacuum chamber.

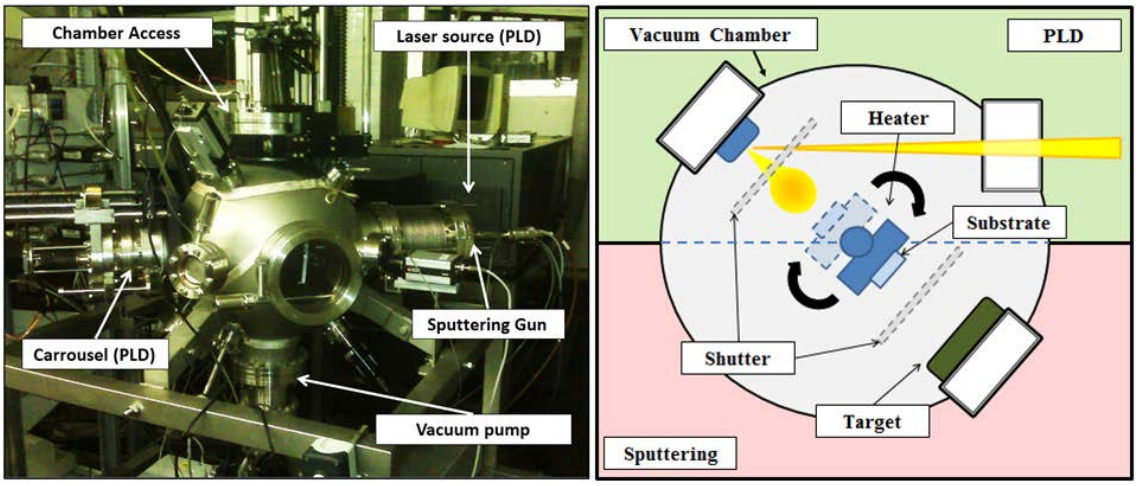

Figure 2.4: *Left side, image of the Sputtering system in the GEFCE group at university of Barcelona. Right side, schematic representation of the inside of the sputtering chamber. Green shaded part refers to the PLD capabilities of the system while light red shaded part corresponds to the sputtering system.*

The chamber has a standard heater controlled by a PID system with a thermocouple sensor. The heater is able to reach temperatures up to 900^{O}C and is mounted on four degrees of freedom clamp controlled by three micrometric screws and a simple knob that controls the spinning around the *z* axis to allow deposits from the PLD or the Sputtering system. Each technique has a shutter that can be used to block and protect either the substrate or the targets not in use.

[2] During the development of this thesis this feature was never used. This protocol was adopted in order to avoid contamination by volatile atoms.

Argon pressure has to be stabilizing manually by a mass flow standard device and by closing the turbo molecular by pass on the chamber. The gas comes from a general line in the building and it has a 99.9995% of purity.

2.2.2.3 RF Sputtering Deposit Protocol

- Lock the vacuum by pass and turn off vacuum pumps
- Ventilate the chamber with pure Ar till atmospheric pressure
- Samples are attached to the heater mechanically or by silver paste, according with the specific application.
- Pump the chamber till reaching a pressure of $1*10^{-5}$ mbar.
- Set the working Argon pressure, till reaching the proper ignition pressure, typically $3*10^{-2}$ mbar.
- Close the shutter to prevent unintentional sputtering.
- Set working voltage, adjust the impedance matching box and activate RF power source.
- Start Plasma
- Reduce argon pressure, to the desired working pressure. (Typically $3*10^{-3}$ mbar).
- Remove the shutter.
- Deposition phase.
- Close the Shutter
- Stop RF source.
- Stop Argon gas
- Ventilate chamber till ambient pressure in order to remove samples
- Leave empty chamber in maximum vacuum.

2.3 Characterization Techniques

2.3.1 X-Ray characterization techniques

2.3.1.1 X-Ray Diffraction (XRD)

X-Ray diffraction, XRD, is a nondestructive technique widely used to characterize thin films. This technique relays on the particularity that the X-ray wavelength, of the order of Å, is within the length of inter-planar distances in the crystals that compose the thin film. XRD is used to find structural and chemical information of crystalline materials by irradiating them with an X-ray (usually from a Cu source λ=1.5405 Å) beam that penetrates them in depth, allowing the precise measurement of characteristics such as the lattice constants, crystal orientation and generally, the crystallographic

structure and quality of each material. The measuring consists on projecting an X-ray beam with a determined wavelength onto a crystalline material at a certain angle. The crystalline properties of every material added to the interaction between the X-ray beam within its atomic planes, produces a diffraction-interference pattern that is recorded and afterwards is studied to obtain the structural information searched. The angles of incidence over the sample increase and reduce their magnitude while scanning the entire range of possible crystalline structures and/or orientations. XRD experiments on thin film samples allow finding useful information about the coordination of the atomic distribution between the substrate and the film, that is, the lattice parallelism between both materials, allowing the measurement of the orientation of the crystalline material growth [**19**,**20**].

When an incident X-ray beam, ideally monochromatic, interacts with a given material, it produces an interference pattern that follows the Bragg`s law, it means that a material diffracting the X-ray beam would produce an intense peak at define angle of incidence due to the constructive response of parallel planes interfering with the beam. The **Equation 2.1** explains this phenomenon by a given wavelength.

$$2d \cdot \sin\Theta = m\lambda \quad \textbf{Equation 2.1}$$

Where d is the distance between planes in the crystal lattice, θ is the angle of the incident x-ray beam, m is an integer related to the diffraction order and λ is the X-ray's wavelength. As can be observed different parallel configurations would generate intense peaks at different angles. **Figure 2.5** illustrates this behavior on a crystalline structure.

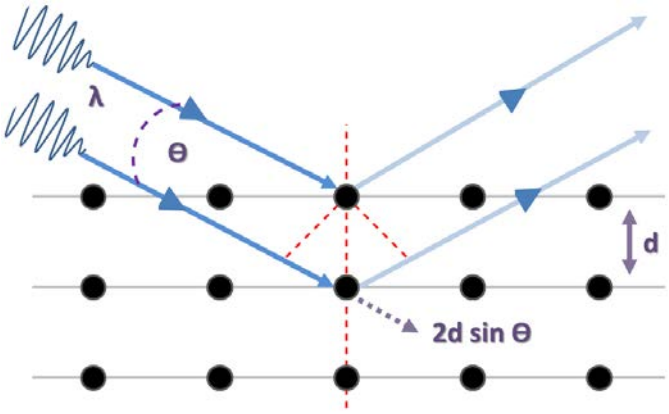

Figure 2.5: *Schematic representation of an incident X-ray on a crystalline structure.*

The *m* integer of the equation is related to the Miller index, which means is related to the spacing between primary diffraction peaks and secondary peaks. This is very important since a known distance between primary reflections and higher order diffractions allow to easily identifying crystalline structures on the samples. In a polycrystalline sample, many families of crystals are randomly organizing parallel to the substrate plane. So by swiping the θ angle in what is known as a θ-2θ scan, all out of plane crystalline orientations will be identifying by their known interplanar distances.

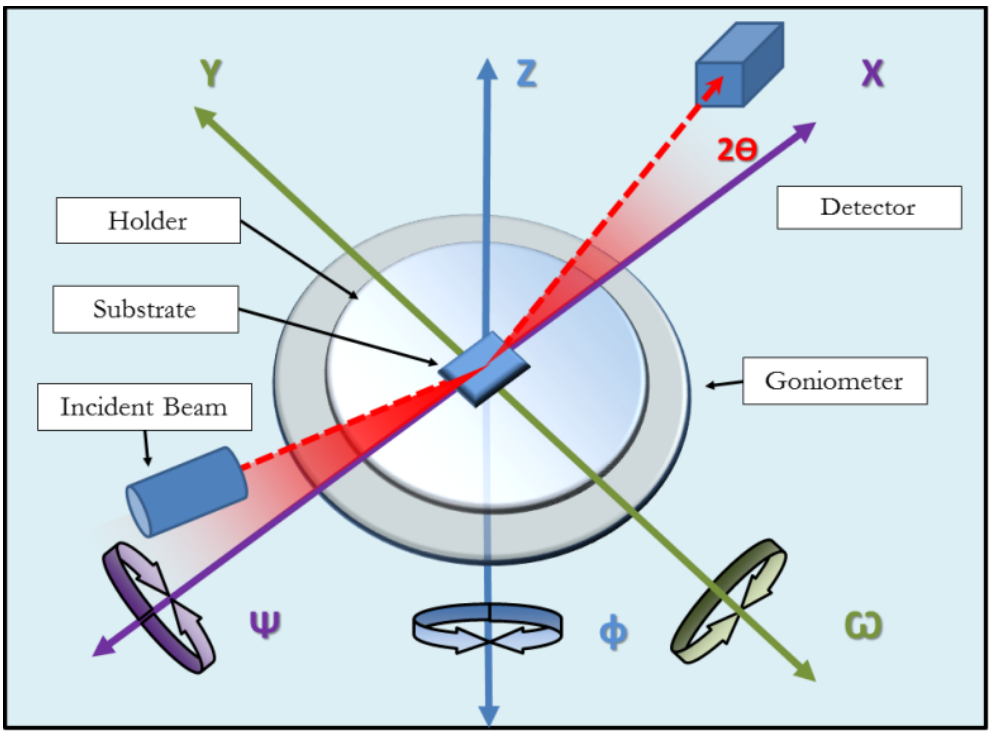

Figure 2.6: *Schematic representation of a ray diffraction goniometer with the azimuthal angles ϕ (around z axis), ω (around y axis) and Ψ (around x axis).*

In thin films, there are few scenarios that take place, a grown film could be, amorphous, polycrystalline or fully textured. In the first scenario XRD would not give any valuable information, a part of the confirmation of the amorphous character of the film, since no parallel planes can be found in this scenario is the lest relevant to discuss. Polycrystals can be studied as it was previously explained, allowing to the carefully detections of multiple orientations and crystalline structures. However, in the case of a fully textured film, with a single out of plane orientation, it is possible to study in depth many other aspects of the film. In essence the incident X-ray beam would have the best scenario for refraction, with a well-defined interference pattern following a given

crystalline orientation. It is not difficult to assume that by playing with different angles of diffraction other families of parallel planes, within the film, can be observed and studied, as long as they are parallel to the diffraction angle. In **Figure 2.6** a schematic representation of the XRD apparatus is described. In this system the film can be rotated in three degrees of freedom, along the azimuthal angles ϕ (around z axis), ω (around y axis) and Ψ *(*around x axis*)*, by doing so, the so called asymmetric reflections of the film can be observed and studied, allowing to deeper characterization of thin films texture.

2.3.1.1.1 Rocking curve (ω scan)

Although not considered as one of the analysis performed in asymmetrical configuration (phi-scans or pole figures) since it analyses plane parallel data, it is worthed to mention it due to the important information that provides regarding the crystal quality of the film.

Fully textured thin films are usually grown onto commercially available high quality single crystalline substrates. Although the theoretically angle at which a given reflection should diffract, should be unique, in practice it follows the convolution of a Gaussian and Lorentizian distribution, also known as Voigt profile. This distribution talks about of the crystal and film mosaicity, which is the measure of the long range disorder of a crystal.

In this analysis, the so-called Rocking curves (also known by ω scan), the x-ray source and detector are fixed, while the ω angle is swept around ω = ɵ within a short range, as depicted in **Figure 2.6** changes a relatively small range. Mosaicity in thin films can be as low as the respective substrate allows them, therefore the standard measure compares the signal`s full width at half maximum (FWHM) from the film, to the one measured on the substrate. Thus, narrow Rocking curve peaks, characterized by full width at half maximum (FWHM), become a figure of merit of high crystal quality films

2.3.1.1.2 Phi-scans (φ)

The first of the asymmetrical reflection is the so-called Phi-scan. In this configuration the in-plane texture and orientation of the thin film is studied. In order to access this information a previously not parallel crystalline or direction, is place in a parallel configuration by rotating the Ψ angle while keeping ω=0 at all times. The Miller index used is typically any who satisfy components both in plane and out of plane, both for the film and the substrate. Finally the shifting angle at which the sample has to be moved is described by the films crystalline group.

Once an asymmetrical reflection is placed parallel to the incident beam, the 360^{O} rotation of the ϕ angle is performed. Due to the geometry of the analysis as many peaks will be observed as parallel configurations observed in the scan, this means that the in-plane symmetry can be directly observed and compared with the substrates symmetry, allowing determining the epitaxial relationship between the film and the substrate.

It is important to notice the relevance of angular optimization, due to experimental issues, such small angle miss alignment on ω or Ψ axis both from the clay used to attach the samples or the substrate holder. These miss alignments can produce a precession that would miss some of the Braggs parallel planes, or have a considerably important loss of intensity, or even missing some of the reflections.

2.3.1.1.3 Pole figures

Pole figures are the second of the asymmetrical measurements; in this case a 2 dimensional map is generated by expanding the standard ϕ scan, described in the previous paragraph, as a function of different angles of Psi, (ϕ -Ψ). In this case, the stereographic projection obtained, corresponds to the angular relationship between lattice planes and directions. This is due to the fact that any plane in a crystal can be just as well represented by the inclination of the normal to the plane relative to some reference plane as by the inclination of a plane itself. This means, that any set of planes, can be represented or identified by a group of normal planes radiating from a given point within the crystal. These plots, allow to identify epitaxial relationships and to deeply assess the quality of highly oriented and textured thin films.

2.3.1.1.4 Reciprocal space maps (Q-Plots)

Finally, the reciprocal space maps plots are introduced. This asymmetrical measurement is widely used in thin films, due to the capability to expand the information of epitaxial relationships and determine in-plane lattice parameters in epitaxial films. The concept of the reciprocal lattice was proposed by German physicist Ewald in 1921, in order to explain some diffraction effects of diffuse scattering at non-Bragg angles. The measurement configuration corresponds to a series of standard Θ/2Θ scans performed at not symmetrical configuration (Θ≠ω). In the reciprocal space map plot each set peaks corresponds to a set of planes with in the crystal, describing completely the set of planes and more importantly orientation and spacing of the given planes. As example, let a given crystal have a unit cell defined by the vector $\boldsymbol{a_1}$,$\boldsymbol{a_2}$ and $\boldsymbol{a_3}$. The corresponding reciprocal lattice would be defined by the vectors $\boldsymbol{b_1}$, $\boldsymbol{b_2}$ and $\boldsymbol{b_3}$ accordingly with the following equations.

$$b_1 = \frac{1}{V}(a_2 \, x \, a_3) \quad \textbf{Equation 2.2}$$

$$b_2 = \frac{1}{V}(a_3 \, x \, a_1) \quad \textbf{Equation 2.3}$$

$$b_3 = \frac{1}{V}(a_1 \, x \, a_2) \quad \textbf{Equation 2.4}$$

Where V corresponds to the unit cell volume and the corresponding scalar product between the vectors constructs the reciprocal vector. In order to understand this representation, we will assume a general triclinic cell, a triclinic cell is one of the 7 crystalline systems, a simple representation is given by a ≠ b ≠ c and α ≠ β ≠ γ . This structure would show, quite clearly, the geometrical relevance of the reciprocal representation.

First, the vectors that represent the real space of the unit cell are obtained, in **Figure 2.7 a)**, the geometrically representation of the scalar product between two vectors. It can also be described as $\mathbf{a} \cdot \mathbf{b} = \boldsymbol{ab} \cos \boldsymbol{\alpha}$ and **Figure 2.7 b)** shows the vector product (cross product) of vector $\boldsymbol{a_1}$ and $\boldsymbol{a_2}$, written as $\boldsymbol{a_1} \times \boldsymbol{a_2}$, that can be explained as $\mathbf{c}=\boldsymbol{ab} \sin \boldsymbol{\alpha}$. Notice that the magnitude of c is the area of the parallelogram constructed on $\boldsymbol{a}$ and $\boldsymbol{b}$. Finally, by following the **Equation 2.4** as described on the **Figure 2.7 c)** it can be clearly appreciate that the vector $\mathbf{b_3}$, is normal to the plane constructed by the $\mathbf{a_1}$ and $\mathbf{a_2}$ vectors, as follows:

$$b_3 = \frac{1}{V}(a_1 \, x \, a_2) \quad (1)$$

Equation 2.4

$$b_3 = \frac{(B.A)}{(B.A * h)} \quad (2)$$

$$b_3 = \frac{1}{h} \quad (3)$$

$$b_3 = \frac{1}{d_{001}} \quad (4)$$

Where ***V*** is the volume of the unit cell, ***B.A***, is the Base Area and ***h*** the high of the unit cell. Notice that the final product is simply the interplanar distance ***d***, in the (001) direction. Therefore, the reciprocal matrix can be defined as the collection of vectors normal to the plane described by two vectors, and which individual magnitude corresponds to the volume of the represented plane. As shown in **Figure 2.8**, the reciprocal matrix can be represented by the normal vectors to the planes, which magnitude is the inverse of the interplanar distance along the real direction.

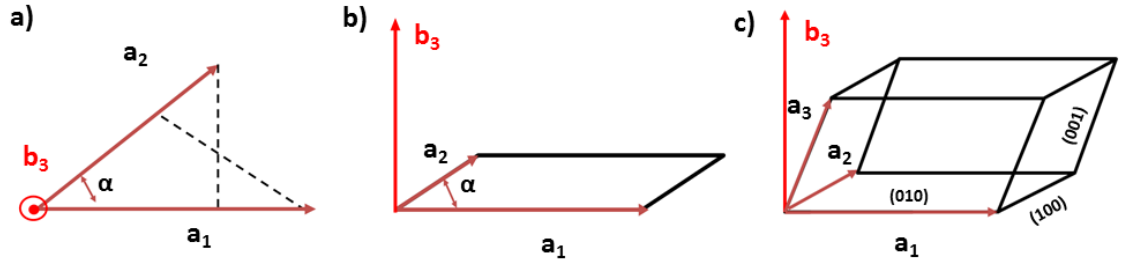

Figure 2.7: *Illustration of the construction of reciprocal vectors. a) Illustrates the scalar product between to vectors. b) shows the vector product or cross product and c)illustrates the magnitude and direction of the reciprocal vector.*

In thin films, as said at the beginning of this section, a series of standard Θ/2Θ scans performed at not symmetrical configuration (Θ≠ω). First a (hkl) reflection which is not parallel to the texture of the film must be selected; this condition allows fulfilling the geometrical restriction of the reciprocal vectors. Moreover, the ω=2Θ/2-Ψ where Ψ corresponds to the angle between the [hkl] reciprocal direction and the texture of the film. In this positions, a 2-D map of (2Θ,ω) containing the reciprocal peaks can be obtained. Then according to the geometrical nature of the reciprocal space maps, the following equations can be used to extract the lattice parameters:

$$a = \frac{2}{\lambda}\frac{h}{qx};\ q_x = \sin(\theta)\sin(\theta - \omega) \quad \textbf{Equation 2.5}$$

$$c = \frac{2}{\lambda}\frac{l}{qz};\ q_z = \sin(\theta)\cos(\theta - \omega) \quad \textbf{Equation 2.6}$$

Notice that the 2-D data is often represented in the reciprocal space coordinates' $\boldsymbol{q_x}$ and $\boldsymbol{q_y}$, It is important to remember that the experimental value extracted from this plots, is often distorted due to small angular miss alignments in the system or the sample montage, and more importantly due to epitaxial strain induced by the substrate. In order to compensate for these artifacts, a bigger plot is performed to include the reciprocal reflections of the substrate, in this way, the known interplanar distance and lattice parameter of the reciprocal data from the substrate, would allow a correction of the reciprocal information of the film (see **Appendix 2**). Another interesting feature of the reciprocal plots, corresponds to the epitaxial strain, in general, if both in plane parameters, substrate and film, have the same value, the film has grown strained respected to the substrate, or relaxed if on the contrary have different values.

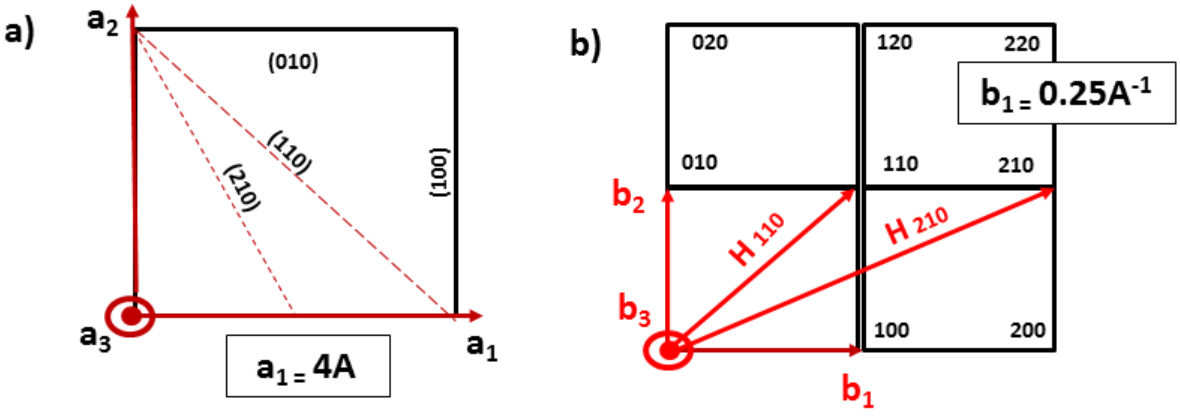

Figure 2.8: *Diagram of the relation between the real space and the reciprocal space. a) Shows the real dimension and planes. b) Shows the associated magnitude and direction of the reciprocal vectors.*

Finally, the selection of the appropriate [*hkl*] reflection is very important, since higher order reflection, with smaller separation distances, would imply that the magnitude of the resultant reciprocal vector, would overcome the detector capabilities, and low miller indexes are subjected to the condition of $\omega = 180^{o} - \Theta - \Psi_{hkl} > 0$ for the angle between the reciprocal vectors and the film direction.

2.3.1.2 X-Ray Reflectivity (XRR)

The XRR is a nondestructive technique that is widely used in the analysis of thin films[**21**,**22**]. In this work the intrinsic capability of accurate measuring the thickness of a thin film was used. Moreover, the reflected beam contains information regarding the roughness and density of the films studied, giving and extra source of relevant information of the studied samples. Optimal samples range from 2-100 nm, for which the typical maximal resolution is of 1-2 Å.

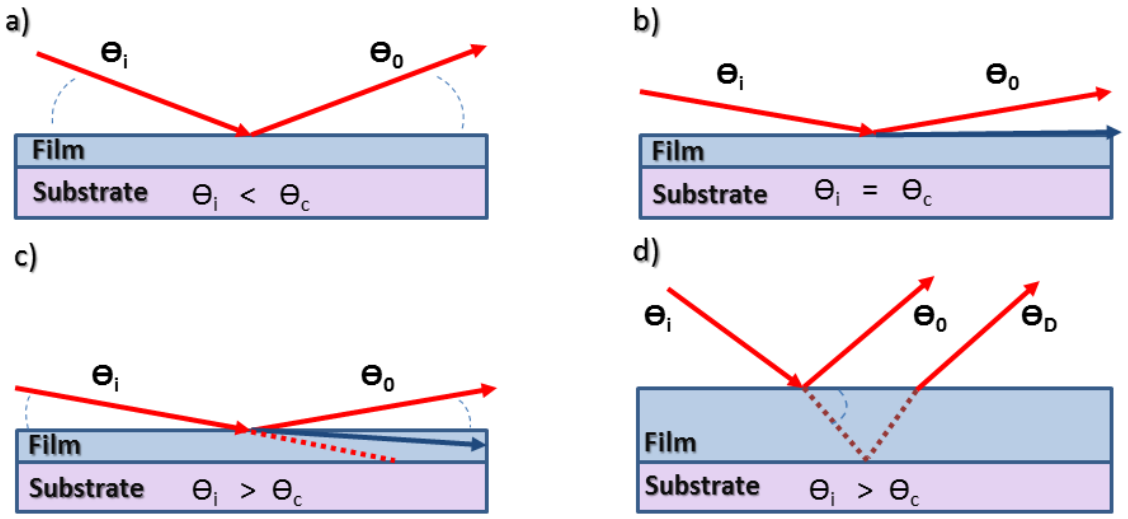

Figure 2.9: *Reflection and refraction with different glazing angels. a) when the incident angle is smaller than the critical angle. b) Critical angle is equal to the incident angle. c) Incident angle is higher than the critical angle. d) Sketch of the XRR experiment; note that the Θ_o and Θ_D are parallel.*

In a XXR experiment, the beam is incident onto a sample surface at a very low angle and reflected. The incident beam generates specular reflections that can be monitored and analyzed. The x-ray beam is projected at a given angle Θ_i while the detector is placed at Θ_0, following the Θ_i=Θ_0. **Figure 2.9** shows the relation of incident angle with the critical angle. The critical angle of the material Θ_C could be described as the angle at which the reflectivity effect is lost, this is directly associated to the electronic density of the material. At first, if the incident angle is inferior of the critical angle of the material, therefore full reflection of the beam is observed, **Figure 2.9 a)**. Then a decrement on the reflectance of the material is observed due to the critical angle of the material, at this point, some of the incident beam is propagated along the surface

and away from the detector, **Figure 2.9 b)**. Finally the incident angle is bigger than the critical angle of the material, and the XRR effect is observed **Figure 2.9 c)**. Some of the incident beam is reflected, at the Θ_0 angle, while some part of it penetrates de film and is diffracted inside and out Θ_d. Both beams are parallel and may present interference fringes depending on the optical path travelled by the diffracted beam **Figure 2.9 d)**.[**23**]

The recorded data would then contain information of the film roughness, density and thickness. A comparison of the typical results, detailing each kind of contribution, and the reflected behavior on the XRR plot, can be observed in **Figure 2.10**. The film thickness can be extracted from the **Equation 2.7.**

$$2 \cdot d\sqrt{\sin^2(\theta_i) - \sin^2(\theta_c)} = n \cdot \lambda \quad (1) \qquad \textbf{Equation 2.7}$$

$$\sin^2\theta_i = \sin^2\theta_c + \left(\frac{\lambda}{2 \cdot d}\right)^2 \cdot n^2 \quad (1)$$

Where d is the thickness of the film, Θ_i accounts for the incident and outgoing angle (Θ_i=Θ_0), Θ_c refers to the critical angle, λ to the wavelength of the X-ray source and n to the refraction index. Since the critical angle can be identified as the drop of reflectivity on the film, it can also be expressed by the $\Theta_c = arccos(n)$ where n is the index of refraction. This critical angle is proportional to the square root of the electronic density of the material. Finally, the thickness can be extracted from **Equation 2.7(2)**, by computing the positions of Θ_i *and* $\sin^2\theta_i$ a linear dependency can be expected, thus the linear fit should provide both the thickness (slope) and critical angle θ_c.

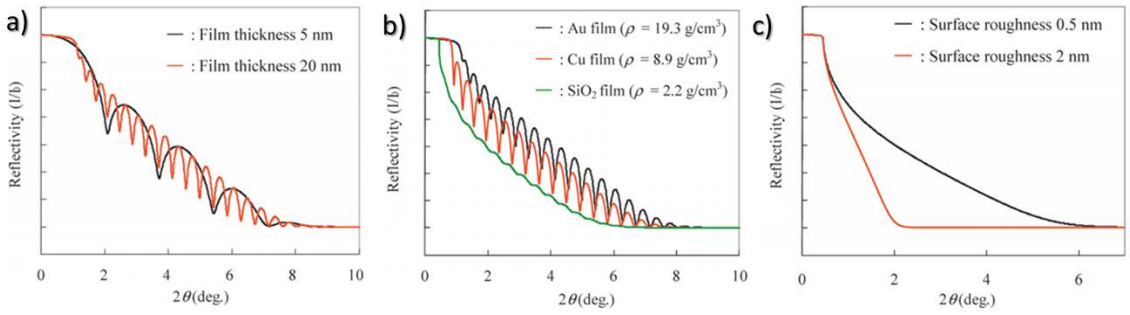

Figure 2.10: *Experimental results of XRR measurements. a) The thickness effect of two films of Au/Si. b) Density influence on tree different films of 20 nm. c) Roughness influence on the XRR measurement.* [**23**]

2.3.1.3 X-Ray Apparatus description

XRD and XRR measurements were performed at the university of Barcelona, in the Scientific and Technological Centers (Centres Científics i Tecnològics Universitat de Barcelona) under the supervision and collaboration of Dr Josep Maria Bassas. XRD measurements in this work were performed on the 4- circle Philips Materials Research Diffractometer (MRD) working with wavelength of 1.540598 Å (Cu). The system was equipped with a texture goniometer, working in parallel optics, a Bartels monochromator, a crystal analyzer and finally a proportional detector. XRR measurements where performed on a Siemens D-500 diffractometer.

2.3.2 Microscopy Techniques

2.3.2.1 Transmission Electron Microscopy (TEM)

In principle an electron microscope works in the same way as the traditional optical counterpart, however, as the technique`s name allows to discern, electrons are used instead of light. In this technique, mono-energetic electrons are targeted to the sample and accelerated using an electrical potential, the focusing of these electrons is done by metal apertures and magnetic lenses. Electrons have energies ranging from 100 to 1000 keV and are capable of penetrate thin portions of the sample, typically less than 200nm. When incident electrons interact with the sample many mechanisms of dispersion take place. These interactions between electron and atoms in the sample, allow to reconstruct an image that reflects the internal structure, based on inelastic interactions with intrinsic features, such as: grain boundaries, dislocations, density variations, etc. The beam suffers spatial variation in beam intensity, in this way an image that reflects this interactions can be produce.

Two set of images can be obtained with this technique, direct diffraction or interactions can be collected, including not diffracted beams, this configuration is *called bright field* geometry. When the image is formed by the diffracted electrons and the un-diffracted electrons are neglected, a *dark field* image is taken [**24**].

2.3.2.1.1 High Resolution Transmission Electron Microscopy (HR-TEM)

High resolution transmission electron microscopy is an imaging mode of the traditional TEM equipment. The main feature of this mode is that crystallographic

properties of materials, such as: lattice parameter, crystalline orientation, individual atomic dopants or atomic-scale defects, are resolved [**25**]. When the electron beam is focused on the sample, the crystalline order of the materials interacts with it; the diffraction process follows the Braggs Law, as in X-ray diffraction. However, the information related to the crystalline nature of the film is obtained by carefully analyzing the phase of the electrons detected. During transmission process the incident electron wave is scattered (or diffracted in the case of a crystal) at the potentials of the atoms, and thereby the phase of the electron wave is changed. At the exit surface of the specimen the object wave is formed, which carries direct and highly resolved information on the object.

2.3.2.1.2 Sample Preparation

Sample preparation is the most important step, prior the direct observation of the sample, in the TEM & HR-TEM technique. Samples have to be prepared to the point of electrotransparency, which implies that the sample thickness should not be superior to the electron penetration length of the material, in most of the cases the thickness is between 80-160 nanometers. In the cross-section geometry, where the interface of the thin films is parallel to the incident electron beam, a careful preparation process has to be performed.

2.3.2.1.3 Sample Preparation Protocol

- Cut of a section of the sample by mechanical means. Diamond saw.
- Wear sample by micrometric polisher.
- Thickness of the polished foil has to be of around 30 μm.
- Ion beam milling at 5 keV.
- An angle of 7^{O} is used in order to make a thickness gradient on the sample.

2.3.2.1.4 TEM Apparatus description

Samples were prepared and characterized at the university of Barcelona, in the Scientific and Tchnological Centers (Centres Científics i Tecnològics Universitat de Barcelona) under the frame of Josep Rebled thesis in the group of Dr. F. Peiro. The equipment used was JEOL JEM 2010F, working at 200 kV transmission electron microscope with field emission tube equipped with electron energy loss spectrometer (EELS), image filter (GIF) and Z-STEM unit with high-angle annular detector.

2.3.2.2 Atomic Force Microscopy (AFM)

Atomic force microscopy allows the surface characterization of samples. [**26**] The obtained topographical information is important for the thin films field due to its influence on the material growth and concordant align of heterostructures. The AFM technique relies on the atomic interactions of attraction and repulsion that a nanometric tip, colloquially referred as the cantilever, experiments when is in proximity of samples surface.

A schematic representation of the technique can be found in **Figure 2.11**. In this technique a special tip is used, this tip has two active sides. The "back" of the cantilever has a reflective film that's is as focus point and reflecting surface by solid state laser. The "front" part of the cantilever has a sharp tip with a radius of curvature of few nanometers. This tip is mounted on an electro-mechanical head, driven by piezoelectric components, typically with nonmetric spatial resolution in the ***x*** and ***y*** axis and sub-nanometric in the ***z***. A laser is focused on the back of the cantilever and is deflection detected by a highly sensitive photodetector that ultimately will transform the changes on the deflection angle into an image.

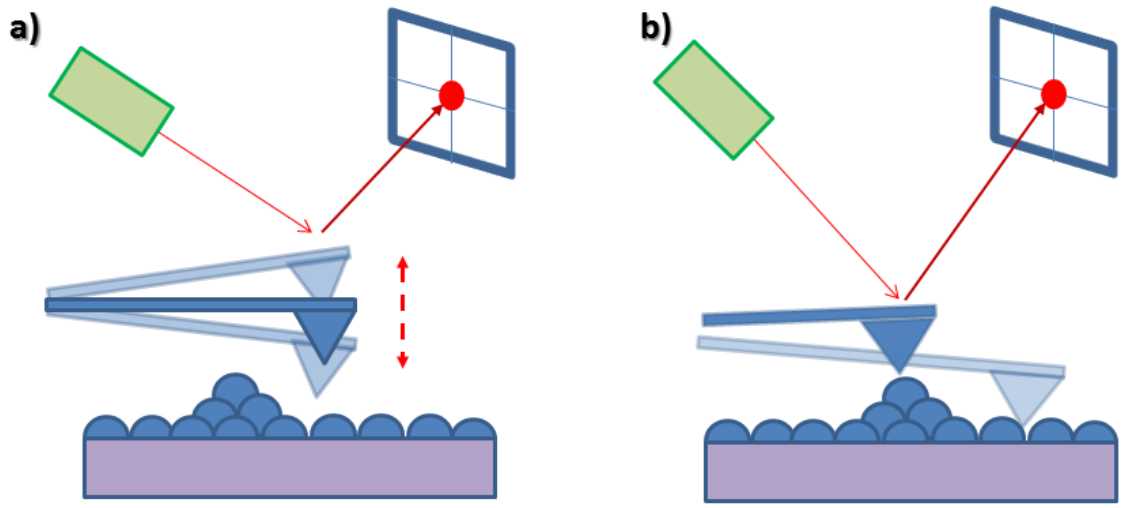

Figure 2.11: *Sketch of the Atomic Force Microscopy technique. Representation of the a) tapping and b) contact mode.*

There are two main modes of operation of the AFM, the first one, **Figure 2.11 a)** is known as tapping mode. In this mode an oscillation, perpendicular to the surface, is

induce on the cantilever. This resonance depends on the cantilever material and dimensions. This oscillation generates a constant displacement of the tip on the normal axis. When the tip approaches the surface its amplitude of oscillation changes, due to Van der Walls interactions between the tip and the surface. **Figure 2.11 b)** illustrates the contact mode, in this case the tip is pressed on to the surface generating a small bending on the cantilever, in this mode the applied strength and materials mechanical properties influence the tip selection. The changes on the reflected laser, directly relate to the surface morphology of the sample. It can be easily appreciate the advantages and applications of both modes. None contact mode grants longer life span for the cantilevers, sacrificing some resolution, while the contact mode works conversely.

2.3.2.2.1 AFM apparatus description

AFM micrographs were taken at University of Barcelona in three different set of equipment. First, AFM Bruker Extended Multimode with Nanoscope IIIA controller electronics and Bruker Multimode 8 with Nanoscope V controller electronics were used at the Scientific and Technological Centers (Centres Científics i Tecnològics Universitat de Barcelona) under the supervision and collaboration of Dr Jordi Diaz and Dr. Gerard Oncins. Finally, an Agilent 5100 AFM/SPM Microscope was used at the GECFE group in the Applied Physics Department. Some of the samples were measured by Laura Rodriguez in the frame of her Master thesis and AFM training. Images were treated using Gwyddion[**27**] and WSxM v5.0[**28**] scanning probe microscopy software.

2.3.3 Compositional Characterization

2.3.3.1 X-ray photoemission spectroscopy (XPS)

This technique is widely used in the thin films field as a source of stoichiometric control. XPS technique allows assessing the chemical composition of a sample and its valence state. XPS is based on the photoelectric effect. In this technique a beam of x-rays is focused on the sample, typically from Kα of Mg or Al sources, with energy from 1253.6 to 1486.6 eV respectively. This generates an expulsion of the internal electrons of the superficial atoms, the beam penetration is around 5-10 nm. The ejection of electrons is dominated by the **Equation 2.8**, were E_c, is the kinetic energy that corresponds to the initial photon energy, this minus the $h\nu$ work function, ϕ, depends of

each spectrometer and E_B is the bounding energy or potential barrier for the ejection. **Figure 2.12** shows the XPS emission process.

$$E_B = h\nu - \phi - E_C \quad \textbf{Equation 2.8}$$

The kinetic energy *Ec* can be measured by a coaxial cylindrical analyzer or hemispheric concentric and the work function can be calibrated with a reference material, so E_B can be extracted accordingly; this bounding energy depends on the atomic electronic configuration and chemical surroundings. Thus, a shift on the E_B is expected as a function of the electronic redistribution of different atoms bounding to a specific element. Moreover the holes generated in the internal levels of the atom, have different relaxation times associated, these holes could induce changes on the E_B allowing discerning between two, or more, types of bounding in the same atom.

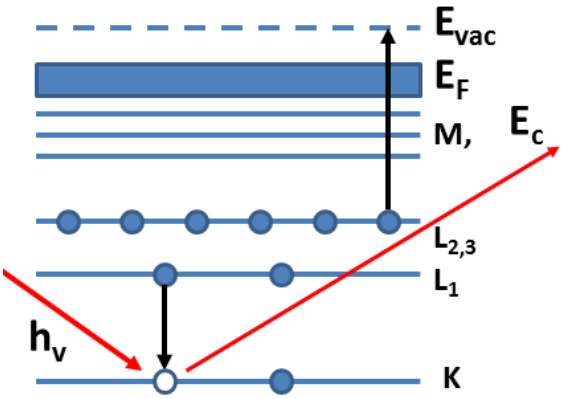

Figure 2.12: *Sketch of the X-ray Photoemission Spectroscopy. E_{vac} stands for Vacuum Energy, E_F energy at the Fermi level.*

The amount of information given by this technique is relatively easy to extract, thus, this technique is widely used in chemical analysis. However, it is limited to the surface composition; few atomic layers can be analyzed by the incident beam, mainly due to the shielding effect that superficial atoms produce on the internal ones, preventing their ejection. This issue can be overcome by using argon sputtering. In this case, the surface is sputtered at regular and controlled intervals, after which a standard XPS measurement takes place. In this way, internal atoms can be analyzed. Thickness of the sample could be obtained by XRR pre-experiment or by standard perfilometry post experiment. This approach helps to assess cationic migration and interfacial phenomena. It is important to notice though, that there is a typical effect mostly

observed in Thin Films samples. Due to nature of the argon sputtering technique, a typical diffusion from film to substrate is observed. This happens due to the "push" at what the surface atoms are exposed by the Ar^+ plasma. Therefore, migrations from the substrate to the samples can be taken as "real data" while migration from the films to the substrate effects should usually be considered artifacts or side effects of the set up.

2.3.3.1.1 XPS Apparatus description

Measurements were performed on three different systems. *i)* Perkin-Elmer ESCA-PHI 5500 equipment working with the Al. Kα radiation (1486.6 eV) at the Scientific and Technological Centers (Centres Científics i Tecnològics Universitat de Barcelona) under the supervision of Dr. Lorenzo Calvo Barrio. *ii)* SPECS SAGE HR 100 system equipped with a 100 mm mean radius PHOIBOS analyzer at CIC biomaGUNE in San Sebastian under the supervision of Dr. Luiz Yate and *iii)* Custom build Omicron Electron Spectroscopy for Chemical Analysis – ESCA at NanoBiomedical Centre at Adam Mickiewicz University.

2.3.3.2 Electron Energy Loss Spectroscopy (EELS)

In this technique the distribution of energy of initially monochromatic electrons going through the sample is analyzed. The EELS spectrometer is commonly installed in some HR-TEM equipment. As previously explained, in the TEM technique, samples have to be milled down to the electro transparence level. This allows collecting these electrons going through the samples and analyzed them by means of an energy detector. Incident electrons can undergo different interactions with the sample, such as *i)* Electrons could have no scattering with the sample (Direct beam). *ii)* Electrons scattered elastically with the sample (***e-*** scattered by the atomic nuclei) and *iii)* electrons undergo inelastic scattering. The first two phenomena account for the bright and dark field modes on the traditional TEM, while the last one accounts for the electron-electron interactions. The electron-electron interactions can bring many interesting information about the sample and is the core of the Electron Energy Loss Spectroscopy [**24**].

Typically an EELS plot has an intense peak at lower energies, below 100 eV, that is known as the Zero-Loss peak. This peak is formed by the electrons that have not undergone an inelastic scattering and is usually used as a "quality reference" of the whole experiment, since it width will talk about the energy resolution of the experiment.

Peaks in the higher regions of the spectra, above 100 eV would contain finger prints of specific elements in the sample as well as their relative quantity and oxidation state.

2.3.3.2.1 EELS Apparatus description

EELS spectra were acquired using a microscope JEOL JEM-2010F working on Scanning Transmission Electron Microscopy mode at 200K. Equipped with an EELS spectrometer GIF2000 (Gatan Imagin Filter). Samples were prepared and characterized at the university of Barcelona, in the Scientific and Technological Centers (Centres Científics i Tecnològics Universitat de Barcelona) under the frame of Josep Rebled thesis in the group of Dr. Francesca Peiro.

2.3.3.3 Secondary Ion Mass Spectrometry (SIMS)

The secondary ion mass spectrometry (SIMS) is a technique widely used to characterize chemical composition of sample. In this technique ions are used to bombard the sample and extract atoms from the surface of the sample that later are collected by a mass spectrometer. Ions of Ar^+ or O_2^+ are used to sputter the surface, as previously described in the XPS technique, ions sputter the surface of the sample, allow to characterize new atoms as the sample is sputtered, giving a profile of composition in depth. The mass spectrometer analyzed charge/mass of ions emitted, thus neutral species are not detected. This technique is one of the most sensitive technique, capable of detecting light elements (<1 ppm) with an outstanding topographical composition. However, this technique, opposite from the previously described XPS technique, does not allow to quantify compositions but rather confirm composition or characterize contamination or atomic diffusion within the samples.

2.3.3.3.1 SIMS Apparatus description

SIMS measurements were performed on Atomika A-DIDA 3000-30 equipment. O^{2+} was used to sputter the surface with energy of 9 keV and 500 nA of current. Samples were prepared and characterized at the university of Barcelona, in the Scientific and Technological Centers (Centres Científics i Tecnològics Universitat de Barcelona) by Dr. Francisco Lopez.

2.3.4 Magnetic Characterization

2.3.4.1 Superconducting quantum interference device (SQUID)

Superconducting quantum interference device (SQUID) is a pretty standard technique to characterize magnetic properties in materials. In this technique a very sensitive magnetometer, made of a superconducting coil, with a so called Josephson junctions (known as a superconductor–insulator–superconductor junction, or S-I-S). The magnetic measurement comes from the displacement of the sample along the vertical axis between two coils connected to a Josephson junction, which turns the magnetic flux variation into voltage and transmitted as an electric signal. This technique allows a measuring resolution of 10^{-7} emu.

2.3.4.1.1 SQUID Apparatus description

Magnetic measurements were performed in two set ups. 1) SQUID Quantum Design MPMS XL at the University of Barcelona, in the Scientific and Technological Centers (Centres Científics i Tecnològics Universitat de Barcelona) by Nuria Clos. And 2) SQUID Quantum Design MPMS XL-5 at the NanoBiomedical Centre at Adam Mickiewicz University by Dr. Karol Zaleski.

2.3.4.2 Vector network analyzer ferromagnetic resonance (VNA-FMR)

Conventional FMR experiment is conducted in a standard Electron Paramagnetic Resonance (EPR) spectrometer. In standard setup, FMR measurement is done by sweeping an external magnetic field, while the frequency is kept constant. Sample is placed in a microwave cavity which limits the usage of different microwave wavelengths.

To measure FMR in broad frequency range the microwave cavity is replaced by a coplanar waveguide. CPW consists of three coplanar conducting stripes. Microwave magnetic field is induced by microwave current generated by VNA around the center stripe line (signal). The other two are ground lines. The sample is located at the waveguide with the thin film close to the center conductor. VNA allows characterization of transmitted and reflected signals, which are described by the so called S-parameters. There are several methods of evaluating raw VNA-FMR data [**29**].

The most used is the evaluation of the S21 parameter, which describes a transmission through coplanar waveguide.

The VNA-FMR setup be used in two modes. In the first mode, the external magnetic field is set constant and the frequency of the microwave field is swept. Resonance signal is obtained from the absolute value of S21 parameter. To subtract background from experimental data two measurements are required. First is made at low fields (experimental data) and second at maximum field, which is treated as the reference one. The second mode is similar to conventional FMR, the frequency of the microwave magnetic field is constant and the DC magnetic field is swept. In this method the transmission coefficient (S21) is recorded while varying the field. In both methods a Lorentzian profile of the FMR absorption is obtained, although in the case of manganites a rather broader spectra is the norm.

2.3.4.2.1 VNA-FMR Apparatus description

VNA-FMR measurements were performed in the group of Prof. Dr. Hab. Janusz Dubowik in the Institute of Molecular Physics of Polish Academy of sciences. Samples were measured by Dr Hubert Głowińsk. Samples were swept in the range of 0-40GHz under a maximum applied external field of 2 Teslas.

2.3.5 Dielectric Characterization

In this section a short description of the multipurpose dielectric measurements chamber would be given. Ferroelectric measurements were previously performed in the institute of material science of Barcelona, ICMAB. However, during the development of this thesis, the need of a more immediate alternative for these measurements was evident. The following described equipment was developed conjunctly, by Jofre Ventura, in the frame of his PhD thesis, and Emerson Coy.

2.3.5.1 Multipurpose dielectric measurements chamber

The idea behind the design of the measurement chamber was the development of a versatile platform for dielectric characterization. The chamber should allow a diverse range of AC/DC measurements and exploit the cryogenic capabilities of the cold finger. As a result a 4 tip measurement system with a close cycle Leybold cryostat was implemented.

A mayor problem of the cold finger montage was the vibration associated with the compressor and the gas expansion cavity. After several unsuccessful montages, involving lateral connections to commercially available probe stations, the coupling of the cold finger with other equipment was discarded, mainly due to the high displacement of the cold finger head, estimated in 200 μm; value comparable to the standard electrode use in the film. Tests performed in this configuration shown an increment on signal noise and, more importantly, severe damage to the platinum electrodes, making measurements irreproducible. After much deliberation a different approach was introduced.

The system was altered, so the cold finger would be placed perpendicular to the floor, allowing using the flat surface of the cold finger, parallel to the floor, as sample holder. The sample holder was made of aluminum, molded on a circular plate of 1 cm of thickness. The plate has 4 movable tips mounted in the vertices of an inscribed square, the tips are mounted on a dielectric base, in order to avoid short circuits and protect the cold finger electronics, and a torque spring system in order to keep tip contact with the sample. The tips are gold coated with a spherical contact at the end and small spring to avoid over pressure on the sample. Notice that in this configuration the whole system, tips and sample, move cooperatively so the vibrations are neglected. Performance studies showed a total resistivity of 23 Ω and a self-inductance of 10^{-7} H. Moreover there was no evidence of damage to the platinum electrodes or contact lost during experiment.

The whole montage is covered by a stainless steel jacket that acts as vacuum chamber. Internal vacuum can be as low as $1*10^{-5}$ mbar and temperatures can go down to 20K. Minimum working temperature can be reach within 1 hour of operation. The temperature stability is 0.05 K in the whole range of temperature.

2.3.5.2 Ferroelectric response

A common characteristic of ferroelectrics is the capability of switching between two meta-stable states, commonly by the application, or removal of an electric field, *E*. This mechanism is known to take place in domains that extend beyond the unit cell scale, although its origin is associated to a small distortion of the unit cells.

A typical characterization technique for ferroelectric materials, the ferroelectric response is plotted as the polarization, *P*, versus electrical field, E. However

polarization is not measured directly, instead the current I as function of the voltage V is typically plotted, and then the polarization is computed using the **Equation 2.9**. In this equation *Q* is the measured charge of the film and A is the area of the electrodes.

$$P = \frac{Q}{A} = \int I(t)dt/A \quad \textbf{Equation 2.9}$$

In thin films, the so called parallel plate configuration is used; this configuration has 2 main variants **Figure 2.13 a)**. 1) Tp electrodes of a given metal are placed on the film, while the film is grown on a conductive substrate or a conductive material. In this configuration the film thickness *d* is evaluated in the area directly in between the two electrodes. However, in this configuration, asymmetries in the ferroelectric loop can be observed, in general this effect is correlated to the different nature of the electrodes which typically are not from the same material. This effect allows the implementation of the second configuration. **Figure 2.13 b),** 2) In this configuration, films are measured in the so called top-top geometry. The advantage of this method relies on the symmetry involved on the measurement. Any dielectric anomaly related to the transport in the electrodes is compensated by the extra distance added to the measurement. In fact any disproportionation measured in one direction (i.e: Top electrode +, Bottom electrode -) is compensated by their inverse configuration. Bottom electrode + and Top electrode -, thus allowing a cleaner measurement of the ferroelectric response of the film **[29]**. However, it is important to remark, that other effects, us such as dielectric anisotropy, grain size and other non-trivial interactions can also promote a non-symmetric *I(V)* cycle.

A simple triangular signal is often used to characterize the ferroelectric films, however, there are many effects that contribute to multiple artifacts and rather inconclusive measurements. Typically a voltage sweep is performed on the sample, however thin films ferroelectrics, and moreover, multiferroic materials, are known for their poor insulating features. In fact a small portion of the voltage effectively charges the capacitor, while the rest of the voltage is converted in electric current that flows along the film. This current is known as leakage and is a common feature in multiferroics and thin films. Leakage can be understood as a resistor that competes with the capacitive features of the film. However, it is this resistor, who is responsible for one of the most common artifacts in the literature **[30]**.

A typical resistor would show a pseudo hysteretic behavior when a voltage swept is performed, hiding any capacitive response of the film or providing a false ferroelectric-like response. The so called rugby shapes or bananas [**30**,**31**].

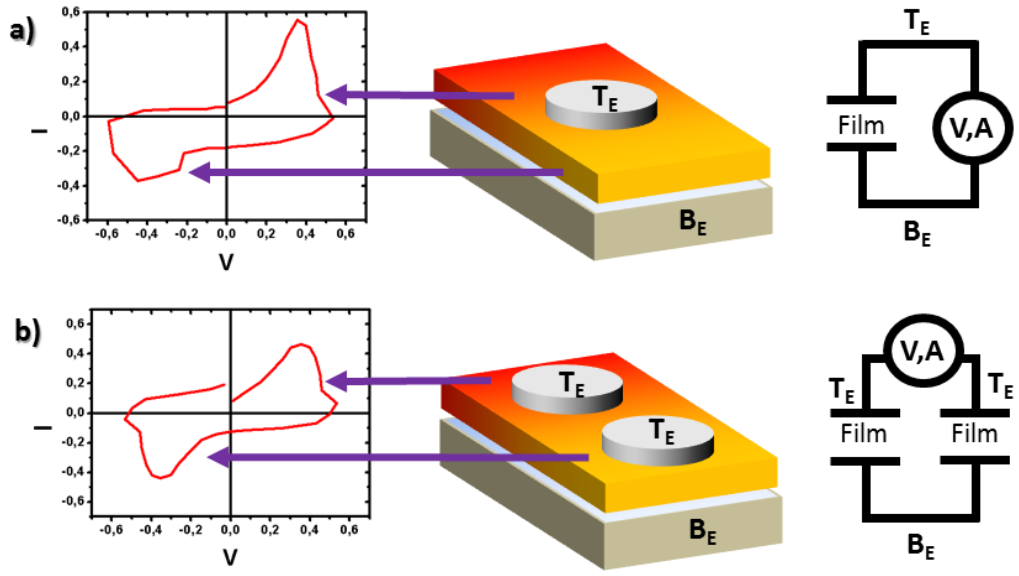

Figure 2.13: *Representative sketch of the electrodes influence on the shape of the I(V) cicle. a) top – bottom configuration. b) top-top configuration.*

In order decouple this effect a technique known as PUND is commonly used. PUND stands for Positive UP, Negative Down. In this method a costume signal is used to polarize the film. In the typical triangular I(V) measurement, both the ferroelectric and the leakage components of the measurement work cooperatively in both positive (+) and negative (-) applied voltages. In the PUND method, the first pulse, P, drives both the leakage and the polarization to the positive region of the voltage. Afterwards the second part of the pulse, U, will retrace the positive part of the voltage. Notice that any polarization of the film, in the positive region, happened in the first P pulse, while the leakage will be present in both P and U pulses. The same would be true for the negative part N and D of the signal. It is clear now, that any capacitive response of the sample would be only observed in the P and N segments of the signal, while the leakage, can be observed in the entire signal. A simple subtraction of P-U and N-D is needed to eliminate the leakage contribution and extract the capacitive component of the films.

It is important to remark, that these measurements as also affected by the frequency of the applied signal. Faster Relaxation times than the second polarization cycle are commonly observed at low frequencies, more over frequency dependent phenomena tents to prevent the successful identification of dielectric contributions, further details, see Impedance spectroscopy.

This technique has been used and discussed in the PhD dissertation of Dr. E. Langenberg[**32**] and Dr. I. Fina[**33**]. Moreover, the method is pointed as one of the standards for non-volatile characterization of memories by Keithley, leading company in electronic testing equipment[**34**].

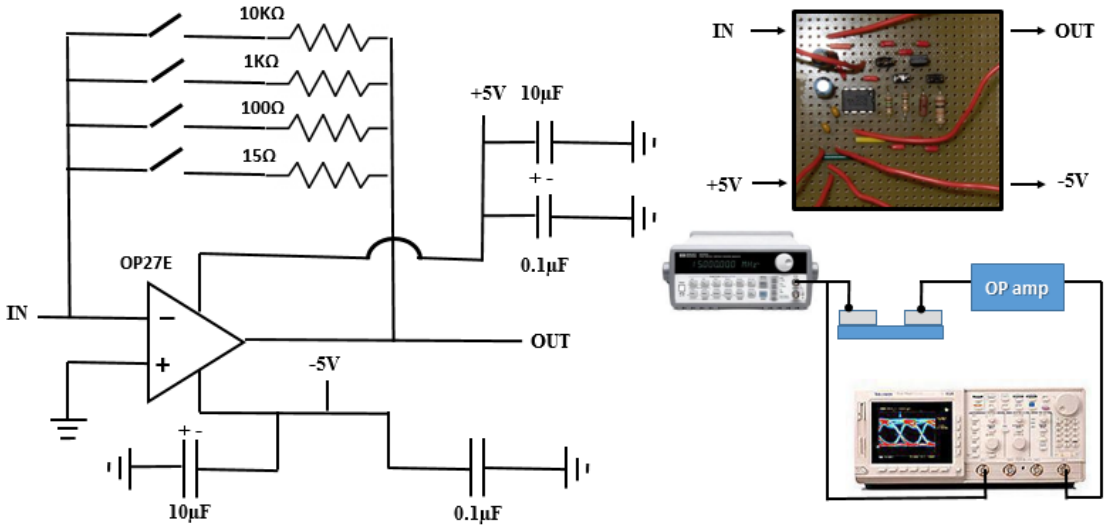

Figure 2.14: *Schematic of the operational amplifier. Insets show the setting up and the assembled circuit.*

2.3.5.2.1 Ferroelectric measurements Set-Up description

Electric measurements for ferroelectric characterization were performed in two set-ups. 1) by Dr. I. Fina in a PPMS (Quantum Design Co.) placed at Institut de Ciència de Materials de Barcelona (ICMAB, CSIC) using the commercial ferroelectric tester TF Analyzer 2000 (AixACCT Co.) as pulse generator and current detector. Triangular voltage pulses of typically 25 µs of rise time were used. 2) by Emerson Coy and Jofre Ventura at University of Barcelona, using a HP4192A signal generator, coupled with an oscilloscope Tektronix Tds420 4 Channel Digital, Signal was applied to the sample

throw coaxial cables connected to a probe station. The output signal was integrated by a custom made operational amplifier circuit, **Figure 2.14**, and finally collected in the second channel of the oscilloscope. The whole system works using Labview application developed by Emerson Coy which integrates all the electronics. Final data was loaded into an ASCCI file and corrected in order to be analysed on Zview ® software.

2.3.5.3 Ferroelectric Measurements Protocol

- Place the sample on the vacuum chamber and probe station
- Connect equipment: Signal generator, Oscilloscope and Integrator circuit.
- Set up safety configuration of equipment.
  - Low voltage and frequency.
  - Manual Burst of arbitrary signal.
  - Trigger synchronization between signal generator and Oscilloscope
- Setting up Vacuum.
- Minimum Vacuum for safe operation 10^{-4} mbar
- Allow minimum temperature to stabilize.
- Perform, test measurement at 100Hz and low voltage.
- Search for ferroelectric features.
- Check different electrodes.
- Calculate maximum electric field.
- Maximum operation frequency is 10 mHz and 10 volts.
- Load data to computer
- Stop measurements.
- Allow temperature to increase in vacuum.
- Stop vacuum.
- Remove sample.

2.3.5.4 Temperature dependent Complex Impedance Spectroscopy (IS)

Complex impedance spectroscopy, also known as dielectric spectroscopy, is technique that analyses the dielectric response of a given material, at different frequencies. This method is used in diverse fields such as electrochemistry [**35**], polymers [**36**,**37**]and solid solutions [**36**,**38**]. Its versatility relies on the fact that different mechanism, such as dipolar interactions, conduction mechanisms and electronic barriers, have different frequency regimes, allowing an effective decoupling of their influence in the total behavior of the sample.

In thin films, this technique is known for the capability of decoupling external effects (interfaces, electrodes, grain boundaries, etc...) from intrinsic effects of the samples [**39**]. The impedance response of the thin film is usually recorded in a top-top configuration, due to similar reasons as explained previously in ferroelectric

measurements. Impedances is typically recorded as |Z|, and the phase, θ, in the complex representation: $Z^* = |Z|e^{i\theta} = Z' + i\,Z''$, where $Z' = |Z|\cos\theta$ and $Z'' = |Z|\sin\theta$ are the real and the imaginary part, respectively. It is important to notice that the behavior in an ideal insulator should follow the capacitor, **Equation 2.10**, where C and ω stand for the capacitance of the dielectric and the angular frequency (2πν) of the applied alternating voltage, respectively. Thus, the phase, θ, should be -90^0.

$$Z_C^* = \frac{-i}{\omega C} = \frac{1}{\omega C} e^{i(-\frac{\pi}{2})} \quad \textbf{Equation 2.10}$$

However, as mentioned before, thin film samples tend to have a high contribution of leakage. Therefore the circuit that better describes the system is a capacitor ($Z = \frac{1}{i\omega C}$) in parallel with a resistor ($Z = R$). This leads to a circuit commonly known as RC which formula can be expressed as follows:

$$Z *_{RC} = \frac{1}{\frac{1}{R} + i * \omega C} = \frac{R}{1+\omega^2 C^2 R^2} - i * \frac{\omega R^2 C}{1+\omega^2 C^2 R^2} \quad \textbf{Equation 2.11}$$

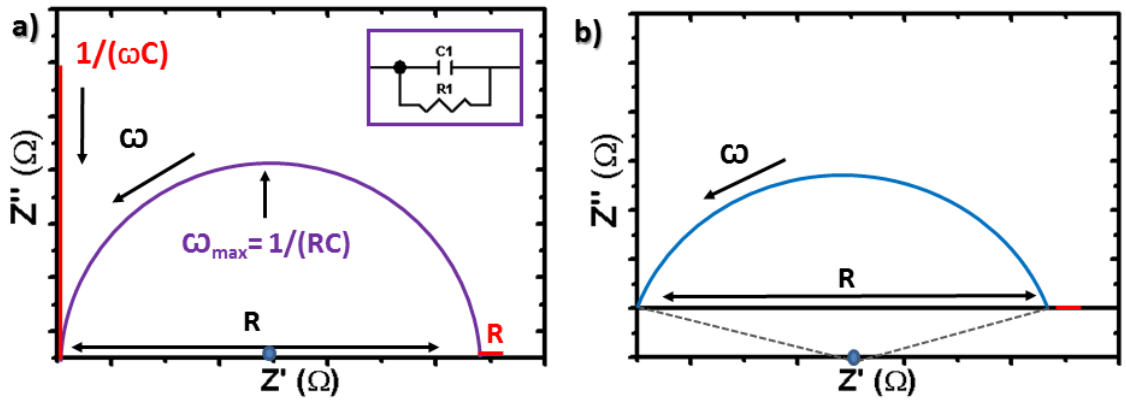

Figure 2.15: *Nyquist representation of a) R-C ideal behavior, Red lines along the Y-axis and X-axis, represent the Ideal capacitor behavior and resistor respectively b) Typical plot observed in non-ideal R-C circuits..*

However, in practice, this modelling does not allow to reproduce the experimental behavior of most of the dielectric systems[**40**]. In practice the impedance of a capacitive system can be represented in by the so called Nyquist plot (also called the Cole-Cole plot or Complex Impedance Plane plot), this plot comprehends the imaginary part of the

impedance vs the real part *(Z"(Z`))*, for an ideal capacitor, this representation should follow a semicircle, with center in *x*-axis., however, the experimental data looks like a depressed semicircle centered somewhere below the *x-axis* **Figure 2.15**.

The large distribution of relaxation times in the samples, usually attributed to the presence of inhomogeneous regions of the films [**36**,**38**,**41**,**42**], is typically entitled responsible for this behavior. A common method to give meaning to this behavior is the substitution of the capacitive component of the circuit, for the so called constant phase element *CPE*. The CPE contains a frequency dependent element, which can mimic the impedance dependence on the frequency of real dielectric, the equation is as follows:

$$Z_{CPE} = \frac{1}{Q(i*\omega)^{\propto}} \qquad \textbf{Equation 2.12}$$

In this case, α denotes de phase of the CPE element, which is typically $\alpha \leq 1$ (when $\alpha=1$ the behavior is considered ideal) while Q, although denotes amplitude, Q does not have the dimension of capacitance, i.e. [F], but its units are given by $[F \cdot s^{(\alpha-1)}]$ and thus allowing the extraction of the "real capacitance".

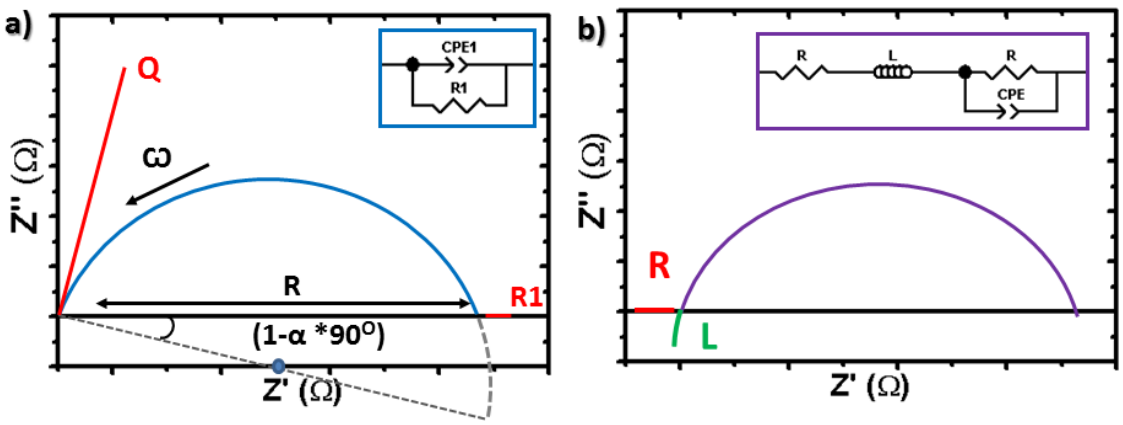

Figure 2.16: *Nyquist representation of a) R-CPE behavior, Red line shows the graphical meaning of Q, notice that the semicircle is shifted to compensate the semicircle depressed shape. b) The influence of different extrinsic elements in the Nyquist representation.*

Notice that the element has no truly physical meaning, since its behavior is merely a mathematical construct that allows giving meaning to the flattening of the capacitive semicircles, and allows to "measure" how far from ideal the behavior of a

capacitor is. **Figure 2.16 a)** shows a graphical understanding of the influence of the Q and α in the Nyquist plot. As it can observed, the R-CPE and RC circuits have a similar behavior in the circuit modelling part and by using the Nyquist representation, the influence of both elements can be easily understood. In essence, R will account for the diameter of the semicircle while the C/CPE element will account for the diameter of arc and shape of the circumference. However, this representation allows a clear identification of some elements that are usually overlooked in the models, **Figure 2.16 b)**. The two main features observed, are the shift from in x-axis of the semicircle and the crossing into negative regions of the plot (high frequencies); the first is the finger print of a resistor series with the R-C/CPE, its magnitude can be directly extracted and modelled from this separation, while the second one is the self-inductance of the circuit, that critical frequency can be determined and further excluded from the analysis.

Finally, to exalt the importance of the Nyquist representation is worth to mention the identification of intrinsic and extrinsic contributions in the experimental set-up. Self-inductance and the resistor shown in **Figure 2.16(b),** as expected, are not related to the sample itself, but rather are part of the extrinsic effects of the analysis, one related to the equipment wiring and the second to their resistance. However, there is a secondary extrinsic contribution, a parasitic capacitance that is usually found in thin film capacitors [**43**,**44**]. This parasitic capacitance has been attributed to depletion areas in the interface with the electrode and the film, due to the difference in work function of the materials. Although its origin still on debate, it is clear that corresponds to an external capacitance that tents to overlap, and in many cases hide, the intrinsic dielectric behavior.

One way of decouple this extrinsic effect is by increasing the range of frequency swept in the experiment; however this is rather a difficult task, due to the frequency range at which self-inductance takes “control” of the impedance spectra. A second approach is to lower the temperature of sampling, in this case, high frequency effects move to lower frequencies where are easier to identify, both qualitatively and quantitatively[**33**,**45**].

2.3.5.4.1 Capacitance and Dielectric permittivity

Extracting the dielectric permittivity from the impedance plots is possible using a well know relationship in plane-parallel capacitor $C=\varepsilon^*A/t$. Where the capacitance (C),

depends on the dielectric permittivity (ε) multiplied by a geometric factor (A=electrode area and t=thickness of the film). Notice that in the top-top configuration the geometric factor includes follows the expression $A/2*t$, **Figure 2.13**. The complex dielectric constant ($\varepsilon^* = \varepsilon' - i\cdot\varepsilon''$) [**35**,**36**,**38**,**40**]can be directly related to the complex impedance measurements by the following formula:

$$Z^* = \frac{1}{(i * \omega_{\varepsilon 0} * \left(\frac{A}{2 * t}\right) * \varepsilon^*)} \qquad \textbf{Equation 2.13}$$

Thus, a direct relationship between the *R-CPE* circuits and the ε^* can be expressed as follows:

$$\varepsilon^*_{R-CPE} = -\omega^{\alpha-1} * \frac{Qi^{\alpha+1}}{\varepsilon_0 * \frac{A}{2t}} - i\frac{1}{\omega\varepsilon_0 \frac{A}{2t} R} \qquad \textbf{Equation 2.14}$$

Notice that for α=1 the behavior follows the ideal R-C circuit[**41**].

2.3.5.4.2 Impedance spectroscopy Set-Up description

Electric measurements of Impedance Spectroscopy characterization were performed in two set-ups. 1) by Dr. I. Fina at the Institute of Material Sciences of Barcelona (ICMAB) using an impedancemeter HP4192A LF (Agilent Co) connected to a PPMS Physical Properties Measurement System (PPMS) of Quantum Design Co, able to work at a temperature range of 4-400K. 2) by Emerson Coy, with the collaboration of Jofre Ventura at University of Barcelona, Department of Applied Physics, using a the same impedance analyzer (HP4192A LF) connected to a multi-purpose dielectric measurements system (aspects of the system, detailed previously).

2.3.5.5 Impedance spectroscopy Protocol

- Set impedance analyzer to desired parameters
- Connect cables to probe station.
  - Do not turn on the impedance analyzer, while the tips are in contact.
  - Remember to ground the tips.
- Perform single frequency swept at room temperature and open chamber
- Repeat sweeps with different electrodes to obtain better signal.
- Close vacuum chamber.

- Wait for maximum working vacuum
- Start measurements.
- After finish measurements, allow the system to thermalize till room temperature while keeping the chamber at maximum vacuum.
- Remove sample.

References

[1] Eason, R. (2006) **Pulsed Laser Deposition of Thin Films: Applications-Led Growth of Functional Materials** [Internet]. Pulsed Laser Depos. Thin Film. Appl. Growth Funct. Mater. John Wiley & Sons, Inc. http://dx.doi.org/10.1002/9780470052129

[2] Dinescu, G., Aldea, E., De Giorgi, M.L., Luches, A., Perrone, A. and Zocco, A. (1998) **Optical emission spectroscopy of molecular species in plasma induced by laser ablation of carbon in nitrogen**. *Applied Surface Science*, **127-129**, 697–702.

[3] Acquaviva, S. and De Giorgi, M.. (2002) **Temporal and spatial analysis of plasmas during graphite laser ablation in low-pressure N2**. *Applied Surface Science*, **197-198**, 21–6. http://dx.doi.org/10.1016/S0169-4332(02)00297-0

[4] Kim, J.H., Jeon, K.A., Shim, E.S. and Lee, S.Y. (2002) **Laser wavelength effect on the light emission properties of nanocrystalline Si on Si substrate fabricated by pulsed laser deposition**. *Materials Science and Engineering: B*, **89**, 70–2. http://dx.doi.org/10.1016/S0921-5107(01)00759-0

[5] Aguiar, R., Trtik, V., Sánchez, F., Ferrater, C. and Varela, M. (1997) **Effects of wavelength, deposition rate and thickness on laser ablation deposited YSZ films on Si(100)**. *Thin Solid Films*, **304**, 225–8. http://dx.doi.org/10.1016/S0040-6090(97)00201-0

[6] Delgado, J.C., Sánchez, F., Aguiar, R., Maniette, Y., Ferrater, C. and Varela, M. (1996) **ArF and KrF excimer laser deposition of yttria-stabilized zirconia on Si(100)**. *Applied Physics Letters*, **68**, 1048. http://dx.doi.org/10.1063/1.116244

[7] Lunney, J.G. (1995) **Pulsed laser deposition of metal and metal multilayer films**. *Applied Surface Science*, **86**, 79–85. http://dx.doi.org/10.1016/0169-4332(94)00368-8

[8] Willmott, P.R. and Huber, J.R. (2000) **Pulsed laser vaporization and deposition**. *Reviews of Modern Physics*, **72**, 315–28.

[9] Husmann, A., Wesner, D.A., Schmidt, J., Klotzbücher, T., Mergens, M. and Kreutz, E.W. (1997) **Pulsed laser deposition of crystalline PZT thin films**. *Surface and Coatings Technology*, **97**, 420–5. http://dx.doi.org/10.1016/S0257-8972(97)00222-3

[10] Phipps, C. (2007) **Laser Ablation and its Applications** [Internet]. 1st ed. Phipps C, editor. Springer US, Boston, MA. http://dx.doi.org/10.1007/978-0-387-30453-3

[11] Guo, H., Sun, D., Wang, W., Gai, Z., Kravchenko, I., Shao, J. et al. (2013) **Growth diagram of La0.7Sr0.3MnO3 thin films using pulsed laser deposition**. *Journal of Applied Physics*, **113**, 234301. http://dx.doi.org/10.1063/1.4811187

[12] Yamagata, Y., Sharma, A., Narayan, J., Mayo, R.M., Newman, J.W. and Ebihara, K. (2000) **Comparative study of pulsed laser ablated plasma plumes from single crystal graphite and amorphous carbon targets. Part I. Optical emission spectroscopy**. *Journal of Applied Physics*, **88**, 6861. http://dx.doi.org/10.1063/1.1321783

[13] Huang, X.J., Xu, S.Y., Ong, C.K., Yang, Z., Si, L. and Li, Y. (2002) **Dependence of pulsed-laser deposition parameters on the microstructure and magnetic property of Nd–Fe–B thin films grown at high substrate temperature**. *Journal of Applied Physics*, **91**, 4666. http://dx.doi.org/10.1063/1.1448893

[14] Irissou, E., Le Drogoff, B., Chaker, M. and Guay, D. (2002) **Correlation between plasma expansion dynamics and gold-thin film structure during pulsed-laser deposition**. *Applied Physics Letters*, **80**, 1716. http://dx.doi.org/10.1063/1.1458534

[15] Sambri, A., Amoruso, S., Wang, X., Granozio, F.M. and Bruzzese, R. (2008) **Plume propagation dynamics of complex oxides in oxygen**. *Journal of Applied Physics*, **104**, 053304. http://dx.doi.org/10.1063/1.2975363

[16] Langenberg, E., Varela, M., García-Cuenca, M.V., Ferrater, C., Sánchez, F. and Fontcuberta, J. (2007) **Thin films in ternary Bi–Mn–O system obtained by pulsed laser deposition**. *Materials Science and Engineering: B*, **144**, 138–42. http://dx.doi.org/10.1016/j.mseb.2007.07.080

[17] Langenberg, E., Varela, M., García-Cuenca, M. V., Ferrater, C., Polo, M.C., Fina, I. et al. (2009) **Epitaxial thin films of (Bi0.9La0.1)2NiMnO6 obtained by pulsed laser deposition**. *Journal of Magnetism and Magnetic Materials*, **321**, 1748–53. http://dx.doi.org/10.1016/j.jmmm.2009.02.005

[18] Marti, X. (2009) **Growth and characterization of magnetoelectric YMnO 3 epitaxial thin films**. Autonomus University of Barcelona.

[19] Als-Nielsen, J. and McMorrow, D. (2011) **Elements of Modern X-ray Physics** [Internet]. Elem. Mod. X-ray Phys. Second Ed. John Wiley & Sons, Inc., Hoboken, NJ, USA. http://dx.doi.org/10.1002/9781119998365

[20] Paganin, D. (2006) **Coherent X-Ray Optics** [Internet]. Coherent X-Ray Opt. Oxford University Press. http://dx.doi.org/10.1093/acprof:oso/9780198567288.001.0001

[21] Fujii, Y. (2013) **Improvement of X-ray reflectivity calculations on a multilayered surface**. *Powder Diffraction*, **28**, 100–4. http://dx.doi.org/10.1017/S0885715613000110

[22] Fujii, Y. (2014) **Improvement of surface and interface roughness estimation on X-ray reflectivity**. *Powder Diffraction*, Cambridge University Press. **29**, 265–8. http://dx.doi.org/10.1017/S0885715614000359

[23] Yasaka, M. (2010) **X-ray thin-film measurement techniques V. X-ray reflectivity measurement** [Internet]. Rigaku J. p. 1–9.

[24] Schneider, R. (2011) **Surface and Thin Film Analysis** [Internet]. Friedbacher G, and Bubert H, editors. Surf. Thin Film Anal. A Compend. Princ. Instrumentation, Appl. Second Ed. Wiley-VCH Verlag GmbH & Co. KGaA, Weinheim, Germany. http://dx.doi.org/10.1002/9783527636921.ch4

[25] Op de Beeck, M., Van Dyck, D. and Coene, W. (1996) **Wave function reconstruction in HRTEM: the parabola method**. *Ultramicroscopy*, **64**, 167–83. http://dx.doi.org/10.1016/0304-

3991(96)00058-7

[26] Pennycook, S.J., Lupini, A.R., Varela, M., Borisevich, A., Peng, Y., Oxley, M.P. et al. (2007) **Scanning Microscopy for Nanotechnology** [Internet]. Zhou W, and Wang ZL, editors. Scanning Microsc. Nanotechnol. Tech. Appl. Springer New York, New York, NY. http://dx.doi.org/10.1007/978-0-387-39620-0

[27] Nečas, D. and Klapetek, P. (2012) **Gwyddion: an open-source software for SPM data analysis**. *Open Physics*, SP Versita. **10**, 181–8. http://dx.doi.org/10.2478/s11534-011-0096-2

[28] Horcas, I., Fernández, R., Gómez-Rodríguez, J.M., Colchero, J., Gómez-Herrero, J. and Baro, A.M. (2007) **WSXM: a software for scanning probe microscopy and a tool for nanotechnology.** *The Review of Scientific Instruments*, **78**, 013705. http://dx.doi.org/10.1063/1.2432410

[29] Bilzer, C., Devolder, T., Crozat, P., Chappert, C., Cardoso, S. and Freitas, P.P. (2007) **Vector network analyzer ferromagnetic resonance of thin films on coplanar waveguides: Comparison of different evaluation methods**. *Journal of Applied Physics*, **101**, 074505. http://dx.doi.org/10.1063/1.2716995

[30] Scott, J.F. (2008) **Ferroelectrics go bananas**. *Journal of Physics: Condensed Matter*, **20**, 021001. http://dx.doi.org/10.1088/0953-8984/20/02/021001

[31] Loidl, A., Krohns, S., Hemberger, J. and Lunkenheimer, P. (2008) **Bananas go paraelectric**. *Journal of Physics: Condensed Matter*, **20**, 191001. http://dx.doi.org/10.1088/0953-8984/20/19/191001

[32] Langenberg Pérez, E. (2013) **Growth and characterisation of Bi-based multiferroic thin films** [Internet]. Universitat de Barcelona.

[33] Fina Martínez, I. **Ferroelectricity and magnetoelectric coupling in magnetic ferroelectrics and artificial multiferroic heterostructures** [Internet]. Universitat de Barcelona.

[34] Module, P.M.U.U.I., Amplifier, R.P.M.R. and Model, T. **Application Note Se - ries Pulse I-V Characterization of Non-Volatile Memory Technologies**. *Keinthley - Technical Reports*, 26. http://dx.doi.org/http://www.keithley.com/data?asset=56338

[35] Orazem, M.E. and Tribollet, B. (2008) **Electrochemical Impedance Spectroscopy** [Internet]. Electrochem. Impedance Spectrosc. John Wiley & Sons, Inc., Hoboken, NJ, USA. http://dx.doi.org/10.1002/9780470381588

[36] Macdonald, J.R. (1992) **Impedance spectroscopy**. *Annals of Biomedical Engineering*, Kluwer Academic Publishers. **20**, 289–305. http://dx.doi.org/10.1007/BF02368532

[37] Roy, M., Nelson, J.K., MacCrone, R.K., Schadler, L.S., Reed, C.W., Keefe, R. et al. (2005) **Polymer nanocomposite dielectrics - the role of the interface**. *IEEE Transactions on Dielectrics and Electrical Insulation*, **12**, 629–43. http://dx.doi.org/10.1109/TDEI.2005.1511089

[38] Kakarla, D.C., Jyothinagaram, K.M., Das, A.K. and Adyam, V. (2014) **Dielectric and**

Magnetodielectric Properties of R 2 NiMnO 6 (R = Nd,Eu,Gd,Dy, and Y). Viehland D, editor. *Journal of the American Ceramic Society*, Blackwell Publishing Inc. **97**, 2858–66. http://dx.doi.org/10.1111/jace.13039

[39] Schmidt, R., Ventura, J. and Langenberg, E. (2012) **Magnetoimpedance spectroscopy of epitaxial multiferroic thin films**. *Physical Review B*, **86**, 035113. http://dx.doi.org/10.1103/PhysRevB.86.035113

[40] Schmidt, R., Eerenstein, W., Winiecki, T., Morrison, F. and Midgley, P. (2007) **Impedance spectroscopy of epitaxial multiferroic thin films**. *Physical Review B*, **75**, 245111. http://dx.doi.org/10.1103/PhysRevB.75.245111

[41] Morrison, F.D., Jung, D.J. and Scott, J.F. (2007) **Constant-phase-element (CPE) modeling of ferroelectric random-access memory lead zirconate-titanate (PZT) capacitors**. *Journal of Applied Physics*, **101**, 094112. http://dx.doi.org/10.1063/1.2723194

[42] Fina, I., Martí, X., Fàbrega, L., Sànchez, F. and Fontcuberta, J. (2010) **Dielectric anomalies in orthorhombic YMnO3 thin films**. *Thin Solid Films*, **518**, 4710–3. http://dx.doi.org/10.1016/j.tsf.2009.12.065

[43] Lunkenheimer, P., Krohns, S., Riegg, S., Ebbinghaus, S.G., Reller, A. and Loidl, A. (2010) **Colossal dielectric constants in transition-metal oxides**. *The European Physical Journal Special Topics*, **180**, 61–89. http://dx.doi.org/10.1140/epjst/e2010-01212-5

[44] Lunkenheimer, P., Bobnar, V., Pronin, A. V., Ritus, A.I., Volkov, A.A. and Loidl, A. (2002) **Origin of apparent colossal dielectric constants**. *Physical Review B - Condensed Matter and Materials Physics*, **66**, 521051–4.

[45] Fina, I., Fàbrega, L., Langenberg, E., Martí, X., Sánchez, F., Varela, M. et al. (2011) **Nonferroelectric contributions to the hysteresis cycles in manganite thin films: A comparative study of measurement techniques**. *Journal of Applied Physics*, **109**, 074105. http://dx.doi.org/10.1063/1.3555098

CHAPTER 3

Thin Film of $Y(Ni_{0.5}Mn_{0.5})O_3$

The following chapter focuses on the studies performed on $Y(Ni_{0.5}Mn_{0.5})O_3$ **(YNMO)**. First, the growth conditions and morphology of the thin films will be discussed. Secondly, the single phase stabilization will be addressed, followed by the morphological and compositional characteristics. Finally the functional properties of the films will be carefully assessed, principally the magnetic and dielectric properties.

3.1 Target Synthesis

Targets of YNMO have been synthesized by mixing stoichiometric powders of Y_2O_3, NiO and MnO_2 into an agate mortar. In order to synthesize the perovksite formula the B site ordered compound (Y_2NiMnO_6) was considered.

$$\mathbf{Y_2O_3 + NiO + MnO_2 \rightarrow Y_2NiMnO_6}$$

The proportions and dimensions of the sintered target are described in detail in the **Appendix 1**. Lattice constants and unit cell volume was taken from *JPC 1-74-7519* diffraction tablature, based in the work of M. Mouallem-Bahout e*t al*[**1**]. X-ray powder diffraction pattern of the obtained target is shown In **Figure 3.1**. Detail analysis performed using the X`Pert PANAnalitical package software, showed the coexistence of the solid solution of the YNMO and Y_2O_3 in the target. Interestingly enough, no traces of NiO or MnO2 are found in the diffraction plots. The corresponding estimated proportions of YNMO and Y_2O_3 are shown in **Figure 3.1** inset. It is important to remark

that the apparition of the solid YNMO solution on the target is not a prerequisite for film growth, since is the stoichiometry of the target the factor that would strongly influence the final composition of the film. SEM-EDX analysis showed a concordant stoichiometry of the film surface.

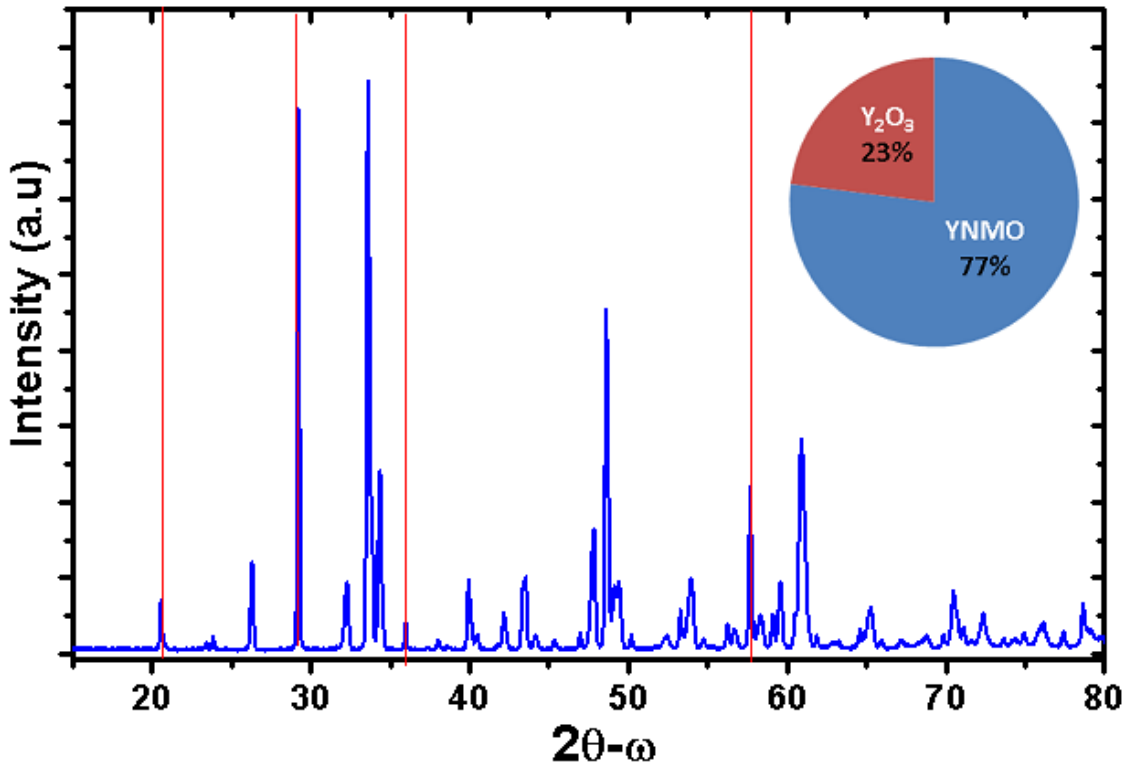

Figure 3.1: *Diffractogram of YNMO target, the peaks clearly show the primary contribution of YNMO and Y_2O_3 (red). Inset depicts a pie chart that compares the relative influence/presence of the materials in the graph.*

3.2 Thin films deposition

3.2.1 Initial considerations

As explained previously in Chapter 1. Thin film engineering is a very important part of thin films growth. The unit cell constants of YNMO, shown in **Table 3.1**, allow to make few pre experimental assumptions. As it can easily observed the YNMO lattice constants are considerably bigger than the STO lattice, a priori, texturized films could growth with a 45^{O} in-plane shifting. The STO lattice (3,905 Å) suits the YNMO-a/√2 = 3.692 Å, YNMO-b/√2 = 4.007 Å. This film configuration has been observed before in the literature in the same compound [**2**] and in a close relative $YMnO_3$ (YMO)[**3**].

Initial deposition parameters are taken from carefully reviewing similar publications in YNMO and $YMnO_3$ films[**4**,**5**]. It is a rather common issue that optimal parameters vary, from group to group, due to particularities of different experimental set-ups. Therefore, the initial part of this chapter will be devoted to the single phase stabilization of YNMO thin films on STO(001) substrates.

LATTICE CONSTANTS

Lattice Constant	YNMO	STO
a(Å)	5,2258	3,905
b(Å)	5,5573	3,905
c(Å)	7,4824	3,905
$\alpha(^{O})$	90	90
$\beta(^{O})$	89,76	90
$\gamma(^{O})$	90	90
$V(Å^3)$	217,30	59.547

Table 1: *Lattice constants of YNMO and STO.*

3.2.2 Single Phase Stabilization

3.2.2.1 Temperature dependency

In order to explore the influence of temperature in the quality of YNMO films, an arbitrary, but close to the ones reported obtained in the set-up for YMO, set of parameters was selected. First, the following parameters were selected: a repetition rate of 2 Hz, an oxygen pressure of 0.6 mbar and a fluence of 2 J/cm^2. The temperature was swept from 550 to 850^{O}C.

Samples obtained after 7000 pulses were characterized by means of XRD, shown in **Figure 3.2**. The 2θ-ω plots show the highly intense STO(00*l*) family of peaks, at ≈22^{O}, ≈46^{O} and ≈72^{O}, for the (001), (002) and (003), respectively. In most of the samples, each set of substrate peaks is followed closely by a smaller peak, at ≈23 ^{O}, ≈48^{O}, ≈76^{O}C respectively. This peaks correspond to the YNMO(00*l*) family, specifically the peaks (002), (004) and (006) of the indexed tables. It is important to notice that the superior order of the reflections, responds to the monoclinic nature of the unit cell. In simple terms, the almost double size of the YNMO monoclinic unit cell,

along the *c* axis, accounts for this effect, correlating to the STO(00*l*) reflections with a double YNMO(00*(2*l)*) index.

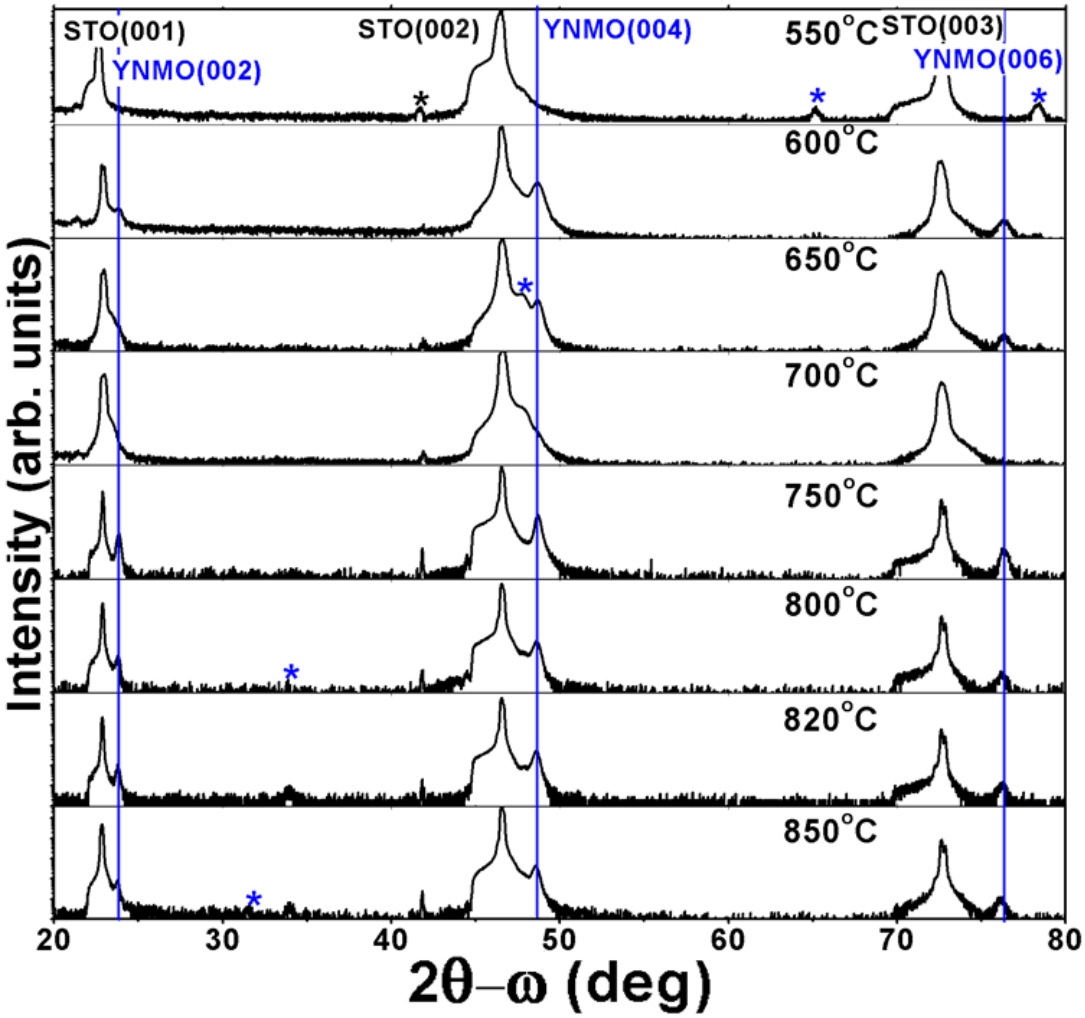

Figure 3.2: *2θ-ω scans of YNMO films deposited on STO(001) at different temperatures. Lines show the expected bulk position of the (00l) peak on the images, black * shows the Cu – Kβ, while blue * show the apparition of secondary orientations on the films. Upper and lower panels of figure*

It is clear from **Figure 3.2**, the tendency of the films of growing texturized in the range of 600 ^{O}C to 800^{O}C. Samples out of this range show the apparition of different orientations. In order to investigate the crystalline quality of the films, within the single texture window, two methods are studied. First the rocking curves of both the substrate and the films are measured and plotted as a function of temperature of growth, **Figure 3.3 a)**. Rocking curves are analyzed by measuring the FWHM in both the film and the

substrate, and the decoupled as shown in **Equation 3.1.** Secondly, the relative intensity of the film, calculated as the quotient between the substrate and films intensity in a given reflection, in this case the most intense reflection STO(002) **Figure 3.3 b)**, as shown in **Equation 3.2**.

$$\sqrt{F_i^2 - F_o^2} \quad \textbf{Equation 3.1}$$

$$I_R = \frac{I_F}{I_S} \quad \textbf{Equation 3.2}$$

Equation 3.1 allows the extraction of the "real" value of FHWM, *Fi* and *Fo* are the FWHM values, measured for the film and the substrate, respectively. Relative intensity, can be applied when the substrate intensity (I_S) has been carefully set at a rather constant value, which means that the detector has similar counts for the substrate peak between samples, therefore, the films intensity (I_F) properly reflects the quality of the film and the ratio properly evaluates the quality of the film.

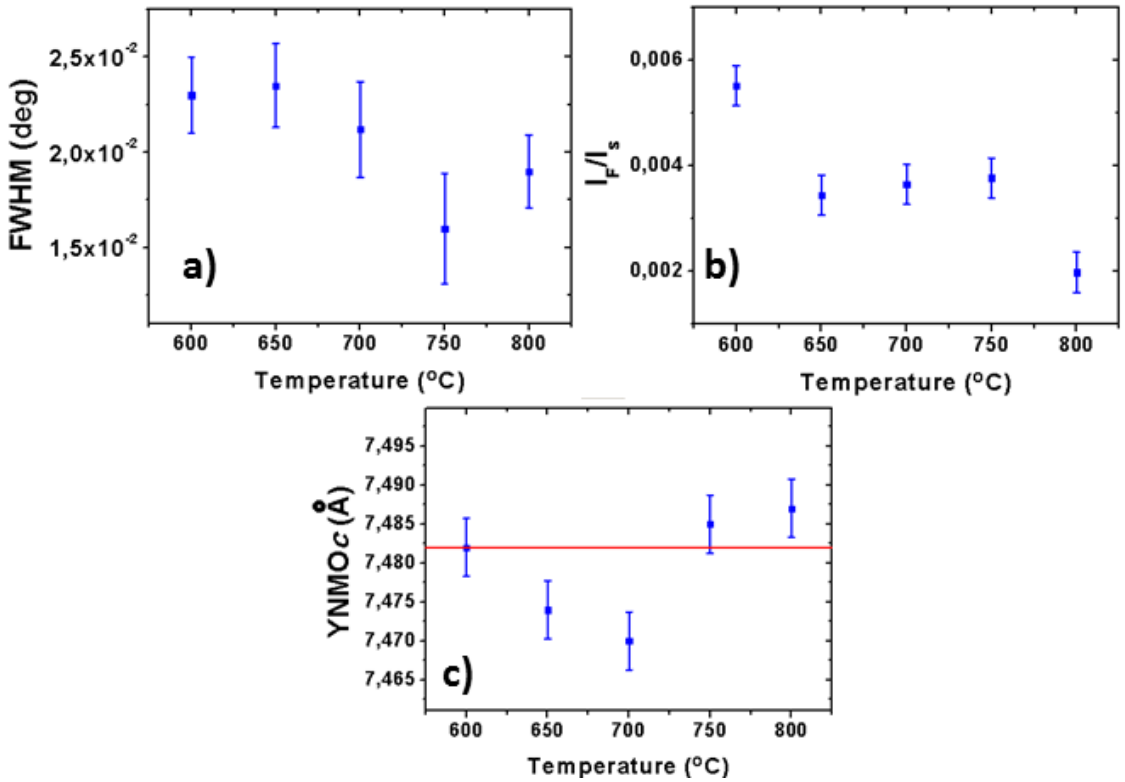

Figure 3.3 *Dependency of a) FWHM, b) relative intensity (extracted from YNMO(004)/STO(002)) and c) out of plane parameter on substrate temperature during deposition. Red line represents the bulk value.*

Rocking curves obtained from the 600 to 800^{O}C range, show the constant increment of crystallinity of the film up to the maximum 750^{O}C (**Figure 3.3a**), after this temperature the FWHM ratio increases its value, which translates in a detriment of quality. On the other hand, the relative intensity shows an early decrement after 600^{o}C, between 650^{o}C and 750^{o}C a small platoon is reached and at 800^{o}C a further decrement is observed, this shows a progressive increment of film intensity as function of temperature, with a rather low effect on the 650-750^{o}C range (**Figure 3.3b**), compatible with the FWHM observations. Upon further analysis, a third parameter was considered regarding, the temperature dependency on the YNMO unit cell. The out of plane parameter can be extracted from the 2θ-ω diffractograms, **Appendix 2**, assuming a simplified orthorhombic unit cell for the YNMO as shown in **Figure 3.3 c)**. The extracted out of plane parameter reaches its minimum at 700^{O}C and then growths continuously up to 800^{O}C. Notice that the red line in **Figure 3.3c**, corresponding to the YNMO*c* bulk value, is in between both 750^{O}C and 800^{O}C and falls in the experimental error of both extracted values.

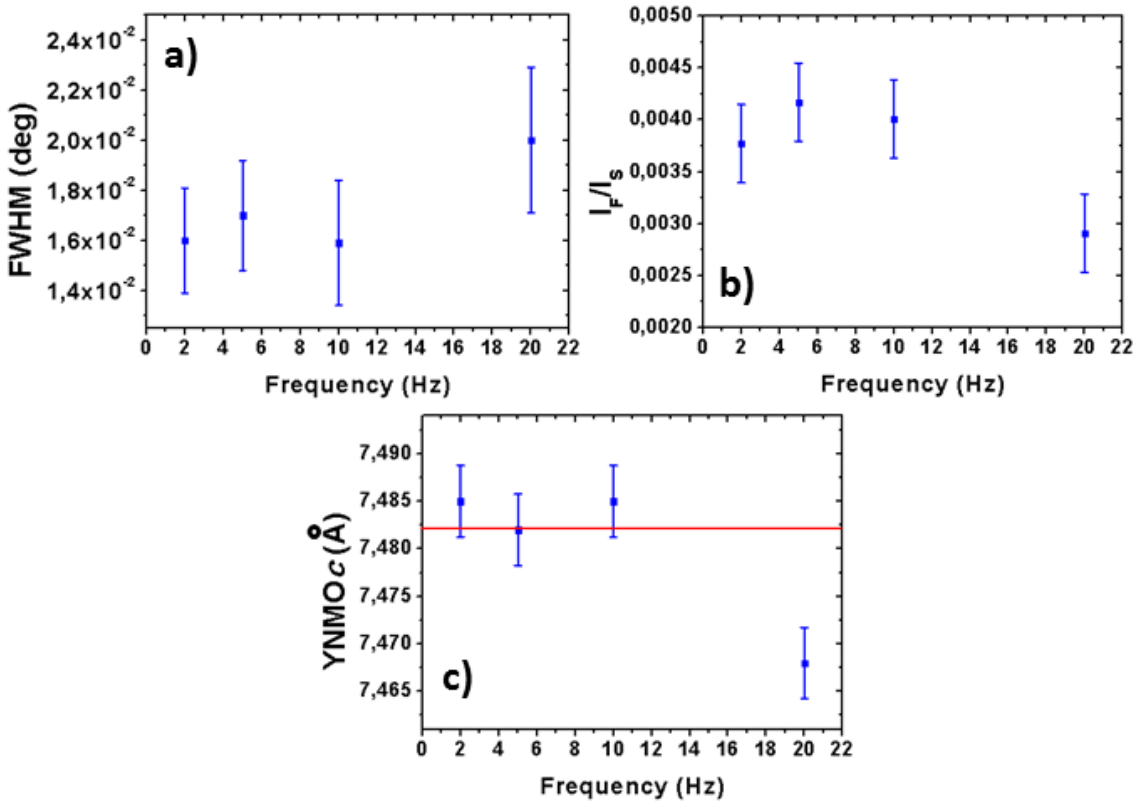

Figure 3.4 *Dependency of a) FWHM, b) relative intensity from YNMO(004)/STO(002) and c) out of plane parameter on the ablation rate. Red line represents the bulk value.*

As a result of this analysis, it is clear that textured YNMO films can be obtained in a large window of temperatures, from 650^{O}C to 800^{O}C. However, after careful analysis based on relative intensity, rocking curves and the similarity of the samples with the bulk values, it was found that samples grown at 750^{O}C show optimal crystalline properties and single YNMO(00*l*) reflections.

3.2.2.2 Repetition rate and oxygen pressure dependency

Focus is now shifted to both frequency of laser pulses and oxygen pressure influence on the quality of YNMO(001)/STO(001) samples. First, repetition rate was swept from values of 2,5,10 and 20 Hz, while oxygen pressure and temperature were kept constant at 0.6 mbar and 750^{O}C respectively. A similar analysis as the one performed on **section 3.2.2.1** was performed, in order to evaluate the influence of both frequency and oxygen pressure.

FWHM values, extracted from XRD rocking curves, were plotted as a function of repetition rate, as shown in **Figure 3.4 a)**. a somewhat stable behavior was observed in the frequency range between 2 and 10 Hz while an important detriment of the out of plane orientation of the film is observed at 20 Hz. Interestingly enough both relative intensity analysis **Figure 3.4 b)** and out of plane lattice constant studies **Figure 3.4 c)**, shown a similar tendency. Red line, show the bulk the YNMO*c* lattice constant value that falls in between 2, 5 and 10 Hz and their respective experimental error. This analysis suggests that, the ablation frequency has very little, if any, influence on the crystalline quality of the film at lower repetition rates than 10Hz.

Low repetition rates are known to influence the growth rate of the films, mainly due to the lowering or increasing rate at which the material is ejected from the target and arrives on the film. Although this statement is only relevant if the growth rate is expressed in Å/s or in similar way, otherwise (Å/pulse) it deals with the total length of the experiment. Nevertheless, lower repetition rates; provide a longer surface diffusion time, somehow advantageous for atoms mobility and nucleation process, being this one of the main reasons to compromise growth rate vs intrinsic surface reconstruction and ion mobility.

Interestingly enough, oxygen pressure analysis performed on samples deposited at 0.2, 0.6 and 0,9 mbar, while temperature and repetition rate was kept constant at 750^{O}C and 2 Hz respectively, shown a rather similar behavior between them. **Figure 3.5 a)**,

shows the FWMH ratio, plotted as a function of oxygen pressure. Notice that higher oxygen pressures (0,9 mbar) have no influence on the quality of the films **Figure 3.4 b), c)** while lower pressures seem to have affect in the quality of the film (0,2 mbar). Moreover, the use of high pressures leads lower growth rate, although, the oxygen pressure assures low oxygen vacancies are promoted at this stage of the growth, the higher oxygen lowers the energy of the particles which can influence negatively the crystalline properties of the film.

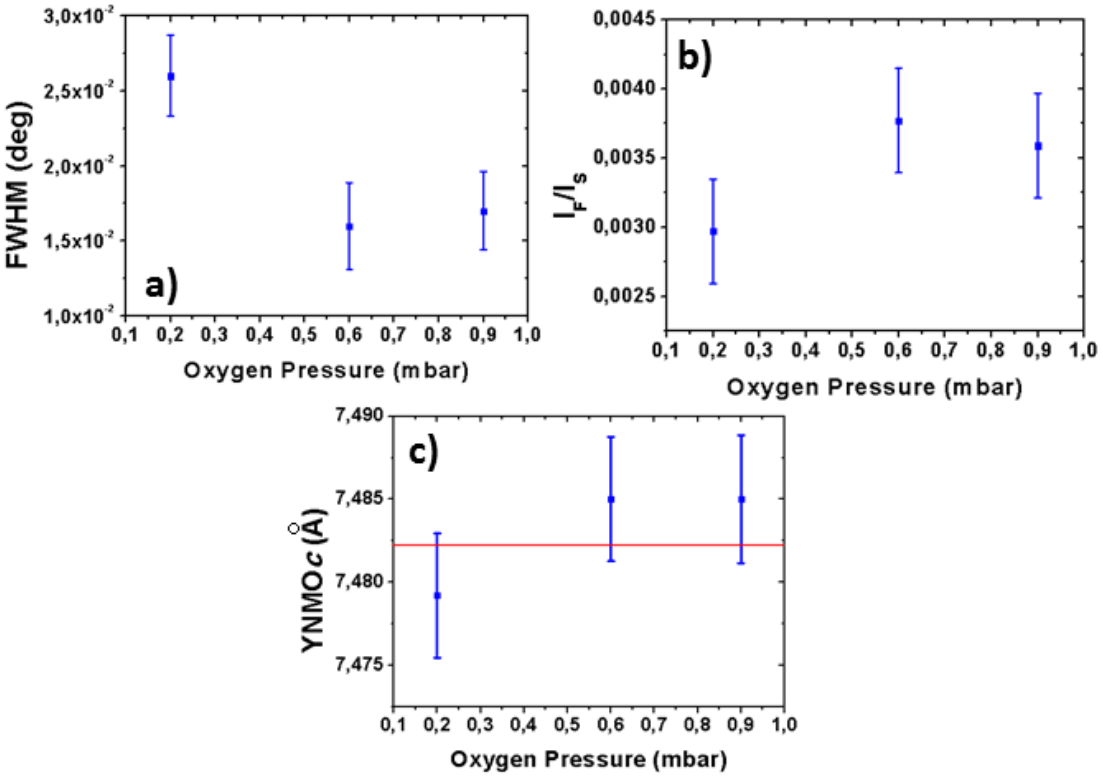

Figure 3.5 *Dependency of a) FWHM, b) relative intensity from YNMO(004)/STO(002) and c) out of plane parameter on the oxygen pressure. Red line represents the bulk value.*

As a summary, the crystalline quality of the YNMO(00*l*) film, has been studied and as a result, the experimental data shows that the crystalline quality of the samples is mainly affected by the use of higher repetition rates (above 10 Hz) and low oxygen pressures, (around 0,2 mbar), as a result, 0,6 mbar and 2 Hz were chosen as deposition parameters, due to the low effect on the growth rate of the film and high surface mobility ions on the substrate surface.

3.2.2.3 Thickness normalization

Numbers of pulses directly influence the thickness of the growing film. Thickness normalization between different samples is an important parameter to control in further studies of thin films. Typically, two approaches are used to determine this parameter. The simplest approach is to set a small substrate of spare material, typically silicon (SiO_2) with part of surface covered by a contact surface, as in shadow masking, this the covered surface will be protected from the directional plume of the PLD experiment, while the uncovered surface will be coated with the ejected material. In this way, by using a contact profilometer the step between the film and substrate can be characterized according to the number of pulses. The second method relies on the X-rays reflectometry and the extracted values, as described in Chapter 2.

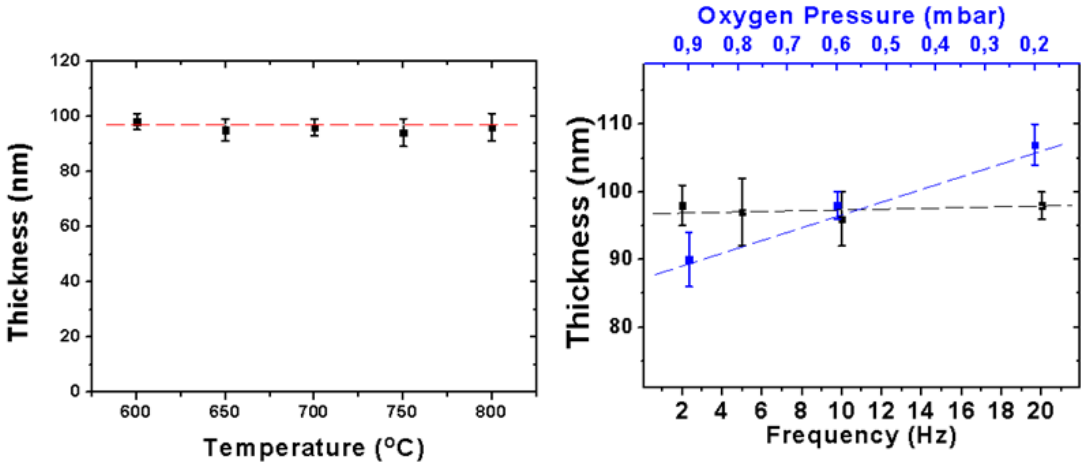

Figure 3.6 *Thin films thickness as function of a) substrate temperature b) repetition rate and (top axis) oxygen pressure. Dashed lines are a guide to the eye.*

In these studies, the initial values are 750°C, 0.6 mbar and 2 Hz, when one parameter is shifted the other ones remain unchanged. Thickness results obtained from the silicon shadow masking method are plotted vs temperature **Figure 3.6 a)**, oxygen pressure and frequency **Figure 3.6 b)**. It is clear now that oxygen pressure strongly influences the film thickness while repetition rate and substrate temperature have little influence on the film thickness.

Taking these results in consideration, a control sample was grown using the 750°C substrate temperature, 0.6 mbar, and 2Hz repetition rate, however in this case the thickness was set to prevent the relaxation of the strain provided by the substrate. It was

shown in similar materials[**6**], that thickness above 80 nm may lead to a sort of secondary phases in the film, thus keeping the samples well below 80 nm thickness is important for any strain induced studies. Therefore, a nominal thickness of around 70 nm was standardized in all the samples, with total ablation pulses of 5000.

X-ray reflectometry was used in order to confirm the proper control of the film thickness, based on the growth rate extracted from the previous studies. As shown in **Figure 3.7**, the fitting allows the extraction of the film value that in this case is 71.7 nm, a value in good agreement with the profilometer measurements. The final growth rate for the given experimental set up was calculated as 0,143 Å/Pulse, for films deposited using 750°C, 0.6 mbar, 2 Hz and 5000 pulses.

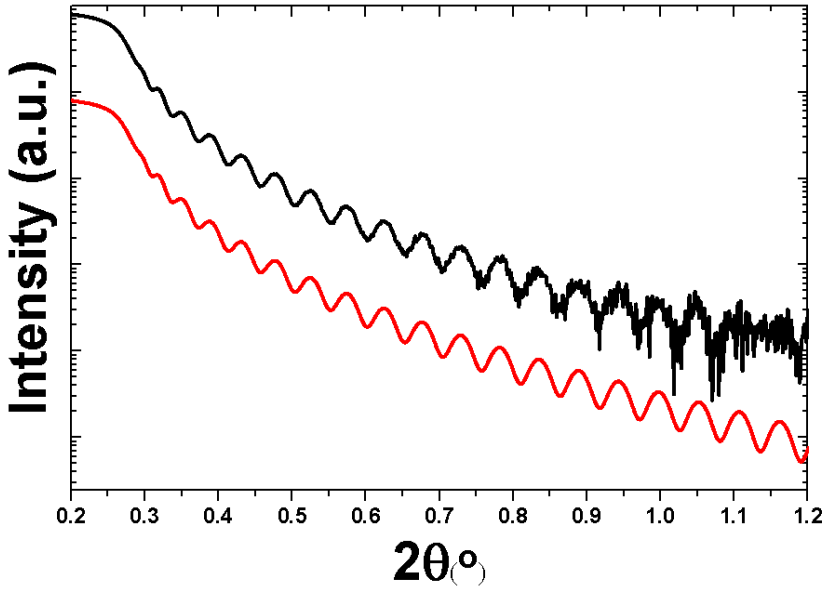

Figure 3.7 *Thin films XRR data measured (black) and simulated data (red), thickness is extracted by the fourier magnitude conversion (X'Pert Reflectivity)*

3.2.3 Epitaxial relationship of YNMO(001)/STO(001)

After successfully stabilizing and determining the optimal growth parameters of YNMO(001)/STO(001) films. The in-plane ordering of the system is to be addressed. The bulk structure of YNMO is reported to be a monoclinic $P_{21/c}$, with an angle β=89.76º that shows a remarkable similarity to the orthorhombic unit cell (β=90º). The growth of the YNMO pseudo orthorhombic cell on STO (001) (cubic, a = 3.905Å) could, in principle, show a 45º in-plane rotation where the pseudo cubic YNMO(001)

lattice, with a/√2 = 3.692 and Å, b/√2 = 4.007 Å valued, could follow the STO lattice along by following the STO[110].

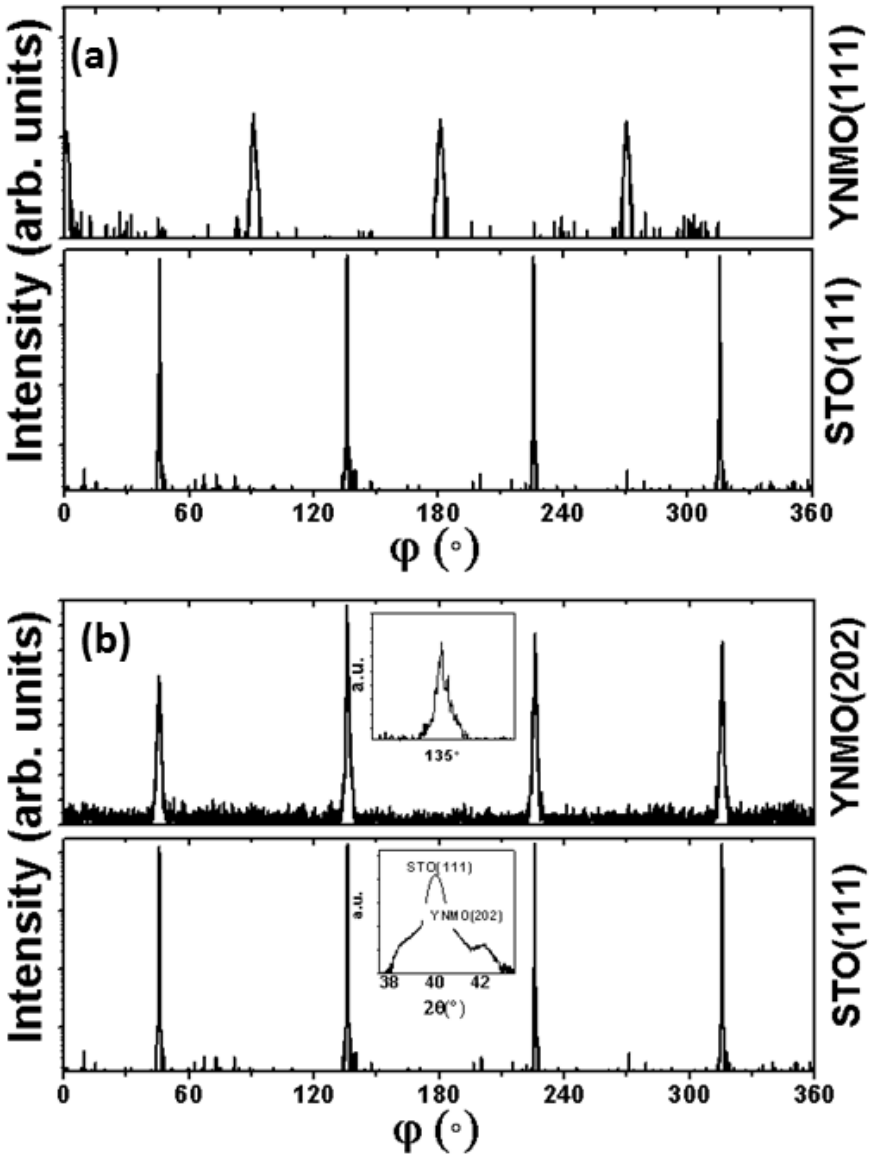

Figure 3.8 *Thin films φ-scans a) around STO(111) direction, and the corresponding YNMO(111), notice the shifting of 45^{O} of the YNMO lattice, respect the STO(111). b) around STO(111) and YNMO(202), the insets show, (superior) the rocking curve of YNMO(202) peak, and (lower) the* 2θ-ω *along STO(111).*

In order to investigate the in plane texture of the film φ-scans are performed along the STO(111) direction. This scan allows accessing all the geometrical reflections following the diagonal of the substrate unit cell. The standard procedure involves a similar φ-scan around the film (111) direction, in order to determine the shifting

between substrate and film unit cells. This is shown in **Figure 3,8 a).** However, it is also convenient, when exploring epitaxial relationships, to perform standard 2θ-ω scans, along the STO(111), or the chosen reflection. In this case the congruent reflections from the film, along the STO(111) direction, will be visible. **Figure 3.8 b)** shows a portion of this scan. It is observed that a single peak, attributed to the YNMO(101) is present. This peak follows closely the diagonal of the STO and has no shifting in the value of φ, suggesting that the YNMO cell, growths congruently on its sides (YNMO(100)) fitting the diagonal of the STO substrate (STO(110)).

So far, these observations seem to point to a cube on cube epitaxial growth, with a 45^{O} in-plane rotation. However, by using the same methodology along the STO(101) direction, the lateral side on the STO substrate can be investigated. A not congruent set of peaks, corresponding to the YNMO(112) reflection are observed. **Figure 3.9**; these peaks show a splitting along the lateral sides of the STO unit cells. The splitting on φ, of 1.45^{O}, and the periodicity of this peaks, every 90^{O}, clearly shows the presence of two in plane domains rotated between them. It can inferred, that each of the domains observed in the φ-scans, corresponds to a family of crystals, aligned a-YNMO(100) or b-YNMO(010) parallel to the STO(100). Finally, Pole figures performed on both, sample and substrate reflections; corroborate the absence of secondary orientations on the film. **Figure 3.10**.

According to the φ-scan data, a o-YNMO(001) unit cell, is placed on the cubic STO(001) with its c axis collinear to each other. However, a shift of 45^{O} in plane is observed, following the orthorhombic notation. The closer look to the data, evidence a congruent growth along the STO(111), with no splitting or whatsoever. While the STO(101), (referring to the sides of the cubic cell) shows a splitting along a YNMO(112) direction, corresponding to the diagonal in-plane diagonal of the o-YNMO films, pole figures along this direction are also showed in **Figure 3.10**.

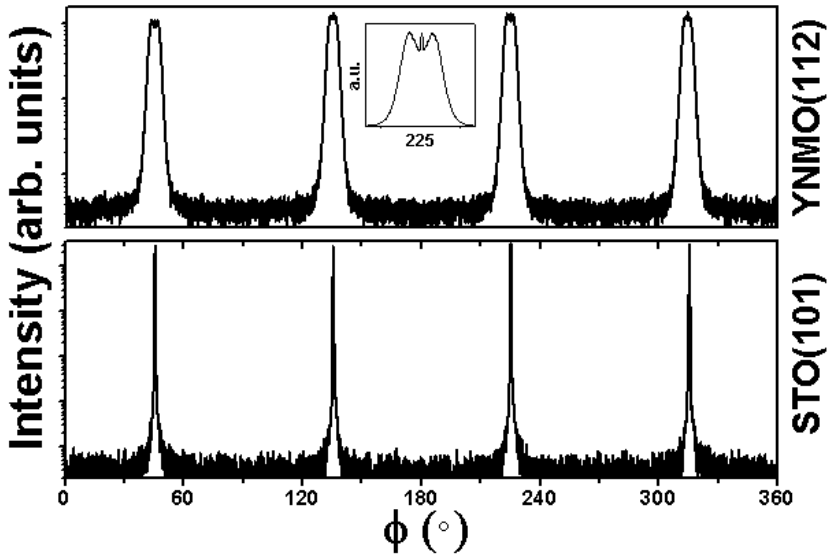

Figure 3.9 *Thin films φ-scans around the STO(101) direction, that corresponds to the YNMO(112). Inset shows the splitting of the YNMO peaks.*

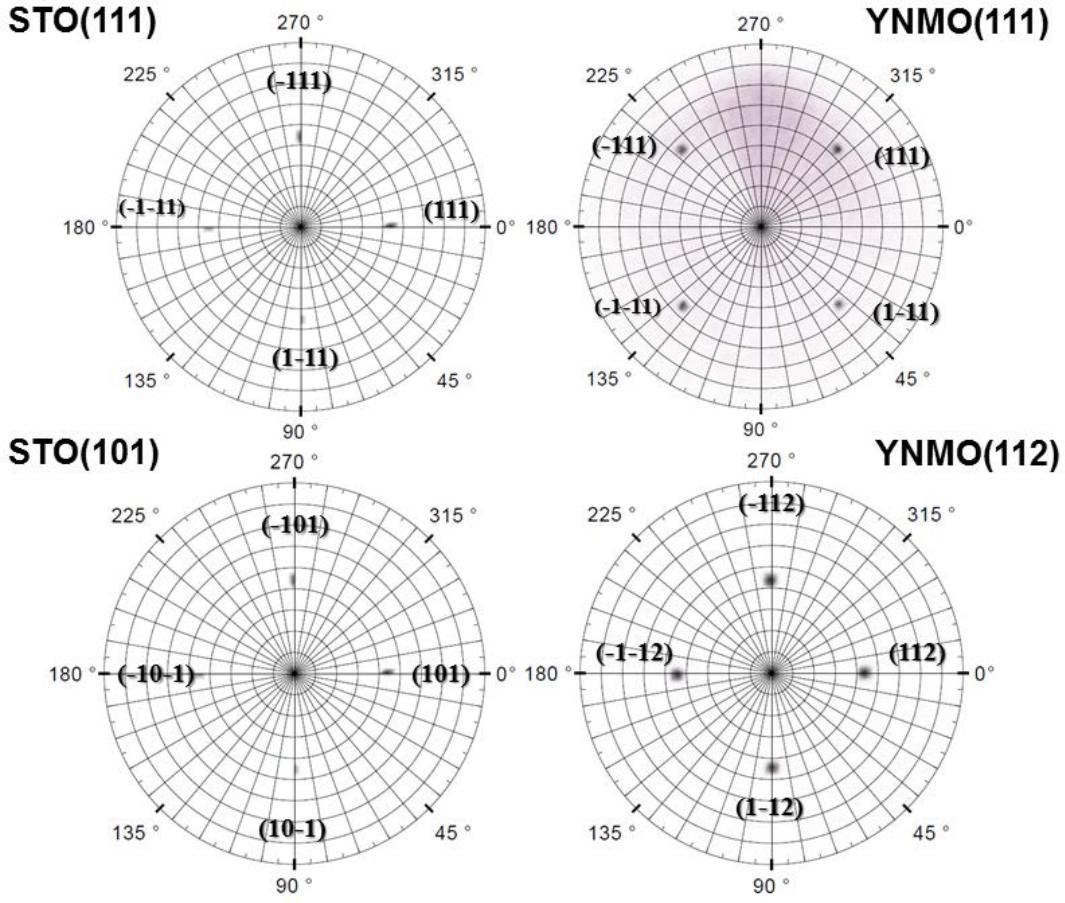

Figure 3.10 *Pole scans performed on STO(111) - YNMO(111) and STO(101) – YNMO(112).*

Reciprocal space maps were performed, **Figure 3.11**, in order to extract the in-plane lattice values of both crystalline domains. A reciprocal space map around the STO(113) reflection is performed. Along this direction, two peaks are observed, one following closely the in-plane stress of the STO lattice, and the second one, fully relaxed. This two peaks correspond to the o-YNMO(026) and o-YNMO(206) reflections. Therefore, by using the equations in **Appendix 2**, the values of both *a* and *b* YNMO lattices can be extracted as shown in **Table 2**, moreover, the epitaxial strain and deformation can be evaluated.

As a result, it can be appreciated that the in-plane parameters *a* and *b*, **Table 2**, are respectively expanded and compressed due to the epitaxial strain induced on the film by the substrate. This observation is congruent with the pseudo orthorhombic growth of the material on the STO(001) substrate. Predicted in plane mismatch of YNMO on STO bulk lattices parameters (considering the 45° rotation of the film orientation respect to the substrate) differs from the one observed experimentally, showing that parameters *a* and *b* are relaxed and stressed, respectively. Notice that the lattice mismatch (*f*) observed along the *f*[010] is noticeably different from the one observed in YMO films [**4**], though this is understandable due to the volume and lattice reduction as a result of Ni partial substitution is important to keep it in mind that anisotropic stress (ε) of the film has almost double of the values for YNMO along the ε[010], while the ε[001] has triplicated its deformation. This strongly suggest that the [001] direction is energetically favorable for the perovskite system YNMO and YMO.

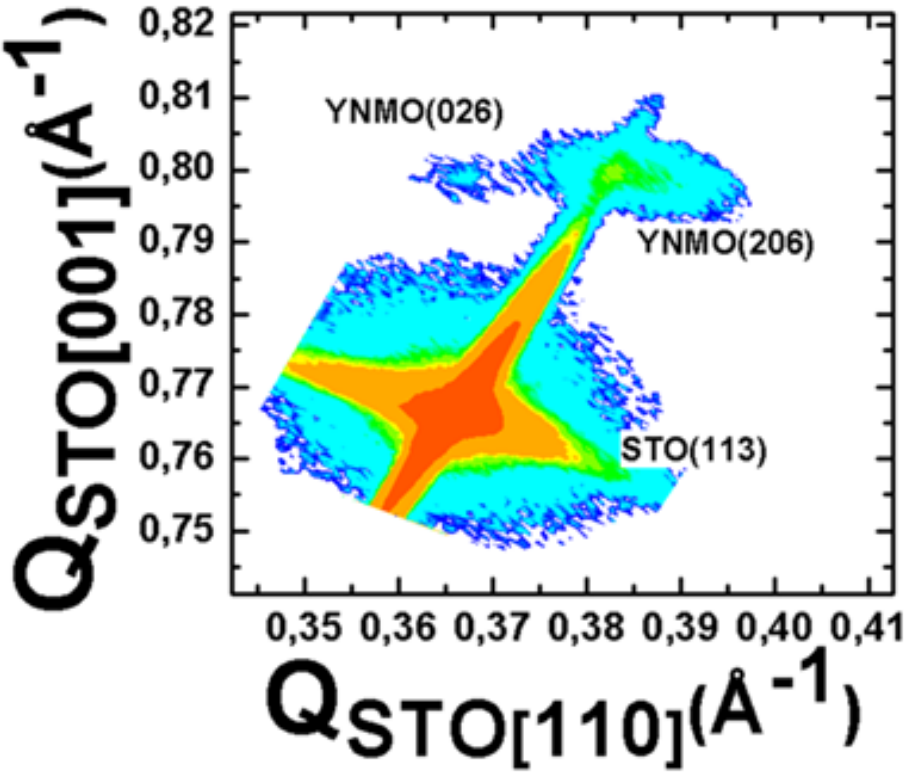

Figure 3.11 *Reciprocal space map image taken along the STO(113) direction, both in-plane domains are visible in the graph.*

As a conclusion of this section, The films grown on STO(001) show a single out of plane orientation, with two in-plane domains, which present the epitaxial relationship [100]YNMO(001)‖[110]STO(001) and [010]YNMO(001)‖[110]STO(001).

3.2.3.1 Parameters extrapolation for STO(011) & STO(111)

The use of multiple substrate orientations, allow the characterization of different textures and effects, resulting of the in-plane stress[**4**,**7**–**9**]. In order to examine such effects, YNMO films were grown on different STO substrates, using the optimal growth conditions found previously for YNMO(001). Shown in **Figure 3.12** are the results of 2θ-ω plots of samples growth in a single run using 750^{O}C, 2Hz and 0.6 mbar on STO(011) and STO(111).

Figure 3,12 a) shows the results of the 2θ-ω plots, a set of peaks at 19^{O} 34^{O} 50^{O} and 74^{O}, are concordant with a YNMO(*h*00) family. Peaks are intense and well defined, showing a evident preferential growth orientation on the STO(011) substrate. On the other hand **Figure 3.12 b)** shows the results for samples grown on STO(111). As in the

case of STO(011) intense peaks are observed, however, a different set of peaks are observed at 20^{O}, 34^{O}, 64^{O} and 74^{O}. These peaks, are congruent with the indexed values for the family YNMO(*h*0*h*)

Films quality was investigated by comparing rocking curves measured around the STO(011) to YNMO(200) and STO(111) to YNMO(202) and extracting their contributions on a similar way as that for the YNMO(001)/STO(001) films. The measured values of FWHM were: 0.0021º for YNMO(100)/STO(011) and 0.0024º for YNMO(101)/STO(111). It is clear that the quality of the films of STO(011) and STO(111) films were comparable to the one observed for YNMO(001) grown on STO(001).

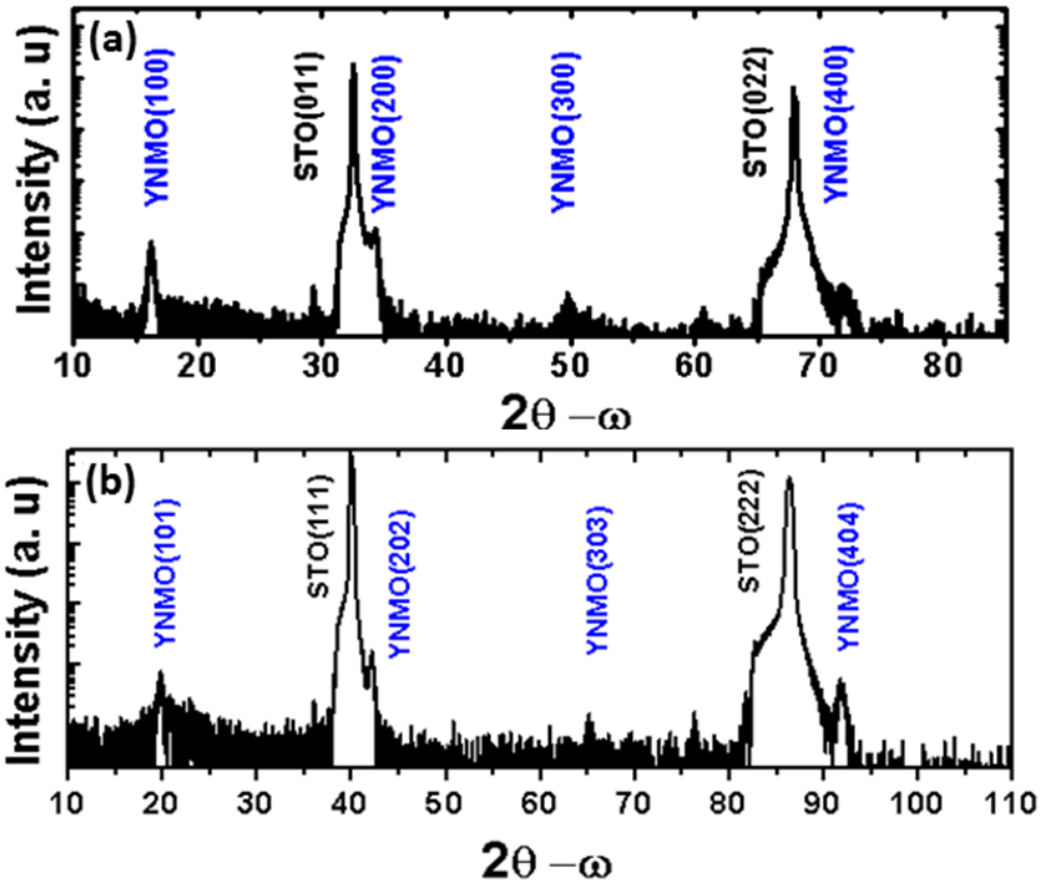

Figure 3.12 *2θ-ω scans of YNMO films deposited on a) STO(111) and b) STO(011).*

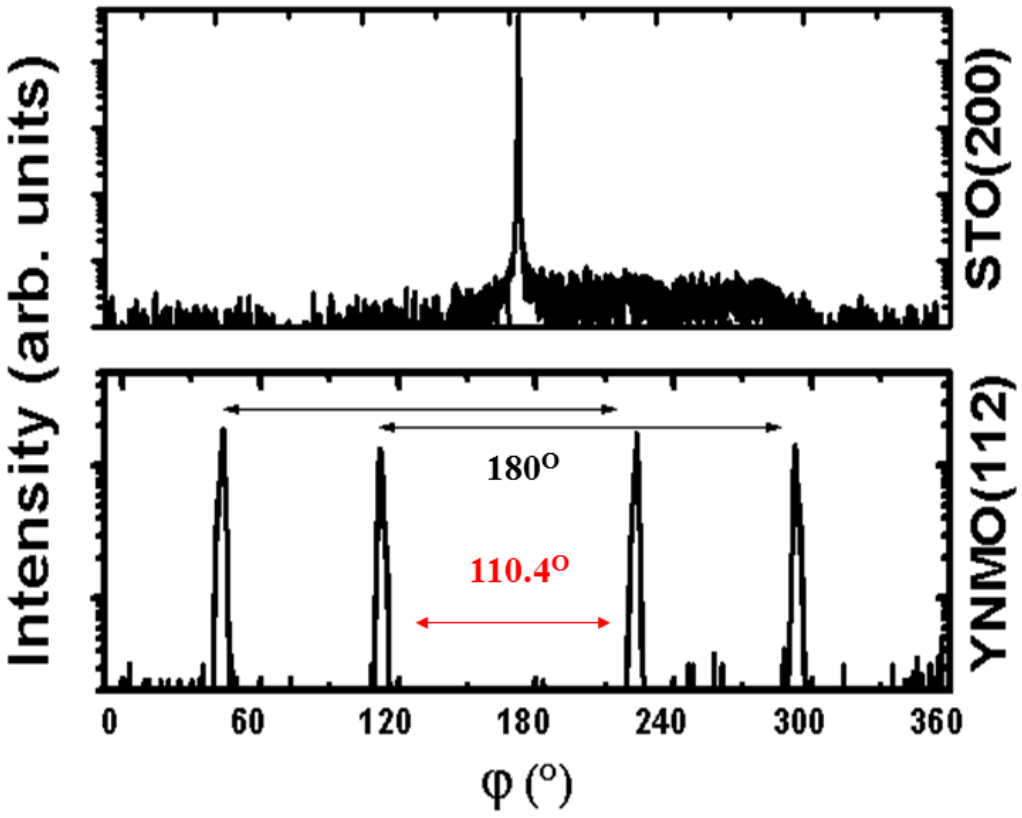

Figure 3.13 *Thin films φ-scans around the STO(200) direction, that corresponds to the YNMO(112). Lines show the separation of the two set of peaks.*

3.2.3.2 Epitaxial relationship YNMO(100)/STO(011)

In order to obtain information about the in-plane ordering of the film, φ-scans were performed around STO (200) (**Figure 3.13**). The results show a set of peaks separated by Δφ = 110.4º, typical of a tetragonal lattice on STO(110) confirming a corresponding single out of plane orientation. Similar case was observed in [**4**] from where the **Equation 3.3** can be obtained, relating the parameters *b* and *c*.

$$\frac{b}{c} = \frac{\tan(\frac{\Delta\varphi}{2})}{2} \quad \textbf{Equation 3.3}$$

This equation allows us to extract the b parameter, after choosing an appropriate reciprocal reflection. It is important to notice that φ scans confirms the existence of a single in-plane domain.

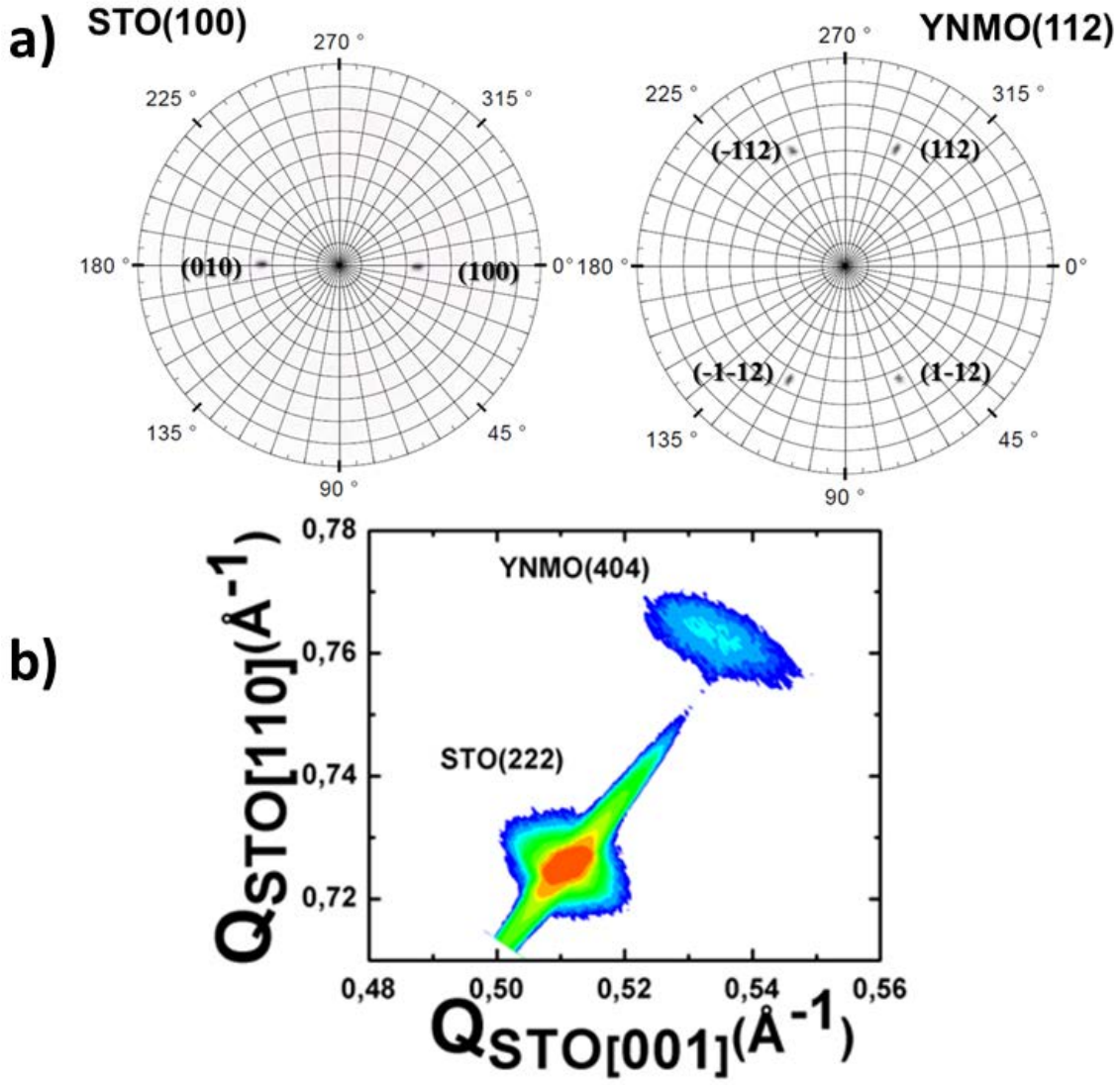

Figure 3.14 *a) Pole scans performed on STO(100) - YNMO(112), notice the non-symmetric distribution of the peaks in YNMO(112). b)) RSM performed around the STO(2 2 2) reflection.*

Pole figures were performed around STO(100) **Figure 3.14a**, as well as reciprocal space maps around STO(222) (**Figure 3.14b**), showing the single out-of-plane domain and confirming the fully textured growth with an epitaxial relationship of [001]YNMO(100)‖[001]STO(110).

Reciprocal space maps showed an elongated peak corresponding to the film due to the axial selection of the image both a and b parameters are present, which means that the c parameter can be directly obtained from the data, while a and b constants had to be calculated by both b/c ratio and $Q[011]=(1/b^2+1/c^2)^{1/2}$ equations. The obtained values

for the lattice constants are expressed in the pseudo orthorhombic indexation in **Table 2**. Moreover, the peak shape could suggest a progressive relaxation along the growth axis. Evaluation of lattice parameters leads to the analysis of the strain of the material, where in-plane parameters anisotropically strain with positive lattice mismatch along both directions. The calculated cell volume is established to be 219.8 $Å^3$ (2,198e-28 m^3). That, although it differs from the bulk data of 217 $Å^3$ (2,17e-28 m^3), is within the accepted error from the calculations.

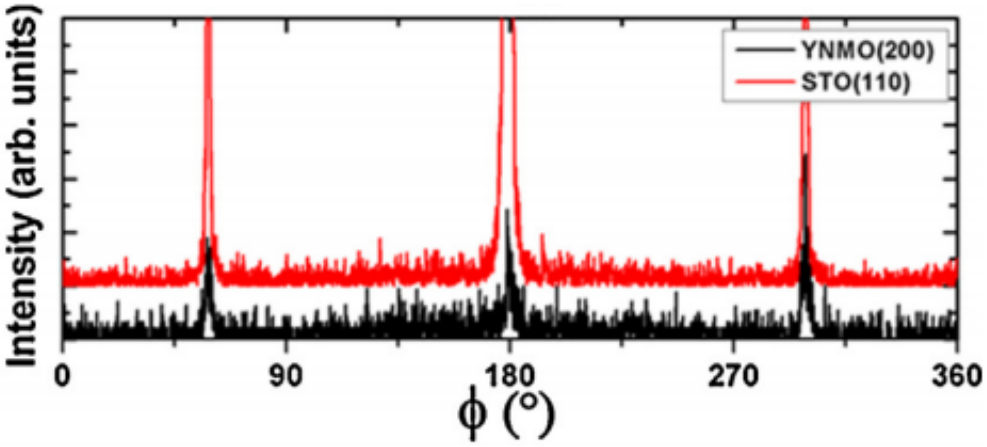

Figure 3.15 *Thin films φ-scans around the STO(110) direction, that corresponds to the YNMO(200).*

3.2.3.3 Epitaxial relationship YNMO(101)/STO(111)

Samples show the apparition of the YNMO(101) family of peaks **Figure 3.12b**, moreover, **Figure 3.15** shows φ-scans performed around STO (110) where three well defined peaks, that clearly follow a structure with the three-fold symmetry of the YNMO(110) planes are observed. The epitaxial relationships of the domains are [101]YNMO(101)‖[112]STO(111), [101]YNMO(101)‖[121]STO(111) and [101]YNMO(101)‖[211]STO(111).

Pole figures around YNMO(200), **Figure 3.16b,** corroborate the single out-plane domain and single reciprocal space map image around [110]STO(111) **Figure 3.16a** allows to continue determination the lattice constants. Since epitaxial relations are equal to the ones observed on YMO/STO(111) a very similar procedure was used in order to determine the lattice parameters [**4**].

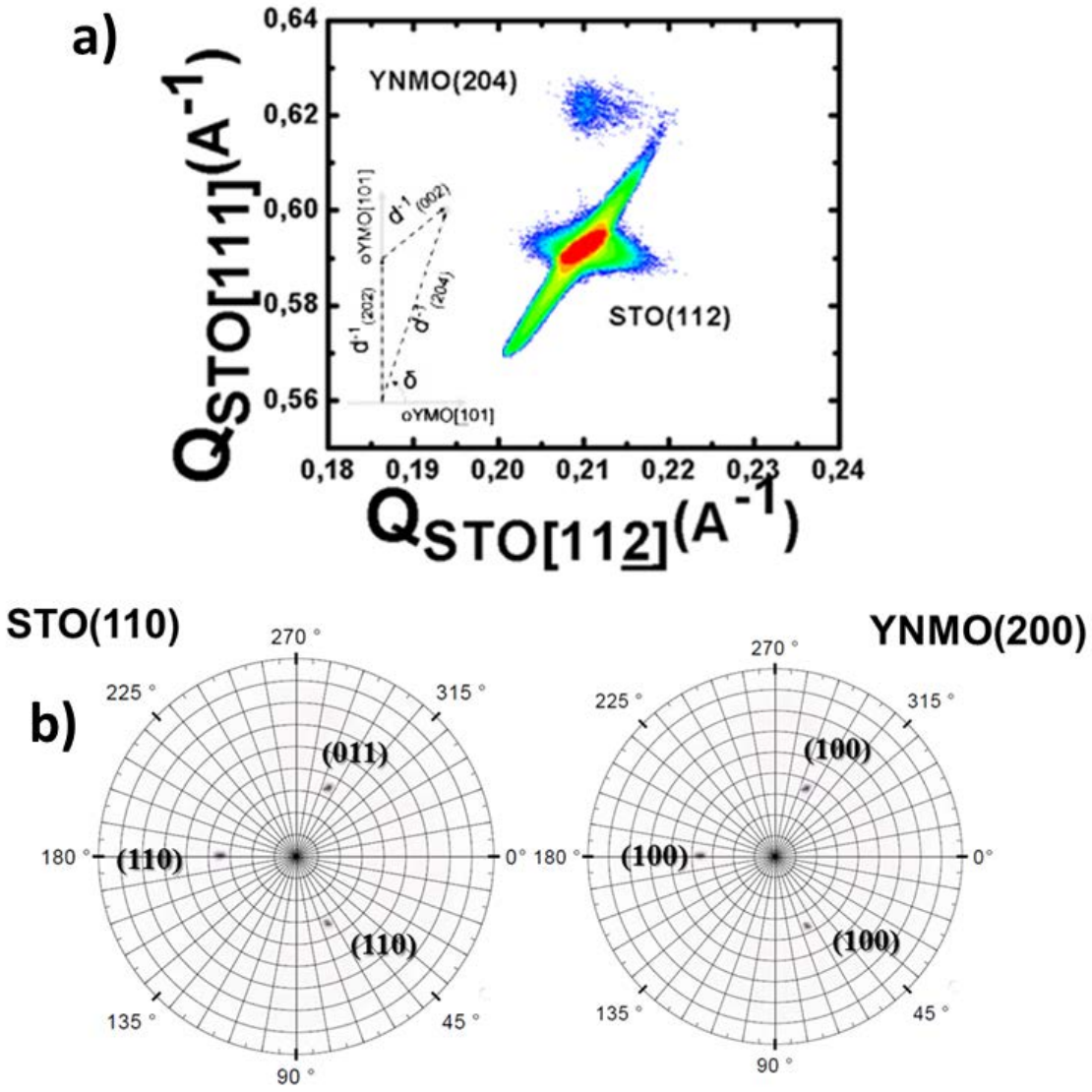

Figure 3.16 *a) Reciprocal space map image taken along the STO(112) direction with the YNMO(204, inset is reproduced from* [**4**] *b) Pole scans performed on STO(011) - YNMO(200) showing the clear single out of plane orientation of the three fold symmetry film.*

The procedure to determine *a* and *c* lattice parameters is reproduced from reference [**4**] in **Figure 3.16 a) inset.** The reciprocal space map coordinates of the (204) reflection allow us to determine the angle using $\delta = arctan(0.625/0.214) = 71.09°$, and the associated interlunar (204) distance. Then, using the (202) interplanar distance extracted from the 2θ-ω scan, the segment labeled $d^{-1}(002)$ can be determined by using cosine law as:

$$\sqrt{\langle \boldsymbol{d^{-2}(202) + d^{-2}(204) - 2 * d^{-1}(202) * d^{-1}(202) * \cos(90 - \delta)} \rangle} \quad \textbf{Equation 3.4}$$

While the parameter *c* can be obtained as 2 · *d*(002). Notice that *a* parameter can be obtained using the following formula:

$$\boldsymbol{a = c * \tan\left(\sin^{-1}\left(\frac{d(101)}{c}\right)\right)} \quad \textbf{Equation 3.5}$$

As a result, a = 5.18(1) Å and c = 7.76(2) Å, are extracted and indexed in the **Table 2**. It is observed that the out-of-plane parameter d(101)=4.336Å has expanded significantly from the bulk value (4,2759Å), the diagonal value of the unit cell is calculated as 9.155 Å, that is slightly bigger than he bulk value (9.126Å) showing an elongation along the [10-1] direction of ε[10-1]= 0,34%. Therefore the lattice constants have suffered a compression along the *b* and *c* and a relaxation along the direction, explained by the bigger mismatch with the substrate.

LATICCE CONSTANTS

	a(Å)	b(Å)	c(Å)	vol.(Å^3)
$YNMO_{BULK}$	5,22	5,55	7,48	217
$YNMO_{(001)}/STO_{(001)}$	5,26	5,52	7,48	217.1
$YNMO_{(100)}/STO_{(110)}$	5,31	5,41	7,63	219,8
$YNMO_{(101)}/STO_{(111)}$	5,33	5,46	7,44	217 [a]
YMO_{BULK}	5,26	5,85	7,36	226.5
$YMO_{(001)}/STO_{(001)}$	5,27	5,8	7,44	227.1
$YMO_{(100)}/STO_{(110)}$	5,27	5,72	7,48	225,9
$YMO_{(101)}/STO_{(111)}$	5,18	5,63	7,76	226.5 [a]

Table 2: *Lattice constants of YNMO bulk, YNMO(001), YNMO(100) & YNMO(101), compared with their counterparts from YMO. (a) Denotes values obtained by volume conservation.*

3.2.4 Lattice mismatch and strain

After successfully determining the lattice values of YNMO(001), YNMO(100) and YNMO(101) thin films, it is possible to investigate the effect of the epitaxial

relationship $\boldsymbol{\varepsilon}$ strain of the material as a function of the $\boldsymbol{f}$ lattice mismatch. Lattice mismatch is defined as showed in **Equation 3.6**.

$$\boldsymbol{f = 100x(a_{substrate} - b_{film})/b_{film}} \quad \textbf{Equation 3.6}$$

Where, $a_{substrate}$ and b_{film} are the lattice constant values along a given direction. The values calculated for all the samples are shown in **Table 3**.

Epitaxial strain is also useful to determine, since it talks about the unit cell deformation due to the previously named lattice mismatch. Strain is calculated as shown in **Equation 3.7**, Where n_{film} is the lattice of the film along the specific direction and n_{bulk}, the lattice value in bulk along the same direction.

$$\boldsymbol{\varepsilon = 100x(n_{film} - n_{bulk})/n_{bulk}} \quad \textbf{Equation 3.7}$$

It is important to notice the fundamental similarity between both values, indubitably a long mismatch.

Comparative **L**attices **C**onstants of **YNMO**(*hkl*) & **YMO**(*hkl*)

	***a*(Å)**	***b*(Å)**	***c*(Å)**	**vol.(Å^3)**	**$\varepsilon_{[100]}$ [a]**	**$\varepsilon_{[010]}$ [a]**	**$\varepsilon_{[001]}$ [a]**	**$f_{[100]}$ [b]**	**$f_{[010]}$ [b]**	**$f_{[001]}$ [b]**
$YNMO_{BULK}$	5,22	5,55	7,48	217	-	-	-	5,80%	-0,50%	-
$YNMO_{STO(001)}$	5,26	5,52	7,48	217.1	0,77%	-0,54%	-	4,99%	0,05%	-
$YNMO_{STO(110)}$	5,31	5,41	7,63	219,8	1,72%	-2,52%	2,01%	-	2,08%	2,36%
$YNMO_{STO(111)}$	5,33	5,46	7,44	217 [c]	2,11%	-1,62%	-0,53%	4,51%[e]	0,49%	-
YMO_{BULK}	5,26	5,85	7,36	226.5	-	-	-	4,99%	-5,60%	6,11%
$YMO_{STO(001)}$	5,27	5,8	7,44	227.1	0,19% [d]	-0,85%	1,09% [d]	4,79%	-4,78%	-
$YMO_{STO(110)}$	5,27	5,72	7,48	225,9	0,19% [d]	-2,22%	1,63%	-	-3,45% [d]	4,41% [d]
$YMO_{STO(111)}$	5,18	5,63	7,76	226.5 [c]	-1,52% [d]	-3,69%	5,43% [d]	5,74%[e]	-5.60%	-

Table 3: Comparative lattice constants in YNMO and YMO. a= 100 x ($n_{film} - n_{bulk}$) / n_{bulk}. .Where n_{film} is the lattice of the film along the specific direction and n_{bulk}, the lattice value in bulk along the same direction. b= 100 x ($a_{substrate} - b_{film}$) / b_{film}), where $a_{substrate}$ and b_{film} are the substrate and film lattice along that direction. c= Obtained by volume conservation. d= Calculated in this work from the original reported data. e= Refers to $f_{[101]}$ with ($\sqrt{6}$ x $a_{substrate}$) as lattice parameter and $\sqrt{(a^2 + c^2)}$ as b_{film}.

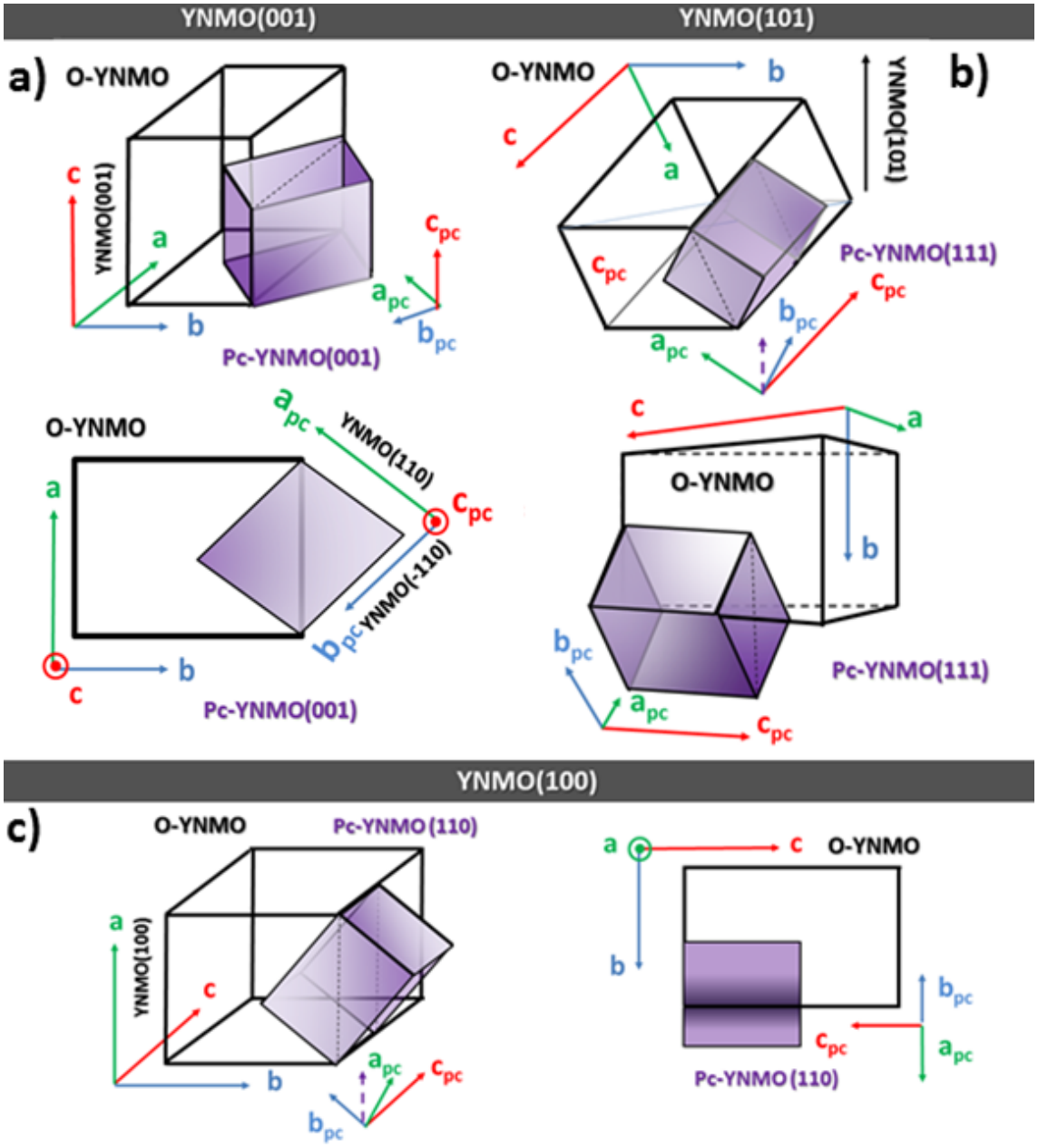

Figure 3.17 *Diagrams of O-YNMO unit cell conversions to Pc-YNMO unit cell. a,c,b: are lattice values for the orthorhombic unit cell, while a_{PC} , b_{PC}, c_{PC} show the corresponding pseudo cubic lattices. a) YNMO(001, b)YNMO(101), c) YNMO(100).*

3.2.5 Lower symmetry conversion

The epitaxial relationship of the orthorhombic o-YNMO film with the STO substrate has been identified, however, it is worth pointing few nomenclature considerations towards the pseudocubic (*Pc)* indexing of this orthorhombic (*o*-) perovskites, useful in further studies due to the simplification of their indexes.

Graphical representation of the crystal relationships can be found in **Figure 3.17.** For the sample YNMO(001)/STO(001), the corresponding pseudo cubic lattice can be expressed as o-YNMO(002) = P_C-YNMO(001), **Figure 3.17 (a).** The collinear alignment of both out of planes components allows them to be expressed as single plane, o-YNMO(001) || P_C-YNMO(001). However, the in-plane configuration, the splitting and partial alignment of the O-YNMO(112) plane with the STO(101) tells us that O-YNMO(112) is somewhat equal to P_C-YNMO(100) & P_C-YNMO(010), referring to the P_C- *a* and P_C-*b* axis. From reciprocal space mapping it can be observed that one lattice is stressed and the other one is relaxed. In principle, it can be assumed that the strained lattice corresponds to the P_C-YNMO(010) || o-YNMO(1-12) and the relaxed lattice is P_C-YNMO(100) || o-YNMO(-112), due to their proximity with bulk values.

In the case of YNMO(100)/STO(110), shown in **Figure 3.12 b),** the transformation can be quite simple, although somehow miss leading. o-YNMO(100) is aligned with STO(110). Therefore, in this case o-YNMO(100) can be expressed as P_C-YNMO(110) (**Table 3**). Also, due to the o-YNMO(112) already established relation with the STO(101), it can be observed that no splitting or multiphase are observed. Besides, the P_C-YNMO(001) lays totally in-plane. It is important to notice, that P_C-*a* and P_C-*b* axis are not directly resolved and, more likely, are collinearly mixed in the film, due to substrate epitaxial strain. Moreover, the observed lattice constants show the biggest tendency towards the tetragonal cell; this seems to be related to the more convenient fitting of the o-YMNO unit cell on a cubic STO substrate.

Finally in the YNMO(101)/STO(111) samples, **Figure 3.12 a),** it can be observed that o-YNMO(101) || P_C-YNMO(111) for each in-plane domain. This follows the previously observed relation on STO(001) substrates **Figure 3.17 b)**. However, is important to remark that, provided the previously established relationship between o-YNMO(112) and the P_C-*a* and P_C-*b* axis, and additionally, the higher distortion of the unit cell observed in the sample, when compared with YNMO(100)/STO(011), the P_C-YNMO(100) and P_C-YNMO(010) has a larger difference between Pc-a and Pc-a, and, cannot be collinear in a given in-plane domain.

3.2.6 Growth mechanism

After successfully determining the epitaxial relationship of the YNMO/STO films, attention is focused on understanding the growth mechanism and the morphological characteristics of the films. Films of different thickness were deposited on

YNMO(001)/STO(001) in order to investigate the morphology dependency on the thickness. **Figure 3.18**, shows 4 samples corresponding to the STO(001) substrate, YNMO(001) of ≈5, ≈10 and ≈17 nm respectively.

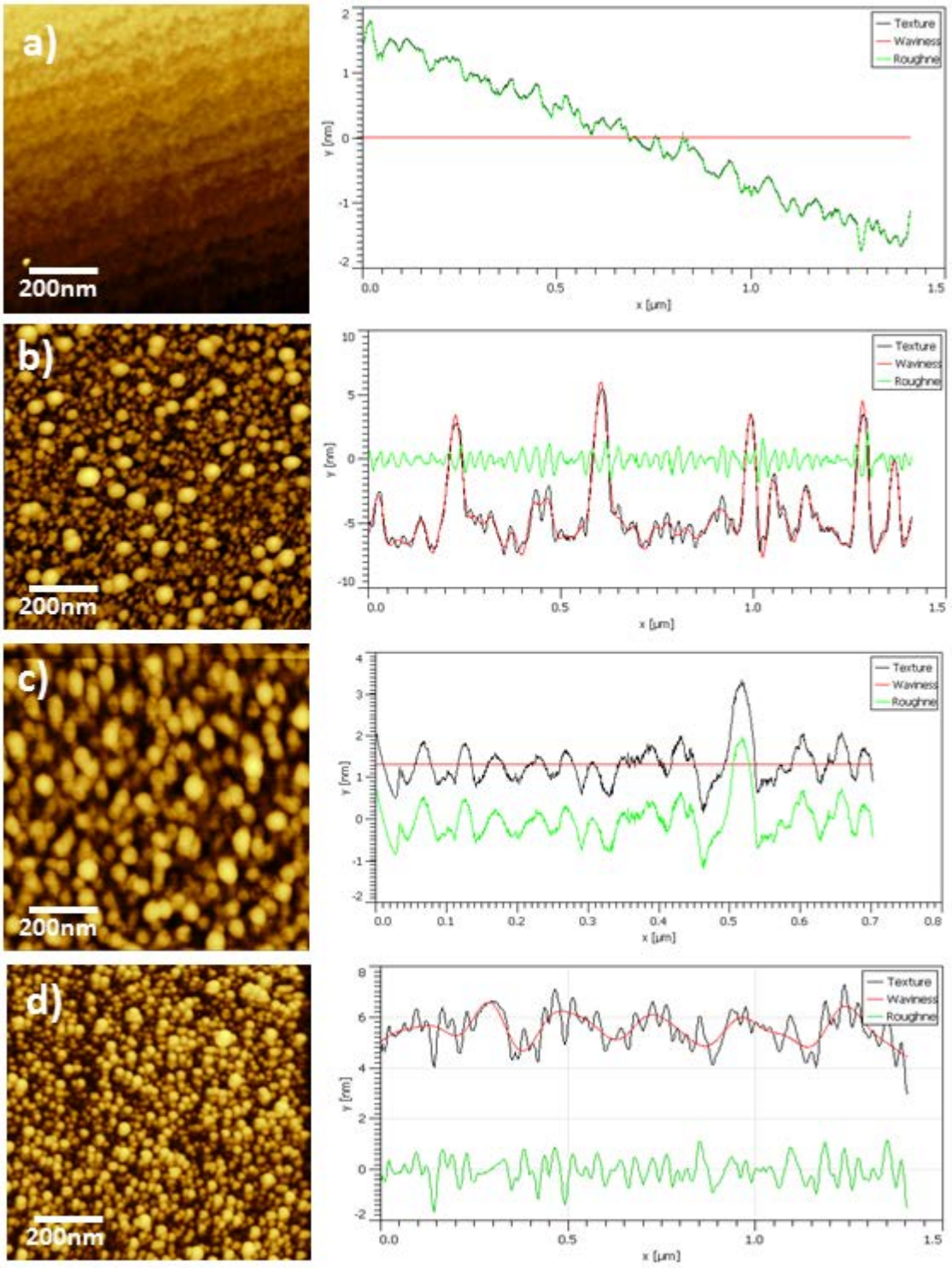

Figure 3.18 *AFM micrograph of a) STO(001) substrate, b) YNMO~5nm film, c)YNMO~10nm film and d) YNMO~17nm film.*

The STO(001) bare substrate shows small terraces with a very low roughens typical of fresh substrates. YNMO(001)~8nm shows a rapid increment in roughness as different nucleation points appear on the surface. The coalescence point is found below the 17 nm thickness showing a rapid diffusion of the incoming material, with a roughness of 2 nm. Moreover the reduction on roughness as the thickness of the film increases suggests a late homogenization of the film, well after the coalescence of the film.

Accompanying plots in **Figure 3.18** represent the extracted texture, waviness and roughness of selected profiles of the images. It is important to understand the relationship between waviness and roughness, in order to comprehend the represented data. Waviness is related to the changing on slope per lines plotted in the AFM micrograph. This function gives a visual representation of drastic changes on the morphology of the surface analyzed. On the other hand, roughness is typically associated to the real values of the profile investigated, meaning that changes on absolute values along the profile image are normalized giving a zero centered version of the profile analyzed. Typically the roughness is extracted from the mean value of such plot.

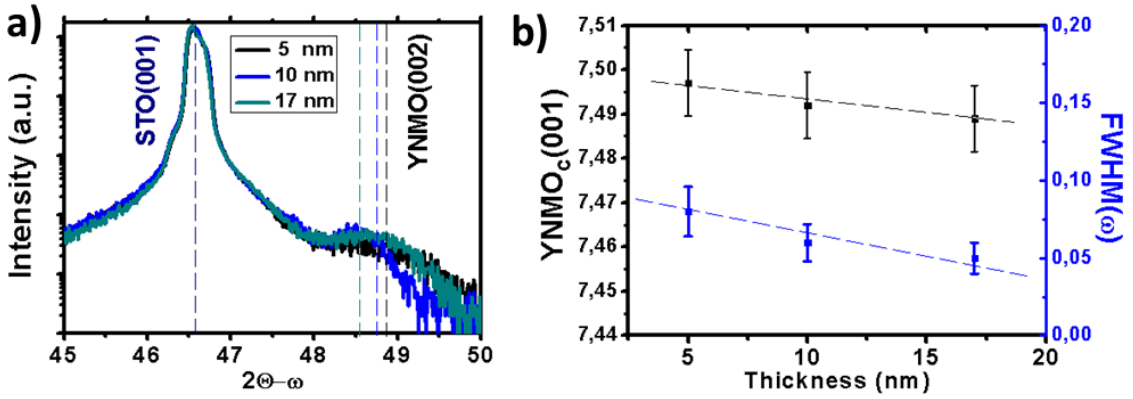

Figure 3.19 *X-ray plots of a) YNMO(002) & STO(002) peak at different thickness. b) out of plane parameter and FWHM as a function of the film thickness.*

Figure 3.18 a) is represented by a long decedent profile, following the observed terraces, as a result the roughness of the film follows a monotonically lowering value, in this case the waviness gives a rather accurate idea of the total topological behavior of the film. Another way of interpreting such a data could be extracting a profile along a

single terrace. As previously mentioned, results suggest a 3D columnar growth and a homogeneous film. Thickness of the film was standardized according to data obtained by X-ray reflectometry resulting in thicknesses of ≈70 nm; the nominal thickness of the films in **Figure 3.18** was calculated according to the growth rate of 0.136Å/pulse.

As observed, the roughness of the particles on the surface seems to decrease with thickness. In this case new incoming particles arrive to the surface and diffuse along reaching an already growing island. This process would ultimately lead to a highly granular surface just below the coalescence point, which is fast enough to happen below the 17 nm, then after reaching the coalescence point, the film would reduce its roughness film as new material arrives mainly as a result of provided long time of surface migration by the low repetition rate and high temperature of deposition rate used in the deposition of the films.

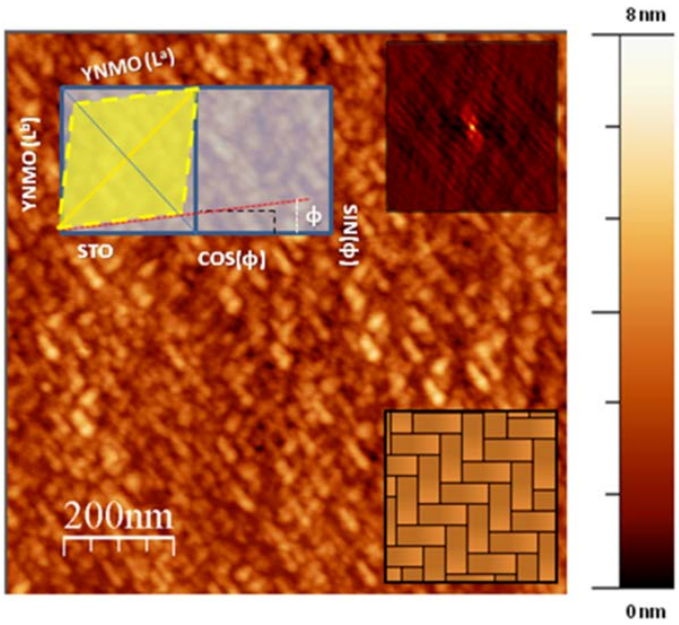

Figure 3.20 *AFM image of YNMO(001)/STO(001). The insets describe the geometrical relation with* ***Equation 3,8*** *self-correlation function of the film and a guide to the eye for the mound formation observed in the film.*

X-ray analysis performed at different stages of the film growth is shown in **Figure 3.19.** Films deposited where analyzed by standard 2Θ-ω plots and rocking curves, both performed along the YNMO(002) and STO(002) reflection. **Figure 3.19 a)** shows the progressive apparition of the distinctive YNMO(00*l*) reflection with thickness

increment, it is important to notice the progressive relaxation of the out of plane lattice with the thickness increment **Figure 3.19 b).**

It is clear then, that the out of plane parameter suffers a progressive relaxation as the thickness of the film grows; this is fully explained by the epitaxial strain that ultimately leads to the mismatch observed in the film. Also, it is observed that the film increases its crystallinity as the coalescence point is reached, due to the nucleation of different grains a commonly observed effect in thin films[**10**]

3.2.7 Surface morphology of YNMO(001)/STO(001)

Fully grown epitaxial YNMO(001)/STO(001) thin film, 71 nm, is now examined by AFM. Images obtained from STO (001) slightly differ from the granular surface observed previously. **Figure 3.20** shows well defined mounds, with the particularity of showing elongated particles with a grain size distribution centered on ≈40 nm, in its long axis and ≈20 nm in the shortest. In addition, mounds seem to follow a *zigzag like* distribution along the surface. This morphology has been previously observed in the literature in YNMO [**4**] although its origin was never related to the presence of two in-plane domains observed in X-ray analysis.

Aiming to correlate the structural formation found by AFM in YNMO(001)/STO(001) samples with information obtained from X-ray analysis, the epitaxial relation between the film and substrate was considered. First, the distance between the two in-plane domains and the substrate from the STO (101) φ-scans (**Figure 3.9**), the angle φ=1.45^{o} was obtained. This angle represents the deviation between the two YNMO in-plane domains along the STO (101) direction. Since scans performed around STO (111) showed no evidence of splitting or variation from the cubic cell, it is clear that the diagonal of the STO cell is the matching position. In order to correlate the diffraction information and the AFM data we used the pseudo cubic values of the YNMO cell (*a*=3,719 Å and *b*=3,903 Å). Thus allowing us to follow simple formulas to satisfy the geometrical constrictions and the epitaxial relationship along both *a* and *b* directions, as shown in **Equation 3.8**.

$$N * L_{STO} = M * (\cos\varphi * L^{a}_{YNMO})$$
$$N'' * L_{STO} = M * (\sin\varphi * L^{b}_{YNMO}) \qquad \textbf{Equation 3.8}$$

Where N is the amount of lattices of STO (L_{STO}), M corresponds to the amount of lattices for YNMO (L^{x}_{YNMO}) in a given direction and in the pseudo cubic index (as shown in the illustrative diagram in **Figure 3.20 inset**). A numerical approach to these equations showed that lattice a and b got relative accurate matches when N=45 and N"=125, values that, when multiplied for the lattice constants, give a comparable result to the extracted from AFM micrographs of M_a=16.393 nm and M_b=46.492 nm. These results match the AFM observations and seem to confirm that, in fact, the mound observed are related with the epitaxial growth of the YNMO film, were each of the 90° shifted mounds could be associated to an in-plane crystalline domain.

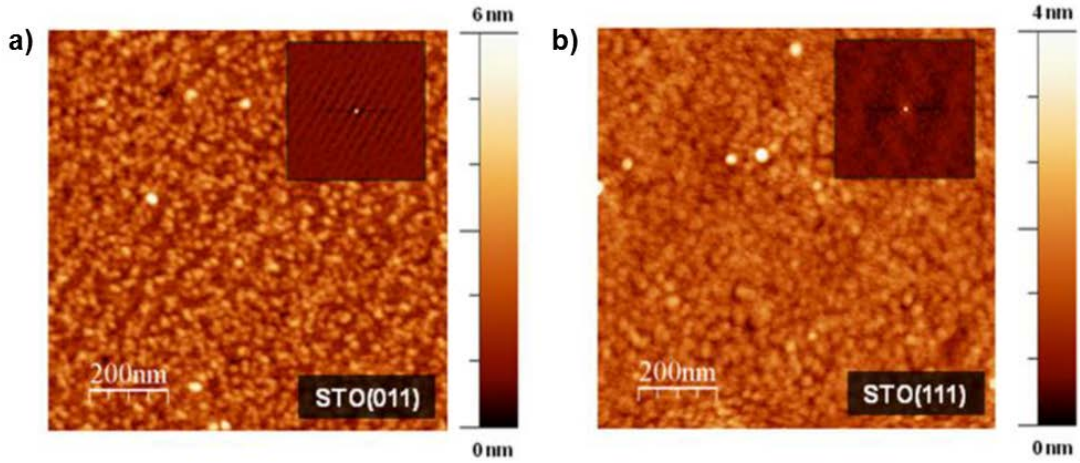

Figure 3.21 *AFM image of a) YNMO(100)/STO(011) and b) YNMO(101)/STO(111) The insets show the self-correlation function of the film. Notice how a) shows a periodicity strongly similar to terraces in flat films*

3.2.8 Surface morphology of YNMO(100)/STO(011) & YNMO(101)/STO(111)

Figure 3.21 shows the AFM images from YNMO(100)/STO(011) and YNMO(101)/STO(111). Both samples show a roughness similar to the one observed on STO(001) (**Figure 3.20**) with values of ≈5 nm for YNMO(100) and ≈3 nm for YNMO(101) and a grain size distribution of ≈25 nm. Additionally, in the case of YNMO(100), although terraces were not clearly appreciated in the topography images and the 3d growth and granular nature of the film could prevent their appearance, the self-correlation analysis allows us to identify a terraces-like growth, where the grains would follow the cut direction of the substrate, showing a very smooth and high quality sample (**Figure 3.21 a) inset**).

Self-correlation analysis of YNMO(111), **Figure 2.21 b) inset**, shows a typical feature for highly granular films, in which grains would allocate in random positions and distribution without following any specific substrate morphology but rather the grain nucleation points, which are also influenced by the three in-plane domains present in the film. A common characteristic, shared with films of YNMO grown on STO(001) is low roughness increasing with the film thickness.

3.2.9 HR-TEM on YNMO(001)/STO(001)

Low magnification transmission electron microscopy characterization was performed on different areas of the YNMO(001)/ STO(001) film, **Figure 3.22**. Images are compatible with the aforementioned 3D growth and reveal an evident roughness on the surface.

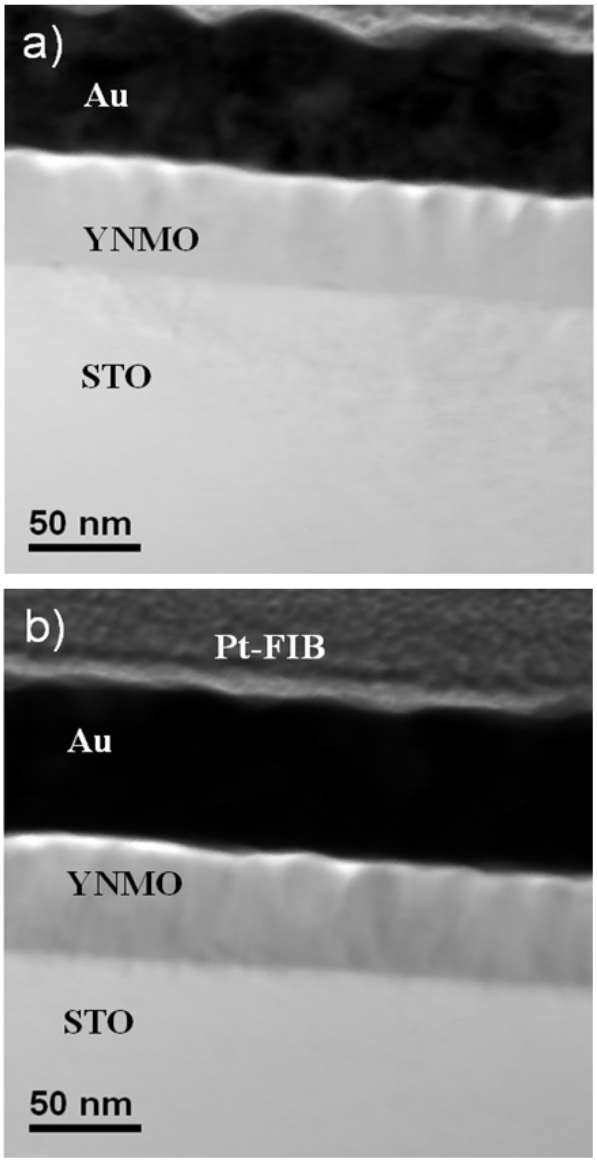

Figure 3.22 *Low magnification TEM Images, showing 2 different areas of the film, separated by 2 µm. Images show a rather sharp interface and clear roughness of the surface.*

HR-TEM images revealed a growth along [-110] direction (zone axis), **Figure 3.23**. Images show a sharp interface and unequivocally confirm the 3D growth of the films. The growth direction is found to be YNMO(001) concordant with the X-ray diffraction experiments.

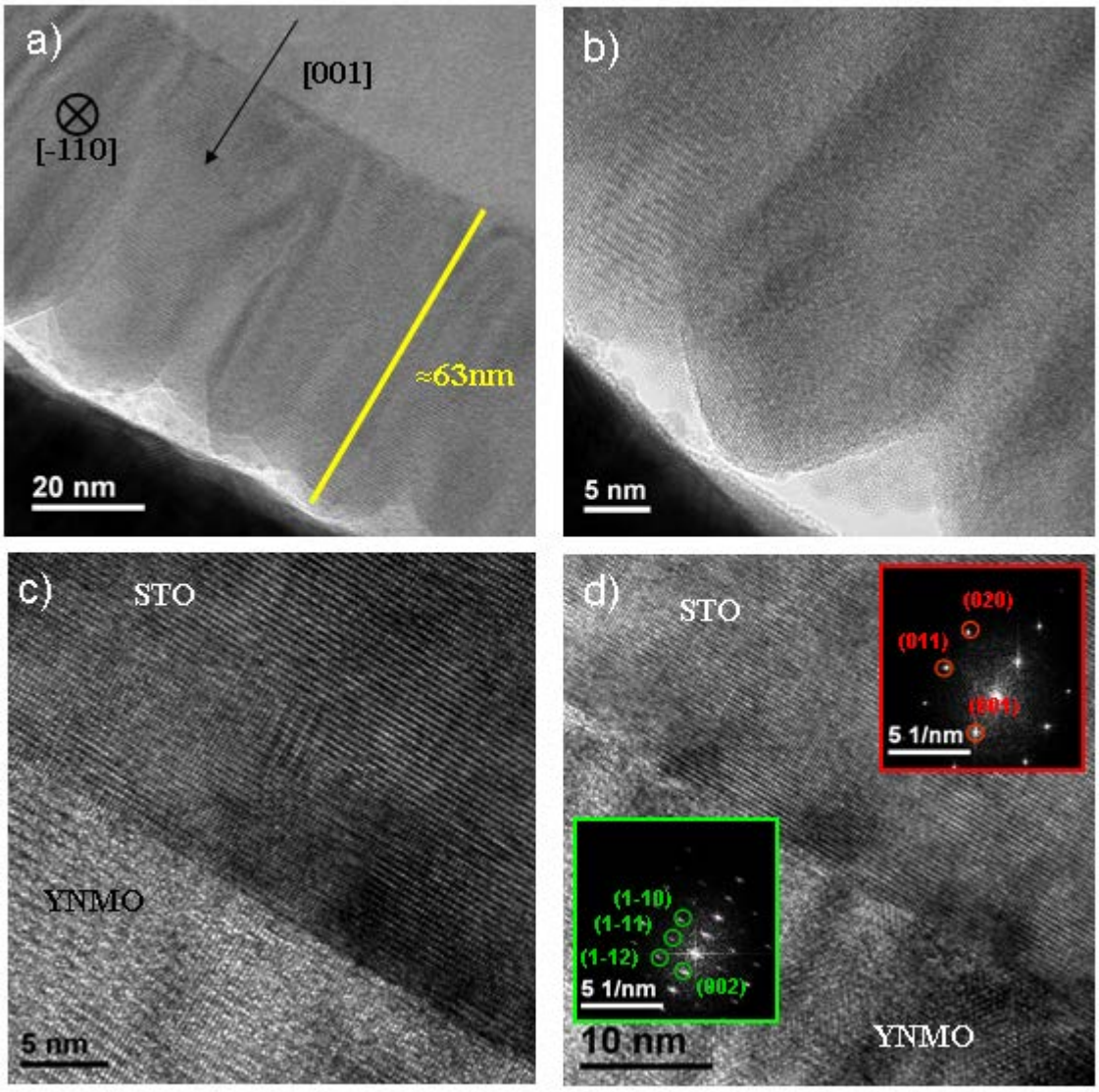

Figure 3.23 *High resolution images of YNMO(001)/STO(001) characterized, showing a) Film of 63nm . b) Grain boundaries and clear 3D growth c) Sharp Interface and d) epitaxial relationship [100]YNMO(001)/[100]STO(001) congruent with X-ray analysis.*

Fast Fourier transformation, **inset Figure 3.23 d)** shows the distinguishable patter of both STO and YNMO lattices with zone axis (110). Peaks are indexed accordingly and the epitaxial relationship [100]YNMO(001)/[100]STO(001) which is concordant with the XRD studies.

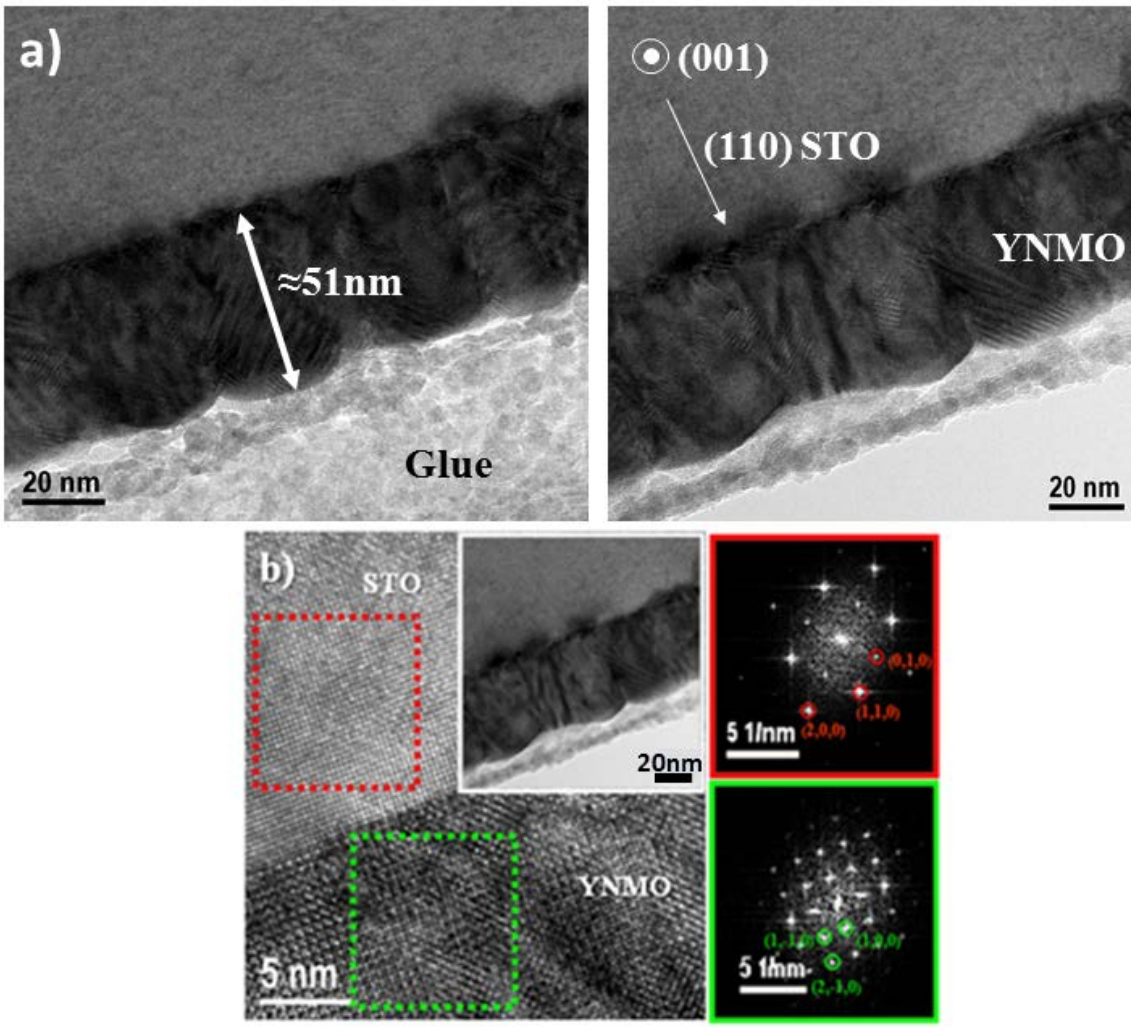

Figure 3.24 *High resolution images of YNMO(100)/STO(011) characterized, showing a) Film of 51nm. b) FFT and low magnification image of YNMO(001)/STO(001) congruent with X-ray analysis.*

3.2.10 HR-TEM on YNMO(100)/STO(011) & YNMO(101)/STO(111)

Now, the attention is focused on the films YNMO(100)/STO(011) and YNMO(101)/STO(111). First STO(011) films will be addressed and then STO(111).

Sample of YNMO(100)/STO(011) was observed on a STO(001) zone axis. **Figure 3.24** shows few HR-TEM micrographs where a rough surface can be observed, the increment in roughness, from the one observed in AFM is attributed to the FIB preparation and perhaps particularities of the analyzed section. The columnar growth is evident in all the micrographs and small crystallites are observed in the proximity with the interface. Interface is sharp and Fast Fourier transform (FFT) analysis, **inset Figure 3.24 b)** confirm the epitaxial relationship extracted from X-ray measurements.

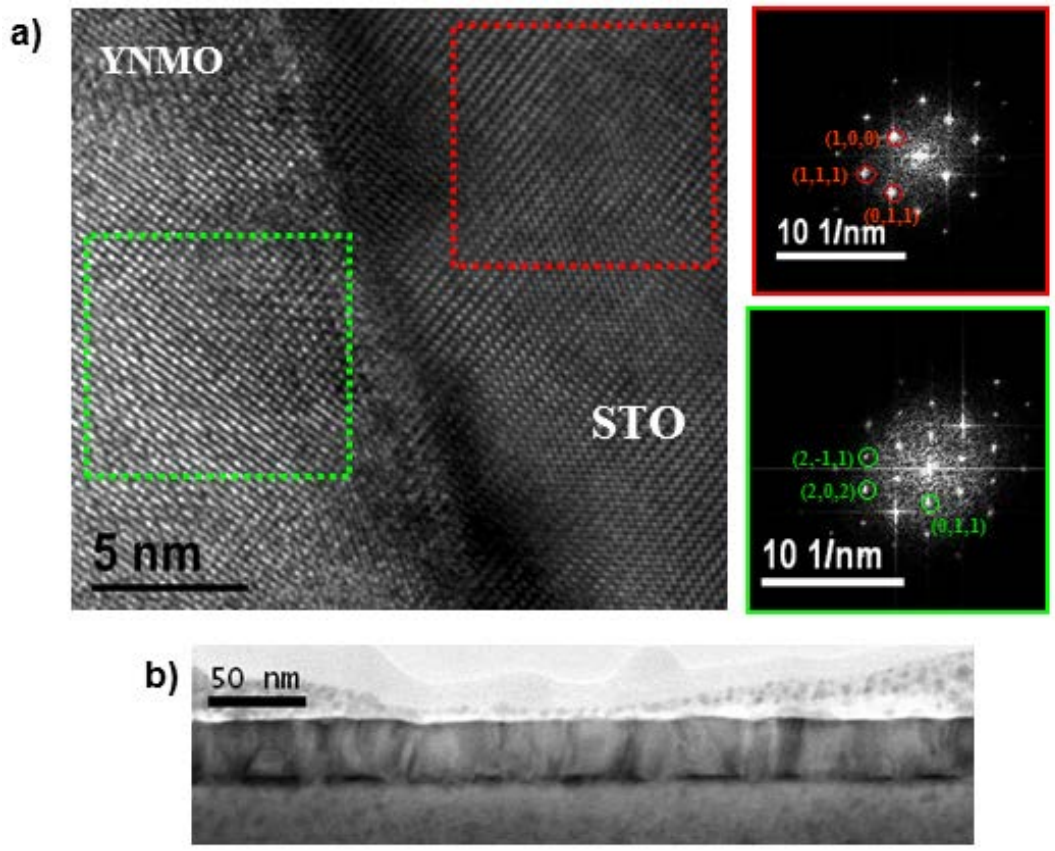

Figure 3.25 *High resolution images of YNMO(100)/STO(111) characterized, showing a) cross section between substrate and film, boxes show the place from where FFT insets were obtained b) low magnification image of YNMO(101)/STO(111) covered with glue.*

Images of samples grown on STO(111) are shown in **Figure 3.25**, as in previous substrates, a sharp interface and 3D growth observed. Roughness is comparable to the one observed in AFM micrographs. Finally, insets in **Figure 3.25 a)** confirm the epitaxial relationship obtained from X-ray measurements.

It is important to remark that samples for HR-TEM measurements were grown in a single run in a PLD experiment. The plume was carefully centered to cover the small

substrates, specifically cut for this specific purpose, thus the discrepancies do not arouse due to experimental errors. As a result, the films show a clear growth anisotropy related to the different surface energy of the STO(001), STO(011) & STO(111) crystalline planes. Further studies are needed to fully understand role of such anisotropy.

3.2.11 Compositional Analysis

In this section chemical analysis of the films are shown. Results from XPS, SIMS and EELS will be presented and discussed.

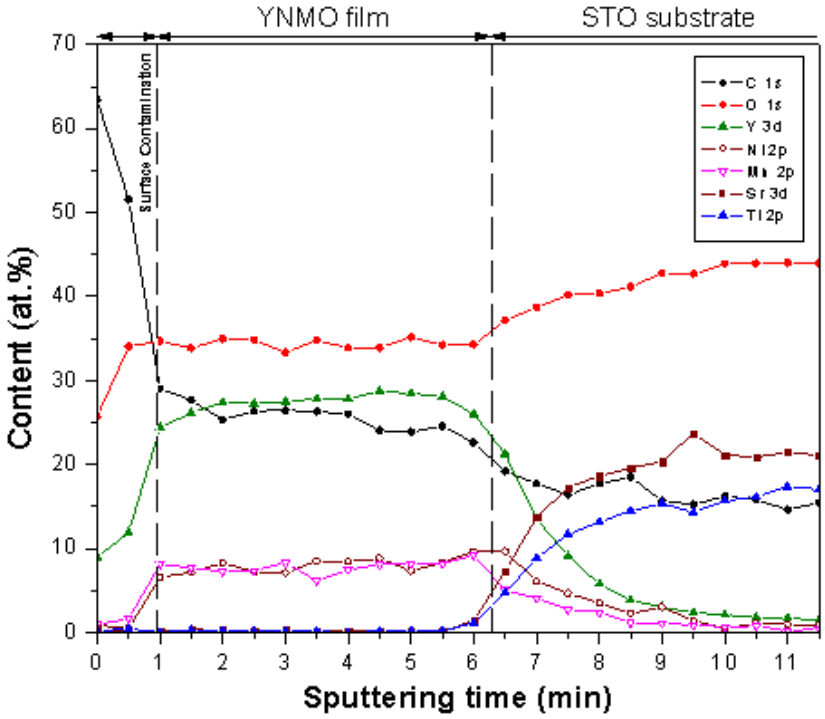

Figure 3.26 *YNMO(001)/STO(001) composition profiling showing three clear regions, Surface contamination, YNMO film and STO substrate.*

3.2.11.1 X-ray photoelectron spectroscopy

3.2.11.1.1 Samples on STO(001)

XPS measurements were performed and are presented according with the "depth profiling" method, described in Section 2. **Figure 3.26** shows the results of such experiments on a sample deposited on STO(001).

Elemental quantification was performed using the area under the peak curves and plotted as a function of the sputtering time. It can be observed the presence of three

distinctive regions on the image. The first region, left side on the plot in **Figure 3.26**, corresponds to surface contamination and is rapidly cleaned by the Ar^+ sputtering, also evidenced by the quickly detriment of the C intensity. The second region shows rich contents of Y, Ni and Mn and is placed in the middle of the aforementioned plot. Finally, the third area shows a quick increment in the Sr and Ti contents followed by a progressive reduction on the Y, Ni and Mn content, this area is attributed to the interface and substrate composition.

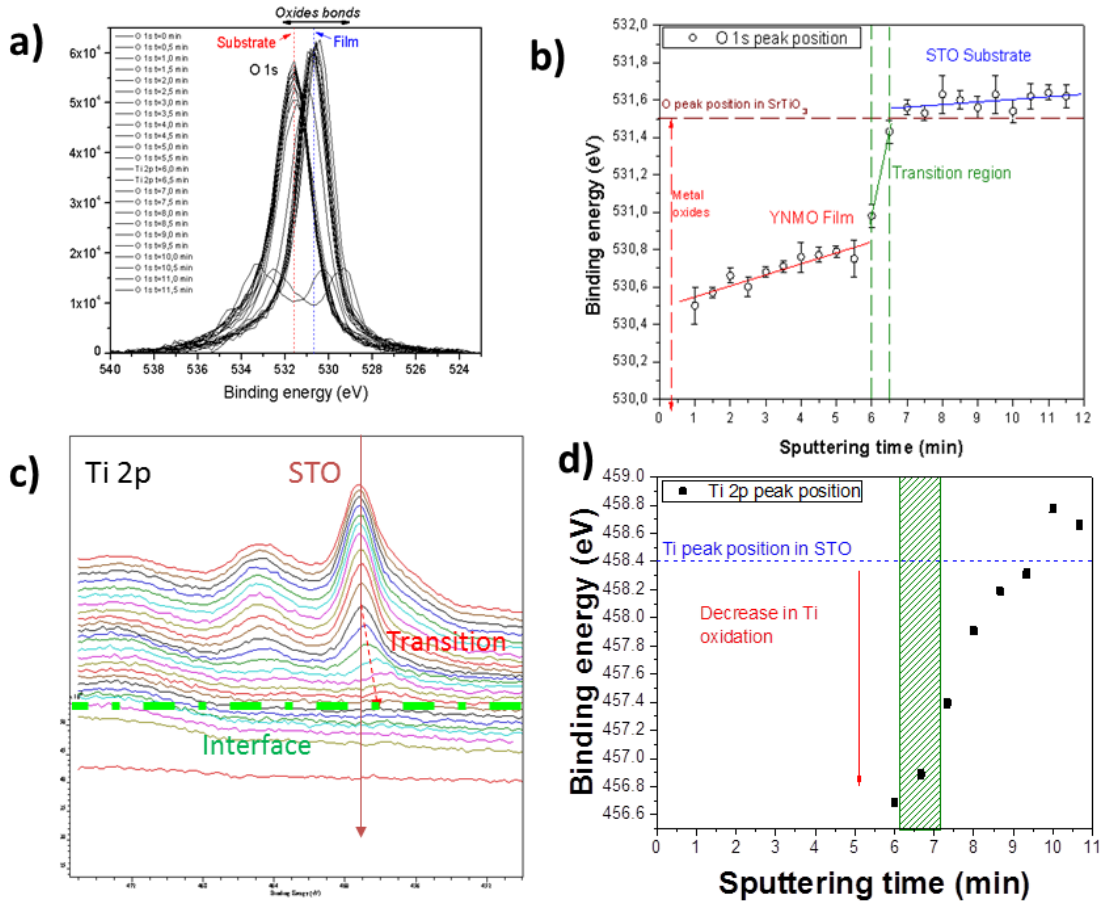

Figure 3.27 *YNMO(001)/STO(001) XPS analysis a) shows the change on binding energy of the O1s peak. b) shows the peak shifting vs sputtering time. c) shows the Ti2p peaks, where a clear shifting, towards the interface is observed d) shows the* $Ti2p_{3/2}$ *peak shifting vs sputtering time..*

Nominal values for Y, Ni, Mn are 27, 9, 10, 34 at% showing an oxygen deficiency on the YNMO(001)/STO(001) films, also observed on the increment of the oxygen peak at the substrate interface in **Figure 3.27**. Nominal ratio of Ni, Mn is congruent with the

$YNi_xMn_{1-x}O_3$ and its supported by the results of the substrate area; where Sr, Ti & O show 25, 22 and 46 % values that closely follow the $SrTiO_3$ formula.

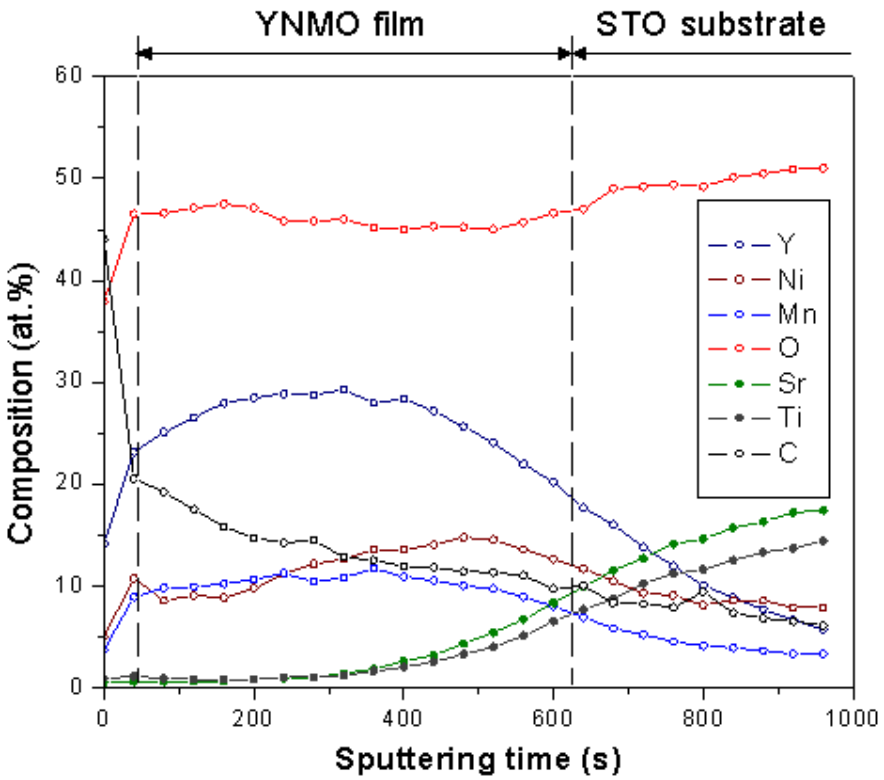

Figure 3.28 *YNMO(101)/STO(111) composition profiling showing three clear regions, Surface contamination, YNMO film and STO substrate.*

Oxygen quantity increases in the substrate region, while quantification clearly shows a lack of oxygen in the films. Close inspection upon the oxygen peak is shown in **Figure 3.27a.** It is important to investigate the effect of oxygen vacancies on the film and their influence on the stoichiometry of the film. **Figure 3.27 a)**, shows a superposition of oxygen peaks at different depths (sputtering times). In this plot, two clearly defined groups of peaks are observed, this is concordant with the different bounding scenarios of the single perovskite formula (STO) vs the double perovskite (YNMO). **Figure 3.27 b)** shows the abrupt change on binding energy of both regions, and moreover, shows the progressive increment on oxygen binding energy of the film, towards the interface and the sudden jump on the interface towards the substrate. Upon further inspection, Ti $2p_{3/2}$ peak shows an interesting behavior near the substrate/film interface. **Figure 3. 27 c)** collects all the spectra from Ti 2p peak, in this plot, the slight

shifting of the peak towards higher energies is observed, **Figure 3.27 d)**, clearly shows the increment on binding energy of the Ti $2p_{3/2}$ peak in the vicinity of the YNMO/STO interface.

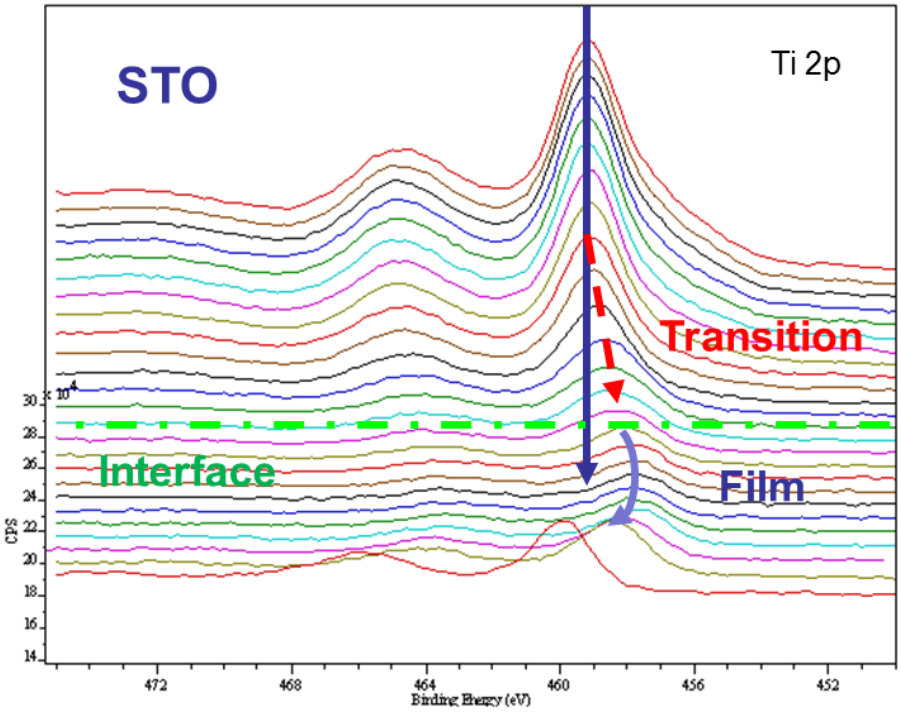

Figure 3.29 *YNMO(101)/STO(111) XPS analysis of Ti 2p peak vs sputtering time, three regions are clearly observer, substrate area (STO –upper part), a interface area (Transition) and finally the film area in which Ti 2p peaks are still visible and move to higher energies. Data normalized to Oxygen content.*

According with the data presented, it can be stated that oxygen vacancies on the film seem to promote higher binding energies on substrate`s titanium. These higher energies could allow ionic diffusion from the substrate to the film, although such effect is not observed in the sample.

3.2.11.2 Samples on STO(111)

Similar studies were performed on STO(111) substrates, these experiments are shown in **Figure 3.28**. Again, three areas are clearly appreciated, first the surface contamination, then the YNMO film and finally the STO substrate.

In this case, there is a clear elongation of the interfacial area, the line in **Figure 3.28** is an estimation of the transition region between YNMO and STO, Notice that the

Y %at concentration starts to decrease much earlier and slower than in STO(001), more interestingly, notice that Ti concentration appears much early in the film, even when O concentration has not started rising, a previous feature of the interface region. A closer study on the Ti 2p peak is presented in **Figure 3.29**, where an extra effect, after the transitional area, can be observed, the peak from Ti 2p is still visible and move towards higher energies.

It seems clear now, that in the case of samples grown on STO(111) there is a diffusion of Ti ions from the substrate to the film. As previously explained in this work, samples were grown in similar condition so substrates are the main comparison factor, are deposited in a single run experiment in order to guarantee their similarity. In this case, STO(111) shows a clear diffusion of Ti, while STO(001) and STO(011) show no Ti diffusion. It can be argue that different energetic surfaces, provide different Ti stability, which combined to the observed epitaxial relationship on each substrate, lead to a different Ti migration velocity. It seems clear at this point that oxygen vacancies account for the higher instability of the Ti ions in the substrate; this fact, added to the observed growth anisotropy and the orientation dependent Ti migration has been observed in the literature [**11**], however, in this study migrations of Ti are observed on (001) substrates and prevented on (111). These observations are congruent with an ionic migration promoted by the STO surface energy of the crystalline surfaces and the oxygen vacancies of the film. The total Ti migration is calculated as below 10% in reaching the 25% of the film´s total thickness, above this point is below 3% except for some sudden increment at the surface, related to the lower oxygen content and it respective influence on the normalization.

3.2.12 Electron energy loss spectroscopy (EELS)

In order to corroborate the XPS observations EELS cross-sectional analysis were performed on YNMO(001)/STO(001) and YNMO(101)/STO(111) samples. Plots are shown in Figure 3.29, as in the case of XPS measurements, plots show different regions, corresponding to the free surface, YNMO layer and finally STO substrate. In these plots, Yttrium has been removed, due to a Sr and Y peaks overlapping, intensities are shown normalized to the oxygen content. **Figure 3.30 a)** shows results of STO(001) samples, Nickel and Manganese relative content are congruent with previous XPS measurements and are close to the 1 to 1 concentration in the YNMO formula,

moreover Ti concentrations rapidly decreases at the interface area and there are not visible traces of Ti content on the film. **Figure 3.30 b)** shows the results of EELS experiments on STO(111) films, again, Ni and Mn concentrations are congruent with the YNMO formula and Ti content rapidly reduces at the interface. Moreover, as in XPS measurements, a visible trace of Ti is uniformly observed along the YNMO(101) film, thus confirming the XPS results, and ruling out any possible discontinuity on the YNMO(101) film as the possible origin of the Ti migration observed in the XPS experiments.

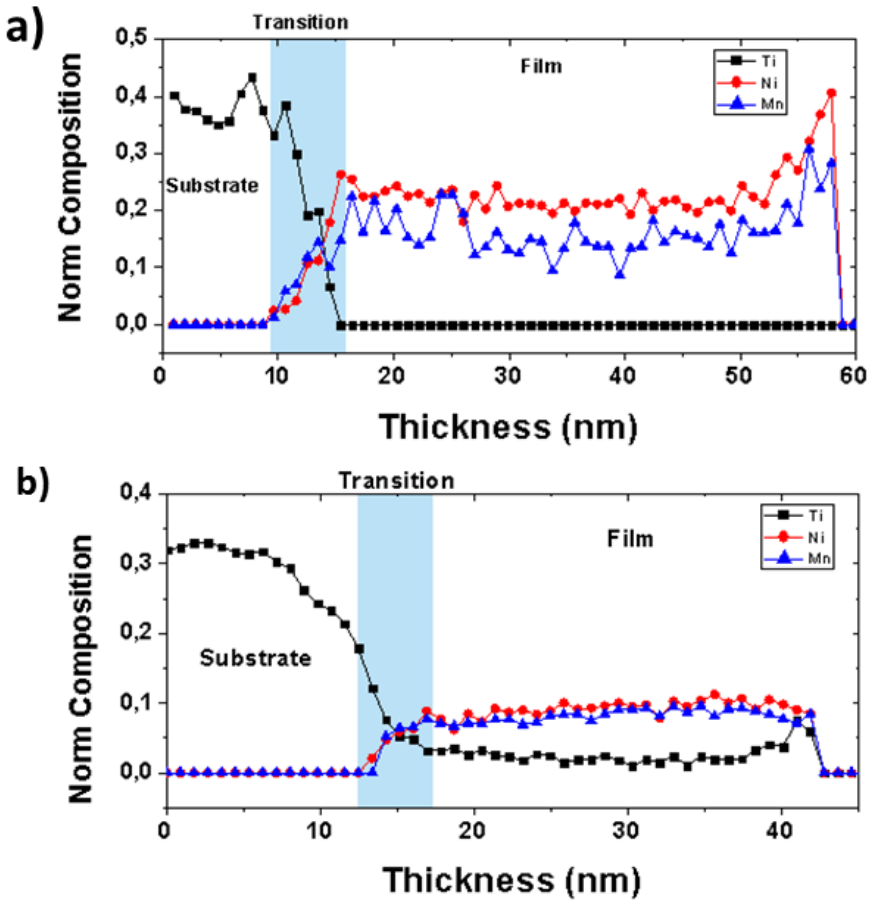

Figure 3.30 *EELS normalized content of a) YNMO(001)/STO(001) and b) YNMO(101)/STO(111). Blue regions are attributed to the interface of YNMO/STO*

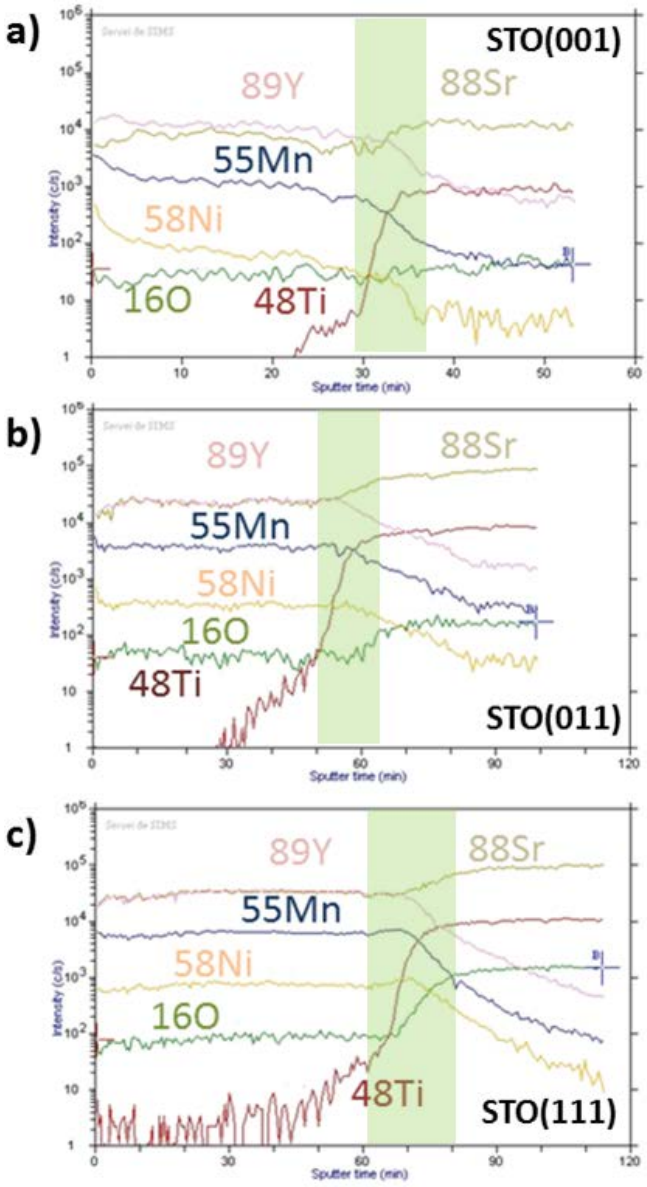

Figure 3.31 *SIMS depth profiling from a)YNMO(001)/STO(001), b) YNMO(100)/STO(011) and c) YNMO(101)/STO(111). Light green regions are attributed to the interface of YNMO/STO.*

3.2.13 Secondary ion mass spectrometry (SIMS)

It can be argued that Ti diffusion could in fact be present on STO(001) substrates, although in concentrations below the XPS technique sensitivity. SIMS technique has an outstanding sensitivity to atomic species, in the range of ppm, however it lacks of the capability of quantifying such atomic concentrations. Therefore, SIMS measurements were performed on STO(001), STO(011) and STO(111).

SIMS spectral analyses are shown in **Figure 3.31**, in order to improve detection and sensitivity the sputtering system was set to a very low power, leading to long measuring experiments. In the plots the interfacial region is marked in green. As in the case of XPS, diffusion from the film to the substrate cannot be investigated due to the sputtering plasma that pushes elements from the film into the substrate.

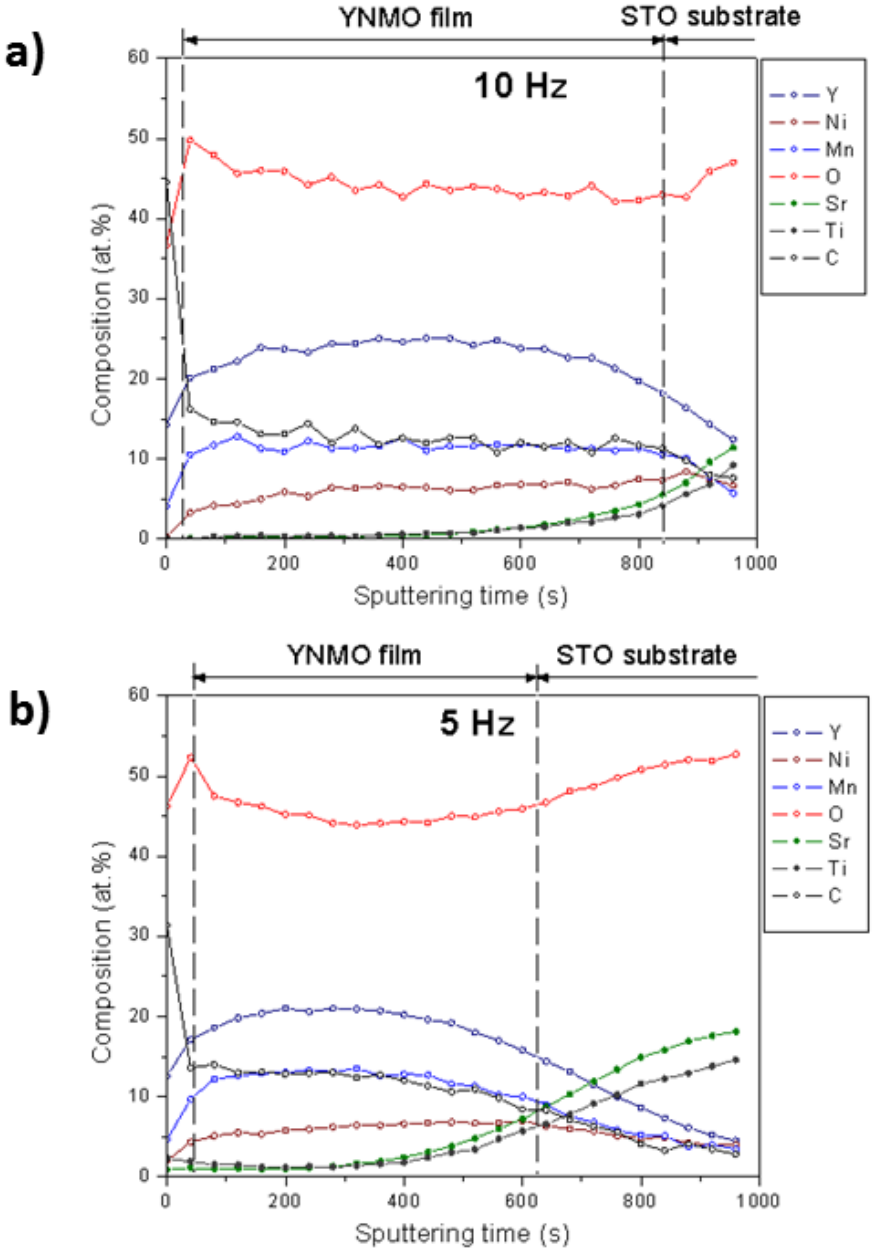

Figure 3.32 *XPS profiling of YNMO(101)/STO(111) samples, deposited at a) 10 Hz and b) 5 Hz.*

Experiments clearly show a small diffusion of substrate Ti to the YNMO film on the samples grown on STO(001) and STO(011). **Figure 3.31 a) & b),** In the case of

STO(001), the diffusion rapidly decreases at a "distance" of 15% from the interface. While in STO(011) the diffusion reaches the ≈40% of the film thickness. These diffusions are so small that they could not be observed in XPS experiments and in that sense they are neglectable in front of other environmental elements such as carbon.

Finally, **Figure 3.31 c)** shows the depth profiling experiments on STO(111) film, which corroborates the XPS measurements by showing a long diffusion of Ti along the YNMO films.

3.2.14 Titanium Diffusion

Interfacial migration of titanium on STO(111) samples, can be investigated under the assumption that Ti migration is temperature dependent. Since the crystallinity of the film was optimized in the previous section of this chapter, a sensible approach is to play with the repetition rate parameter, since this parameter directly influences the growth rate of the films and reduced the time at which the substrate is exposed to the deposition temperature. In **Figure 3.4**, the dependency of film crystallinity was studied as a function of the repetition rate. It was shown that frequencies of 2,5 and 10 Hz have little effect on the crystalline quality of the films therefore it is decided to analysis profiles of samples deposited at those frequencies by XPS depth profiling.

Profiling of the samples shown in **Figure 3.32**, presents remarkable similarity to the one in **Figure 3.27**, with three clear areas that correspond to the film, interface and substrate, the presence of Ti, as expected, diminishes with the increment of deposition frequency, making it clear that this is one of the technological parameters to have in mind in the discussion of the functional measurements on YNMO(101)/STO(111) samples.

Although the origin of the Ti diffusion on STO(111) can be reduced by increasing the deposition rate, as shown in the comparison between **Figure 3.32a & Figure 3.32b** the fact that crystalline orientation of the substrate plays an important role on this diffusion, evidenced by the lack of diffusion STO(001) and STO(011), requires further research and data. A further analysis of this phenomenon is described later in this text and cross related to some functional measurements.

3.3 Functional Characterization

In order to understand the effect of the stabilized crystalline orientation in the functional properties of the films, magnetic and dielectric measurements were performed.

3.3.1 Magnetic measurements

Samples were measured by means of SQUID magnetometer with a magnetic field applied perpendicular to the sample, first the magnetization vs temperature M(T) will presented and then magnetization vs field M(H).

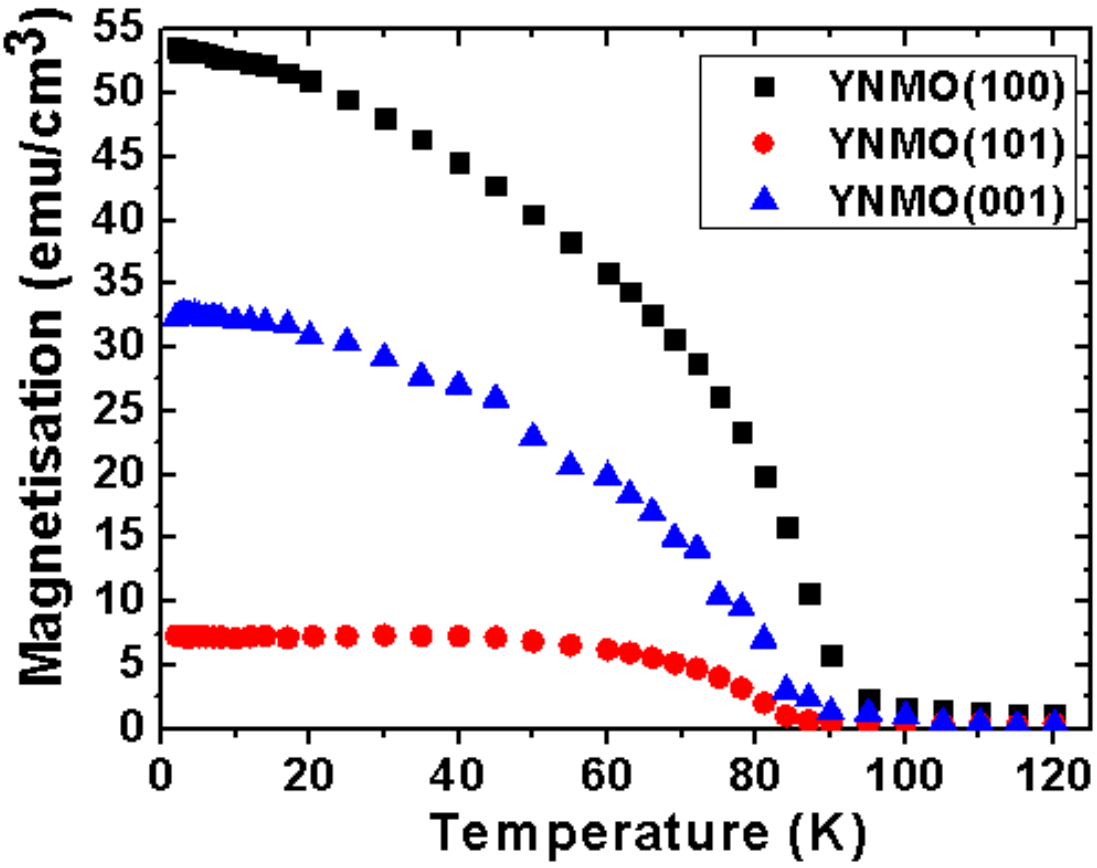

Figure 3.33 *Magnetization vs temperature curves M(T) for ■ YNMO(100), ●YNMO(101) and ▲YNMO(001), transition temperature is 97K for all samples.*

In bulk, YNMO shows a ferromagnetic to paramagnetic phase transition at a temperature, Tc, around 79 K [**12**,**13**]. In thin films, this ferromagnetic transition has also been reported [**2**,**5**,**14**] and in this work we study this behavior for the obtained

films. **Figure 3.33** shows the field-cooled measurements (F_C) of YNMO(001), YNMO(100) and YNMO(101) performed under a 1000 Oe applied field. A clear ferromagnetic transition is observed at around 97 K in all the samples, demonstrating their ferromagnetic nature. Differences on magnetization are attributed to magnetic anisotropy of the films. In principle, in the Re_2NiMnO_6 formula, ferromagnetism arouses from the so called B-site ordering, this full fill the superexchange mechanism between Ni and Mn atoms thus allowing the ferromagnetic response of the sample. In order to evaluate such a ordering the YNMO films are evaluated from the results of M(H) measurements. In principle a fully ordered YNMO unit cell, should present a total magnetization of 5 μB/f.u.. However, in all the literature reviewed for this material in bulk, this is not the case; best values are closer to 4.8 μB/f.u [**13**], slightly lower than the nominal value.

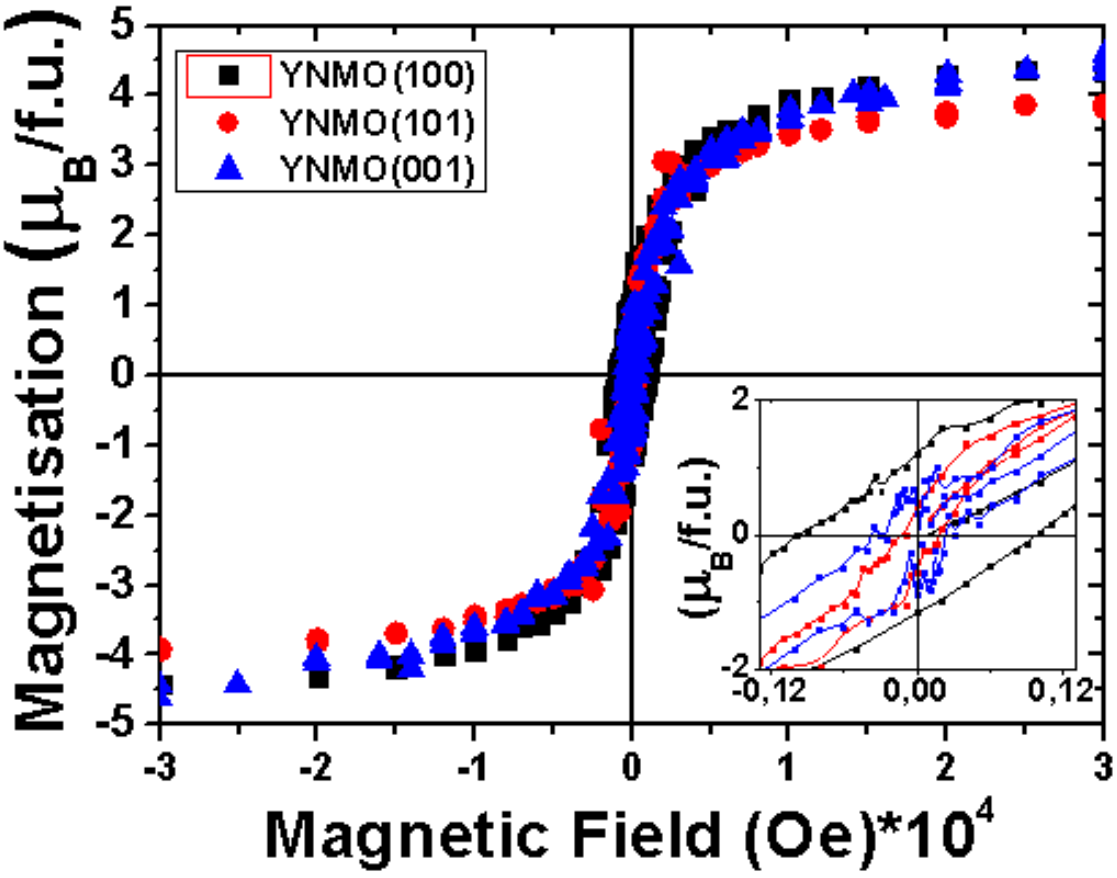

Figure 3.34 *Hysteresis loops (M(H)) measured at 5K for ■ YNMO(100), ●YNMO(101) and ▲YNMO(001) films.*

In **Figure 3.34** hysteresis loops performed at 5K with a maximum applied field of 30000 Oesterd, are shown. Magnetic impurities and diamagnetic contribution arousing

from STO substrate were carefully subtracted using the method described in **Appendix 3**. Samples total magnetization is presented as μB/f.u (Ni-Mn pair per formula unit) using the specific lattice constants extracted from reciprocal and 2Θ-ω analysis.

Total magnetic moment are shown in **Figure 3.34** to be YNMO(001)= 4.35μB/f.u, YNMO(100) = 4,4 μB/f.u and YNMO(101) = 3,7μB/f.u, coercive field YNMO(001)=631 Oe , YNMO(100) = 1900 Oe and YNMO(101)= 285 Oe. A clear magnetic difference between the behaviors of YNMO films is observed. Although it could be argued that the origin of such arouses due to anisotropic effect, it could be in fact be more related to unit cell deformation induced by the epitaxial strain and coexistence of multiple in-plane domains than to the existence of intrinsic effects

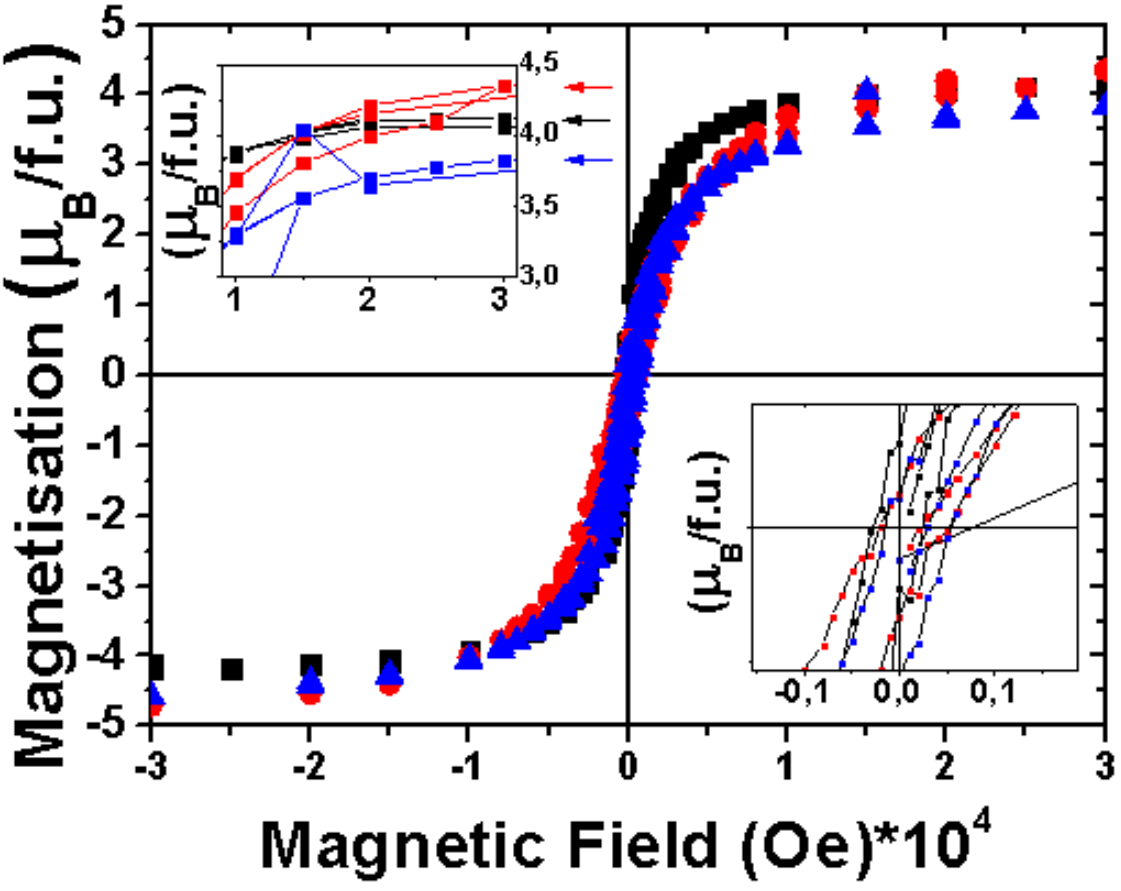

Figure 3.35 *Hysteresis loops (M(H)) measured at 5K for YNMO(001) with a magnetic field applied ■ parallel, ● perpendicular and ▲ rotated 45 degrees from parallel. Upper inset shows total magnetization at saturated field, while bottom right inset shows the existence of coercive field in all measurements.*

To investigate such behavior a sample of YNMO(001) was measured on three different configuration of applied magnetic field. First the magnetic field was applied

perpendicularly to the interface, along the YNMO(001) direction, secondly the magnetic field was applied parallel to the interface of the film, along the YNMO(010), and due to the nature of the YNMO sample, which has two in-plane domains, also along YNMO(100). Finally, the magnetic field was applied along the YNMO(011), approximately 45^{O} in-plane shifted. Results of this analysis are shown in **Figure 3.35**.

Anisotropy measurements performed on YNMO(001), **Figure 3.35**, show well defined M(H) hysteretic loops with clear no zero coercive field. Cycles are saturated at approximately 30.000 Oe in all the scenarios. Perpendicularly applied magnetic field, as in the previous measurements reaches a total magnetization of YNMO⊥(001)= 4.35μB/f.u, while parallel applied field shows a total magnetization of YNMO||(001) = 4.01μB/f.u and finally magnetic field applied with an in plane angle of 45^{O} shows the lower magnetization of the set with YNMO∕(001)=3,79μB/f.u. A clear magnetic anisotropy is therefore observed in the YNMO(001) sample, with remarkably similarity to the results obtained in epitaxial samples of YNMO(101)/STO(111). Interestingly enough in plane measurements, that in principle should give similar results to the perpendicular M(H) curve on YNMO(100)STO(011) show a reduction of 0.4 μB/f.u, this reduction can be attributed to the in-plane structure of the YNMO(001) sample, that exhibits two domains shifted 90^{O} from each other, therefore reducing the total magnetization of the sample.

3.3.1.1 Effect of Ti migration on YNMO(101)/STO(111)

In this section the effect of titanium migration on the magnetic properties of the YNMO(101)/STO(111) films will be studied, as described in the previous section, Ti migration is associated to the growth rate of the film and the implied longer period of heating exposure of the film. In this section, samples deposited at 2, 5, 10 Hz will be presented and compared with the M(T) measurements.

Samples were measured using a perpendicular magnetic field of 1000 Oe, resulting plots are shown in **Figure 3.36**. Samples show a clear transition from paramagnetic to ferromagnetic ordering at 97K. Curves show a clear decrement of total magnetization as ablation frequency decreases, reaching a maximum of 6 emu/cm^3 for 10 Hz and 4.5 emu/cm^3 for 5 Hz. Sample grown using 2 Hz, shows a strange curvature around 30 K where the magnetization decreases continuously till 10K and then rises till the lowest achievable temperature.

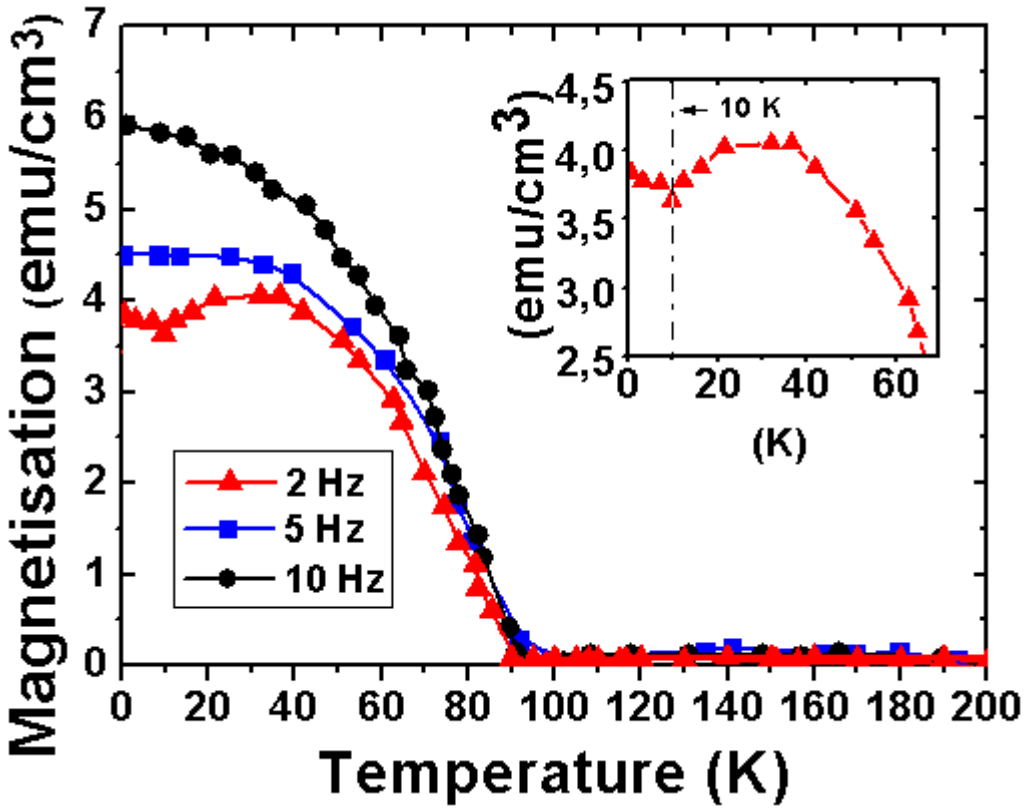

Figure 3.36 *Magnetization vs temperature curves M(T) for ▲ 2Hz, ■ 5 Hz & ● 10 Hz, transition temperature is 97K for all samples. In-set shows a magnification of the anomalous behavior of the 2 Hz sample below 30K*

Sample deposited at 2Hz has the longest amount of titanium diffused into the YNMO film, it is conceivable to assume that such diffusion is responsible for the magnetic decrement of the YNMO(101) film. Using the XPS data, the speed of diffusion can be extracted and plotted. **Figure 3.37** shows the diffusion percentage of Ti in the film based on the nominal thickness of the film, where X_{diff} is the distance reached by the Ti ion inside the film and X_{film} is the total thickness of the film.

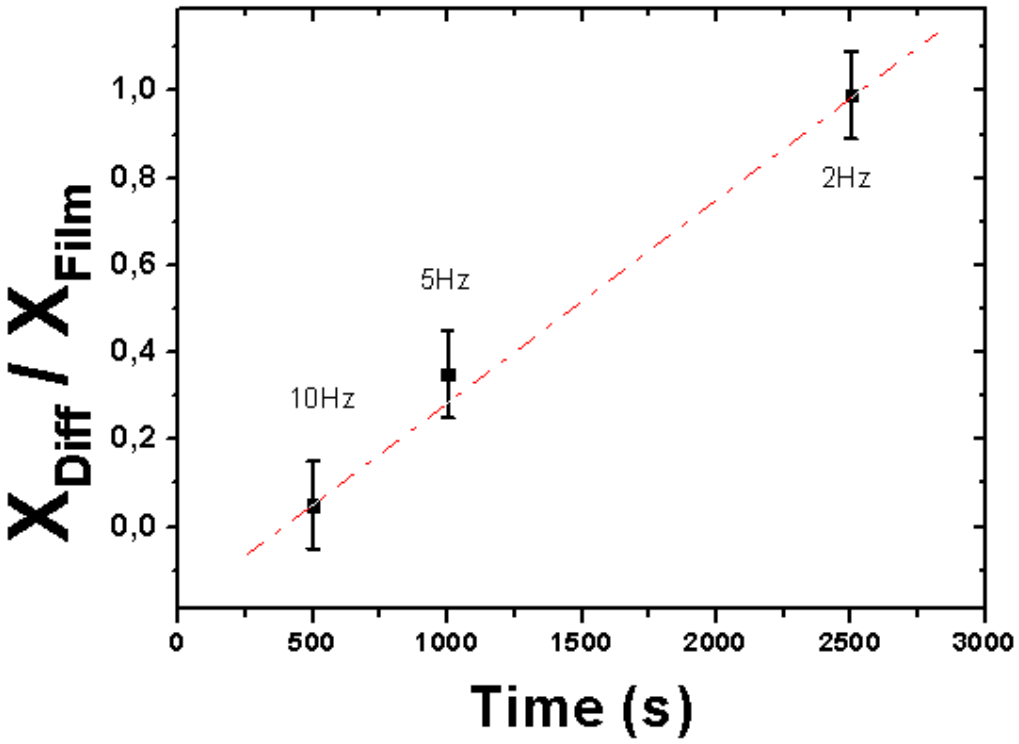

Figure 3.37 *Diffusion percentage vs associated annealing time in seconds of YNMO(101) films grown at different ablation frequency.*

The coefficient of diffusion (D) is estimated according to the characteristic diffusion length, $L=\sqrt{4 * d(t)}$ [**15**][**16**]. The value extracted is 1,56 10^{-15} cm^2/s for 2Hz and 9.97 10^{-16} cm^2/s for 5Hz, the mean value is 1.2±0.9 10^{-15} cm^2/s , This corresponds to a roughly calculation, taking into account the migration percentage, and the area of the Ti 2p peaks for the $750C^{O}$ deposition temperature scenario. Remarkably enough, the amount of material diffused remains close to the 10% of the manganese value, suggesting also a possible chemical mechanism.

Having observed that the value of the titanium diffusion on the films reaches a maximum of 10%, the possible doping of the YNMO(101) unit cell can be assumed. A similar family to the $Re(Ni_{0.5}Mn_{0.5})O_3$ is the $Re(Ti_{0.5}Mn_{0.5})O_3$ (RTMO), in this family of materials some of the studied compounds are Gd_2TiMnO_6[**17**], Sm_2TiMnO_6 [**18**] & Nd_2TiMnO_6 [**19**], these compounds have an orthorhombic unit cell comparable to their cousins on the Re_2NiMnO_6 [**13**] making it feasible their inclusion within the YNMO cell. In the case of RTMO, all compounds found in the literature have a Néel

temperature of ≈20K with a fully antiferromagnetic behavior. Now, some literature examples are presented.

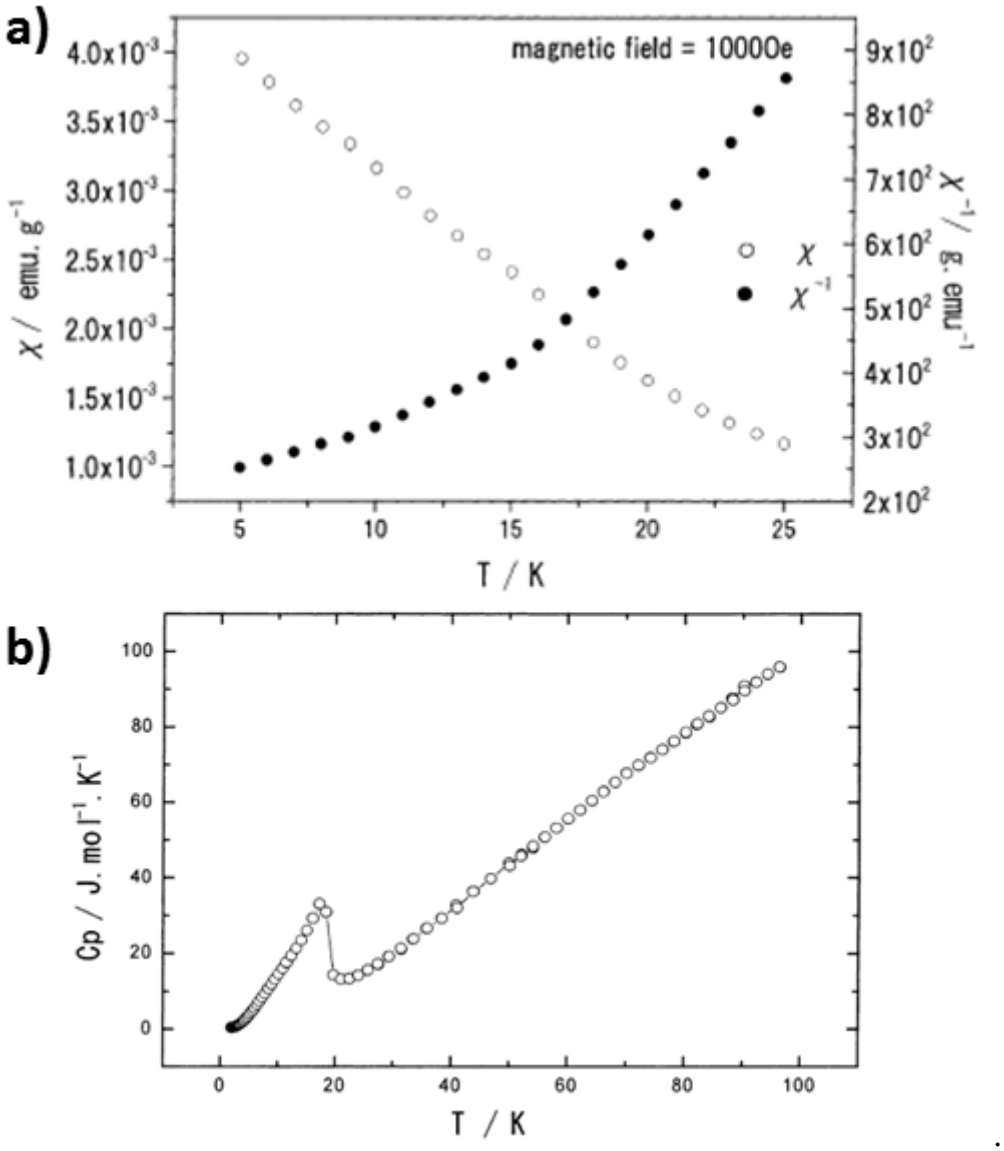

Figure 3.38 *Measurements performed on Gd_2TiMnO_6 a) Magnetic susceptibility measurements and b) differential scanning calorimetry*[**17**]

In **Figure 3.38** results from selected publications regarding Gd_2TiMnO_6 are shown. First the magnetic susceptibility is presented as a function of temperature. In this plot it can be observed a clear slope change below 20K, although attributed to a small discrepancy on the magnetic moments of Mn and Gd atoms in the cell. The $ReTiMnO_6$ formula is known for their antiferromagnetic transition below 20K, aiming to prove this transition differential scanning calorimetry (DSC) experiments were performed. **Figure**

3.38 b) shows the results of such experiments where a clear transition is observed and is attributed to a small portion of antiferromagnetic ordering in the material.

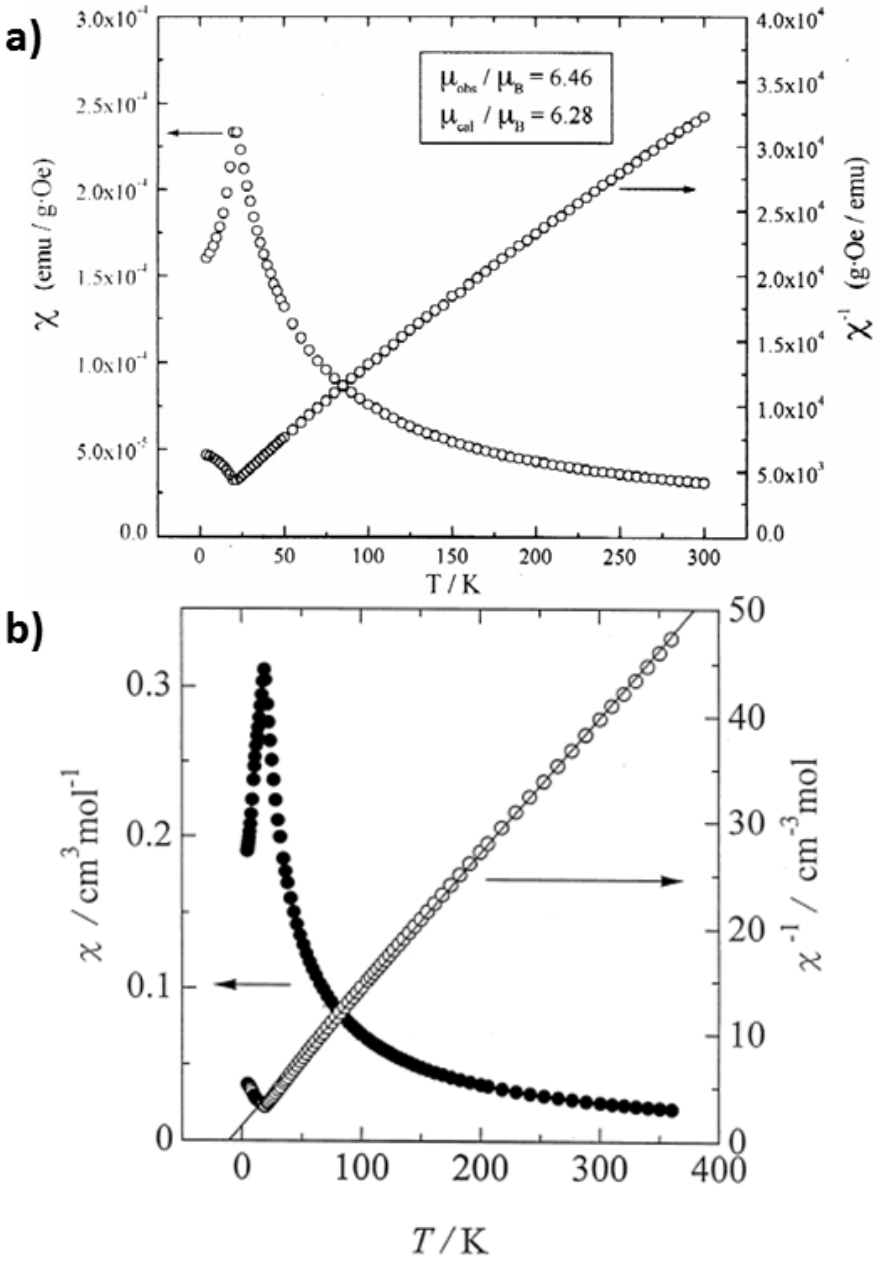

Figure 3.39 *Magnetic susceptibility vs temperature measurements of a)* Sm_2TiMnO_6 [**18**] and *b)* Nd_2TiMnO_6 [**19**]

Further literature review shows other two similar cases shown in Figure 3.39. In both cases, for Sm_2TiMnO_6 and Nd_2TiMnO_6 samples show an antiferromagnetic phase transition below 20K, confirming the tendency of the $ReTiMnO_6$ unit cell of showing such a behavior.

Further studies are needed in order to confirm such transition and the full integration of the Ti ion in the YNMO unit cell, although the preliminary results suggest that the scenario proposed is more than feasible in light of the magnetization and compositional results.

3.3.2 Dielectric measurements

Finally in this chapter dielectric measurements will be performed on the previously characterized samples, with the exception of YNMO(101)/STO(111) with different Ti migration.

First, impedance spectroscopy measurements will be performed for YNMO(001)/STO(001) and YNMO(101)/STO(111) crystalline orientation, and then ferroelectric measurements will presented in order to show the multiferroic nature of the samples. Samples of YNMO(100)/STO(011) are shortly discussed at the end of this section

3.3.2.1 Temperature dependent Dielectric Impedance of YNMO(001)/STO(001)

This technique is used based on previous results of our group on similar perovskites like $BiFeO_3$, $BiMnO_3$[**20**] and Bi_2NiMnO_6 [**21**]. As described in the experimental section, samples were deposited on Nb-5%-STO(001), immediately after platinum top electrodes where deposited on using the sputtering technique and shadow masking method.

Measurements were performed at the Institute of Materials Science of Barcelona (ICMAB-CSIC) with the collaboration of Dr. Ignasi Fina. Samples were measured in the range of 300K to 5K with a constant step of 5K. The typical measurement comprehends the permutation of several electrodes at room temperature in order of maximizing signal from the film. Samples are placed in a PPMS system and measurements are performed while temperature is decreased.

Results are summarized in **Figure 3.40.** As mentioned in the experimental section, the Nyquist plot is very useful in the case of multiple mechanisms coexisting in the dielectric measurement. **Figure 3.40 a)** shows the clear double contributions scenario, evidenced by the apparition of two semicircles in the Nyquist plot. As described in the literature [**20**,**22**,**23**], dielectric mechanism can be de convoluted by increasing the

sweeping frequency, however this range strongly depends on the specific set-up and physical limitations such as self-impedance. Another method is to reduce temperature in order to de couple intrinsic and extrinsic effects. This approach is very useful when transitions or dielectric effects can be studied at low temperature.

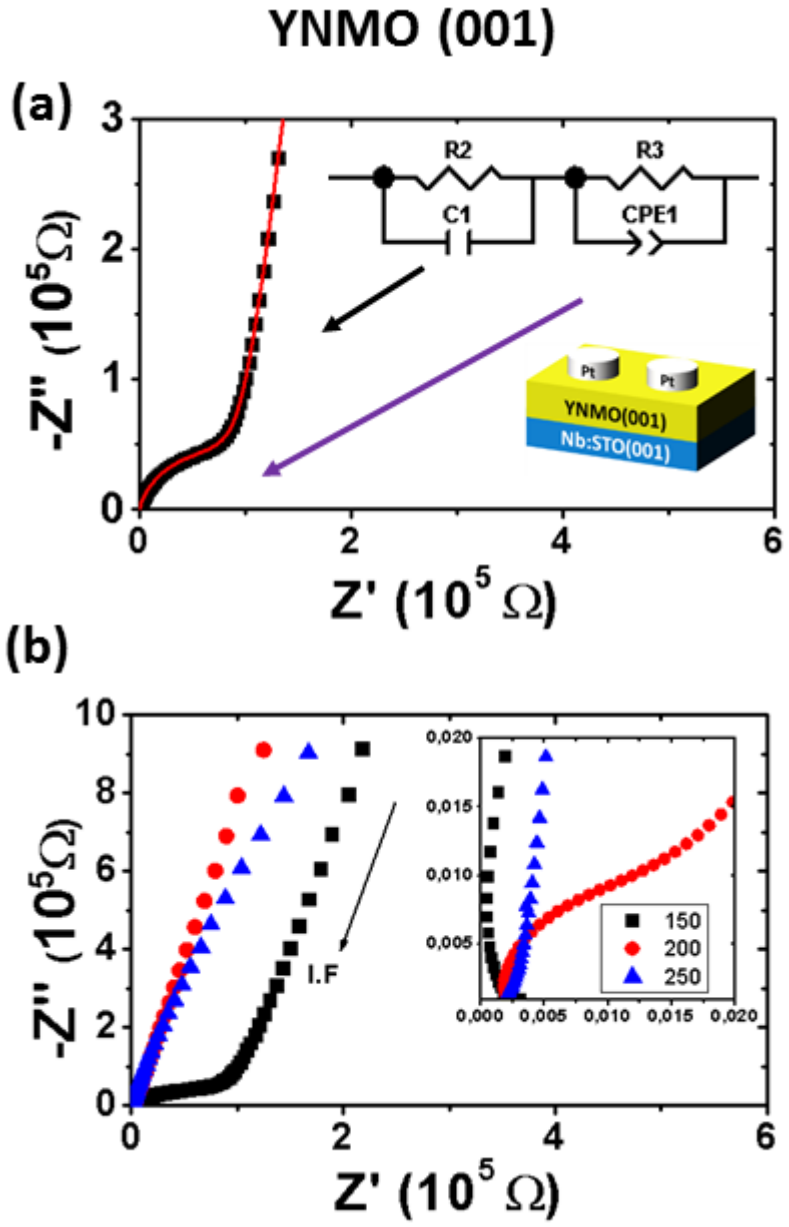

Figure 3.40 *Impedance spectroscopy measurements. a) Shows the appearance of two independent mechanisms in the sample. High frequencies mechanisms are attributed to intrinsic properties of the film. Red line is the fitting for a given measurement. b) Selected temperatures showing the range of temperatures in which the double mechanism is observed and thus the analysis can be performed.*

Figure 3.40 b) shows selected measurements where the progressive dominance of the high frequencies semicircle is evident with the decrement of temperatures. The

appearance of the small semicircle, corresponding to intrinsic mechanisms of the film is firstly observed at 250K, blue dots **Figure 3.40 b),** this feature increases in at 200K, red dots and is fully evident at 150K and below, black dots. Using this method reliable representation of the intrinsic properties of the film can be observed below 150K, range in which the fitting can be trusted. **Figure 3.41** shows the aforementioned increment on dominance of the high frequencies mechanism in the range of 130 to 105K, notice how the semicircle grows rapidly to the point of finally take over the whole spectra.

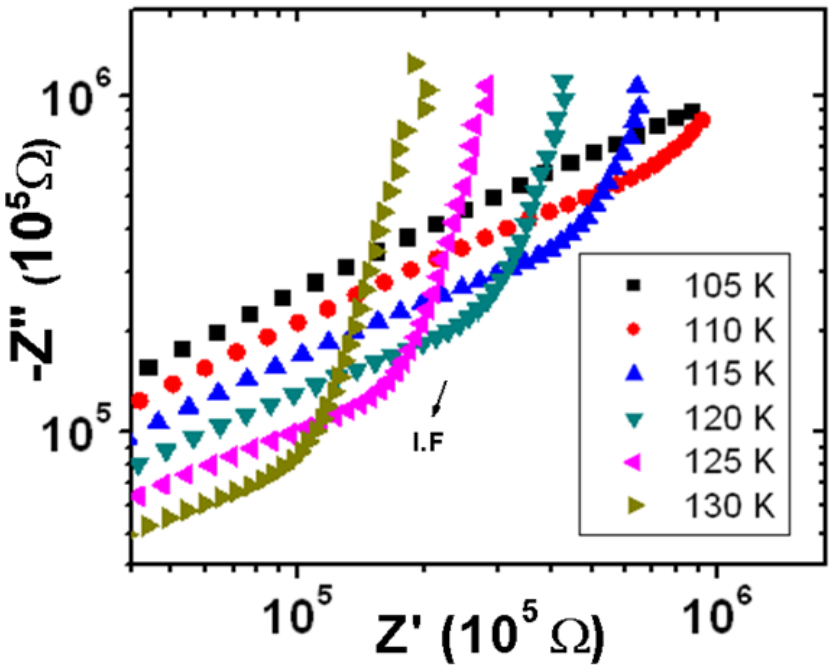

Figure 3.41 *Impedance spectroscopy measurements.in the range of 105 to 130K showing the progressive dominance of the intrinsic contribution of the spectra with the lowering of temperature.*

As described previously in the experimental section of this thesis, each of the semicircles corresponds to a resistor in parallel to a capacitor, R-C. However, as also described in this case the non-ideality of the thin film is better represented by the inclusion of a constant phase element, CPE. In **Equation 3.9** where Q denotes the amplitude and α deals with the phase of the CPE, the typical values range from α ≤0,6-1, being α = 1 for an ideal capacitor, and in this case C=Q. Capacitance, *C*, and dielectric permittivity, ε, values can be obtained according to the relationship $C=(Q\cdot R)^{(1/\alpha)}/R$[**24**] , and C=εA/t, where A accounts for the area of the electrode and t for the thickness of the sample

$$Z^*_{R\text{-}CPE}=R/(1+RQ(iw)^{\alpha}) \qquad \text{Equation 3.9}$$

$$Z^* = R_I/(1+R_I.Q_I.(iw)^{\alpha}_I + R_E/(1+iw.R_E.C_E) \qquad \text{Equation 3.10}$$

Thus, the mentioned two contributions of the equivalent circuit have been fitted at each temperature, using expression in **Equation 3.10**. Where the first term correspond to the intrinsic ($_I$) contribution of YNMO and the second term deals with the extrinsic contributions ($_E$). The two RC contribution of the equivalent circuit are sketched in the insets of **Figure 3.40 a** where the line through data points corresponds to the performed fitting figuring out the goodness of the fit.

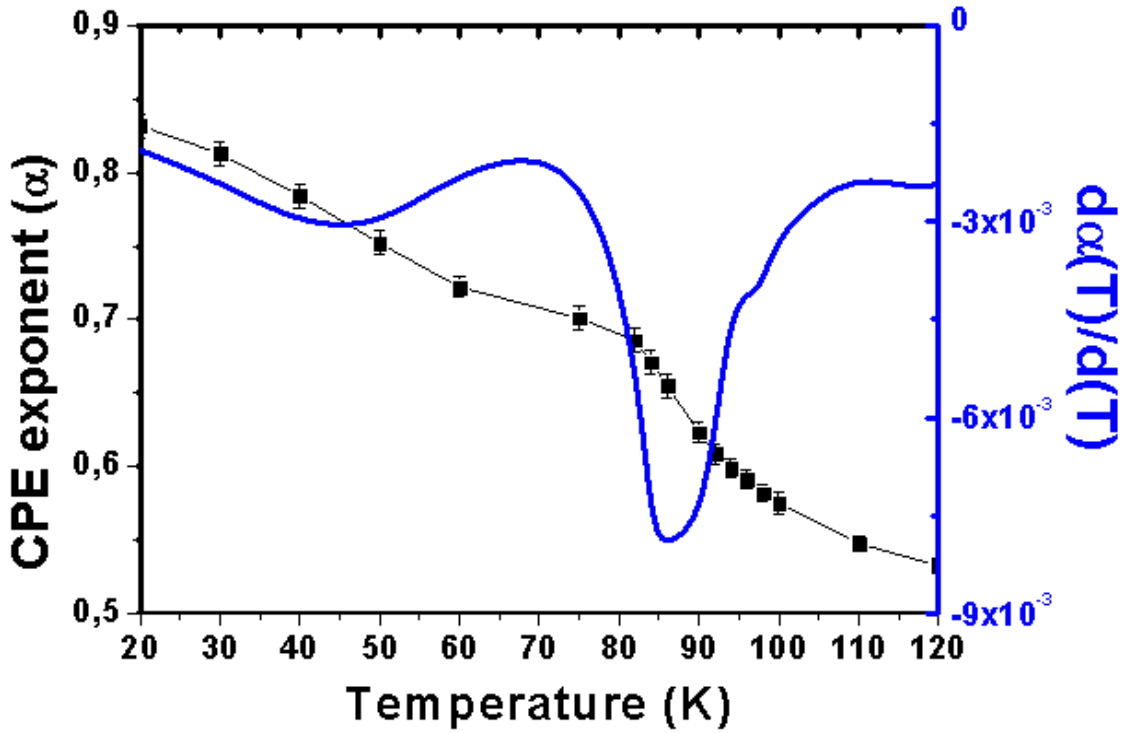

Figure 3.42 *Temperature dependence of the CPE exponent in the intrinsic mechanism*

Fitted data corresponding to the intrinsic contribution of the film are shown in **Table 4**. The reliability of the results in the sample are corroborated by the low goodness-of-fit indicator $\chi 2$ which, in all temperature ranges, is $\sim 10^{-3}$, without any remarkable dispersion. A useful indicator of the behaviour of the film comes from plotting the exponent of the R-CPE element, which in fact tells about the non-ideality of the dielectric behaviour. This plot is presented in **Figure 3.42** where a clear increment in the ideality of the dielectric behaviour can be observed below 100K, interestingly

enough, a peak is clearly visible, upon allowing to visualize the derivative of α as a function of temperature, **Figure 3.42** right axis. This peak is found in the surroundings of the T_{FM} =97K suggesting a small correlation or magneto dielectric effect.

Fitting **R**esults YNMO(001)

T (K)	χ2	Q [$Fs^{\alpha-1}$]	Error Q	α	Error α	R(Ω)	Error R(Ω)[%]
20	0,00076	4,80E-10	2,95E-11	0,832	0,0040	8,8E+08	3,32
30	0,00077	5,10E-10	3,37E-11	0,813	0,0041	6,6E+08	3,91
40	0,00069	6,00E-10	3,14E-11	0,784	0,0042	4,0E+08	3,45
50	0,00049	8,00E-10	3,65E-11	0,752	0,0041	1,7E+08	3,51
60	0,00044	1,65E-09	4,15E-10	0,722	0,0033	1,6E+07	3,21
75	0,00039	2,05E-09	4,55E-10	0,701	0,0040	1,1E+07	3,65
82	0,00034	2,60E-09	4,75E-10	0,686	0,0041	7,6E+06	3,38
84	0,00026	3,15E-09	5,99E-10	0,671	0,0042	5,3E+06	3,77
86	0,00074	3,90E-09	7,44E-10	0,655	0,0041	3,9E+06	3,91
90	0,00031	5,50E-09	1,05E-09	0,623	0,0035	2,8E+06	4,55
92	0,00017	9,20E-09	1,34E-09	0,609	0,0035	1,1E+06	4,70
94	0,00013	1,18E-08	1,51E-09	0,599	0,0033	7,4E+05	5,06
96	0,00032	1,61E-08	1,69E-09	0,591	0,0032	4,2E+05	5,04
98	0,00026	2,13E-08	1,76E-09	0,582	0,0028	2,5E+05	5,03
100	0,00020	2,69E-08	1,92E-07	0,605	0,0036	1,9E+05	4,63
110	0,00020	1,23E-07	3,16E-08	0,568	0,0027	1,3E+05	3,92
120	0,00028	6,65E-08	6,39E-09	0,532	0,0025	7,6E+04	3,91

Table 4: ***Fitting results of the high-frequency R-CPE element, sketched in Figure. 3.40(a).***

The intrinsic dielectric permittivity of the film can then be plotted as function of temperature in the given range, below 120K. To extract the ε value for each temperature the set of equations described in **Equation 3.11** can be applied.

$$\varepsilon = C \cdot \left(\frac{2t}{\varepsilon_o A}\right)$$

$$C = \frac{(Q \cdot R)^{(1/\alpha)}}{R} \quad \textbf{Equation 3.11}$$

$$p = {A \cdot R}/{(2t)}$$

Where *A* accounts for the area of the electrode and *t* for the thickness of the sample, since the sample was measured on top-top configuration, this value is doubled. Dielectric permittivity is represented as function of temperature in **Figure 3.43 a)**.

Remarkably enough, curve shows a small dielectric peaks around the FM transition temperature, previously observed in **Figure 3.42** related to the increment on ideality of the CPE element. The right axis represents the derivative of the data, plotted in order to clearly identify any transition or abnormality, The peak is found in the surroundings of the T_{FM} =97K suggesting, once again a small correlation or magneto dielectric effect on the film.

Finally the dependence of resistivity with temperature, ρ(T), is shown in **Figure 3.43 b)**, the behavior observed is compatible to the semiconductor behavior previously reported for similar multiferroic perovskites [**20**]. In previous work from E. Langenberg [**21**] this was also observed with similar behavior. Resistivity decreases from $\approx 10^9$ Ω*cm at 20K to 10^2 Ω*cm at 200K with tree distinctive areas. The first area comprehends temperatures from 200K down to ≈96K, where the resistivity shows a thermally activated behavior, second segment can be observed just after the T_{FM} in the area between ≈96 - 76 K where a small deviation from the Arrhenius law is observed, finally the segment corresponding to the ≈76 to 20K, where the resistance shows a completely different behavior from previous segments, denoting a fundamental change on the conduction mechanism.

For temperatures above the T_{FM}, 96K, since the resistivity shows a typical thermally activated behavior, the Arrhenius law can be applied as shown in **Equation 3.12** and in the blue line in **Figure 3.43 b)**.

$$\boldsymbol{\rho = \rho_0 exp\left(\frac{Ea}{k_B T}\right)} \quad \textbf{Equation 3.12}$$

The activation energy extracted from this fitting is 140±3 meV. This value is in good agreement with DFT calculations performed for YNMO bulk material, 200 meV [**25**] and remarkably similar to the one reported for solid solution, 130 meV[**26**]. Interestingly enough are the important discrepancies with similar materials such Bi_2NiMnO_6 [**22**] and La_2NiMnO_6 [**27**] in which activation energies are 72 and 32 meV respectively. In the case of YNMO thin film there is not shrinking of the bandgap as observed for such materials, in the work of E. Langenberg [**28**] the shrinking of the band gap is attributed the so called B site ordering of the double perovskite formula, favored by the dissimilar electronic configuration of the B-cations and their B-site order. In the case of YNMO thin films no B site ordering was directly observed, although the close values of the total magnetization of the YNMO(001) films, 4,35

μB/f.u, with previously reported experimental data on both thin films [**14**] and bulk materials [**13**] suggest the existence of a considerable amount of ordering on the B site. However, this claim should be further addressed in order to understand the role of B site ordering on the conduction mechanics of R_2NiMnO_6 perovskites.

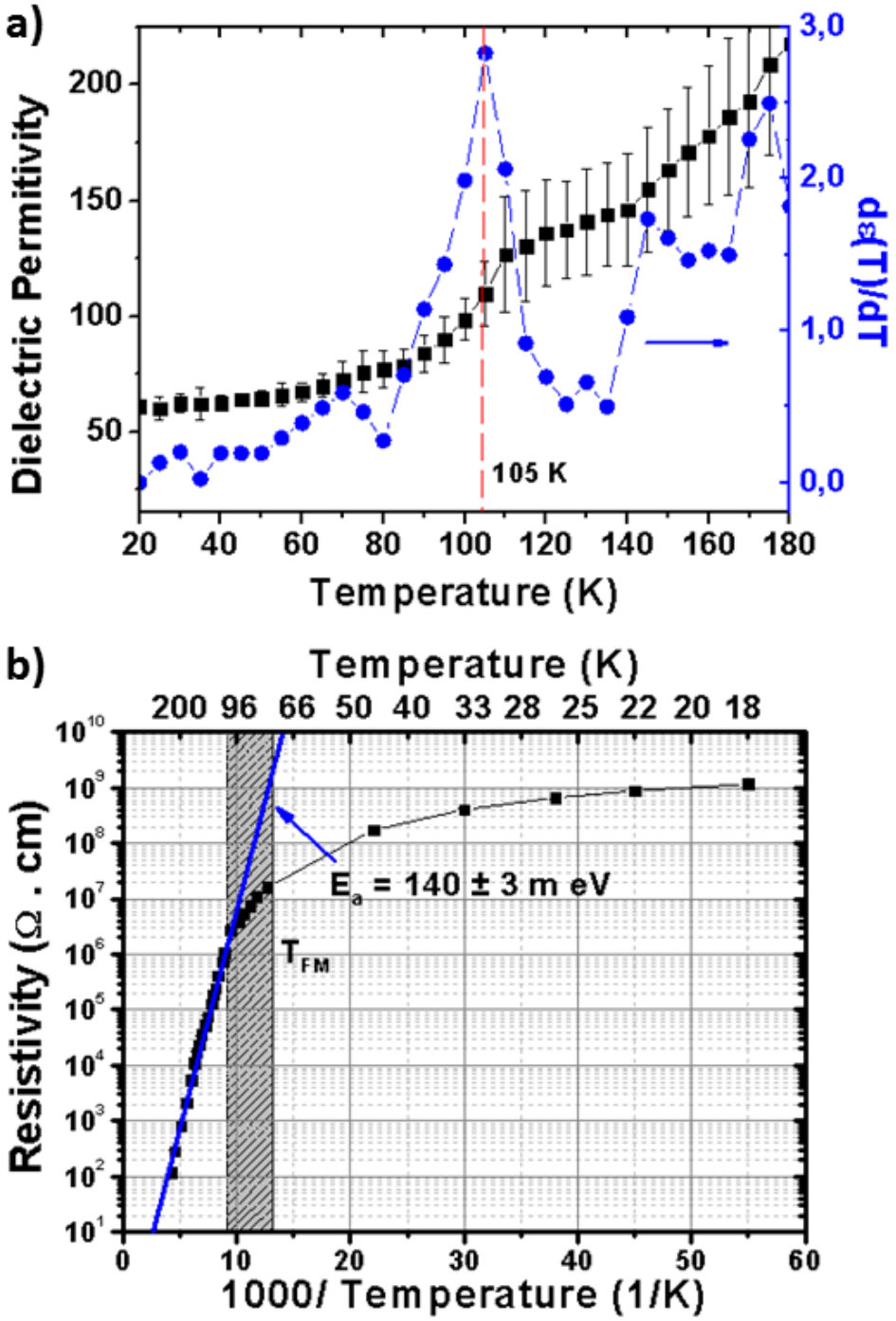

Figure 3.43 *a) (Left axis) plot of the dielectric permittivity of YNMO(001) extracted from the complex impedance spectroscopy, as function of temperature. (Right axis) Dielectric permittivity derivative. b) Temperature dependence of the intrinsic resistivity of the film. The dashed line shows the Arrhenius fitting. Dashed region indicates the magnetic Curie temperature.*

The second and third segments comprehended the temperatures below 98K, show a general change on conduction that rapidly deviates from the Arrhenius law, the fact that this deviation happens at the point in which the T_{FM} strongly suggest the centrosymetric nature of the phase transition has a strong influence on the conduction mechanism, this effect was also observed in Bi_2NiMnO_6 films [**22**,**23**]. It seems logical to consider that the continuous shrinking of the YNMO unit cell, in the scenario in which long range B-site ordering is present, would considerably increase the conduction mechanism of the YNMO, assuming it is related to the electron hopping of the *d*-orbitals of the magnetic ions Ni^{2+} and Mn^{4+}. The influence of such effects on the ferroelectric response of this material is still under investigation and discussion.

3.3.2.2 Temperature dependent Dielectric Impedance of YNMO(101)/STO(111)

Similar studies to the ones previously described for YNMO(001)/STO(001) are now performed on YNMO(101)/STO(111) samples. The corresponding Nyquist plots resulting from temperature dependent measurements are shown in **Figure 3.44**. As in the previous case, plots show clear evidence of a two mechanism present on the sample, one at high frequency and the second one at low frequency. The high frequency semicircle is attributed to the intrinsic mechanism of the sample, while the second semicircle, at low frequencies is attributed to an extrinsic mechanism. The high frequency mechanism is almost imperceptible at room temperature and starts to be present at low temperatures, as in the case of YNMO(001) films.

The schematic in **Figure 3.44 a)** shows the model used to describe the impedance plot, the red line corresponds to the fitting adjusted to the given curve**, Figure 3.44 b)** shows a selected collection of curves in which the increment of the intrinsic mechanism, smaller semicircle at higher frequencies, is observed. Notice that this semicircle appears at lower temperatures than the ones observed on YNMO(001) films, in that case the intrinsic contribution was noticeable below 250K, while for YNMO(111) it starts to be perceptible at 180K, the reason for this variation is not fully understood, but it is attributed to multiple factors, such film inhomogeneity, essentially related to the multiple in-plain domains present in each sample, also possible, dielectric anisotropy of the sample due to the substrates epitaxial strain, which plays an important role in the lattice constant of the YNMO(111) film, as previously described and shown in detail in this chapter, **Figure 3.17.**

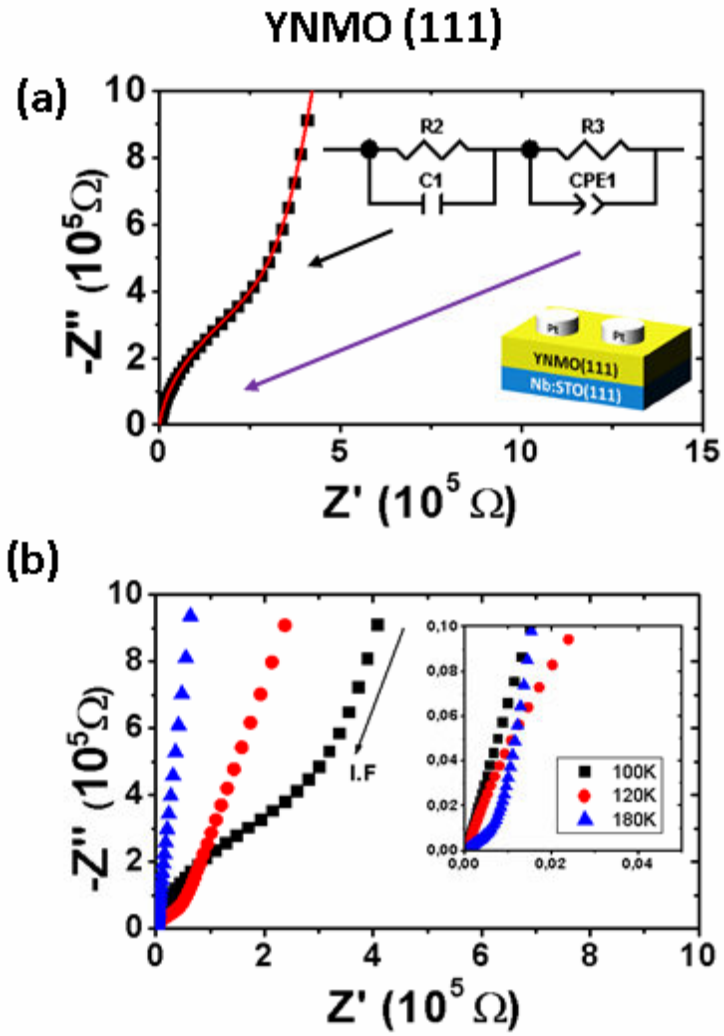

Figure 3.44 *Impedance spectroscopy measurements. a) Shows the appearance of two independent mechanisms in the sample. High frequencies mechanisms are attributed to intrinsic properties of the film. Red line is the fitting for a given measurement. b) Selected temperatures showing the range of temperatures in which the double mechanism is observed and thus the analysis can be performed.*

Following the same procedure described for YNMO(001), the dielectric behavior of the film is fitted using the **Equation 3.10**, with the intrinsic contribution described as a CPE, thus allowing the extraction of the dielectric permittivity, using the **Equation 3.11,** moreover, allowing to examine the dielectric behavior of the YNMO film in the range of 180-20K, covering the magnetic transition T_{FM} of the YNMO, ≈100K. However, before presenting the ε is worth examining the α exponent of the CPE

element. In Figure 3.45, the exponent of the R-CPE element, representing the non-ideality CPE element is showed, is important to notice the progressive evolution of this exponent towards the ideal capacitive behavior with the decrement of temperature, reaching a maximum value of 0.98, rather close to the pure R-C element, α=1. Also important to remark is the visible change in slope, visible in the derivative on the curve, right axis, close to the T_{FM}=97K again suggesting some influence from the ferromagnetic ordering on the capacitive response of the film..

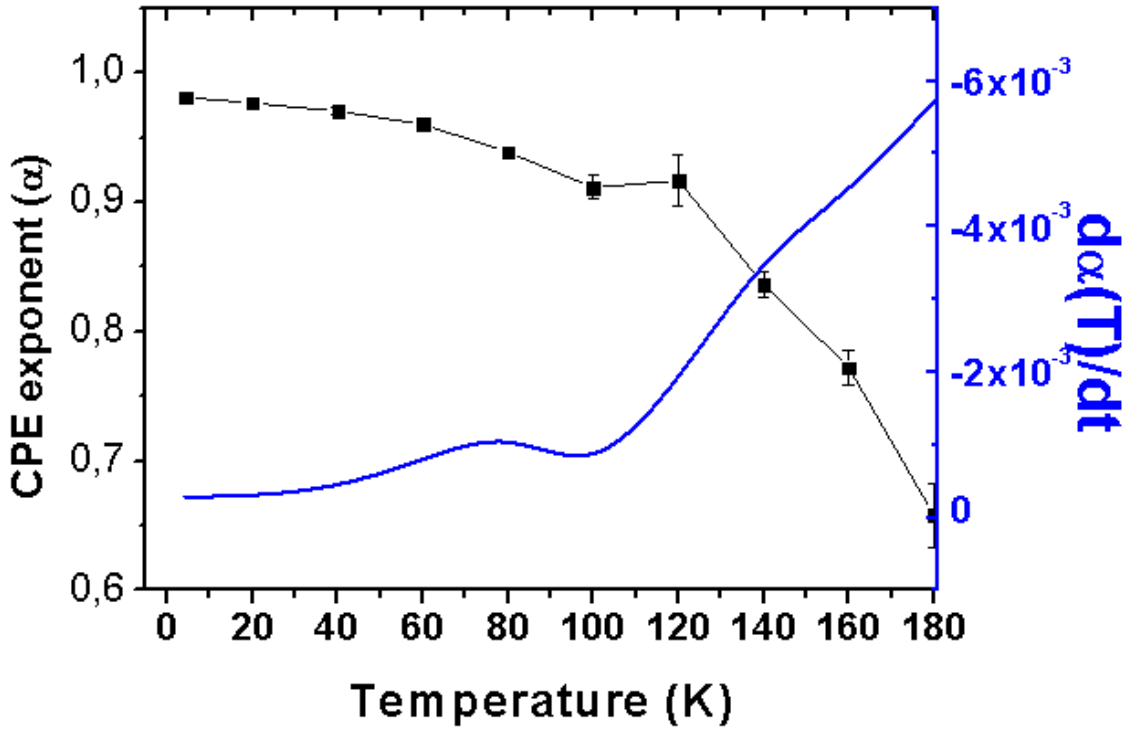

Figure 3.45 *Temperature dependence of the CPE exponent in the intrinsic mechanism*

The extracted dielectric permittivity is plotted as a function of temperature in Figure 3.46, the derivative of the curve is presented for clarity. As in the case of YNMO(001) the dielectric permittivity shows a progressive reduction from 280 to 40, this reduction also shows an abrupt change at 109K, temperature that is very close to the T_{FM}. This confirms the previously observed peak in the sample YNMO(001) given that the curves obtained by the IS method show a much lower error, fitting values for the intrinsic contribution of the film are shown in Table 5. The diminishing of these error bars can be attributed to a possible better alignment of the polarization axis on the

YMNO(111) film, which allows to a clear differentiation of this change. These observations suggest an inherent interdependency between the dielectric properties of the film and the ferromagnetic ordering.

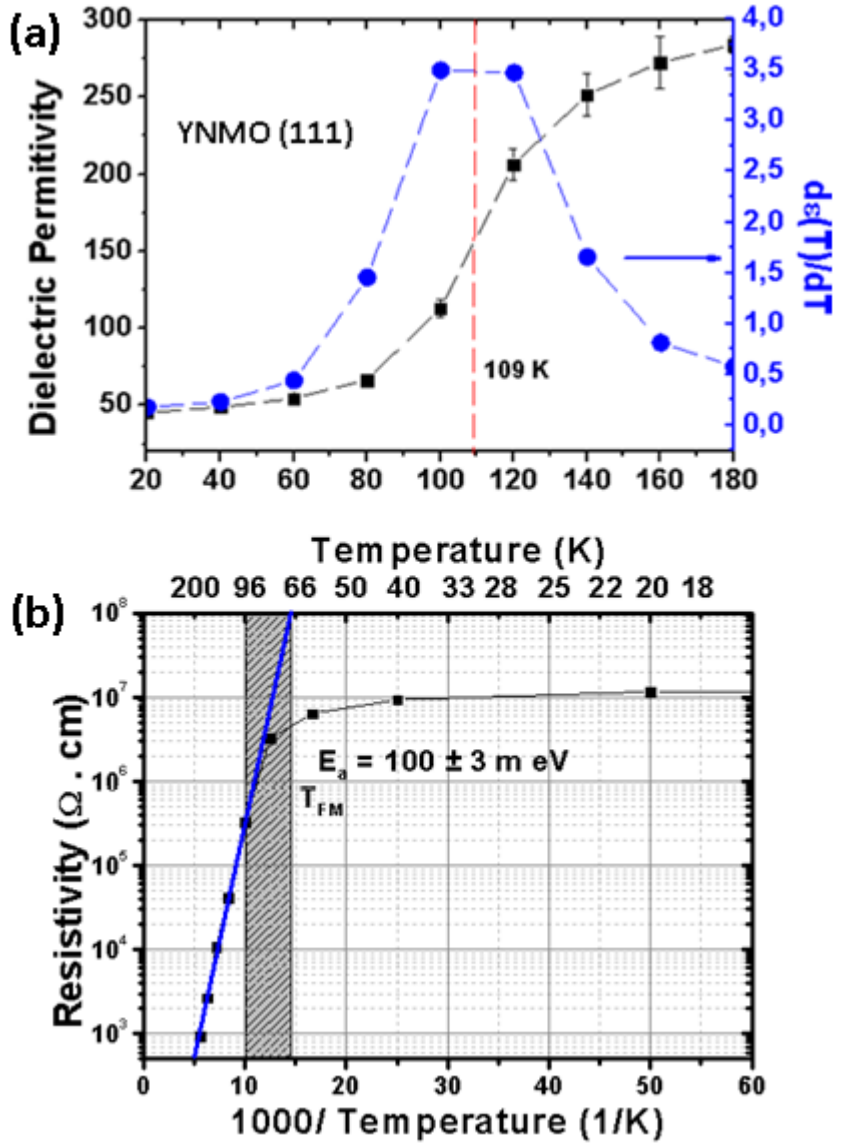

Figure 3.46 *(a) (Left axis) plot of the dielectric permittivity of YNMO(001) extracted from the complex impedance spectroscopy, as function of temperature. (Right axis) Dielectric permittivity derivative. b) Temperature dependence of the intrinsic resistivity of the film. The dashed line shows the Arrhenius fitting. Dashed region indicates the magnetic Curie temperature.*

The activation energy extracted from the Arrhenius plot is shown in **Figure 3.46(b)** using the **Equation 3.12.** As in previous cases, three regimes of the resistivity are observed, the first characterized by a pseudo linear decrement of the resistivity is

observed for temperatures above 97K, the second regime is found in between the 97-66K, well in the surroundings of the T_{FM}, while the last one is found below 66K. In this case, a small shrinking of the band gap is observed when compared with the YNMO(001) film, however this shrinkage is not a dramatic as in the case of BFMO [**22**] and remains rather close to the reported values for bulk YNMO.

Fitting **R**esults YNMO(111)

T (K)	$\chi 2$	Q [$Fs^{\alpha-1}$]	Error Q	α	Error α	$R(\Omega)$	Error R(Ω)
4	0,0068	1,6E-09	6,1E-11	0,981	0,003	1,2E+07	6,3E+06
20	0,0062	1,8E-09	6,6E-11	0,977	0,003	1,2E+07	6,1E+06
40	0,0054	2,0E-09	7,1E-11	0,970	0,003	9,2E+06	3,4E+06
60	0,0046	2,3E-09	8,3E-11	0,960	0,003	6,4E+06	1,5E+06
80	0,0040	3,2E-09	1,2E-10	0,939	0,003	3,2E+06	3,5E+05
100	0,0032	7,3E-09	1,4E-09	0,911	0,009	3,3E+05	1,3E+05
120	0,0022	9,1E-09	1,5E-09	0,92	0,02	4,1E+04	5,6E+03

Table 5: ***Fitting results of the high-frequency R-CPE element, sketched in Figure. 3.44(a).***

In order to conclude this section, the dielectric behavior of both YNMO(001) & YNMO(111) was investigated by impedance spectroscopy, the decreasing of temperature below that of liquid nitrogen allowed to decoupled the intrinsic and extrinsic behavior on the films, being the first one fully visible below 180K for both samples. In many ways it was advantageous that the T_{FM} of the YNMO film was in the observable range, allowing investigating the influence of the dielectric behavior and its relation with the ferromagnetic ordering of the film. The results suggest a correlation between the ferromagnetic ordering and the dielectric response of the material, which in the case of multiferroic materials is highly desirable. However, the ferroelectric nature of this material has not been addressed. In the following section the ferroelectric nature of the films will be investigated in order of assess the multiferroicitiy of the double perovskite of $Y(Ni_{0.5}Mn_{0.5})O_{3.}$

3.3.3 Ferroelectric Response

The ferroelectric response of YNMO thin films was investigated using the Top-Top configuration, described in detail in the experimental section, chapter 2, of this thesis. Measurements were performed by Dr. Ignaci Final at the Institute of Materials of Barcelona (ICMAB). As in the case of impedance spectroscopy measurements, only the out of place ferroelectric response of the films will be accessible in this configuration.

Dielectric Leakage Current Compensation (DLCC) [**29**] and Positive-Up-Negative-Down method (PUND) [**30**] techniques were used to ascertain for the ferroelectric nature of the films [**31**] using a high frequency I-V meter (TFAnalyser 2000, aixACCT Co.). Briefly, in DLCC two I-V loops at the nominal and half of the nominal frequency are recorded, and the leakage is subtracted assuming that it is frequency independent.

For the sake of simplicity and clarity both YNMO(001) and YNMO(101) samples will be addressed in pseudo cubic indexation, as shown in **Figure 3.17.** Also they will be introduced and discussed in parallel.

Due to the epitaxial relationship of the films, it is possible to access the properties along the c-axis for the YNMO(001) sample, and along the diagonal of the *cube* for YNMO(111) sample. In order to examine if the signature of ferroelectric polarization was detected in the same phase as the ferromagnetic ordering, below 97K, films were measured at 5K, this temperature also allows reducing the losses in thin films [**32**]. In **Figure 3.47a)**, current versus electric field loop measured for YNMO(001) sample at 1kHz is depicted. In that, it cannot be observed any signature of the ferroelectric current switching peaks signature of ferroelectric behaviour. Instead only displacive current ($i_{displacive}$=1/C*dV/dt) can be observed. In **Figure 3.47c**, the polarization obtained from the integration through time of the current depicted in **Figure 3.47a**, shows clear paraelectric behaviour, evidencing the absence ferroelectric switching while applying the electric field along the c-axis. The very tinny aperture of the loop at low electric fields is ascribed only to the presence of some low leakage current (due to electronic transport across the film). This effect is commonly observed in thin films and in many cases erroneously attributed to small ferroelectric polarization as described in the literature[**33**,**34**].

Contrary to the observed absence of ferroelectric signatures on YNMO(001), in **Figure 3.47b**, equivalent current versus electric field measurement at 100Hz and 5K, shows the presence of the two ferroelectric switching peaks signalled with corresponding arrows for the YNMO(111) sample. The data have been obtained after applying DLCC; in the inset it is shown the measurement before applying the compensation. In both cases, it can be observed a clear ferroelectric switching peak in the positive electric field side and a significant hysteresis in the negative electric, signalled by arrows. These confirm the ferroelectric nature of the YNMO (111) film. In

Figure 3.47 d), the polarization versus electric field loop shows a polarization value around 10 μC/cm^2. Note the asymmetries found in both loops (Figure 3.47b,d), owing to the top-to-top used method, these can be only be attributed to small differences between the top electrode and film interfaces between the used contacts.

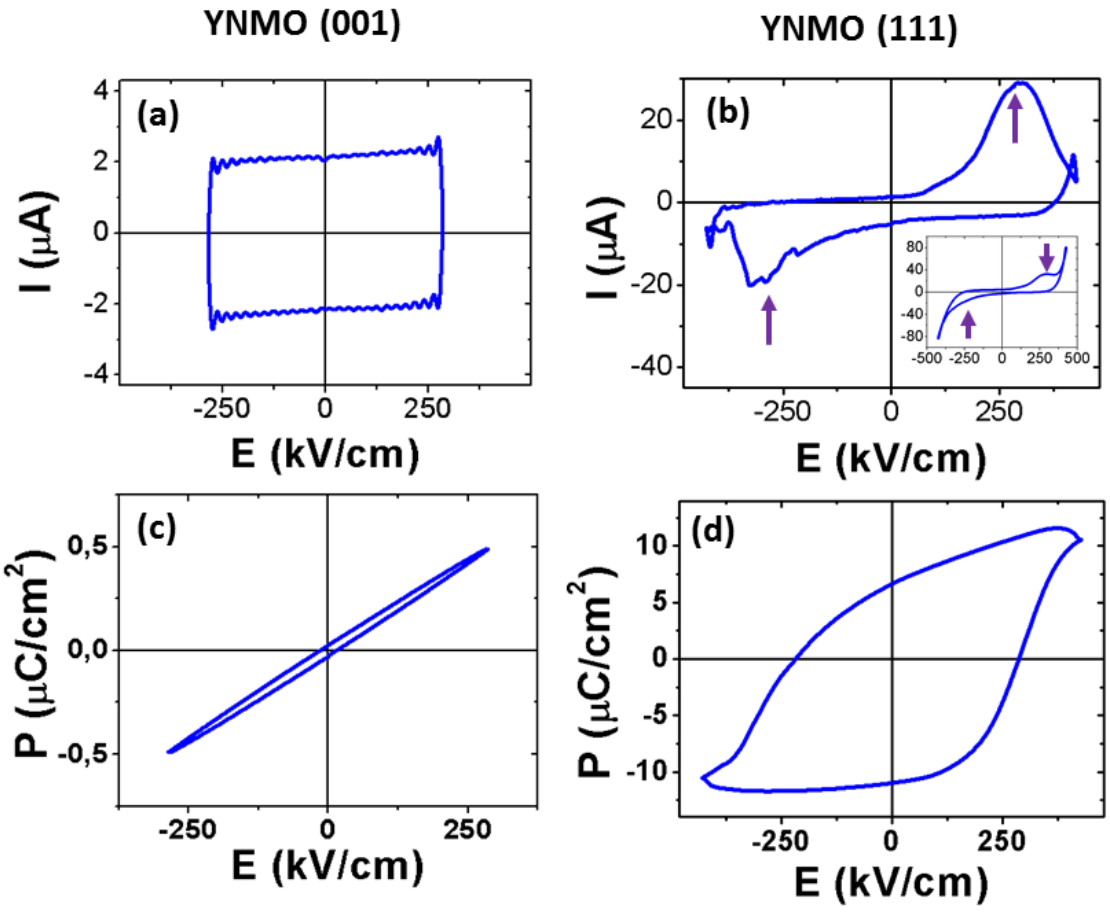

Figure 3.47 *(a) Current versus electric field loop performed in P_C-YNMO(001) sample at 1 kHz and 5 K. (b) Current versus electric field loop performed in P_C-YNMO(111) sample at 100 Hz and 5 K. (c,d) Polarization versus electric field loops obtained from the normalized to the area integration trough time of the current plotted in the figures (a,b) corresponding to samples P_C-YNMO(001) and P_C-YNMO(111), respectively.*

.

It is remarkable that polarization of the YNMO(111) is much bigger than the one reported for a close relative BMNO [**35**]. In fact, this polarization seems unusually large for a material with the dielectric properties described in the Section 3.3.2 of this chapter, in particular with small shrinkage of the band gap and evident changes on the conduction mechanism at temperatures close to liquid helium. It is also known that the DLCC method tents to overestimate the polarization of some samples[**31**], especially in

those samples with high losses, such in this case. The high losses of the sample are inferred by the elongated tails of the inset shown in **Figure 3.47 b** Therefore the PUND method is used in order to extract a more accurate value of the polarization.

In the PUND measurement, the current is measured while applying - + + - - voltage triangular pulse sequence, switchable polarization is obtained from the integration through time normalized to the electrode area of the current resulting from the subtraction of the current measured at the second (P-pulse) from the one measured at the third (U-pulse) and the one of the fourth (N-pulse) one from the one of the fifth one (D-pulse), The result of such pulse sequence are shown in **Figure 3.48**. These measurements are described in detail in [**32**].

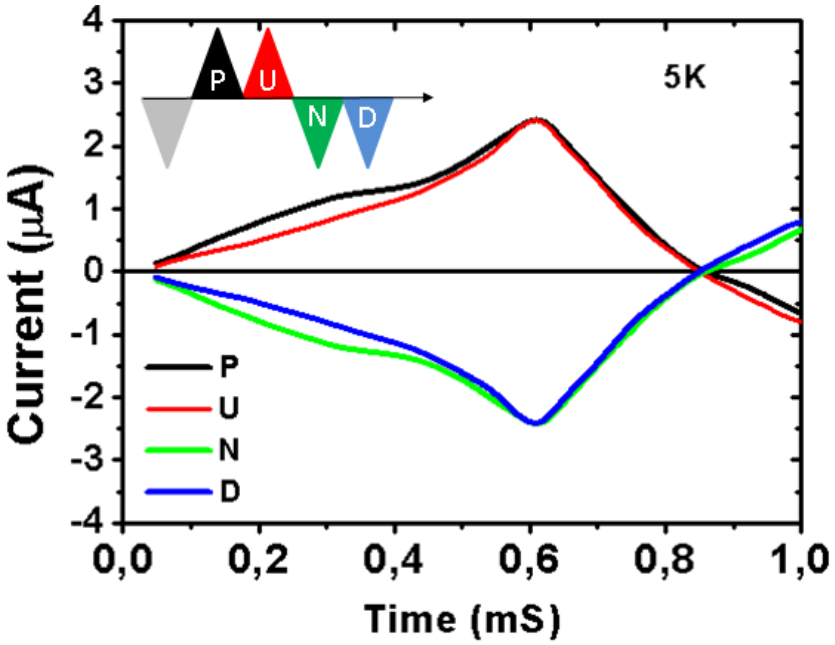

Figure 3.48 *Depiction of the PUND technique, the small differences between PN &UD account for the intrinsic polarization vs the leakage of the film*

In **Figure 3.49a**, the current versus electric field loop measured at 10kHz and 5K after PUND subtraction is plotted. Both clear ferroelectric current peaks are visible, further confirming the ferroelectric nature of the material. In **Figure 3.49b** the integrated polarization loop shows that here the remanent polarization is approximately 3.2 μC/cm^2 with a noticeable asymmetry. The discontinuity on the graph is because the non-constant voltage ramp used, which provokes the discontinuity on the paraelectric contribution of the displacive current. Explanations in detail of this phenomenum can be

found in the Doctoral Thesis of Dr. Ignaci Fina. [**32**]. Morover, ferroelectric characterization has also been performed at higher temperatures, above the T_{FM} of the film; however, the presence of important leakage (rapidly increasing with temperature) hinders a reliable evaluation of ferroelectric polarization upon increasing temperature.

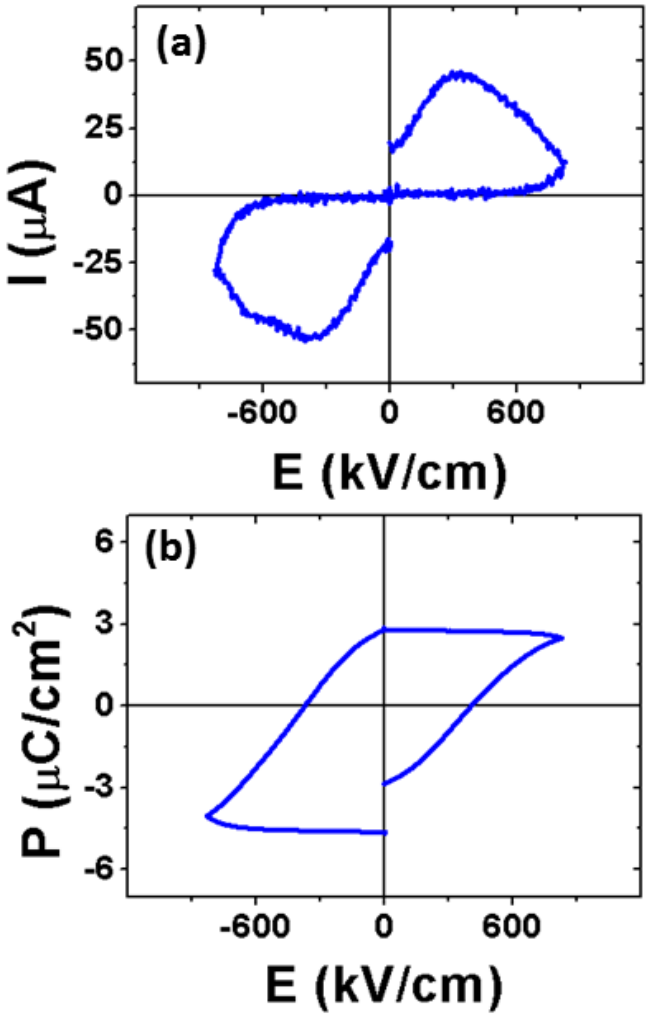

Figure 3.49 *(a) Current versus electric field loop performed in YNMO(111) sample at 100 Hz and 5 K, after PUND subtraction. (b) Polarization versus electric field loops obtained from the normalized to the area integration trough time of the current plotted in the figures (a).*

The PUND results show a more reliable ferroelectric response of the YNMO(111) film of 3.2 μC/cm^2. This value is still higher from the ones reported on other ferroelectric materials such as YMO [**36**] and BFMO [**35**]. Regardless of this, the ferroelectric nature of the YNMO(111) film is unequivocally clear. However, it is important to discuss the absence of similar response on YNMO(001).

3.3.3.1 Origin of the ferroelectric polarization and dielectric anisotropy

The YNMO perovskite is member of the R(Ni0.5Mn0.5)O3 family, which is characterized by a phase transition from monoclinic to a crystalline centrosymmetric unit cell, thus allowing to super exchange between Ni and Mn ions to generate the magnetic ordering observed in this family. However, the centrosymmetric structure forbids the ferroelectric polarization, thus making implausible a ferroelectric response in the magnetic phase of the RNMO perovskite. Regardless of this, here conclusive evidence of the ferroelectric ordering of the YNMO(111) film is shown.

A factor influencing the experimental results could be the epitaxial strain provided by the STO substrate, which makes the YNMO(111) unit cell slightly different from that of YNMO(001) and bulk YNMO, and could play a major role in the ferroelectric polarization observed. Allowing the structure of the perovskite to remain a partially non-centrosymmetric structure, thus allowing the ferroelectric polarization. However, this effect alone could not account for the large polarization observed in the film.

Another explanation is the apparition of improper ferroelectricity, in a published theoretical work of Kumar et al [**25**], In this work the origin of the FE ordering arose due to a re-arrangement between FM state into E*-type magnetic structure, which consists of ↑-↑-↓-↓ spin chains along the in-plane cubic perovskite like (b) direction shown in **Figure 3.50**, with the spins chains organized in a zig-zag AFM configuration with a FM coupling in the out-of-plane direction. This magnetic spin organization has been known to assist the ferroelecticity along the b-axis in perovskites materials[**37**], because the magnetic ordering breaks the spatial symmetry of the centrosymetric YNMO unit cell into a smaller enantiomorphic cell, allowing the uniaxial ferroelectric ordering. However, in their work S. Kumar et al.[**25**] definded YNMO magnetic state as E*-type AFM, which is in contradiction the magnetic measurements shown in this thesis. Regardless of this fact, further calculation proposed that for a similar compound SmNiMnO6 a slight displacement of oxygen atoms can be induced, under an external applied field, the unit cells naturally deforms, provided the ferromagnetic ordering already stablished, this deformation will promote the E*-type AFM state, and thus the ferroelectric polarization.

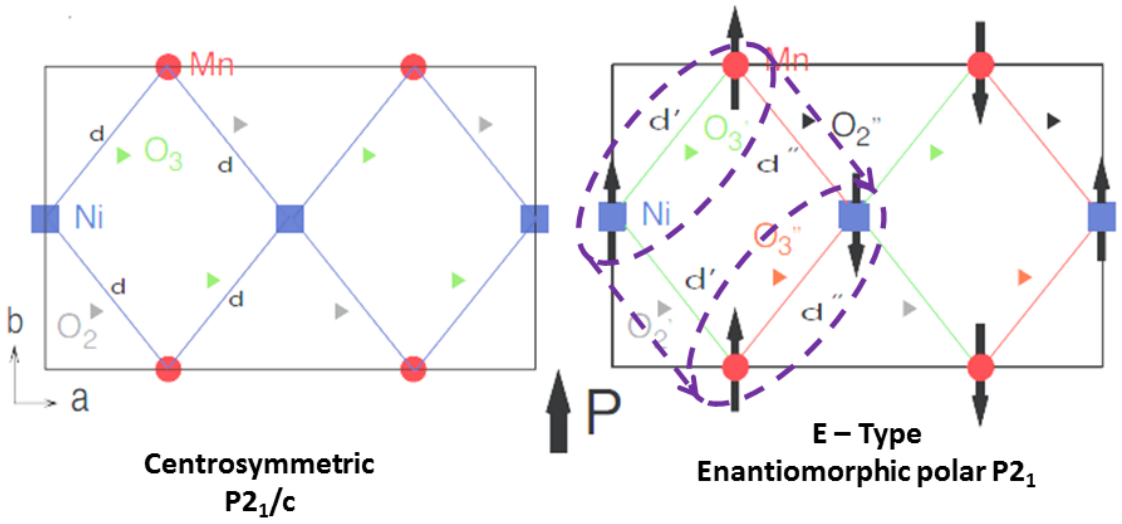

Figure 3.50 *Representation of the Pseudo-cubic YNMO unit cell and the theoretical variation of the O bounds. The dashed lines show the variation of the unit cell angles and distances in order to generate the enantiomorphic polar P21 structure.*[**25**]

The magnetic measurements shown in this thesis and in the literature [**2**,**5**,**14**] clearly establish a ferromagnetic ordering of the YNMO thin films at 97K, ruling out a naturally occurring E-type antiferromagnetic ordering on the samples. However, the theoretical prediction of the externally induced transformation of the unit cell could not be totally ruled out. In the case of ferroelectric measurements, when the electric field is applied, the magnetic state of the perovskite is assumed to be same as in normal magnetometer measurements. However, the change between FM centrosymmetric into enantiomorphic unit cell, during the ferroelectric measurements cannot prove or disproved at this stage. The fact that in their theoretical work Kumar et al, predict an uniaxial ferroelectric polarization along the pseudocubic *b* axis, couples with the experimental results of this thesis, in which YNMO(001) films, with the pseudocubic *b* axis residing totally in-plane show no ferroelectric response, while YNMO(111) films, with the pseudo cubic *b* axis partially projected out of plane, show strong ferroelectric response, seems to support this hypothesis.

In case of this scenario being accurate for the YNMO perovskite, the remanent polarization should be recalculated, considering the measured values a projection of the pseudo cubic polarization axis YNMO(010). Therefore, the remanent polarization of $P_{r\ (111)} \approx 3\ \mu C/cm^2$, which corresponds to a projected component from the total polarization on the *b*-axis of 5 $\mu C/cm^2$, using the as follows relation $P_{r\ (010)=}\ P_{r\ (111)\ /}\ \cos b/$

$\sqrt{(a^2 + b^2 + c^2)}$, where *a, b, c* are the lattice constant values for the pseudocubic perovskite, extracted from the YNMO(111) sample. As a result, the polarization along the *b*-axis of YNMO ($P_{r(010)}$) is near the double of the predicted values from Kumar et al[**25**], which can be ascribed to the discrepancy between the lattice parameters measured in our films, and the bulk values used in the theoretical predictions.

Nevertheless further studies are needed in order to experimentally and conclusively show the FM to AFM E*-Type transformation of the YNMO perovskite. However, a suitable experiment and setup was unavailable at the time of writing this thesis.

3.4 Summary of this chapter

- Ferromagnetic perovskites thin films of $Y(Ni_{0.5}Mn_{0.5})O_3$ were successfully deposited by PLD. The films shown epitaxial growth on STO(001), (110) and (111) single crystalline substrates. A clear influence of substrate temperature on the intensity of the YNMO(00l) peaks and the out–of-plane parameter was observed, while laser frequency showed only to take part at higher ablation frequencies. The epitaxial relationships and strain were quantified by means of reciprocal space map images, tabulated and confronted with similar studies on $YMnO_3$. The partial substitution of Mn with Ni, was observed to reduce the unit cell volume thus reducing the mismatch between the substrate and the YNMO, however keeping a remarkably similarity to the growth observed in orthorhombic $YMnO_3$, contrary to the previously reported experimental data and moreover corroborating that absence of domains presenting in-plane stress of the same sign. Additionally, the pseudo cubic indexing relations were addressed in order to exploit the appearance of multiple in-plane domains in the samples for further applications and studies.
- YNMO growth mechanism was found to be a clear 3D columnar growth, where films with multiple in-plane orientations showed large single domain grains that maintain their epitaxial relationships along growing direction. Also, by correlating the two in-plane domains obtained by X-ray analysis, with the morphology observed in the AFM images, using a simple numerical and geometrical approach, it was possible to determine that the mounds observed by AFM were indeed single in-plane domains. This feature was previously observed in the literature in similar films, but the existence of the two-in plane domains was not reported, thus not

showing a direct relationship with the inner structure of the film and the orthorhombic to pseudo cubic transformation. Moreover, the presence of small crystallites was observed in the samples with multiple in-plane domains, their origin is attributed to the higher surface ad atom mobility provided by the lower ablation rate and high substrate temperature, which allows the crystallites, to stop growing at the coalescence point of the film. Sharp interfaces and correct stoichiometric composition of the films are the norm for all the samples.

- Functional magnetic measurements corroborate the ferromagnetic nature of the films with a magnetic transition at 95K and a magnetic moment of 4,58 μB/f.u in concordance with previously reported data, although lower from the theoretical 5 μB expected.
- In this thesis the coexistence of both ferromagnetic and ferroelectric ordering in the YNMO perovskite has been experimentally proven, with a robust remanent polarization of Pr ≈ 3 μC/cm2, (and Mr ≈ 4 μB/f.u. comparable with the literature). The detection of a dielectric anomaly ≈100 K in both samples, very close to the ferromagnetic transition, indicates magnetoelectric coupling, signature of the correlation between the found ferroelectric nature of the material at low temperature and the magnetic ordering.
- The presented data and the theoretical predictions suggest the coexistence of E*-type antiferromagnetic ordered and anisotropically strained crystalline regions and does not rule out the second scenario in which E*-Type AFM could be induced by the external applied electric field, that ultimately leads to the ferroelectric ordering observed, also supporting the quantitative disagreement between both experiment and theory.
- Further studies are needed in order to clarify the truly origin of the anisotropic ferroelectric response in YNMO, which indicates the presence of E*-type magnetic structure, as predicted. This work demonstrates the potential interest of this manganite nickelate as multiferroic material due to the high FM and FE transition temperatures, with both ferroic orders intrinsically coupled, and paths the way to investigate other similar compounds showing E*-type magnetic ordering.

References

[1] Mouallem-Bahout, M., Roisnel, T., André, G., Gutierrez, D., Moure, C. and Peña, O. (2004) **Nuclear and magnetic order in Y(Ni,Mn)O3 manganites by neutron powder diffraction**. *Solid State Communications*, **129**, 255–60. http://dx.doi.org/10.1016/j.ssc.2003.09.039

[2] Ma, Y., Guilloux-Viry, M., Pena, O. and Moure, C. (2004) **Y(Ni, Mn)O3 epitaxial thin films prepared by pulsed laser deposition**. *Physica Status Solidi (a)*, **201**, 2385–9. http://dx.doi.org/10.1002/pssa.200304911

[3] Salvador, P.A., Doan, T.D., Mercey, B. and Raveau, B. (1998) **Stabilization of YMnO3 in a Perovskite Structure as a Thin Film**. *Chemistry of Materials*, **10**, 2592–5.

[4] Martí, X., Sánchez, F., Skumryev, V., Laukhin, V., Ferrater, C., García-Cuenca, M.V. et al. (2008) **Crystal texture selection in epitaxies of orthorhombic antiferromagnetic YMnO3 films**. *Thin Solid Films*, **516**, 4899–907. http://dx.doi.org/10.1016/j.tsf.2007.09.023

[5] Ma, Y., Guilloux-Viry, M., Barahona, P., Peña, O. and Moure, C. (2005) **Annealing effects on the microstructure and properties of Y(Ni,Mn)O3 thin films**. *Journal of the European Ceramic Society*, **25**, 2147–50. http://dx.doi.org/10.1016/j.jeurceramsoc.2005.03.061

[6] Merckling, C., El-Kazzi, M., Delhaye, G., Favre-Nicolin, V., Robach, Y., Gendry, M. et al. (2007) **Strain relaxation and critical thickness for epitaxial LaAlO3 thin films grown on SrTiO3(001) substrates by molecular beam epitaxy**. *Journal of Crystal Growth*, **306**, 47–51. http://dx.doi.org/10.1016/j.jcrysgro.2007.04.048

[7] Nix, W.D. and Clemens, B.M. (1999) **Crystallite coalescence: A mechanism for intrinsic tensile stresses in thin films**. *Journal of Materials Research*, Materials Research Society. **14**, 3467–73.

[8] Schmidt, R., Ventura, J. and Langenberg, E. (2012) **Magnetoimpedance spectroscopy of epitaxial multiferroic thin films**. *Physical Review B*, **86**, 035113. http://dx.doi.org/10.1103/PhysRevB.86.035113

[9] Little, S. and Zangwill, A. (1994) **Equilibrium microstructure of epitaxial thin films**. *Physical Review B*, **49**, 16659–69. http://dx.doi.org/10.1103/PhysRevB.49.16659

[10] Thompson, C. V. (2000) **STRUCTURE EVOLUTION DURING PROCESSING OF POLYCRYSTALLINE FILMS**. *Annual Review of Materials Science*, **30**, 159–90. http://dx.doi.org/10.1146/annurev.matsci.30.1.159

[11] Rebled, J.M., Foerster, M., Estradé, S., Rigato, F., Kanamadi, C., Sánchez, F. et al. (2013) **Ti diffusion in (001) SrTiO3-CoFe2O4 epitaxial heterostructures: blocking role of a MgAl2O4 buffer.** *Physical Chemistry Chemical Physics : PCCP*, **15**, 18274–80. http://dx.doi.org/10.1039/c3cp00001j

[12] Peña, O., Bahout, M., Ma, Y., Guizouarn, T., Gutiérrez, D., Durán, P. et al. (2003) **Effects of substitution at the manganese site in RE(Ni,Mn)O3 perovskites (RE=Y, Eu)**. *Materials*

Science and Engineering: B, **104**, 126–30. http://dx.doi.org/10.1016/S0921-5107(03)00184-3

[13] Booth, R.J., Fillman, R., Whitaker, H., Nag, A., Tiwari, R.M., Ramanujachary, K.V. et al. (2009) **An investigation of structural, magnetic and dielectric properties of R2NiMnO6 (R=rare earth, Y)**. *Materials Research Bulletin*, **44**, 1559–64. http://dx.doi.org/10.1016/j.materresbull.2009.02.003

[14] Ma, Y., Guilloux-Viry, M., Barahona, P., Peña, O., Moure, C., Ghilane, J. et al. (2006) **YNixMn1−xO3 thin films by pulsed laser deposition: Structure and magnetic properties**. *Thin Solid Films*, **510**, 275–9. http://dx.doi.org/10.1016/j.tsf.2005.12.159

[15] Williams, M.M.R. (1977) **The mathematics of diffusion**. *Annals of Nuclear Energy*, **4**, 205–6. http://dx.doi.org/10.1016/0306-4549(77)90072-X

[16] Gilbert, J.B., Rubner, M.F. and Cohen, R.E. (2013) **Depth-profiling X-ray photoelectron spectroscopy (XPS) analysis of interlayer diffusion in polyelectrolyte multilayers.** *Proceedings of the National Academy of Sciences of the United States of America*, **110**, 6651–6. http://dx.doi.org/10.1073/pnas.1222325110

[17] Haque, M.T., Nakajima, N., Watanabe, K., Kamegashira, N. and Itoh, M. (2003) **Structure, magnetic and thermal properties of Gd2MnTiO6**. *Materials Chemistry and Physics*, **80**, 676–81. http://dx.doi.org/10.1016/S0254-0584(03)00097-X

[18] Kamegashira, N., Nakajima, N., Watanabe, K. and Kobayashi, M. (2000) **Synthesis and crystal structure of Sm2MnTiO6**. *Journal of Alloys and Compounds*, **311**, 74–8. http://dx.doi.org/10.1016/S0925-8388(00)00865-3

[19] Nakano, H., Nakazima, N., Shirakami, T. and Kamegashira, N. (1999) **Crystal structure of a new oxide, Nd2TiMnO6**. *Materials Research Bulletin*, **34**, 1851–8. http://dx.doi.org/10.1016/S0025-5408(99)00208-1

[20] Schmidt, R., Ventura, J., Langenberg, E., Nemes, N.M., Munuera, C., Varela, M. et al. (2012) **Magnetoimpedance spectroscopy of epitaxial multiferroic thin films**. *Physical Review B*, **86**, 035113. http://dx.doi.org/10.1103/PhysRevB.86.035113

[21] Langenberg, E., Fina, I., Ventura, J., Noheda, B., Varela, M. and Fontcuberta, J. (2012) **Dielectric properties of (Bi_{0.9}La_{0.1})_{2}NiMnO_{6} thin films: Determining the intrinsic electric and magnetoelectric response**. *Physical Review B*, **86**, 085108. http://dx.doi.org/10.1103/PhysRevB.86.085108

[22] Langenberg, E., Fina, I., Ventura, J. and Noheda, B. (2012) **Dielectric properties of (Bi 0.9 La 0.1) 2 NiMnO 6 thin films: Determining the intrinsic electric and magnetoelectric response**. *Physical Review B*, **86**, 085108. http://dx.doi.org/10.1103/PhysRevB.86.085108

[23] Kakarla, D.C., Jyothinagaram, K.M., Das, A.K. and Adyam, V. (2014) **Dielectric and Magnetodielectric Properties of R 2 NiMnO 6 (R = Nd,Eu,Gd,Dy, and Y)**. Viehland D, editor. *Journal of the American Ceramic Society*, Blackwell Publishing Inc. **97**, 2858–66. http://dx.doi.org/10.1111/jace.13039

[24] Berkemeier, F., Abouzari, M. and Schmitz, G. (2007) **Thickness-dependent dc conductivity of**

lithium borate glasses. *Physical Review B*, **76**, 024205. http://dx.doi.org/10.1103/PhysRevB.76.024205

[25] Kumar, S., Giovannetti, G., van den Brink, J. and Picozzi, S. (2010) **Theoretical prediction of multiferroicity in double perovskite Y_{2}NiMnO_{6}**. *Physical Review B*, **82**, 134429. http://dx.doi.org/10.1103/PhysRevB.82.134429

[26] Sharma, G., Tripathi, T.S., Saha, J. and Patnaik, S. (2014) **Magnetic entropy change and critical exponents in double perovskite Y2NiMnO6**. *Journal of Magnetism and Magnetic Materials*, Elsevier. **368**, 318–23. http://dx.doi.org/10.1016/j.jmmm.2014.05.035

[27] Rogado, N.S., Li, J., Sleight, A.W. and Subramanian, M.A. (2005) **Magnetocapacitance and Magnetoresistance Near Room Temperature in a Ferromagnetic Semiconductor: La2NiMnO6**. *Advanced Materials*, **17**, 2225–7. http://dx.doi.org/10.1002/adma.200500737

[28] Langenberg Pérez, E. **Growth and characterisation of Bi-based multiferroic thin films** [Internet]. Universitat de Barcelona.

[29] Meyer, R., Waser, R., Prume, K., Schmitz, T. and Tiedke, S. (2005) **Dynamic leakage current compensation in ferroelectric thin-film capacitor structures**. *Applied Physics Letters*, **86**, 142907. http://dx.doi.org/10.1063/1.1897425

[30] Scott, J.F., Kammerdiner, L., Parris, M., Traynor, S., Ottenbacher, V., Shawabkeh, A. et al. (1988) **Switching kinetics of lead zirconate titanate submicron thin-film memories**. *Journal of Applied Physics*, **64**, 787. http://dx.doi.org/10.1063/1.341925

[31] Fina, I., Fàbrega, L., Langenberg, E., Martí, X., Sánchez, F., Varela, M. et al. (2011) **Nonferroelectric contributions to the hysteresis cycles in manganite thin films: A comparative study of measurement techniques**. *Journal of Applied Physics*, **109**, 074105. http://dx.doi.org/10.1063/1.3555098

[32] Fina Martínez, I. **Ferroelectricity and magnetoelectric coupling in magnetic ferroelectrics and artificial multiferroic heterostructures** [Internet]. Universitat de Barcelona.

[33] Scott, J.F. (2008) **Ferroelectrics go bananas**. *Journal of Physics: Condensed Matter*, **20**, 021001. http://dx.doi.org/10.1088/0953-8984/20/02/021001

[34] Loidl, A., Krohns, S., Hemberger, J. and Lunkenheimer, P. (2008) **Bananas go paraelectric**. *Journal of Physics: Condensed Matter*, **20**, 191001. http://dx.doi.org/10.1088/0953-8984/20/19/191001

[35] Langenberg, E., Fina, I., Gemeiner, P., Dkhil, B., Fàbrega, L., Varela, M. et al. (2012) **Ferroelectric phase transition in strained multiferroic (Bi0.9La0.1)2NiMnO6 thin films**. *Applied Physics Letters*, **100**, 022902. http://dx.doi.org/10.1063/1.3675869

[36] Fina, I., Martí, X., Fàbrega, L., Sànchez, F. and Fontcuberta, J. (2010) **Dielectric anomalies in orthorhombic YMnO3 thin films**. *Thin Solid Films*, **518**, 4710–3. http://dx.doi.org/10.1016/j.tsf.2009.12.065

[37] Picozzi, S., Yamauchi, K., Sergienko, I. a, Sen, C., Sanyal, B. and Dagotto, E. (2008) **Microscopic mechanisms for improper ferroelectricity in multiferroic perovskites: a theoretical review**. *Journal of Physics: Condensed Matter*, **20**, 434208. http://dx.doi.org/10.1088/0953-8984/20/43/434208

CHAPTER 4

Thin Films of $R(Ni_{0.5}Mn_{0.5})O_3$ (R=Sm, Nd &Pr)

The following chapter focuses on the studies performed on the family of $R(Ni_{0.5}Mn_{0.5})O_3$, R=Sm (SNMO), Nd (NNMO) & Pr (PNMO). For each of the aforementioned materials, the growth conditions of the thin films will be discussed. Secondly, the single phase stabilization will be addressed, followed by the morphological characterization of the films. Finally the functional properties, principally the magnetic measurements, will be carefully assessed.

4.1 Target Synthesis

Targets of RNMO have been synthesized by mixing stoichiometric powders of suitable oxides, summarized in **Table 4.1.** Oxides were place into an agate mortar. In order to synthesize the perovskite formula the B site ordered compound (R_2NiMnO_6) was considered.

STOICHIOMETRIC REACTIONS

$\mathbf{Pr_2O_3 + NiO + MnO_2 \rightarrow Pr_2NiMnO_6}$
$\mathbf{Nd_2O_3 + NiO + MnO_2 \rightarrow Nd_2NiMnO_6}$
$\mathbf{Sm_2O_3 + NiO + MnO_2 \rightarrow Sm_2NiMnO_6}$

Table 4.1: *Solid state reaction used in the fabrication of the RNMO targets*

The proportions and dimensions of for each given target are described in detail in the **Appendix 1**. Diffraction tables of the RNMO family are absent in the X`Pert PANAnalitical software. However, based on the detailed crystalline structure, reported

in the literature[**1**–**3**], primary peaks where simulated using the CaRIne Crystallography v3.1 software and compared with powder diffraction experiments performed on the targets. Results, not shown in this work, showed a polycrystalline and multiphase composition, suggesting that the used pressure and temperature was not enough to synthesize the RMNO phase. Regardless of these results, the appropriate stoichiometry of the targets was assessed by XPS measurements. Targets were cleaned by argon sputtering for several minutes in order to clean any surface contamination. Extracted proportions, normalized to oxygen content, are shown in **Table 4.2**.

RELATIVE COMPOSITION

A	B	B`
Sm(35,2%)	Ni (17,2%)	Mn(19,1%)
Pr(33,9%)	Ni (16,8%)	Mn(17,4%)
Nd(34,5%)	Ni (17,6%)	Mn(16.2%)

Table 4.2: *Relative composition of different targets. Values have been normalized to the oxygen content of the spectra.*

4.2 Initial considerations

As previously explained in **Chapter 1** and expanded upon in Chapter 3, thin film engineering is a very important part of thin films growth. The unit cell constants of RNMO compounds are summarized in **Table 4.3**. This allows making few pre experimental assumptions. In the previous case of YNMO, lattice constants were considerably bigger than the STO lattice, with an important difference between lattice constants ***a*** and ***b***. Therefore, texturized films could growth with a 45^{O} in-plane shifting. The STO lattice (3,905 Å) suits the YNMO-a/√2 = 3.692 Å, YNMO-b/√2 = 4.007 Å. This film configuration has been observed before in the literature in the same compound [**4**,**5**] and in a close relative $YMnO_3$ (YMO)[**6**,**7**].

Nevertheless, it is clear that the 45^{O} orientation responds to the highly asymmetry between ***a*** and ***b*** lattice, which ratio, for YNMO, is about *b/a*= 94.03%. In the case only one of the sides of the unit cells fits the geometric restrictions of the STO unit cell. However, such ratios, for RNMO (Sm. Nd & Pr)**[3]**, are $b/a_{(SNMO)}$=97,1%, $b/a_{(NNMO)}$=98,72% and $b/a_{(PNMO)}$=99,54% showing a progressive approximation to a pseudo tetragonal unit cell of the compounds. In principle, it can be expected that SNMO could have a similar behavior as YNMO, with two in-plane domains shifted

45^{O}, in response to the equally geometrical favorable coupling of the ***b*** axis along the two diagonals of STO. On the other hand, NNMO and PNMO ratios, suggest that a single in-plane orientation, with a similar 45^{O} shifting, could take place due to the similarity of the ***a*** and ***b*** lattices. Taking these observations into consideration, this chapter will be devoted to the single phase stabilization of RNMO thin films on STO(001) substrates.

LATICCE CONSTANTS

Lattice Constant	SNMO	NNMO	PNMO	STO
a(Å)	5,3524	5,4145	5,4453	3,905
b(Å)	5,5119	5,4842	5,4701	3,905
c(Å)	7,6103	7,6742	7,6966	3,905
$\alpha(^{O})$	90	90	90	90
$\beta(^{O})$	90,03	90,0011	90,03	90
$\gamma(^{O})$	90	90	90	90
$V(Å^3)$	224,522	227,883	229,257	59,547

Table 4.3: *Lattice constants of SNMO, NMN, PNMO & STO.*

4.3 Thin Films of $Sm(Ni_{0.5}Mn_{0.5})O_3$

4.3.1 Temperature dependency

In order to explore the influence of deposition temperature on crystalline and morphological properties of SNMO films, an arbitrary, but similar to the working range obtained in this thesis for YNMO in the previous chapter, set parameters were chosen. First, the following parameters were selected: a repetition rate of 2 Hz, an oxygen pressure of 0.6 mbar and a fluency of 2 J/cm^2. The temperature was swept from 650 to $800^{O}C$.

Samples obtained after 7000 pulses were characterized by means of XRD, shown in **Figure 4.1.** The 2θ-ω plots show the typical highly intense STO(00*l*) family of peaks, at $\approx 22^{O}$, $\approx 46^{O}$ and $\approx 72^{O}$. For most of the samples, each set of substrate peaks is followed closely by a smaller peak, at $\approx 23^{O}$, $\approx 48^{O}$, $\approx 76^{O}$ respectively, similar to the tendency observed in YNMO. These peaks are attributed to the SNMO(00*l*) family, specifically the peaks (002), (004) and (006) of the monoclinic unit cell. Again, the correlation of STO(00*l*) reflections with a double SNMO(00*(2*l)*) index is observed.

Moreover, a secondary set of peaks is clearly observed at ≈33^{O}, ≈50^{O} and ≈68^{O}, these peaks increment their relative intensity as deposition temperature rises and are identified as the SNMO(0*k*0) family

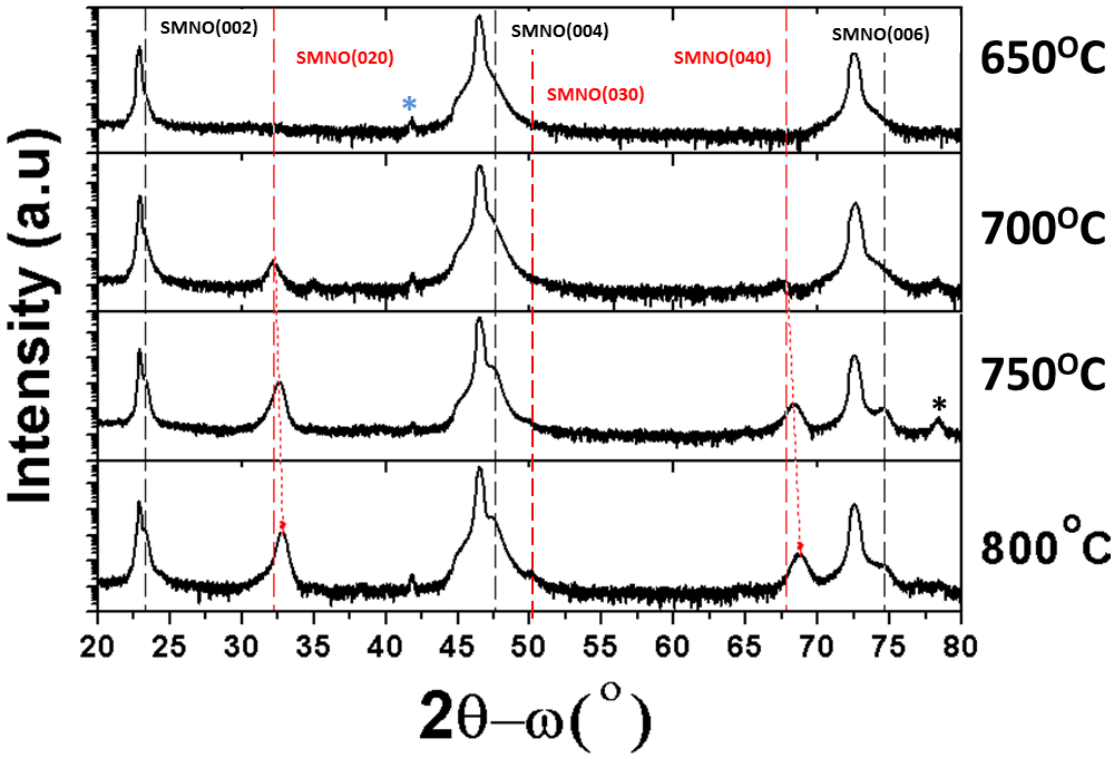

Figure 4.1: *2θ-ω scans of SNMO films deposited on STO(001) at different temperatures. Lines show the expected bulk position of the (00l) peak on the images, * shows the Cu – Kβ and * secondary orientations, while red lines show the position of the (0k0) family.*

It can be observed a clear contrast between films deposited at 650^{O}C and the one deposited at 800^{O}C. Initially we will focus on the SNMO(00*l*) family. In the sample deposited at lower temperature, little can be observed a part from STO(00*l*) peaks, this indicates a poorly crystalline ordering of the film, since all samples where growth in similar conditions (pulses). However, the increment of temperature seems to clarify the appearance of such peaks, which progressively are more visible and intense. On the other hand, the SNMO(0*k*0) family shows sudden apparition at 700^{O}C followed by a rapid increment of intensity. Moreover, a secondary effect is also observed in this family, a shift on peaks position, this behavior is pointed by the red lines in the **Figure 4.1** and contrast with the unchanged place of the SNMO(00*l*) peaks.

In order to investigate the crystalline quality of both families of reflections, similar methods used in the previous chapter are used. First the FWHM is extracted in similar way as described in **Chapter 3** of this thesis. Secondly, relative intensity, as described in the previous chapter, extracted from the RNMO(002) reflection will be plotted and finally the evolution of their respective out of plane parameter, as described in **Appendix 2**, will be addressed.

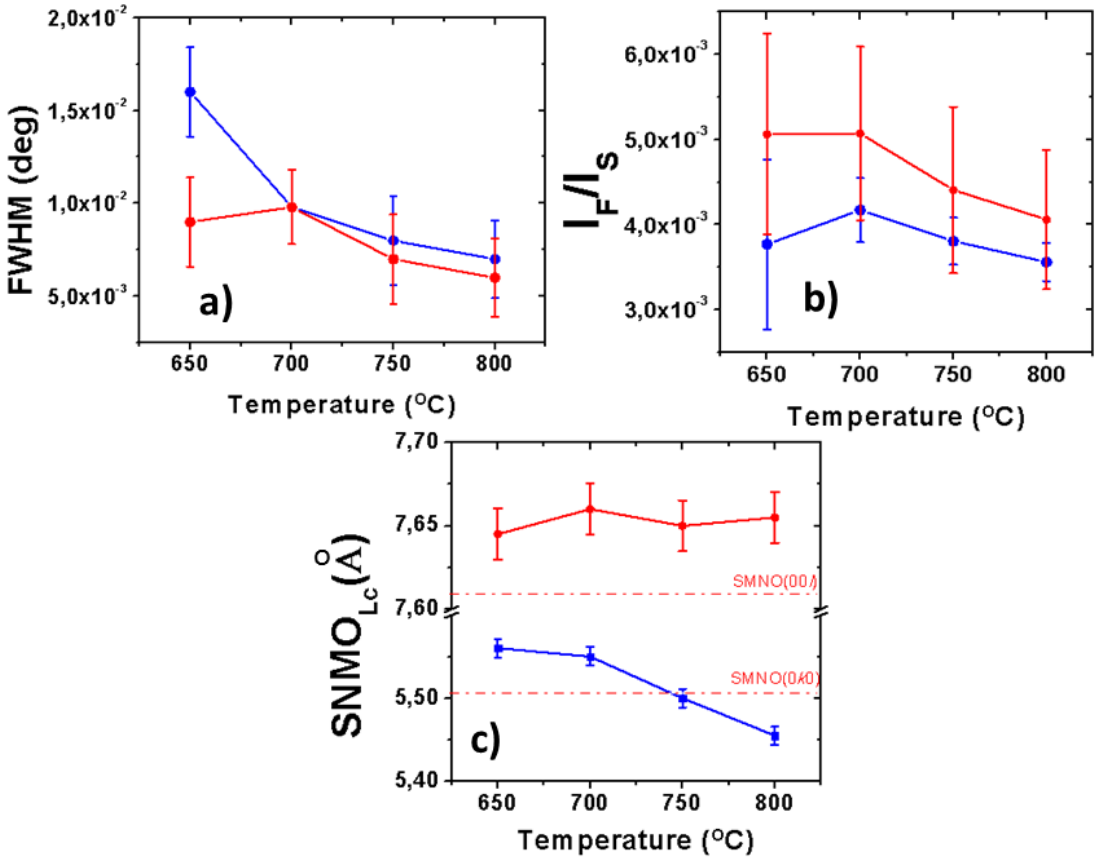

Figure 4.2: *Temperature dependency of a) FWHM, b) relative intensity extracted from RNMO(004)/STO(002) c) out of plane parameter on substrate temperature during deposition.* ●*(0k0)* & ●*(00l)*

Rocking curves obtained from the 650 to 800^{O}C range, **Figure 4.2**, show the monotonically increment of crystallinity for both (00*l*) & (0*k*0) orientations reflected in the decreases of the extracted values, at the same time, relative intensity shows a rather inconclusive behavior due to the large error. On the other hand the extracted out of plane parameter of SNMO(0*k*0) shows a progressive reduction from 5,57Å to 5,45 Å, while the SNMO(00l) family shows little movement, from 7,64 Å to 7,65 Å. It is important to notice the significant reduction of the $SNMO_C$ parameter from the bulk

position, suck an elongation of around 1% of the unit cell is sustained along the whole range of temperatures used.

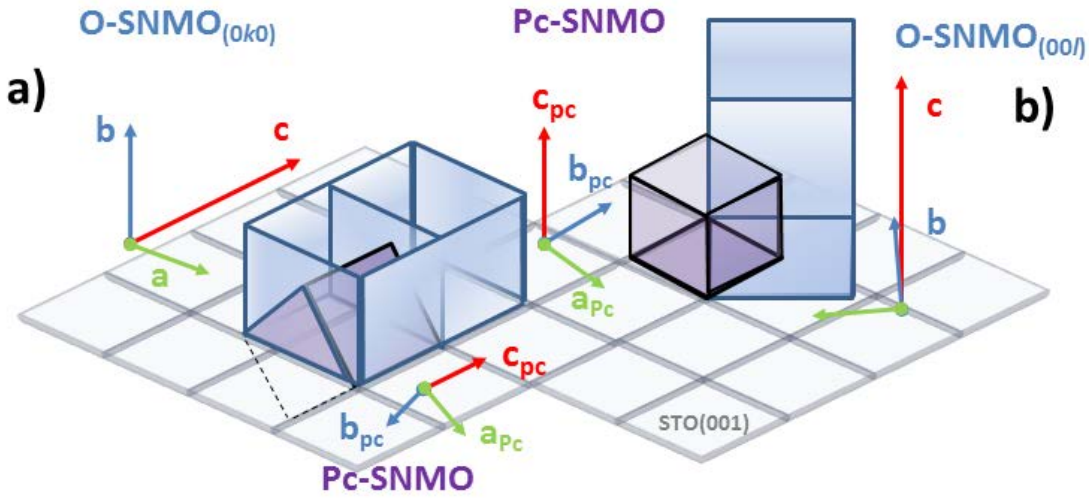

Figure 4.3: *Diagrams of O-SNMO unit cell conversions to Pc-SNMO unit cell showing both growth out of plane crystalline domains observed in XRD diffractograms, a) shows the SNMO(0k0) family and b) the SNMO(00l).*

As a result of this analysis it is clear that a single out of plane domain is not easily achievable in the temperature range studied. It is clear however that the SNMO lattice has two axes, that are remarkably similar to each other in the pseudocubic configuration. Pseudocubic constants for SNMO are: SNMO-a/√2 = 3.78 Å, SNMO-b/√2 = 3,897 Å and SNMO-c/2=3,805 Å. It can be observed that Pc-SNMO*a* and Pc-SNMO*c* have similar values close to 3.80 Å, this leads to assume that both axes could, in principle permutated along the surface purely based on geometrical similarity, although a priory the Pc-SNMOb lattice is the one who closely resembles the STO lattice constant.

Using the information available until now, the **Figure 4.3** can illustrate the results based on lattice constant information. A priori, the SNMO(0k0) family of planes can be placed as SNMO(001)||STO(010) or STO(100), this is, however indication of possibly multiplicity of in-plane domain for this family. Since SNMO-*a* lattice is significantly smaller than SNMO-b and far from the STO lattice value. It is sensible to assume that mismatch between SNMO-a and STO lattice is compensated by multiple unit cells along the SNMO(100) direction, giving chance for two in-plane domains shifted 90^{O} from each other.

In order to back up this assumption φ-scans were performed, aiming to extract in-plane detailed information from both SNMO(0*k*0) and SNMO(00*l*) families.

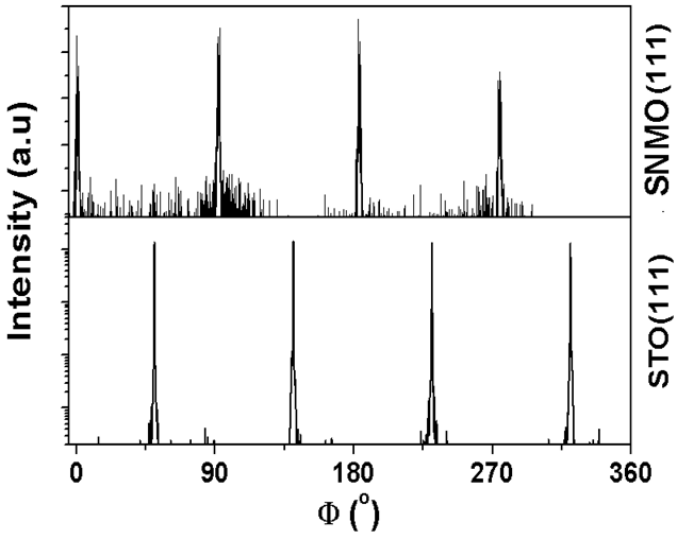

Figure 4.4 *Thin films φ-scans around the STO(111) direction, compared with SNMO(111) showing the clear 45^{O} in plane shifting of the unit cells.*

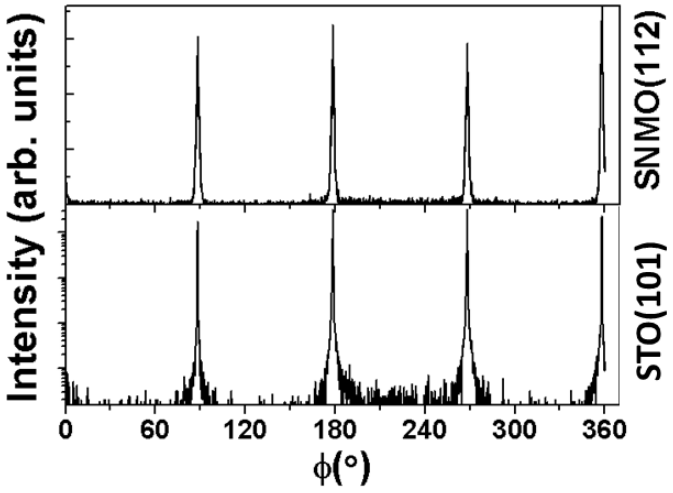

Figure 4.5 *Thin films φ-scans around the STO(101) direction, compared with SNMO(112). Notice that no evidence of peak splitting is found in the diffractograms.*

4.3.2 Epitaxial relationship SNMO/STO(001)

Although single crystalline domain stabilization was not achieved, in this section the in-plane texture of the SNMO(001)/STO(001) family is to be addressed. As a guidance, the previous results from YNMO(001) are taken into account since both

bulk structures are similar and the previous investigations successfully addressed the epitaxial relationship of the system.

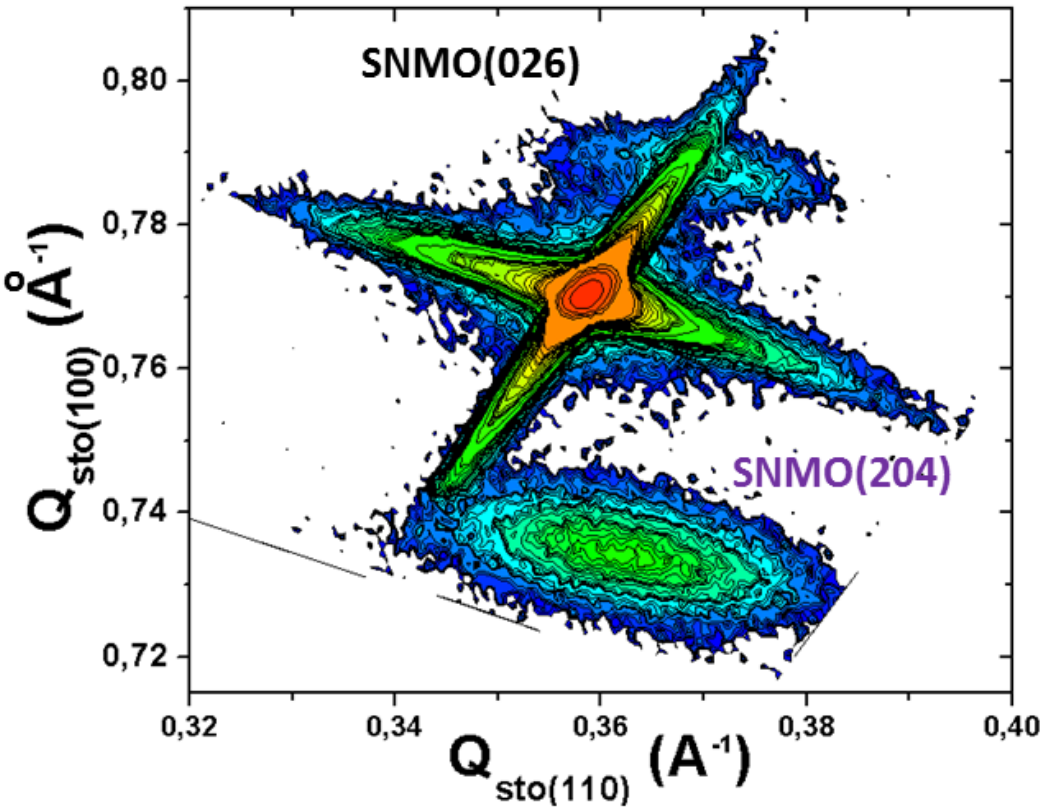

Figure 4.6 *Reciprocal space map image taken along the STO(113) direction, both in-plane domains are visible in the graph. Lower peak is attributed to the SNMO(0k0) & upper one to the SNMO(00l).*

In plane measurements, φ-scans, were performed along the STO(111) direction and SNMO(111) on samples deposited at 750^{O}C for the sake of comparison with YNMO data, diffractograms are shown in **Figure 4.4**. The plot obtained from SNMO(111) shows a set of peaks separated from each other by 90^{O}. Diffractograms were displaced to 0^{O}, 90^{O}, 190^{O} and 270^{O} for simplicity. These set of peaks, accordingly corrected, are clearly shifted 45^{O} from the substrate STO(111) peaks. This is fully compatible with the previous assumption, showing that in principle the epitaxial relationship is [010]SNMO(001)||[011]STO(001). However, as in the previous case of YNMO, it is convenient to perform similar scans along the STO(101) direction, in order to determine the possible existence of multiple in-plane domains for the SNMO(00l) family, due to the non-tetragonal nature of the unit cell, that as in the case YNMO, could promote the apparition of two in-plane domains.

Accordingly, φ-scans were performed around STO(101) as shown in Figure 4.5, both STO and SNMO show a set of four peaks, separated by 90^{O} from each other, however, in this case both family of reflections are collinear and more importantly, there is no evidence of any peak splitting or secondary phases, showing that in fact the SNMO(00l) family has a single in-plane domain with an epitaxial relationship of [010]SNMO(001)||[011]TO(001).

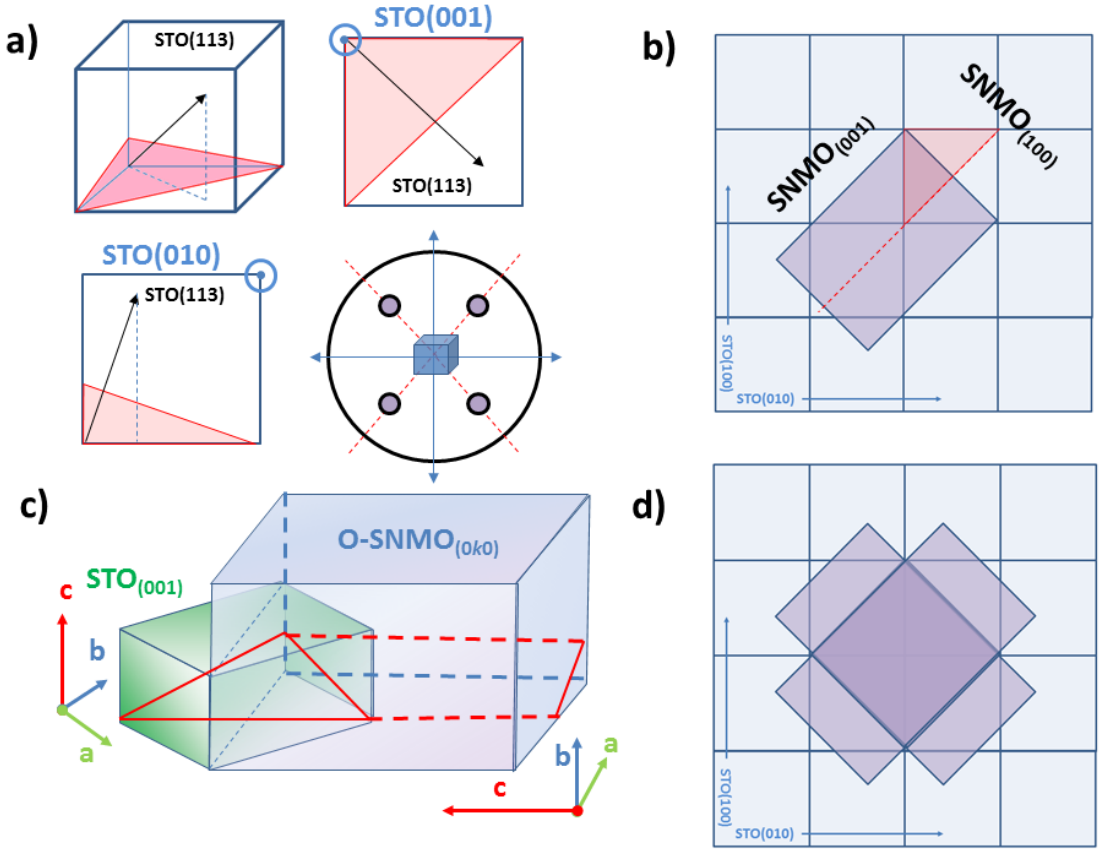

Figure 4.7 *Diagrams explaining the **a)** STO(113) reflection in the STO unit cell & sketch of pole figure, **b)** top view of SNMO(0k0) unit cell respect the STO(113) reflection. **c)** schematic representation of STO unit cell in relationship to the O-SNMO unit cell and **d)** four fold symmetry of the SNMO(0k0) family.*

In order to examine the in-plane lattice constant of the SNMO(00*l*) family, reciprocal space maps have been made in order. In this case, both families would be visible, however, since SNMO(00*l*) crystals, have a pseudo tetragonal configuration, their appearance can be expected as one single peak on the upper part of the reciprocal map along the STO(113). Measurements are shown in Figure 4.6 where as expected, the upper part of the plot, closely resembles the one observed on YNMO and can be indexed as SNMO(026), however, in this case only a single peak is visible, which

represents the single in-plane domain structure of the SNMO(00*l*) family, the shape and position of the peak shows an elongated shape with a center on the right hand of the plot. This suggests a progressive relaxation of the in-plane parameters of the SNMO lattice since no peak splitting was observed in any of the φ-scans previously performed.

A second peak is observed in the lower part of the plot, it shows a large area and egg like distribution, the fact that it is so far below the STO(113) peak suggests that in is related to the SNMO(0*k*0) population. The position of the peak, shows a partially stressed in plane parameter and, as in the upper peak, a progressive relaxation. The indexation of this peak is interesting, since it allows to determine the intrinsic ordering of this population.

LATICCE CONSTANTS

	a(Å)	b(Å)	c(Å)	vol.(Å^3)	ε[100]$_a$	ε[010]$_a$	ε[001]$_a$	*f*[100]$_b$	*f*[010]$_b$	*f*[001]$_b$
SNMO$_{BULK}$	5,35	5,51	7,61	224,52	-	-	-	3,22%	0,22%	-
SNMO$_{STO(001)}$	5,41	5,41	7,645	223,7	1,12%	-1,81%	0,46%	2,08%	2,08%	-
SNMO$_{STO(010)}$	5,32	5,51	7,64[c]	224.52	-1,66%	1,85%	-	3,08%[d]	-	-

Table 4.4 *Lattice constants of SNMO bulk, SNMO(001) & RNMO(010) and their respective mismatch and strain. a), b) values are calculated using Equation 3.7 and 3.6. c) values are calculated by volume conservation and d) value is calculated along the STO(011) and SNMO(100).*

There is one possible candidate for the lower peak, the crystalline direction SNMO(024), in this ordering several geometric considerations are to be taken into account. **Figure 4.7** shows a comprehensive list of consideration for understanding this reflection. The reflection STO(113) is a lower reflection from the STO(111) family, It contains information from the diagonal of the STO lattice. **Figure 4,7 a),** illustrates the relationship between the STO unit cell and the STO(113) reflection. It is important to notice that this reflection, as for the STO(111) shows a 4 fold symmetry therefore four(4) peaks are observed in the typical φ –scans plots. In the case of SNMO(024), the configuration that would allow the O-SNMO(024) to be in the same plane as STO(113) is depicted in **Figure 4.7 b)**, in this case, the lattice of SNMO follows the diagonal of STO as shown on image. In that case, the STO(113) is similar to the SNMO(024) as shown on the **Figure 4.7 c)**. It is important to remark that in this

ordering, only 2 reflections per unit cell will be observed in the typical φ–scans and pole figures, however, because of the SNMO sits on the STO diagonals, four fold symmetry can be observed as shown in **Figure 4.7 d)**, notice that in this case, both the in-plain domains are aligned with the STO(111) plane, making them virtually identical in the φ–scans performed.

To this point, epitaxial relationship of both families of planes is clearly determined, the SNMO(00l) family follows the [100]SNMO(001) ‖ [011]SNMO(001), on the other hand the SNMO(0k0) shows a epitaxial relationship that follows [100]SNMO(010) ‖ [011]SNMO(001). Finally, the lattice constants for both of the populations is extracted, results of both strain and deformations are shown in **Table 4.4**.

It can be observed that lattice constants for SNMO(001) are constricted to an intermediate value of 5,41Å with a lattice deformation that shows an expansion and reduction of SNMO *a* and *b* lattice respectively, lattice mismatch values show a change respect to bulk, as in the case of axial values, the mismatch *f* moves towards a mean value according to the pseudo tetragonal phase. On the other hand SNMO(010) closely resembles values of bulk material. Interestingly enough, epitaxial strain shows inverted values from the ones observed for the SNMO(001) domain.

4.3.3 Surface Morphology

Samples are now examined by AFM in order to study the effect of temperature on surface morphology. Surface morphology of SNMO samples is shown in **Figure 4.8**. Samples show a granular surface that suggests the presence of 3D growth mechanism as previously observed in YNMO films. Sample deposited at 650^{O}C, **Figure 4,8 a)** shows a heterogeneous surface with grain ranging from 20 nm up to 140 nm, the effect of deposition temperature, can be observed in the sample deposited at 700 ^{O}C, **Figure 4,8, b)** where a somehow similar hetereogenous and granular structure can be observed, however in this case the grains are better defined and grain size distribution is reduced, ranging from 20 nm up to 90 nm, with sporadic 140 nm grains. The biggest contrast appears between 700 ^{O}C and 750^{O}C, shown in **Figure, 4.8 c)**, where particles are better defined and surface exhibit a more homogenous distribution and the particle size is close to 35 nm.

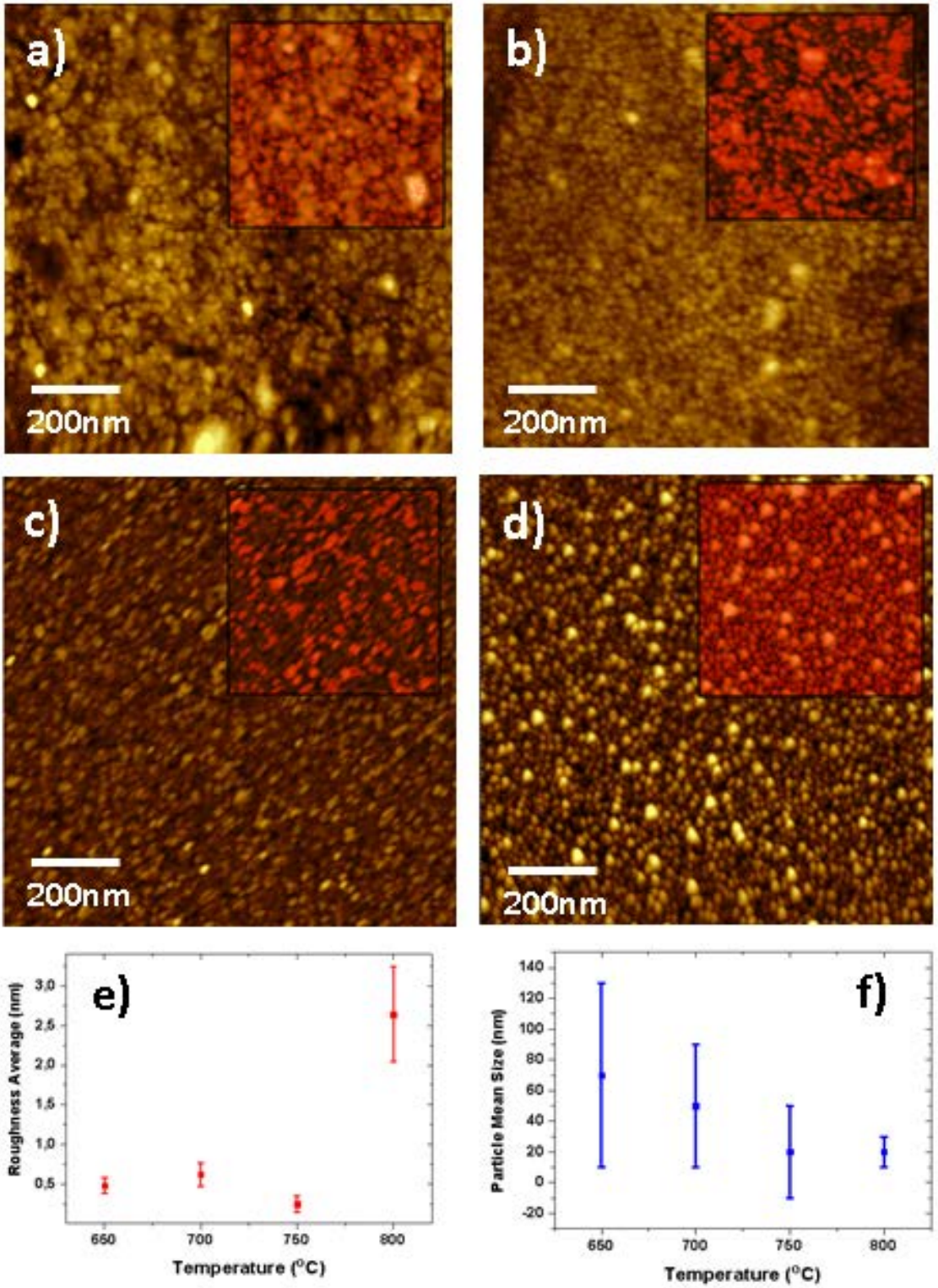

Figure 4.8 *AFM micrograph and roughness analysis for SNMO deposited at various temperatures a) 650°C, b) 700°C, c) 750°C & d) 800°C. (Insets represent the flood mask used for grain size distribution). e) shows extracted roughness and f) shows mean particle size*

Finally, sample grown at 800^{O}C, **Figure 4.8 d),** show a highly homogenous and granular surface with particle size distribution around 20 nm. The influence of deposition temperature in surface morphology of SNMO films can be easily appreciated now by comparing information extracted from each of the micrographs. Insets in **Figure 4.8 a-d)**, show the mask used to determine particle size distribution for each sample. In this approach a flood mask is used to calculate areas and contour of grains, extracted plots from such procedures are shown in **Figure 4,8 e)** while roughness data, extracted using similar procedures as the ones described in **Chapter 3, section 3.2.6**, are shown in **Figure 4.8 f).**

The effect of deposition temperature can be clearly observed in the extracted values of roughness and particle size. Sample roughness, **Figure 4.8 e)**, remains below 1 nm in the range of 650^{O}C to 750^{O}C at this point it increases to 3 nm. This contrasts, however with the mean particle size distribution from figure **Figure 4.8 f)**, where particle size distribution narrows down with the increment of temperature. It can be argued that bigger particle size is in fact the main reason for low roughness of the films, and temperature promotes smaller grains and therefore higher roughness. This analysis can also be extended to relate results shown in **Figure 4.2**, where high temperature accounts for more intense and well defined peaks.

It can be concluded from this section that high temperature of deposition increases roughness by decreasing grain size, however it also promotes high intensity peaks and therefore better crystallinity of both SNMO(0k0) and SNMO(00l) domains.

4.4 Thin Films of $Pr(Ni_{0.5}Mn_{0.5})O_3$

4.4.1 Temperature dependency

In order to explore the influence of deposition temperature on crystalline and morphological properties of PNMO films, an arbitrary, but similar to the working range obtained in this thesis for YNMO & SNMO in the previous chapters, set parameters were selected. First, the following parameters were choosen: a repetition rate of 2 Hz, an oxygen pressure of 0.6 mbar and a fluency of 2 J/cm^2. The temperature was swept from 650 to 800^{O}C.

Samples obtained after 7000 pulses were characterized by means of XRD, shown in **Figure 4.9**. Diffractograms close resemble spectra from YNMO and SNMO, with a set of peaks corresponding to the PNMO at 24^{O}, 48^{O} and 78^{O}, very close to the

STO(00*l*) family. Peaks correspond to the PNMO(00*l*) family and are visible in the whole range of temperature. Low temperatures, 650^{O}C and 700^{O}C show secondary reflections around 38^{O} and 64^{O}. The reflection found at 38^{O} has a clear splitting that correspond to the PNMO(121) and PNMO(211) peaks, the presence of this reflections clearly shows that the film in that range of temperatures has a strong resemblance to the bulk structure, a monoclinic $P2_1/n$.[**2**,**8**].

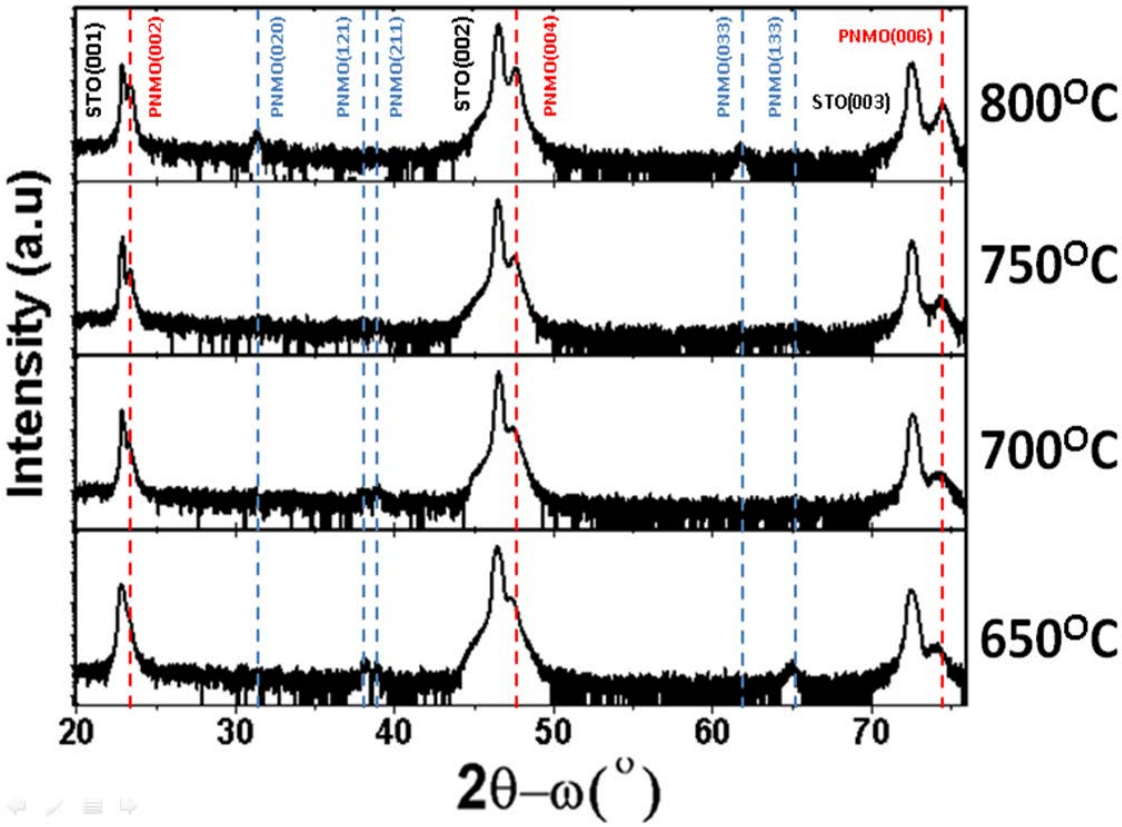

Figure 4.9: *2θ-ω scans of PNMO films deposited on STO(001) at different temperatures. Red dashed lines show the expected bulk position of the PNMO(00l) peak on the images, , while blue dashed lines show the position of the secondary phases.*

Sample deposited at 800^{O}C does not show this feature, however it shows the apparition of the PNMO(020) and PNMO(033) peaks, although the (0k0) peak was observed previously in the SNMO samples, in PNMO only the (020) is visible, no higher order reflections are observed, suggesting very small population of this orientation, moreover peaks of reflection PNMO(033) are also observed, the PNMO(011) peak, in principle more intense, should be found at 23,04^{O}, angle that

falls between the STO(001) and PNMO(002) making it impossible to observe, due to its intensity, that should be two times more than the one observed for PNMO(033), but 60% less than PNMO(002). On the other hand, samples grown at 750^{O}C show a single out of plane PNMO(00*l*) orientation with no visible apparition of secondary phases.

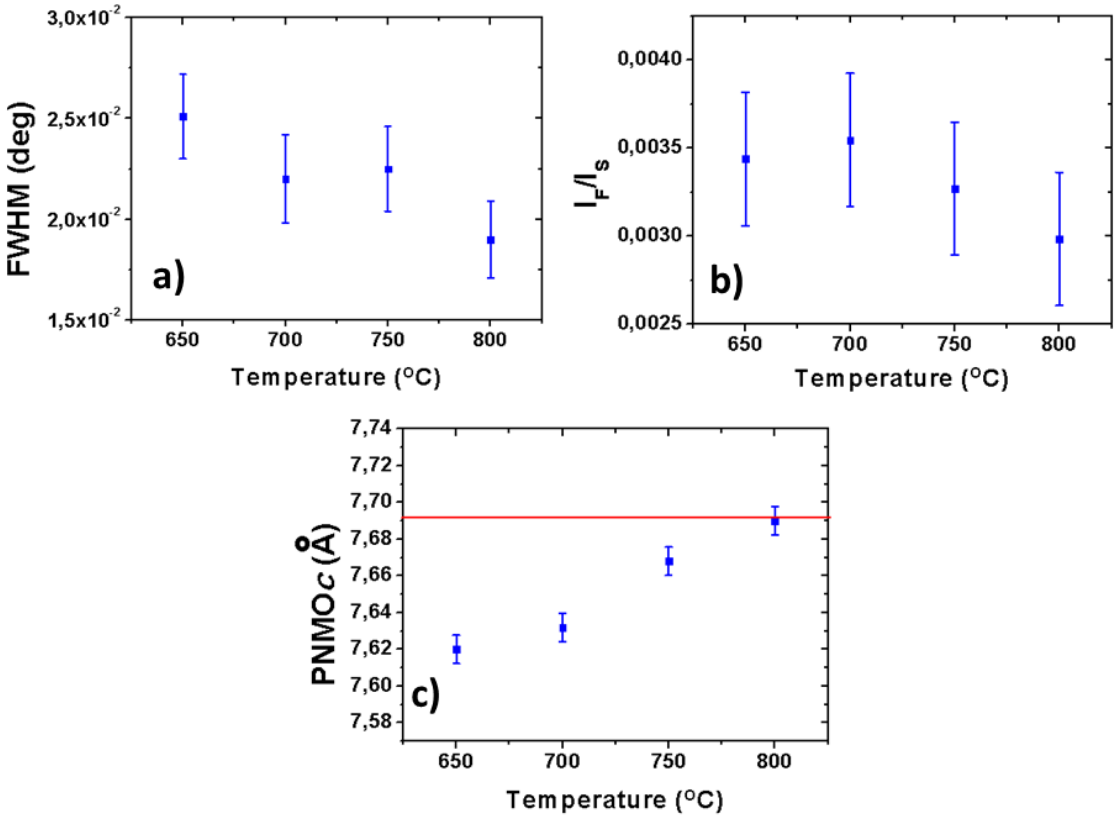

Figure 4.10: *Temperature dependency of a) FWHM, b) relative intensity extracted from PNMO(004)/STO(002) and c) out of plane parameter on substrate temperature during deposition. Red line shows bulk value.*

The effect of temperature on the crystalline ordering of the films is clear from the 2θ-ω scans in **Figure 4.9**. Temperatures below 750^{O}C, have a certain degree of ordering with intense PNMO(00*l*) peaks, but secondary phases that resemble the monoclinic space group. On the other hand, temperatures above 750^{O}C show the most intense PNMO(00l) peaks, but secondary phases are also visible. Crystalline analysis shown in **Figure 4.10**, clearly shows the monotonically increment in film quality and intensity with temperature up to 700^{o}C and then a slight detriments up to 800^{o}C. However, these analyses contrast with the sample grown at 750^{O}C, being the only one who shows a single out of plane domain.

Out of plane constant dependency on deposition temperature is shown in Figure 4.10. A progressive movement towards the bulk values is observed, being sample grown at 800^{O}C the one who shows a value closely to it. However, in this case, the sample that is chosen for further studies in this work is the one deposited at 750^{O}C because its crystalline texture only contains the PNMO(00*l*) peaks.

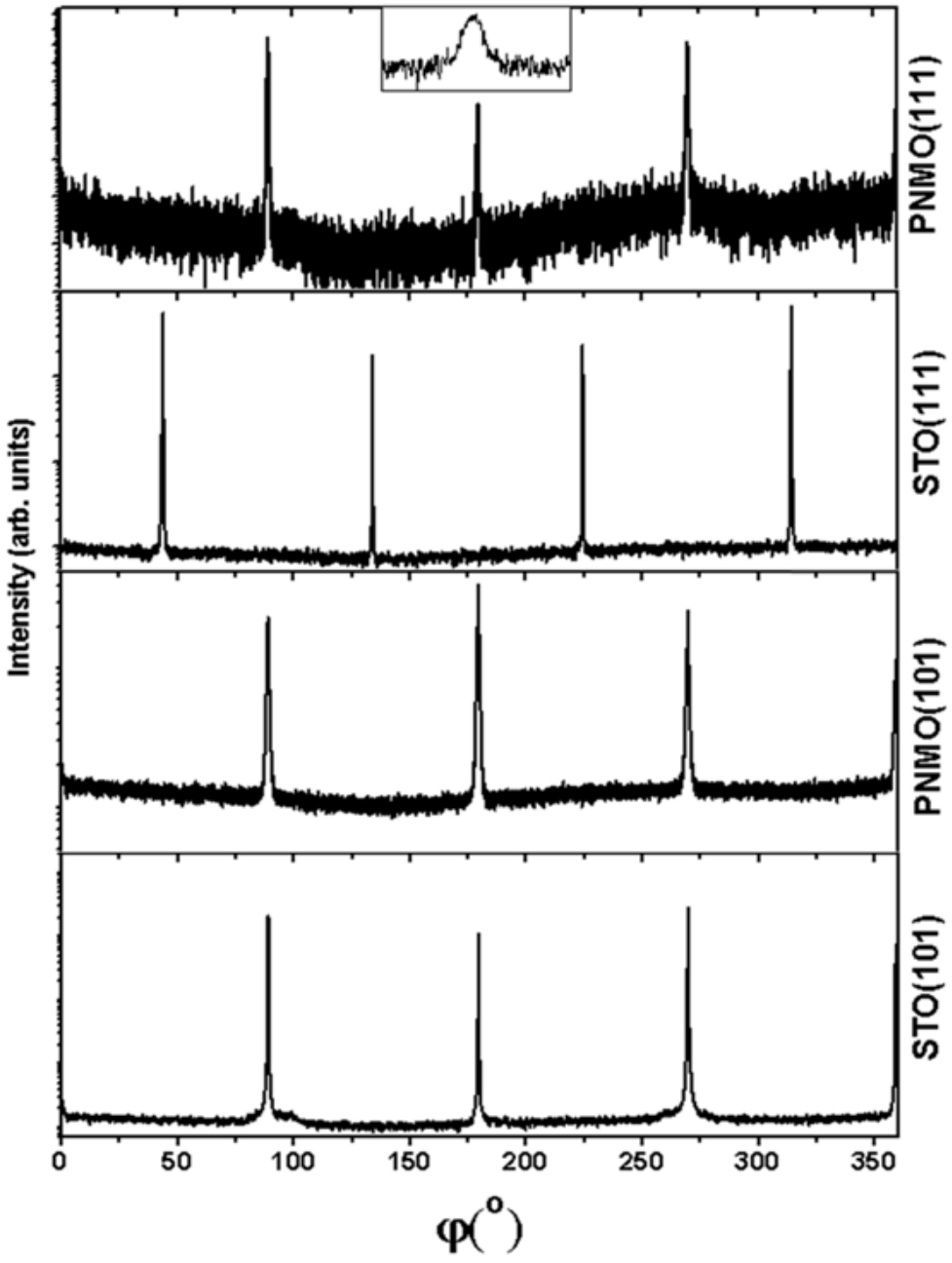

Figure 4.11: *Thin films φ-scans PNMO around the STO(111) & STO(101) direction and the corresponding PNMO(111) & PNMO(101). Inset shows the single component of the peak.*

4.4.2 Epitaxial relationship PNMO/STO(001)

Having successfully stabilized the single phase PNMO thin film, efforts are focused on the determination of its epitaxial relation. As in previous sections of this work, detail φ–scans were performed along the PNMO(111) and STO(111), complemented by PNMO(101) and STO(101) scans shown in **Figure 4.11**. PNMO shows a 4 fold symmetry, characterized by 4 peaks separated by 90^{O}, in this case, peaks are shifted 45^{O} from the substrate, as mentioned before this shows that the pseudo orthorhombic unit cell grows preferably along the diagonal of STO, direction (011) and suggest that the unit cell is fully adapted to the cubic STO lattice.

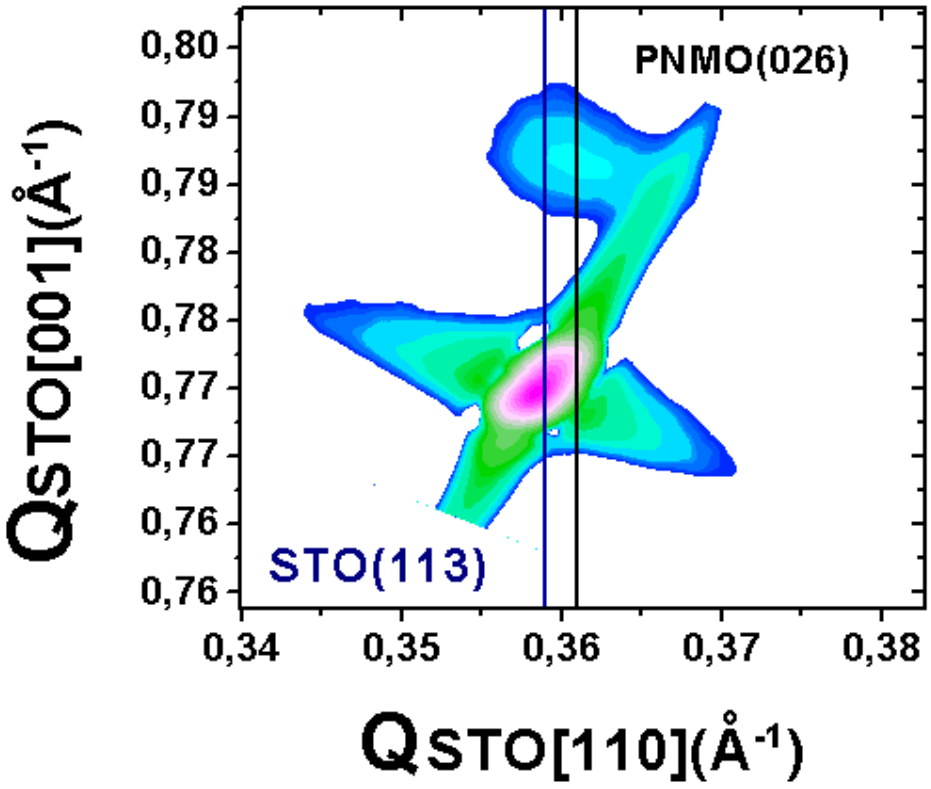

Figure 4.12 *Reciprocal space map image taken along the STO(113) direction, A single peak corresponding to PNMO(026) is visible. Lines are a guide to the eye.*

Reciprocal space maps are now performed along the STO(113) direction in order to extract the in-plane lattice of the PNMO. **Figure 4.12** shows the reciprocal space map of the sample grown at 750^{O}C, the only one without secondary crystalline domains. The Reciprocal Space Map (RSM) plot shows a partially strained peak corresponding to the PNMO(026) reflection. The partial strain can be observed by the close proximity of the films peak with the substrate reflection STO(113). The shape of

the film`s peak, contrast with the one observed in SNMO, showing a rather narrow distribution of lattices in the film and it suggests that the strained unit cell is sustained longer along the growth direction of the film. The in-plane parameter of the PNMO film can be extracted from the plot as 5.49 Å, in this case, compared with the lattice constants of PNMO bulk, **Table 4.5** the film has elongated both in-plane parameters in order to fit to the cubic STO lattice and shows a tetragonal like unit cell, while a slightly reduction on the ***c*** lattice constant can be observed, needed to conserve the lattice volume.

The epitaxial relationship of PNMO(001)/STO(001) films can be fully explain. In this case, the film has a narrow window of temperature, 750^{O}C in which the single phase PNMO(001) orientation can be stable and no traces of other crystalline orders can be observed. According to φ –scans and reciprocal space maps, the unit cell of the PNMO has grown fully adapted to the STO cubic lattice and shows a partially strained in plane parameter. Taking all this into consideration, the epitaxial relationship is determined as follows [100]PNMO(001)/[011]STO(001).

LATICCE CONSTANTS

	a(Å)	b(Å)	c(Å)	vol.(Å^3)	ε[100]$_a$	ε[010]$_a$	ε[001]$_a$	*f*[100]$_b$	*f*[010]$_b$	*f*[001]$_b$
PNMO$_{BULK}$	5,44	5,47	7,69	229,2	-	-	-	1,52%	0,96%	
PNMO$_{STO(001)}$	5,49	5,49	7,645	230,4	0,92%	0,37%	-0,59%	0,59%	0,59%	

Table 4.5 *Lattice constants of PNMO bulk & PNMO(001) and their respective mismatch and strain. a), b) values are calculated using Equations 3.6 and 3.7*

4.4.3 Surface Morphology

Samples are now examined by AFM in order to study the effect of temperature on surface morphology. In this case, films show different orientations and therefore some extra variables can affect the films apart from the direct effects of temperature on their morphological properties. Images are shown in **Figure 4.13**, all samples have a granular structure that clearly shows a change on roughness **Figure 4.13 e)** however, particle size distribution is difficult analyze due to the low roughness and mound like surface morphology, making such a plot unreliable.

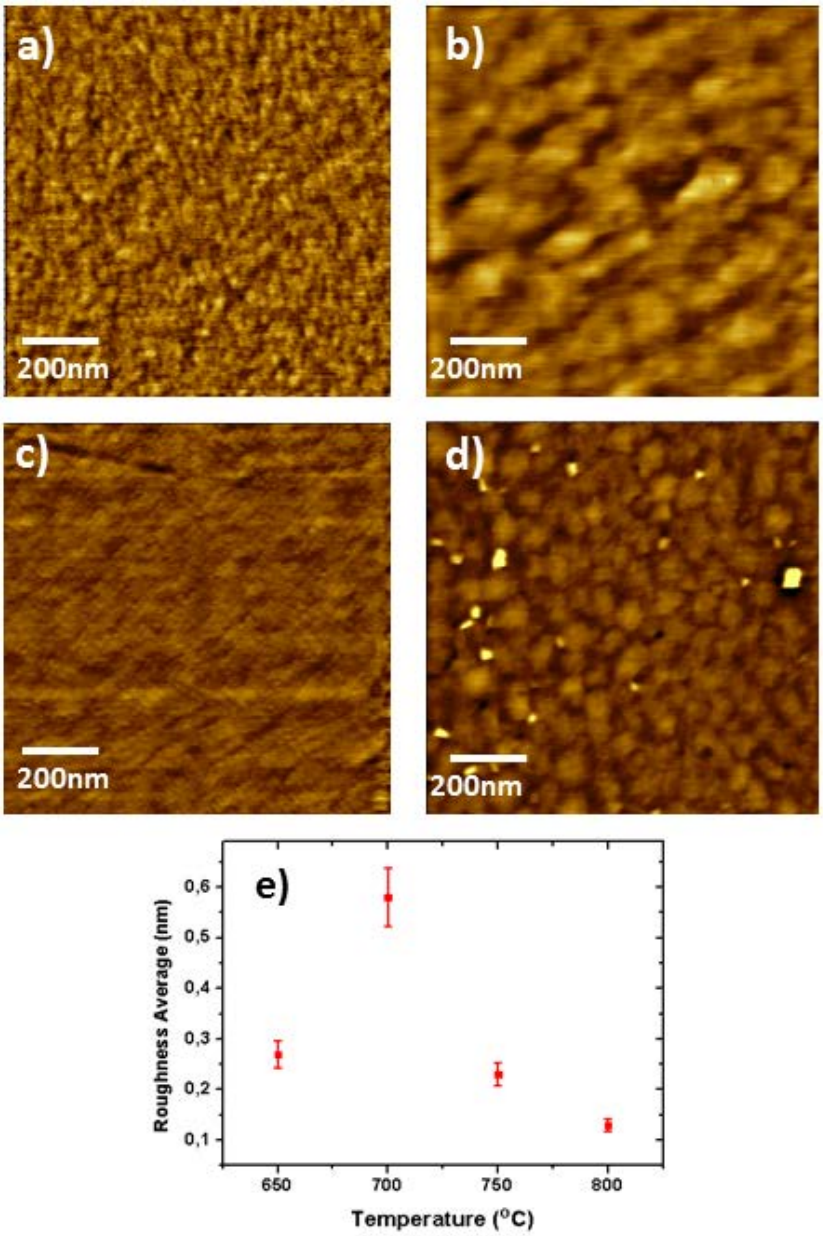

Figure 4.13 *AFM micrograph PNMO deposited at various temperatures a) 650°C, b) 700°C, c) 750°C & d) 800°.*

Extracted roughness is well below the nanometer range in all the samples and very flat surfaces are the norm. As mentioned before, grain size is not easy to extract, however, the surface evolution goes from long mounds structures 650^{O}C to mountain like surfaces 700^{O}C and fish scale-like grains with 120 nm of diameter at 800^{O}C. Nevertheless, the single in-plain domain, growth at 750^{O}C shows vestiges of a previously a periodic structure. **Figure 4.14**, shows the result of two image filtering, based on 2D FFT treatments. The 2D FFT filter allows decomposing images in

periodic contributions, if present in the sample, and separates such contributions from normal noise or roughness, making this analysis suitable in samples who show periodic structures.

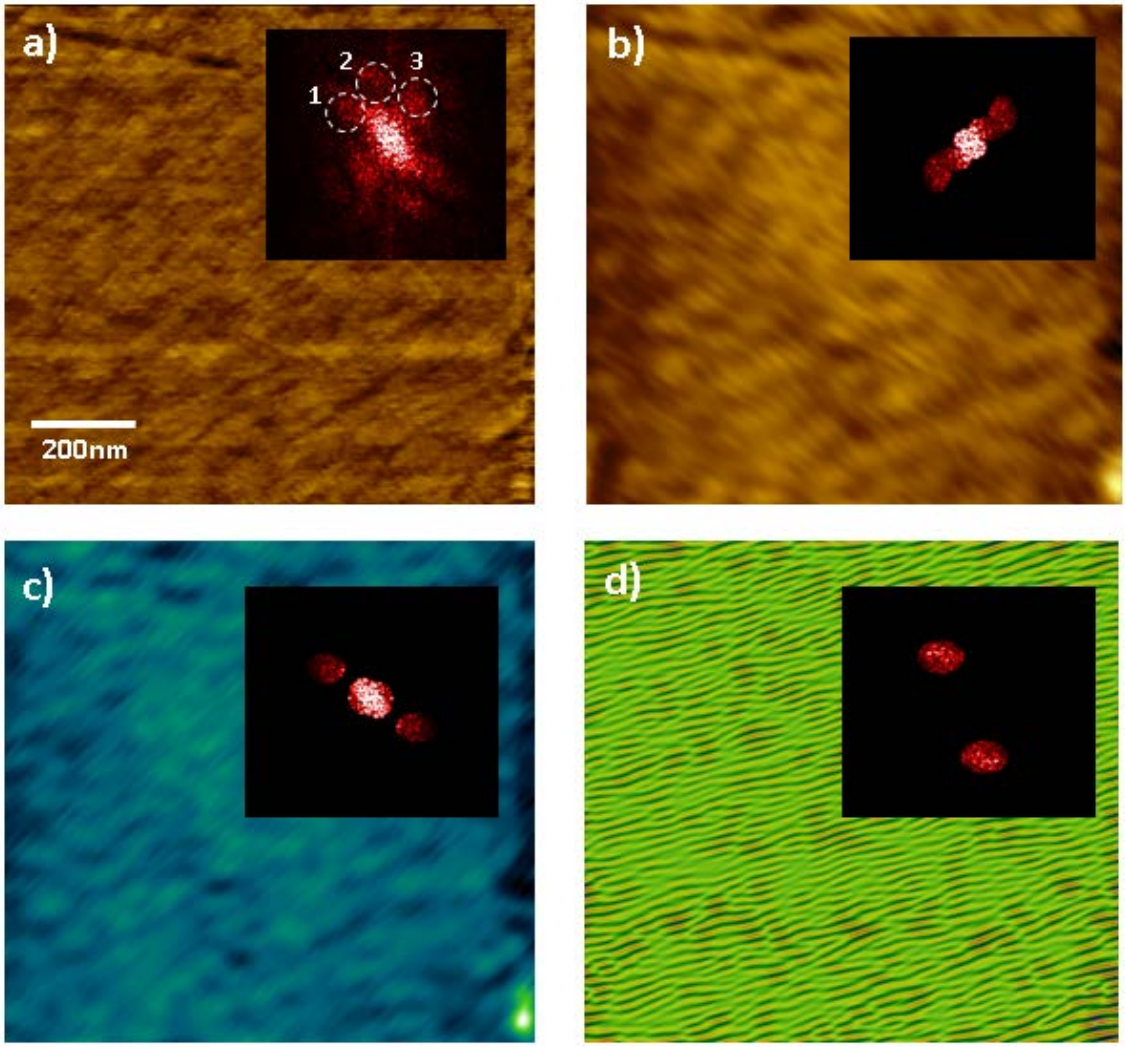

Figure 4.14 *AFM micrographs of PNMO (750^{O}C). Insets correspond to the 2D FFT of the films, a) original film, b) separated from 3 (se insets in a), c) separated from (1) and finally, separated from (2).*

Figure 4.14 a) inset, shows the existence of at least 3 periodic and defined morphological contributions on the sample grown at 750^{O}C, evidenced by the spots on the 2D FFT plot. Contributions 1 and 3 are separated by 87^{O} while 2 is found at almost 45^{O} from 1 and 3. In this case, contribution 1 and 3 are the more intense, although disperse from the whole plot. On the other hand, contribution labeled as 2, is fainted and narrow. Angle accuracy is not to be trusted, since lateral calibration and aspect radio conservation of the AFM used was not calibrated before; nevertheless it can be

used as a guide for the morphology. There is no simple explanation for such pseudo hexagonal 2D FFT observed, however it is presumed that the contributions separated by almost 90^{O} degrees come from the monoclinic crystals, similar to the mounds observed in YNMO(00l), while the one at 45^{O}C can be attributed to the lateral side of the PNMO and STO lattice.

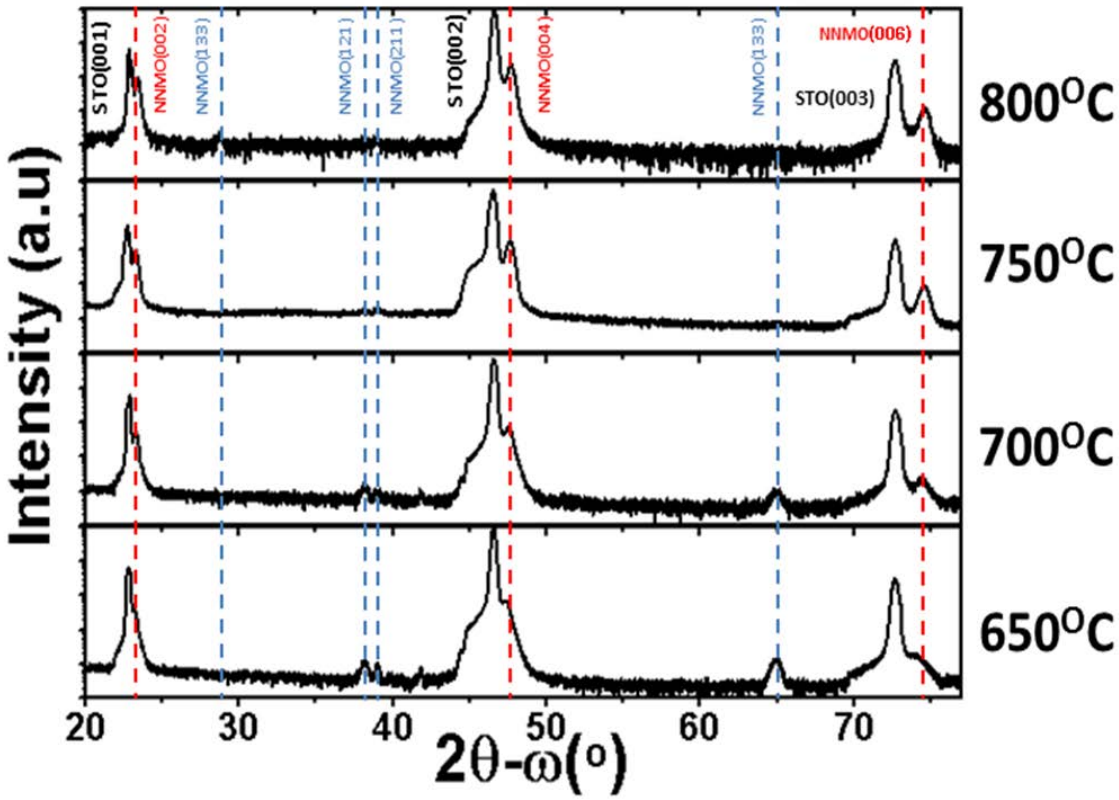

Figure 4.15: *2θ-ω scans of NNMO films deposited on STO(001) at different temperatures. Red dashed lines show the expected bulk position of the NNMO(00l) peak on the images, while blue dashed lines show the position of the secondary phases.*

Even though the origin of such structure is not clear, it shows a highly periodic and ordered surface morphology, that teams up to the low roughness and single fully textured PNMO(00*l*) showing a very high quality of the film.

4.5 Thin Films of $Nd(Ni_{0.5}Mn_{0.5})O_3$

4.5.1 Temperature dependency

The last member of the R(Ni0.5Mn0.5)O3 group to be studied, in this growth section of this chapter, is the NNMO films. As in previously stated, temperature

influence on crystalline and morphology characteristics of NNMO films will be studied. Growth conditions are set as for previous RNMO materials, 2Hz, 0.2 mbar and ≈2 J/cm^2 while temperature is swept between 650 and 800^{O}C, samples are then carefully characterized by 2θ-ω, φ and reciprocal space maps scans.

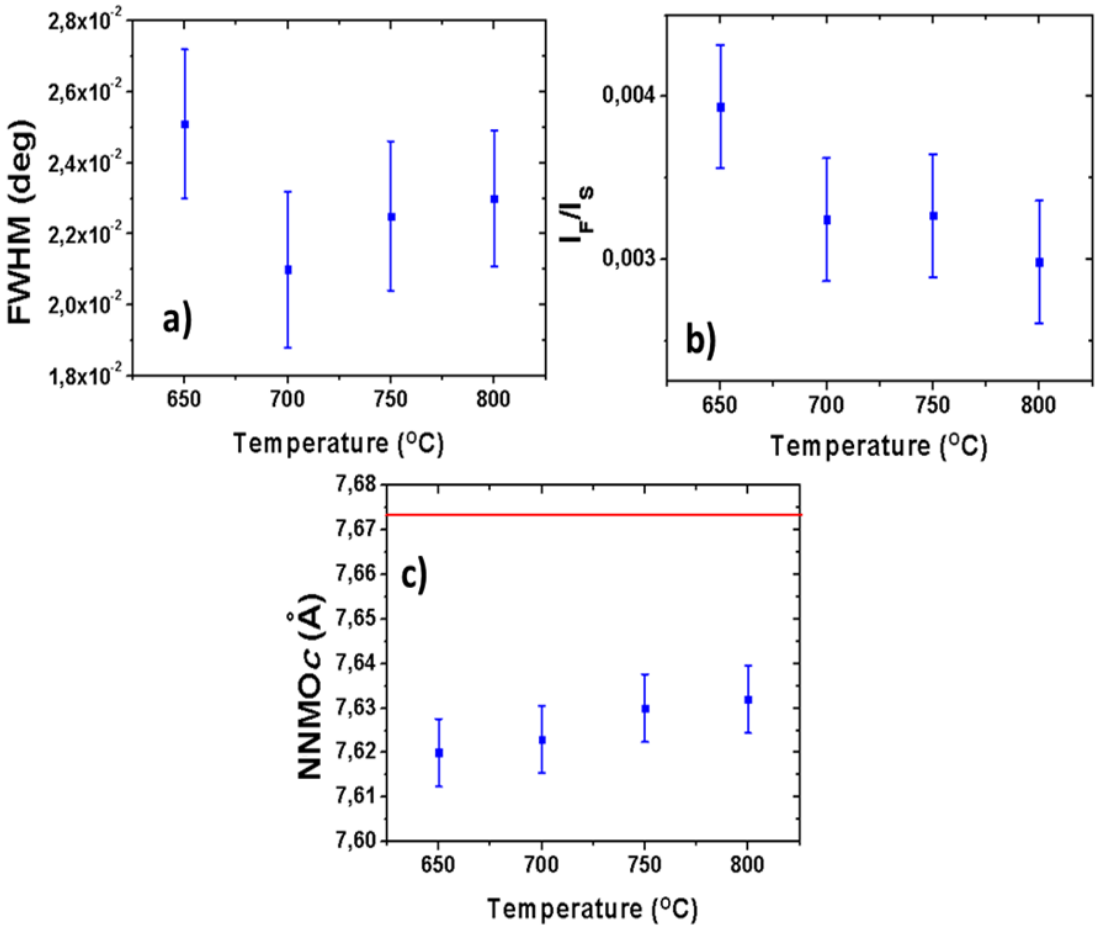

Figure 4.16: *Temperature dependency of a) FWHM, b) relative intensity from NNMO(004)/STO(002) and c) out of plane parameter on substrate temperature during deposition. Red line shows bulk value.*

Results of 2θ-ω are shown in **Figure 4.15**. Films present, as in previous members of this family, almost predominant NNMO(00*l*) orientations observed among the whole range of temperature. Lower temperature samples, 650 and 700^{O}C, show traces of NNMO(033) and NNMO(121)&(211), also observed previously in PNMO. Interestingly enough, 750^{O}C again shows predominant NNMO(00*l*) texture with no, or negligible contributions of secondary orientations, while the sample deposited at 800^{O}C shows multiple small secondary orientations.

Crystalline analyses show, **Figure 4.16,** similar behavior as for previous materials in this chapter, the increment in intensity and crystallinity is monotonically dependent of the temperature, although the apparition of secondary phases also reflects the loss of order in the film. However, an important effect is observed in the out of plane parameter, As in the case of the previous material, PNMO films, an important reduction on the out of plane parameter is observed.

Bulk NNMO, **Table 4.3**, has a ***c*** lattice constant of around 7,67 Å, however as shown in **Figure 4.16 c)**, the out of plane component of the NNMO(00*l*) shows a large reduction, this suggest a large deformation in the in-plane components of the crystal and as a response the out of plane component of the unit cell contracts drastically in order to compensate this response and attempt to sustain volume of the NNMO unit cell. In principle such a large effect can be associate to a highly strained ***a*** and ***b*** lattices, based on NNMO bulk constants, and following the PNMO results, where a 0.5% reduction of the out of plane parameter is observed, the tetragonal lattice should be fully strained and adequately adapted to the STO(011) lattice. In order to investigate these assumptions, φ and reciprocal space maps scans are performed.

4.5.2 Epitaxial relationship NNMO/STO(001)

The in plane ordering of the NNMO(001) films is shown in **Figure 4.17 a)**, φ-scans performed around the NNMO(111) direction show a fourfold symmetry with no visible traces of peak splitting, STO(111) peaks, are shifted 45^{O} respect to the film position, showing in-plane rotation of the NNMO monoclinic crystal with respect to the STO(001) cubic lattice. Complementary plots obtained along the STO(101) and NNMO(101) show a congruent growth with no visible splitting. These results show that in fact the NNMO thin film has a single in-plane domain and a epitaxial relationship that is 45^{O} rotated respect to the STO lattice, similar to the growth observed in PNMO(00*l*), SNMO(00*l*) and YNMO(00*l*) films.

Finally the in-plane lattice constant for NNMO films is extracted from reciprocal space map plots. **Figure 4.17 b)**, shows the RSM image where a single peak of NNMO is visible in the superior part of the plot. The shape of the peak suggests a narrow distribution of values in the film, while its position is congruent with a highly strained lattice. Extracted values are compiled in **Table 4.6**

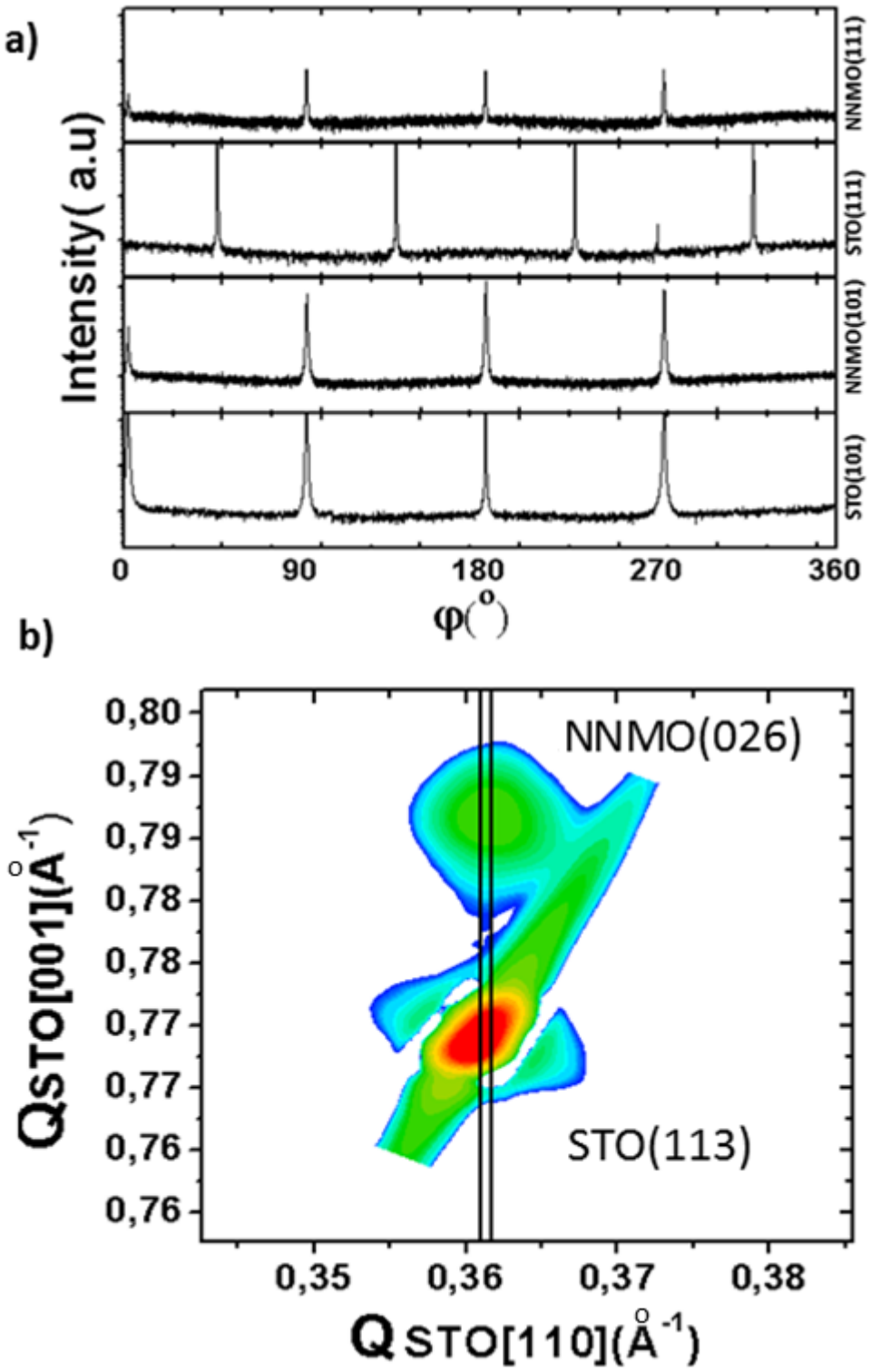

Figure 4.17: *a) Thin films φ-scans NNMO around the STO(111) & STO(101) direction and the corresponding NNMO (111) & NNMO(101). b) Reciprocal space map image taken along the STO(113) direction, A single peak corresponding to PNMO(026) is visible. Lines are a guide to the eye*

In plane lattice constants show an expansion, both ***a*** and ***b*** lattices have elongated in order to adapt to the STO lattice and are equally strain, being lattice ***a***, the one who has elongated the most. To conclude this section, the epitaxial relationship of the samples was found to be **[100]NNMO(001)/[011]STO(001),** It is worth noticing the similarities between PNMO and NNMO lattice parameters and behavior in thin films, both materials show similar growth, deformations and strain when grown in STO(001).

LATICCE CONSTANTS

	a(Å)	b(Å)	c(Å)	vol.(Å^3)	ε[100]$_a$	ε[010]$_a$	ε[001]$_a$	*f*[100]$_b$	*f*[010]$_b$	*f*[001]$_b$
NNMO$_{BULK}$	5,41	5,48	7,67	227,8	-	-	-	2,08%	0,78%	
NNMO$_{STO(001)}$	5,51	5,51	7,63	230,7	1,85%	0,55%	-0,52%	0,23%	0,23%	

Table 4.6 *Lattice constants of NNMO bulk & NNMO(001) and their respective mismatch and strain. a), b) values are calculated using Equation 3.7 and 3.6*

4.5.3 Surface Morphology

The influence of temperature on the morphological properties of NNMO films is now investigated. Images taken by AFM are shown in **Figure 4.18**, and indicate that the surface morphology is generally granular. Grain size distribution is obtained by using a mask and flood method (insets), and is plotted on **Figure 4.18 d)**. Grains evolve continuously with temperature and rapidly increment their size from 650 to 700^{O}C **Figure 4.18 a,b)**. At this stage grain size remains rather constant, however the reconstruction of the surface reveals mound like structure for 750^{O}C **Figure 4.18 c)**, with a pattern previously observed in YNMO(001) films. Those molds are elongated and have 90^O shifting between them following the STO(011) and STO(01-1) directions, satisfying both the epitaxial relations and being indistinguishable from one and other since both lattice constants fall in the same peak of the reciprocal lattice. However, to all purposes, the same pseudocubic transformation reported in the previous chapter can be applied to the sample where a single pseudocubic Pc-NNMO(001) domain is present on the sample. Finally, at 800^{O}C the film shows vestiges of the 750^{O}C morphology, **Figure 4.28 d)** but much less ordered and clearly defined, also an increment on grain size is observed. The films roughness is shown in

Figure 4.18 f) to increase rapidly with substrate temperature, being the 750 and 800 ^{O}C the ones that present higher values.

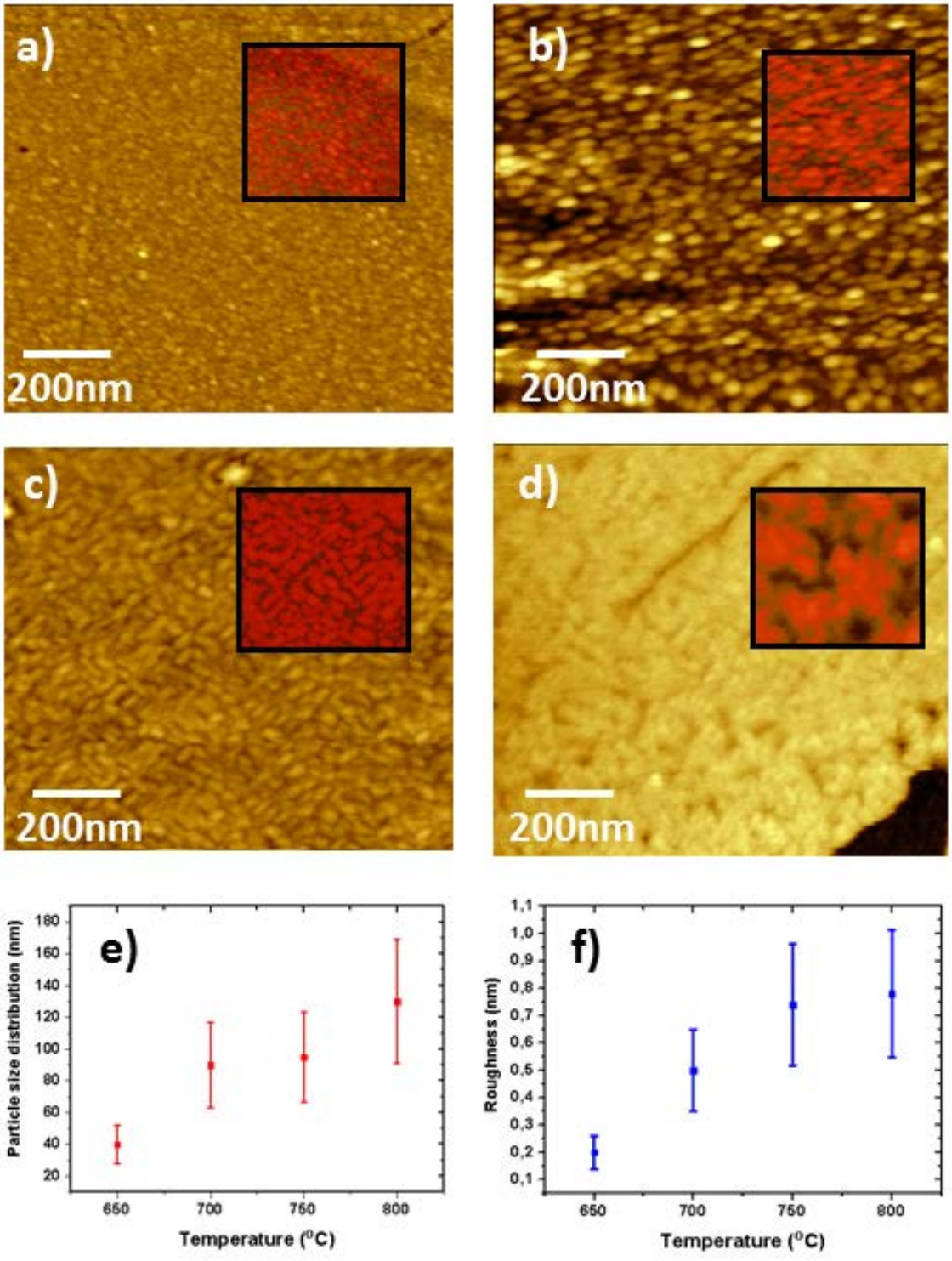

Figure 4.18 *AFM micrograph and roughness analysis for SNMO deposited at various temperatures a) 650°C, b) 700°C, c) 750°C & d) 800°. (Insets represent the flood mask used for grain size distribution). e) shows mean particle size and f) shows extracted roughness*

4.6 Final remarks on thin film growth

In this chapter the effect of deposition temperature on the morphology and crystallinity of thin films of $R(Ni_{0.5}Mn_{0.5})O_3$ (R=Sm, Nd & Pr) deposited on STO(001) substrate by PLD has been carefully studied and discussed. The $R(Ni_{0.5}Mn_{0.5})O_3$ family, in bulk, is a Monoclinic $P2_1/n$, with a β angle not far from 90^O, in most of the cases their deviation from the orthorhombic lattice is of less than half degree [**3**].

In this study, the deposit conditions are narrowed down to a single variable, the influence of substrate temperature, having thoroughly studied the rest of the parameters in the previous chapter for a similar compound, YNMO, which has shown major influence of this parameter in contrast with oxygen pressure and ablation frequency. Results of this study can be summarized in **Table 4.7**, which compiles results of this chapter, regarding crystal orientation, deformation and epitaxial strain.

LATICCE CONSTANTS

	a(Å)	b(Å)	c(Å)	vol.(Å^3)	ε[100]$_a$	ε[010]$_a$	ε[001]$_a$	*f*[100]$_b$	*f*[010]$_b$	*f*[001]$_b$
SNMO$_{BULK}$	***5,35***	***5,51***	***7,61***	***224,5***	-	-	-	***3,22%***	***0,22%***	-
SNMO$_{STO(001)}$	5,41	5,41	7,645	223,7	1,12%	-1,81%	0,46%	2,08%	2,08%	-
SNMO$_{STO(010)}$	5,32	5,51	7,64[c]	224.5	-1,66%	1,85%	-	3,08%[d]	-	-
PNMO$_{BULK}$	***5,44***	***5,47***	***7,69***	***229,2***	-	-	-	***1,52%***	***0,96%***	-
PNMO$_{STO(001)}$	5,49	5,49	7,645	230,4	0,92%	0,37%	-0,59%	0,59%	0,59%	-
NNMO$_{BULK}$	***5,41***	***5,48***	***7,67***	***227,8***	-	-	-	***2,08%***	***0,78%***	-
NNMO$_{STO(001)}$	5,51	5,51	7,63	230,7	1,85%	0,55%	-0,52%	0,23%	0,23%	-
BNMO$_{BULK}$	5,35	5,47	7,65	222.06						

Table 4.5 *Lattice constants of RNMO bulk, RNMO(001) & RNMO(010) and their respective mismatch and strain. a), b) values are calculated using Equation 3.7 and 3.6. c) values are calculated by volume conservation and d) value is calculated along the STO(011) and SNMO(100).*

It can be clearly observed that regardless secondary phases on the films, all of them tend to growth highly oriented RNMO(001), and more importantly the temperature at which they show the maximum crystallinity is the same for the whole group of materials. It can be argued that in fact, despite the R ionic radius of the

double perovskite formula, the $Ni_{0.5}Mn_{0.5}O3$ octahedrons still one of the dominant components of the epitaxial stabilization of the films. Moreover all of the films, can be described by the lower symmetry pseudocubic indexation, as in the case of YNMO, due to the observed single in-plane domain of the crystals RNMO(001).

Another interesting observation, is the one shown in **Figure 4.19**, in this case, the difference between in plane axis $RNMO_{(b/a)}$ is plotted for each compound, this ratio depicts how far from a tetragonal lattice is the RNMO cell for each compound. Values from $La_2(NiMn)O_6$ and $Bi_2(NiMn)O_6$ are taken from a simulation of their $P2_1/n$ unit cell [**9**]. The plot places rare earth, and Y/Bi, on the x axis equidistant from each other and by atomic number, however, Bi and Y are placed in according to the b/c radio. Second Y axis, at the right side of the plot contains the ionic radius in *pm*. The plot shows a continuous increment on the *b/c* showing the progressive deformation of the RNMO unit cell towards a more orthorhombic unit cell. On the other hand, ionic radius for rare earths atoms show that smaller ions move towards the orthorhombic unit cells, Bi and Y show different behavior in this representation.

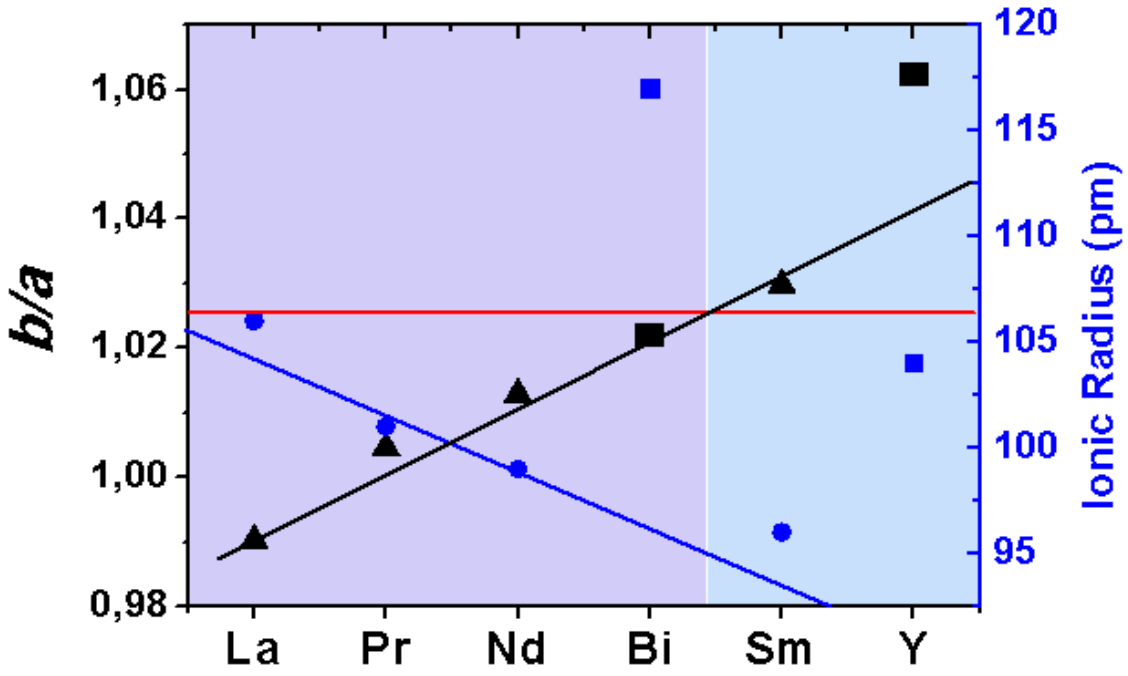

Figure 4.19 *Rare earth (plus Bi and Y marked as ■) ionic radius (**right axis**) and their b/a ratio (**lattice constant b/a**). Red line marks where RNMO materials are not single phase on STO(001). Black and blue lines are guide to the eye for rare earth ions tendency. Light areas separate single epitaxial materials (light purple), from poly domain films (light blue)*

The representation in **Figure 4.19**, allows differentiating two groups among the materials studied. As previously stated, this representation allows to visually following the loss of pseudo tetragonallity on the materials and their progressive transformation into orthorhombic unit cells. The light colored areas in the aforementioned plot represent the single domain/epitaxial and multidomain films deposited on STO(001). The single domain are is painted as light purple and covers materials such La, Pr, Nd and Bi. This group comprehends materials that have been grown on STO(001) and show highly strained unit cells. All these materials, show a similar epitaxial relationship, regarding their orthorhombic unit cell [001]RNMO(001)||[011]STO(001). It is important to remember that highly strain tetragonal RNMO unit cells can be indexed as pseudo cubic unit cells as explained in the previous chapter. For pseudo cubic indexation the epitaxial relationship is [001]Pc-RNMO(001)||[001]STO(001).

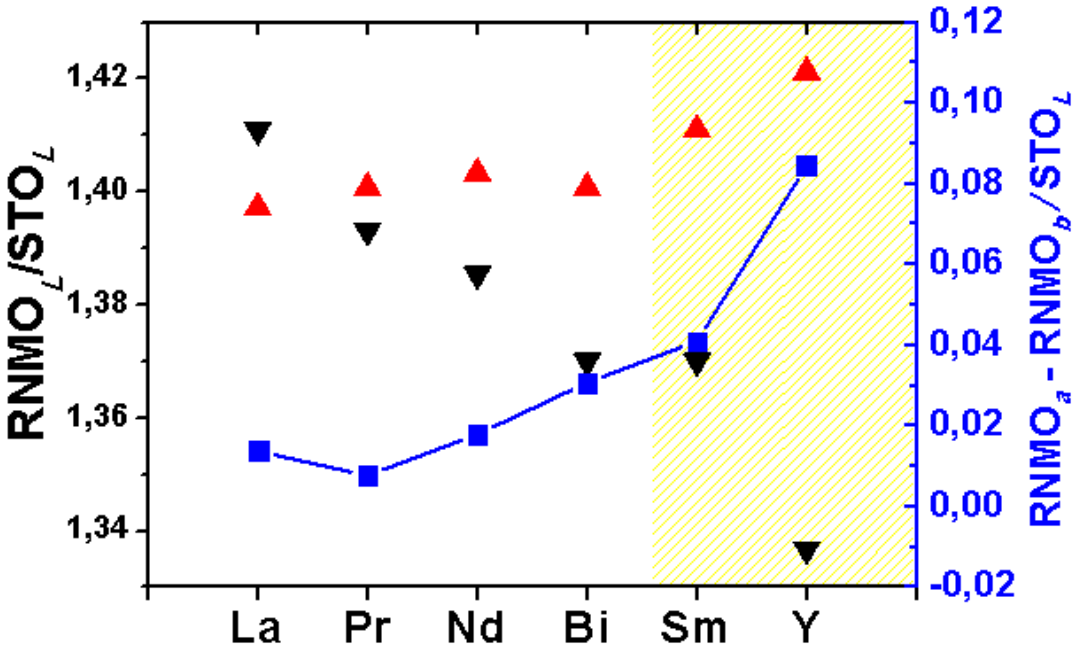

Figure 4.20 *Rare earth (plus Bi & Y), (left axis) ratio between RNMO b and STO lattice (▼), RNMO a to STO(▲) lattice constants. (right axis) absolute value of subtraction between right axis values (■=▼-▲)*

The second group of materials, compose by Y and Sm, are the materials that have not been able to be stabilized in fully epitaxial, single domain structure. In the case of YNMO, a double YNMO(001) domain appears, while for SNMO two domains, SNMO(001) and SNMO(010) are observed. This leads to find the turning

point in which the pseudo tetragonal transformation towards the orthorhombic unit cells, prevents the single domain of RNMO(001)/STO(001) epitaxial thin film to appears, purely based on geometric limitations, the red line in **Figure 4.19**, placed between 1,021 and 1,029 marks this transition threshold.

Figure 4.20 compiles the difference of both RNMO lattice parameters, *a* and *b*, with the STO lattice constant. Right axis shows the absolute difference between both parameters; notice how all the materials that have been grown epitaxially on STO show a maximum difference of 0.02 (Bi), point at which differences are much larger and materials growth in multidomain configuration.

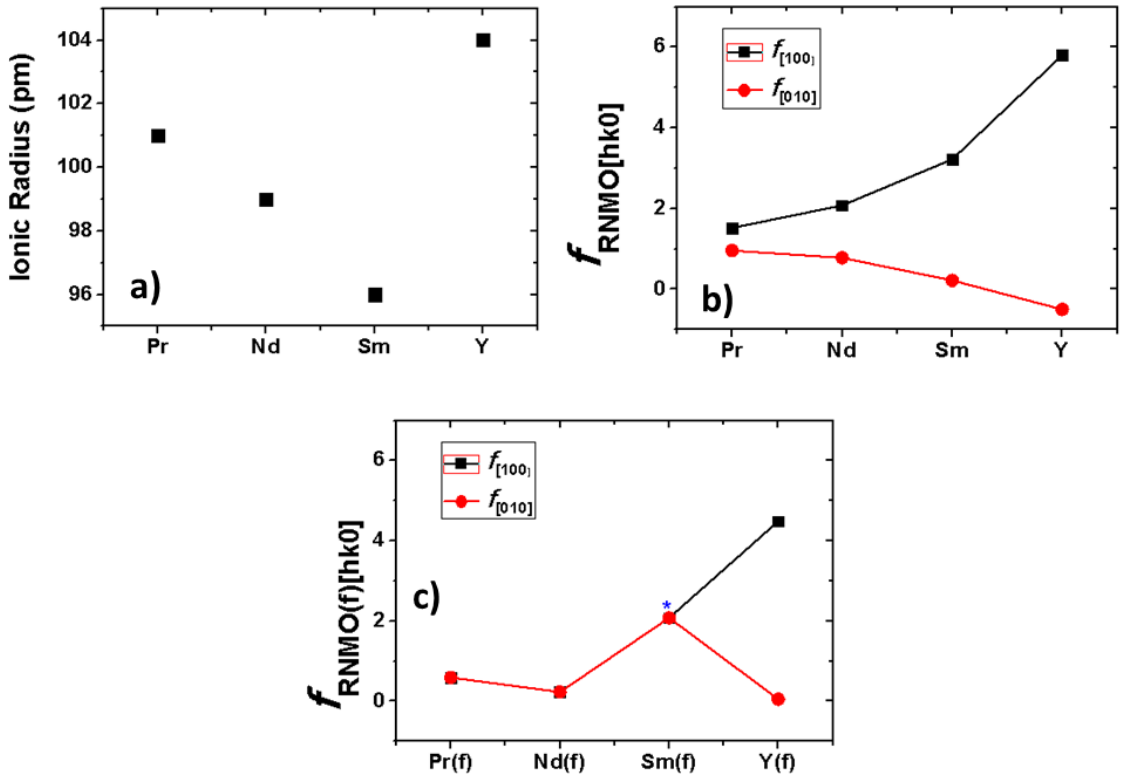

Figure 4.21 *a) Rare earth (plus Y) ionic radius. b) lattice mismatch between bulk RNMO and STO for both lattice constants a and b. c) Lattice mismatch between thin films lattice values of RNMO and STO for both a and b.*

Finally, it is important to show the lattice mismatch between RNMO and STO, for both bulk and films. **Figure 4.21** shows ionic radius for materials growth in this work, Yttrium position is placed at the end of the scale in order to easily compare it with Samarium atoms and, as in previous plots, to follow the b/c ratio. Curves show lattice mismatch of RNMO (**Figure 4.21 b)**) and thin films RNMO(f) (**Figure 4.21 c)**)

with STO. Tendency described by RNMO in bulk is clear, progressively moving to bigger values with the increasingly difference between *a* and *b* lattice of the orthorhombic unit cell. RNMO(f) is calculated according to the lattice constant of the RNMO thin film, therefore initial values for Pr and Nd, films fully adapted to the STO lattice, are close to zero, the strain growths for Sm, remaining strained and finally Y show large mismatch between lattice constants. Remarkably enough, this shows that ionic radius has little influence on the epitaxial texture of RNMO thin films, apart from its influence on the geometric configuration of the unit cell and how far from an ideal tetragonal structure.

4.7 Magnetic Properties of RNMO thin films

$ReNMO_6$ perovskites are a type of materials in which the magnetic ordering arouses by the $Ni^{2+} – O – Mn^{4+}$ interactions, according to the Goodenough–Kanamori rules [**2**,**3**,**8**,**10**–**12**]. In principle most of the members of this family show the monoclinic $P2_1/n$ crystal structure at room temperature, thus in their paramagnetic phase. The structural changes leading to the ferromagnetic ordering are related to the increment of the bounding angle between Ni-O-Mn ions leading to the aforementioned super exchange interactions. It is important to remark that such interactions demand the existence of the so called B-site ordering; in which second neighbors of Ni are always Mn atoms. The existence of such ordering is usually investigated by HR-TEM or synchrotron radiation [**13**], however in our studies, neither of such techniques could be used.

Magnetic measurements were performed by means of SQUID magnetometer at Nanobiomedical Centre – Poland, the mounting protocol includes the positioning of the samples in a standard closed capsule. Therefore some paramagnetic response of O_2 can be expected. The magnetic field was applied perpendicular to the film/substrate interface. First the magnetization vs temperature M(T) plots will be presented, performed under an applied field of 1000 Oe, and then magnetization vs field M(H), performed at 5K.

Magnetism in bulk Sm_2NiMnO_6 in theory should exhibit a T_{FM} at 176K with a total magnetization of 6.6 μ_B/f.u. These values are extracted from the Curie-Weiss plot and [2gJ + 5.2] where theoretical Ni–Mn moment is equal to 5.2 μ_B/f.u [**3**]. However,

the experimental studies in bulk, report values of 157K and 4.9 μ_B/f.u, for B-site ordered perovskites.

In **Figure 4.22**, the M(*T*) measurements, performed on SNMO(001)/STO(001) are presented. The ZFC-FC plots show a slightly increment of the total magnetization of the film from room temperature down to 175K, where the magnetization rapidly increases and continues to do so down to 50K where a second peak is observed. From the M(*T*) measurements, it can be appreciated a magnetic transition around 150K, inset in **Figure 4.22**, temperature that is consistent with reported T_{FM} in bulk. Finally at lower temperatures the magnetization shows a downturn. This behavior was previously observed in bulk material and is presumably attributed to the large magnetocrystalline anisotropy, due to the spin orbit coupling of the Mn-Ni to rare earth. Since the total calculated magnetic moment for the Sm atom is 0.84 μ_B/f.u, it seems likely that the paramagnetic susceptibility of the rare earth is so large that it gives rise to the upturn in magnetization at low temperatures. This is supported by experimental observation on similar compounds with large R magnetic ions, such as Tb, Gd, Ho and Dy [**2**,**8**].

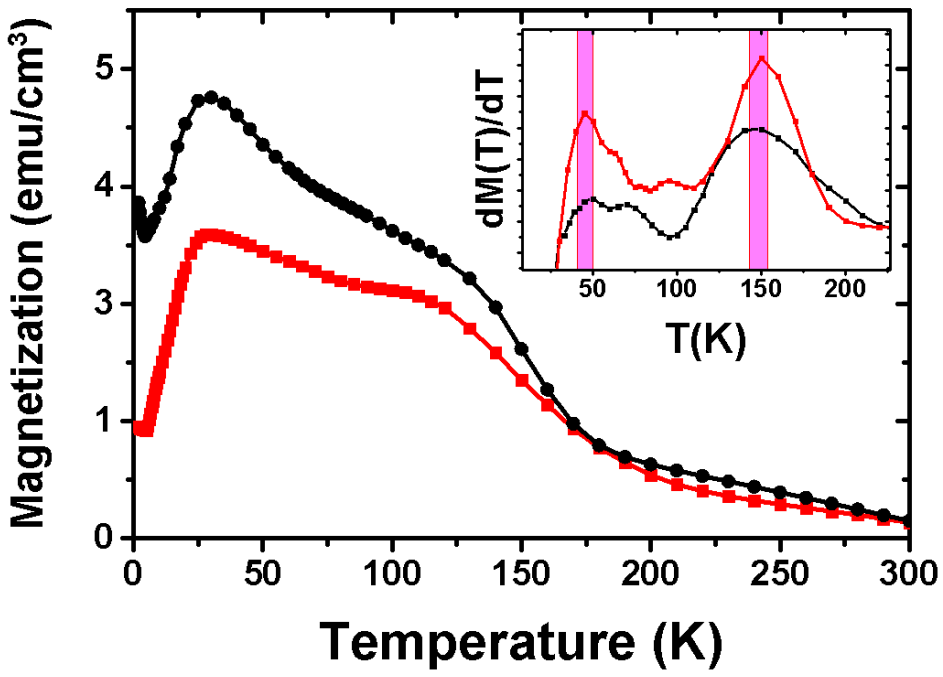

Figure 4.22 *Magnetic measurements, M(T), ZFC(red)-FC(black) for SNMO. Inset shows the derivative of the curve highlighting the two important transitions observed in the film.*

Further analysis, shown in **Figure 4.23**, show the M(H) plot for SNMO. It is worth reminding that the SNMO/STO(001) film, has two out of plane domains, SNMO(010) and SNMO(001), in principle it can be assumed that both domains are equally energetically favorable, therefore the magnetization studied represents an average between the magnetic response of both domains. After the carefully subtraction of the diamagnetic contribution of the substrate, **Appendix 3**, the total magnetization of the film is extracted, giving a value of 4.5 μ_B/f.u. As previously mentioned, the theoretical saturation moment for SNMO is reported as 6.6 μ_B/f.u., however, the measured saturation in the literature is 4.9 μ_B/f.u [**3**]., much lower than expected. In the case of SNMO films, the magnetization measured is 92% of the reported in the literature; the value, although inferior to the nominal one, shows the existence of a considerably important B-site ordering in the film. The small difference of 8% can then be attributed to magnetic anisotropies arousing due to the SNMO(010) & SNMO(001) crystalline domains and some intermixtures of the B-site ions.

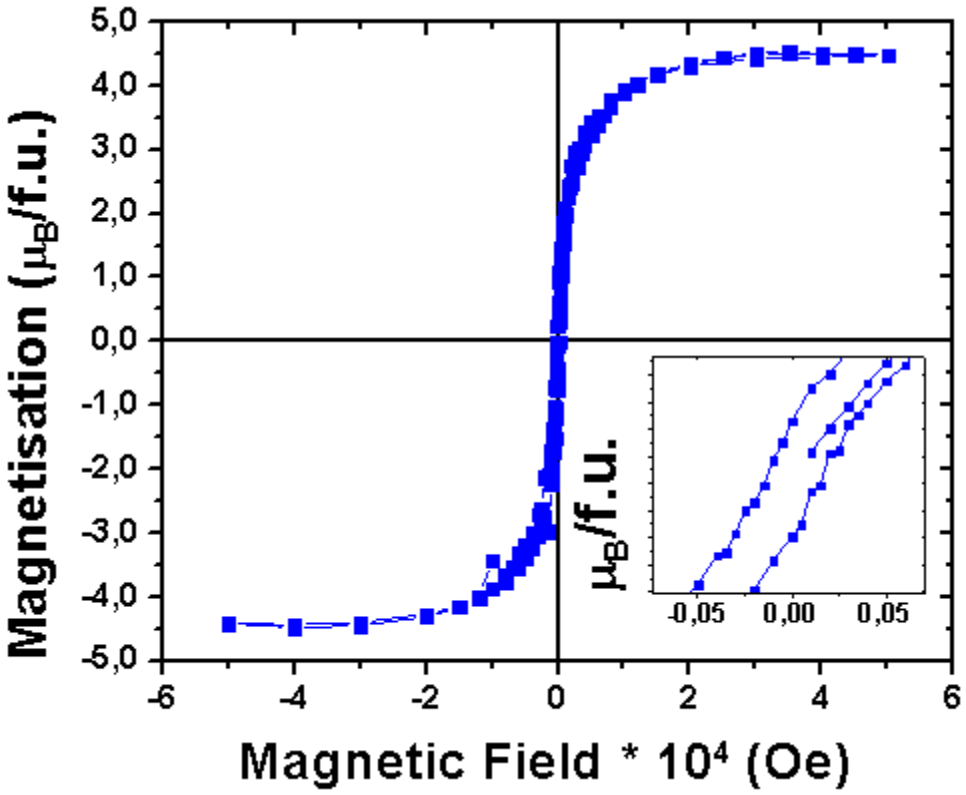

Figure 4.23 *Hysteresis loops (M(H)) measured at 10 K for SNMO sample. Inset shows the coercive field.*

Magnetism in bulk Pr_2NiMnO_6 in theory should exhibit a T_{FM} at 226K with a total magnetization of 11.6 μ_B/f.u. This values are extracted from the Curie-Weiss plot and [2g*J* + 5.2] where theoretical Ni–Mn moment is equal to 5.2 μ_B/f.u. [**2**,**8**]. However, the experimental studies in bulk, report values of 212K and 5.0 μ_B/f.u, for B-site ordered perovskites. The origin of such large discrepancy between the theoretical and experimental saturation moment is not well understood, but suggests that the paramagnetic atom has very little influence on the magnetization of the perovskites, since the total magnetization remains close to the one provided by the Ni-Mn atoms.

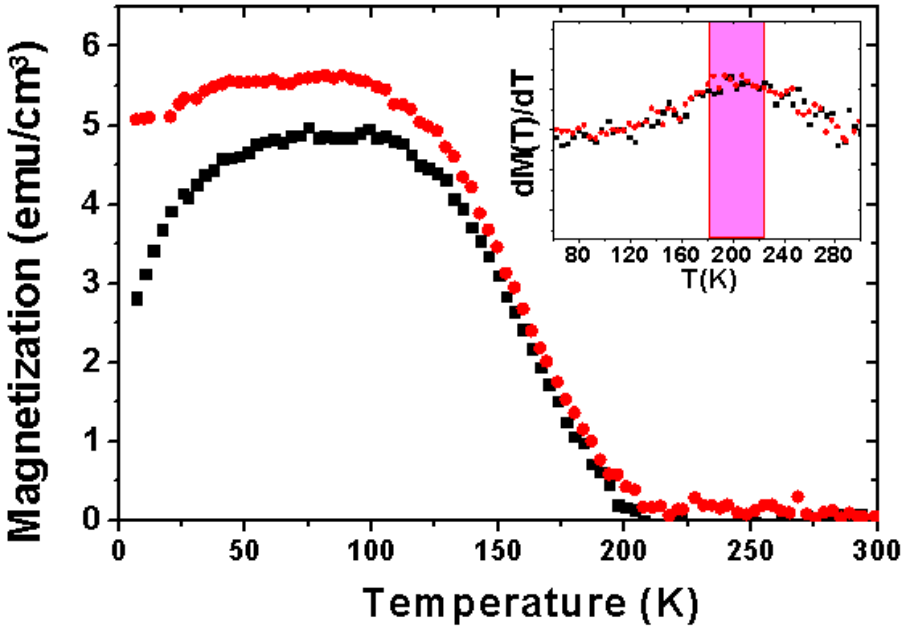

Figure 4.24 *Magnetic measurements, M(T), ZFC(red)-FC(black) for PNMO. Inset shows the derivative of the curve highlighting the phase transitions observed in the film.*

In **Figure 4.24**, the M(*T*) measurements, performed on PNMO(001)/STO(001) are presented. The ZFC-FC plots show a paramagnetic regime from room temperature down to 200K at that point the magnetization rapidly increases showing a well-defined magnetic transition. Inset in **Figure 4.24,** shows the derivative of the magnetization curve, in order to clearly appreciate the T_{FM} of the film. The temperature of ferromagnetic ordering is rather similar to experimentally reported in the literature for bulk material.

Further analysis, **Figure 4.25**, shows the M(H) plot of PNMO. The hysteresis loop shows a rapid magnetization and saturation point at $1.5x10^4$ Oe, a much rapid

saturation point than SNMO films. The inset shows the coercive field of the sample showing the ferromagnetic switching of the film. Total magnetization was calculated after removing the diamagnetic contribution of the STO(001) substrate as shown in **Appendix 4**, the magnetic response of the film was found to be 4.79 μ_B/f.u, the value is far from the 11.6 μ_B/f.u, theoretical magnetization, however it is rather close to the experimental value reported for B-site ordered PNMO, 5.0 μ_B/f.u. This discrepancy still not fully understood but is expected that is related to the low paramagnetic moment of the Pr atom.

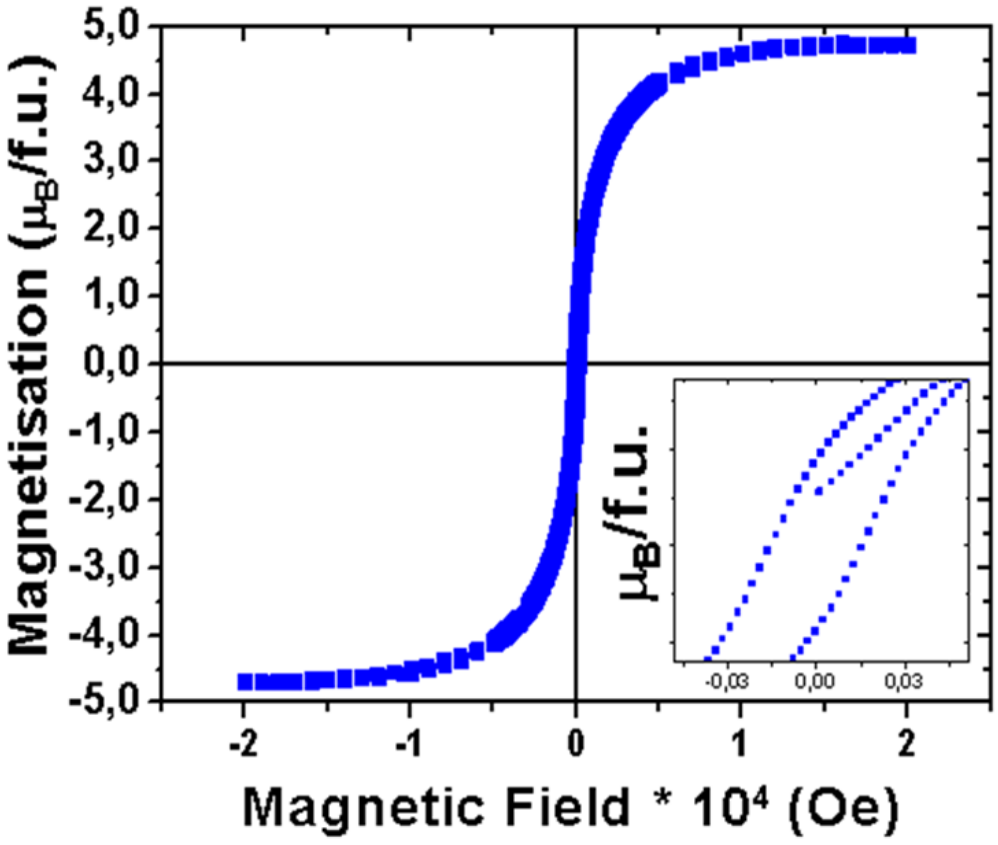

Figure 4.25 *Hysteresis loops (M(H)) measured at 10 K for PNMO sample. Inset shows the coercive field.*

Magnetism in bulk Nd_2NiMnO_6 in theory should exhibit a T_M at 213K with a total magnetization of 11.8 μ_B/f.u. These values are extracted from the Curie-Weiss plot and [2g*J* + 5.2] where theoretical Ni–Mn moment is equal to 5.2 μ_B/f.u [**2**,**8**]. However, the experimental studies in bulk, report values of 194K and 5.6 μ_B/f.u, for B-site ordered perovskites. The origin of such large discrepancy between the theoretical

and experimental saturation moment is not well understood, but as in the case of PNMO, it is attributed to the fact that the paramagnetic atom has very little influence on the magnetization of the perovskites, since the total magnetization remains close to the one provided by the Ni-Mn atoms.

In **Figure 4.26**, the M(*T*) measurements, performed on NNMO(001)/STO(001) are presented. The ZFC-FC plots 3 distinctive regimes. The first one shows the paramagnetic regime from room temperature down to 190K at that point the magnetization rapidly increases showing a well-defined magnetic transition. The second regime is from 190K down to 50K, at this point a small peak is observed, this peak is attributed to the oxygen trapped in the mounting capsule. The final segment is observed at temperature of 10K, where a paramagnetic regime is observed. Inset in **Figure 4.26,** shows the derivative of the magnetization curve, in order to clearly appreciate the T_M of the film, the transition at 50K is also shown. The temperature of ferromagnetic ordering is rather similar to experimentally reported in the literature for bulk material.

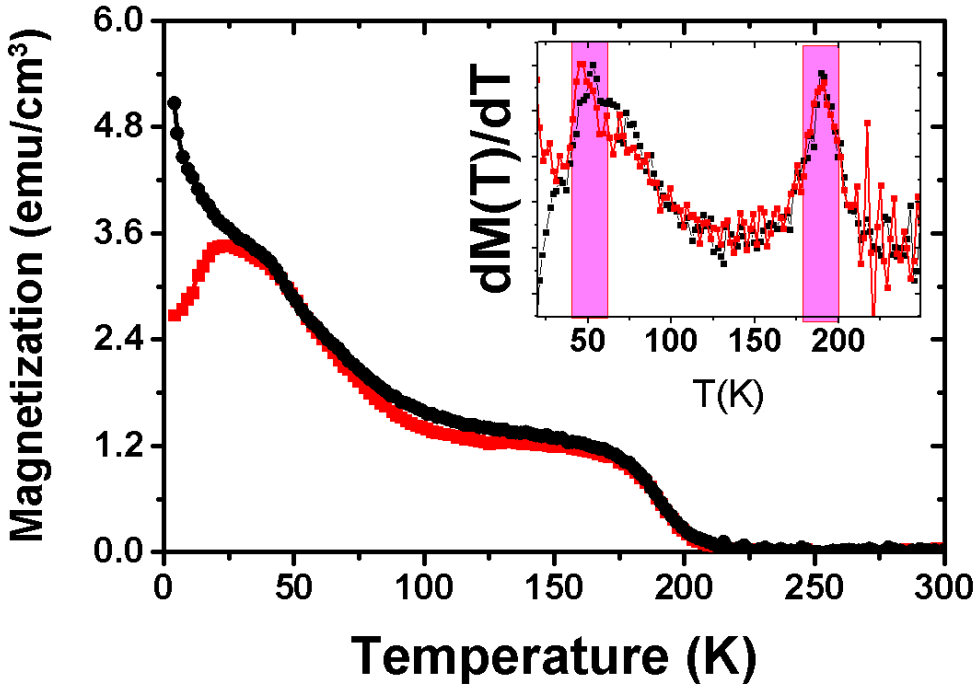

Figure 4.26 *Magnetic measurements, M(t), ZFC(red)-FC(black) for NNMO. Inset shows the derivative of the curve highlighting the phase transitions observed in the film.*

Further analysis, shown in **Figure 4.27**, presents the M(H) plot of for NNMO. The hysteresis loop shows a rapid magnetization and saturation point at 1.5 x10^4 Oe, a much rapid saturation point than SNMO films. The inset shows the coercive field of the sample showing the ferromagnetic switching of the film. Total magnetization was calculated after removing the diamagnetic contribution of the STO(001) substrate as shown in **Appendix 4**. The magnetic response of the film was found to be 5.15 μ_B/f.u, the value is far from the 11.8 μ_B/f.u, theoretical magnetization; however it is rather close to the experimental value reported for B-site ordered PNMO, 5.6 μ_B/f.u. This discrepancy still not fully understood but is expected that is related to the low paramagnetic moment of the Nd atom.

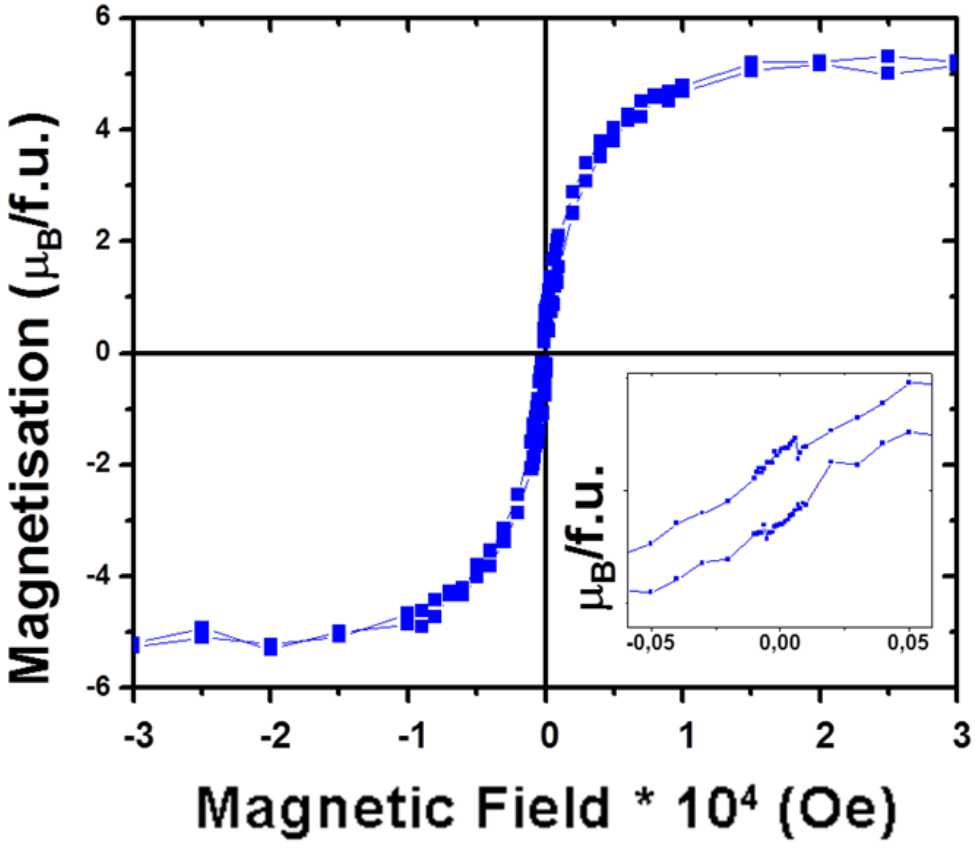

Figure 4.27 *Hysteresis loops (M(H)) measured at 10 K for PNMO sample. Inset shows the coercive field.*

As closing remarks the magnetic measurements, compiled in **Table 4.6**, have shown the ferromagnetic nature of the samples, with saturation magnetization close to the one reported for B-site ordered bulk materials, showing that even though the super structure could not be studied a certain level of b-site ordering is observed in the film.

The discrepancies between theoretical saturation moments in Pr and Nd are not fully understood but the fact that B-site ordered bulk materials, shown similar magnetization suggest that the paramagnetic atoms are not contributing to the total magnetization of the film and the effective magnetic moment measured comes solely from the Ni-Mn interactions.

MAGNETIC MEASUREMENTS

Compound	μ_B/f.u*	μ_B/f.u	T_{FM} (K)
YNMO	5.2	4.58	95
SNMO	6.6	4.5	150
NNMO	11.8	515	190
PNMO	11.6	4.79	200

Table 4.6: *Compiled theoretical saturation moment (*)* [**2**,**3**], *experimental values from this work and FM transition temperature.*

4.8 Dielectric properties of RNMO thin films

Dielectric properties of RNMO thin films were unsuccessfully performed on the samples of Sm, Nd and Pr, due to the impossibility of reaching temperatures lower than 150K, using the nitrogen gas cryostat. At this range of temperature the coupling between intrinsic and extrinsic mechanism of the films is not fully resolved

According with the literature, RMNO family shows a very low dielectric constant, between ε = 15–25, this is attributed to B-site ordering of the perovskites [**3**,**14**]. However, as shown in the previous Chapter, for YNMO such values are observed in the ferromagnetic phase, where the dielectric permittivity rapidly lowers.

Further studies should be carried out in order to map the dielectric behavior of the films at temperatures below liquid nitrogen and perform ferroelectric polarization measurements at liquid helium temperature.

4.9 Summary of this chapter

- Ferromagnetic perovskites thin films of $R(Ni_{0.5}Mn_{0.5})O_3$ R=Sm (SNMO), Nd (NNMO) and Pr (PNMO), were successfully deposited by PLD. The films of

$Sm(Ni_{0.5}Mn_{0.5})O_3$ shown epitaxial growth on STO(001) with two out of plane crystalline domains, SNMO(001) & SNMO(010), the epitaxial relationship was studied and determined as [100]SNMO(001) ‖ [011]STO(001), and [100]SNMO(010) ‖ [011]STO(001).

- Thin films of $R(Ni_{0.5}Mn_{0.5})O_3$ R=Sm (SNMO), Nd (NNMO) & Pr (PNMO) are obtained with similar optimal deposition as the ones studied for YNMO thin films, with an optimal deposition temperature of 750°C. The effect of deposition temperature on the crystalline structure of the films was discussed and described, as a rule the grain size distribution with temperature, while the FWHM decreases showing the increase of crystalline quality of the film.
- Thin films of $Pr(Ni_{0.5}Mn_{0.5})O_3$ and $Nd(Ni_{0.5}Mn_{0.5})O_3$ show a highly strained growth, fitting the substrate geometry rather closely, as compared with thin films of YNMO and SNMO who present multiple in-plane and out plane domains. This observation allows to investigate both ionic radius and lattice b/a ratio as a function of the epitaxial relationship of the films on STO(001). Categorizing the b/c ratio as an important parameter for the fully epitaxial thin films of the RNMO family. The value for single domain thin films is found to be lower than b/c=1.03. It is assumed that *b/c* radius inferior to 0.97 would have similar effect in the thin films for a cube on cube epitaxial relationship.
- Functional magnetic measurements corroborate the ferromagnetic nature of the films with a magnetic transition close to the ones reported in bulk. SNMO 175K with a magnetic moment of 4,52 μ_B/f.u in concordance with previously reported data, although lower from the theoretical 6,6 μB expected value. PNMO, 200K with a magnetic moment of 4,79 μ_B/f.u in concordance with previously reported data, although lower from the theoretical 11,6 μ_B expected and finally, NNMO, 190K with a magnetic moment of 5,15 μ_B/f.u in concordance with previously reported data, although lower from the theoretical 11,8 μ_B expected. The measured magnetization values suggest that the paramagnetic ions do not play any important part on the total magnetization of the unit cell, while the main magnetic response seems to remain close to the values reported for Ni-Mn.
- Further studies regarding the dielectric properties of the films are needed in order to map the magnetic phase transition and observe if similar effects as the

ones observed in YNMO are present in any other member of the RMNO perovksites.

References

[1] Asai, K., Fujiyoshi, K., Nishimori, N., Satoh, Y., Kobayashi, Y. and Mizoguchi, M. (1998) **Magnetic Properties of REMe 0.5Mn 0.5O 3 (RE = Rare Earth Element, Me = Ni, Co)**. *Journal of the Physical Society of Japan*, The Physical Society of Japan. **67**, 4218–28. http://dx.doi.org/10.1143/JPSJ.67.4218

[2] Peña, O., Barahona, P., Gil, V., Tartaj, J. and Moure, C. (2008) **Magnetic behavior of solid solutions REMe0.50 Mn0.50 O3 (RE = Y, La, Pr, Nd, Eu, Gd, Er; Me = Ni,Co)**. *Boletin de La Sociedad Espanola de Ceramica Y Vidrio*, **47**, 138–42.

[3] Booth, R.J., Fillman, R., Whitaker, H., Nag, A., Tiwari, R.M., Ramanujachary, K.V. et al. (2009) **An investigation of structural, magnetic and dielectric properties of R2NiMnO6 (R=rare earth, Y)**. *Materials Research Bulletin*, **44**, 1559–64. http://dx.doi.org/10.1016/j.materresbull.2009.02.003

[4] Ma, Y., Guilloux-Viry, M., Pena, O. and Moure, C. (2004) **Y(Ni, Mn)O3 epitaxial thin films prepared by pulsed laser deposition**. *Physica Status Solidi (a)*, **201**, 2385–9. http://dx.doi.org/10.1002/pssa.200304911

[5] Ma, Y., Guilloux-Viry, M., Barahona, P., Peña, O., Moure, C., Ghilane, J. et al. (2006) **YNixMn1−xO3 thin films by pulsed laser deposition: Structure and magnetic properties**. *Thin Solid Films*, **510**, 275–9. http://dx.doi.org/10.1016/j.tsf.2005.12.159

[6] Salvador, P.A., Doan, T.D., Mercey, B. and Raveau, B. (1998) **Stabilization of YMnO3 in a Perovskite Structure as a Thin Film**. *Chemistry of Materials*, **10**, 2592–5.

[7] Martí, X., Sánchez, F., Skumryev, V., Laukhin, V., Ferrater, C., García-Cuenca, M.V. et al. (2008) **Crystal texture selection in epitaxies of orthorhombic antiferromagnetic YMnO3 films**. *Thin Solid Films*, **516**, 4899–907. http://dx.doi.org/10.1016/j.tsf.2007.09.023

[8] Bull, C.L. and McMillan, P.F. (2004) **Raman scattering study and electrical properties characterization of elpasolite perovskites Ln2(BB′)O6 (Ln=La, Sm...Gd and B,B′=Ni, Co, Mn)**. *Journal of Solid State Chemistry*, **177**, 2323–8. http://dx.doi.org/10.1016/j.jssc.2004.02.022

[9] Lufaso, M.W. and Woodward, P.M. (2001) **Prediction of the crystal structures of perovskites using the software program SPuDS.** *Acta Crystallographica Section B, Structural Science*, **57**, 725–38. http://dx.doi.org/10.1107/S0108768101015282

[10] Mouallem-Bahout, M., Roisnel, T., André, G., Gutierrez, D., Moure, C. and Peña, O. (2004) **Nuclear and magnetic order in Y(Ni,Mn)O3 manganites by neutron powder diffraction**. *Solid State Communications*, **129**, 255–60. http://dx.doi.org/10.1016/j.ssc.2003.09.039

[11] Truong, K., Singh, M., Jandl, S. and Fournier, P. (2009) **Influence of Ni/Mn cation order on the spin-phonon coupling in multifunctional La2NiMnO6 epitaxial films by polarized Raman spectroscopy**. *Physical Review B*, **80**, 134424. http://dx.doi.org/10.1103/PhysRevB.80.134424

[12] Singh, M.P., Truong, K.D., Jandl, S. and Fournier, P. (2011) **Magnetic properties and phonon behavior of Pr[sub 2]NiMnO[sub 6] thin films**. *Applied Physics Letters*, **98**, 162506. http://dx.doi.org/10.1063/1.3575564

[13] Langenberg, E., Rebled, J., Estradé, S., Daumont, C.J.M., Ventura, J., Coy, L.E. et al. (2010) **Long-range order of Ni[sup 2+] and Mn[sup 4+] and ferromagnetism in multiferroic (Bi[sub 0.9]La[sub 0.1])[sub 2]NiMnO[sub 6] thin films**. *Journal of Applied Physics*, **108**, 123907. http://dx.doi.org/10.1063/1.3524278

[14] Langenberg, E., Fina, I., Ventura, J., Noheda, B., Varela, M. and Fontcuberta, J. (2012) **Dielectric properties of (Bi0.9La0.1)2NiMnO6 thin films: Determining the intrinsic electric and magnetoelectric response**. *Physical Review B*, **86**, 085108. http://dx.doi.org/10.1103/PhysRevB.86.085108

CHAPTER 5

Thin Films of $Bi(Fe_{0.5}Mn_{0.5})O_3$

Bi_2FeMnO_6 (BFMO) lies between two of the most well studied multiferroic materials in the field, $BiFeO_3$ [**1**,**2**]and $BiMnO_3$ [**3**,**4**], the characteristics of which are well described in the literature and still focusing much attention among researchers. The widespread interest in $BiFeO_3$ originates due to the stable ferroelectric and antiferromagnetic ordering at room temperature [**5**] (T_N ≈ 643 K). However, pure $BiFeO_3$ has a low magnetic moment in bulk and thin film form (≈0.02 μB//Fe) arising from the antisymmetric Dzyaloshinskii–Moriya (DM) exchange [**6**–**9**], owing to the formation of an incommensurate spin cycloid that minimizes coherent spin canting. On the other hand, $BiMnO_3$ is the only material where the coexistence of true ferromagnetic and ferroelectric order has been reported [**3**,**10**], However, the FM ordering appears at a rather low temperature T_{FM} ≈105 K,[**11**] from the ferroelectric polarization T_C ≈ 450K focusing the efforts into highly doped variations of $BiMnO_3$[**10**,**12**] Some of the efforts are devoted to the synthesis of double perosvkites, as shown **Chapter 1**. This is done by attempting the cationic partial substitutions, which has been focused on Bi_2CoMnO_6 and Bi_2NiMnO_6 [**13**–**18**]. However, a new compound driving strong attention is $Bi(Mn_xFe_{1-x})O_3$, with x=0.5.

Much attention has been focused on understanding the magnetic properties of $Bi(Mn_xFe_{1-x})O_3$ with x=0.0–0.2 in bulk [**5**,**19**] and x=0.5 in "thin films" [**19**] using neutron diffraction and reported a G-type antiferromagnetic spin structure with Neel temperature of T_N= 560 K and T_N = 120K respectively [**20**]. In bulk however, these mixtures are very difficult to stabilize unless high pressures are employed.[**14**], The

common approach is to dope the structure with considerable quantities of lanthanum, however, such an approach complicates the distinction between intrinsic effect and dopant effects in both magnetic and crystalline properties [**21**]. In thin film form, high Mn concentration $Bi(Mn_{0.5}Fe_{0.5})O_3$ can be stabilized without the addition of La due to epitaxial matching on $SrTiO_3$,[**22**] Polycrystalline solid solutions show a distinctive magnetic response, with very low magnetic moment 0.02 μB x=0.2%. Thin films studies however, have shown a small increment of magnetization with $0 \leq x \leq 0.5$ of Mn substitution, while highly strained films, with partial substitution of x=0.5 showed have shown very interesting results. The work reported by of E.-M. Choi *et al* [**22**], showed an impressive increment on the magnetization with ~0.58 μB/B-site ion at room temperature. The strongly enhanced magnetic properties are attributed to the high level of strain induced by the epitaxial growth in the 40nm thick studied film. The most relevant results from this publication are shown in **Figure 5.1**.

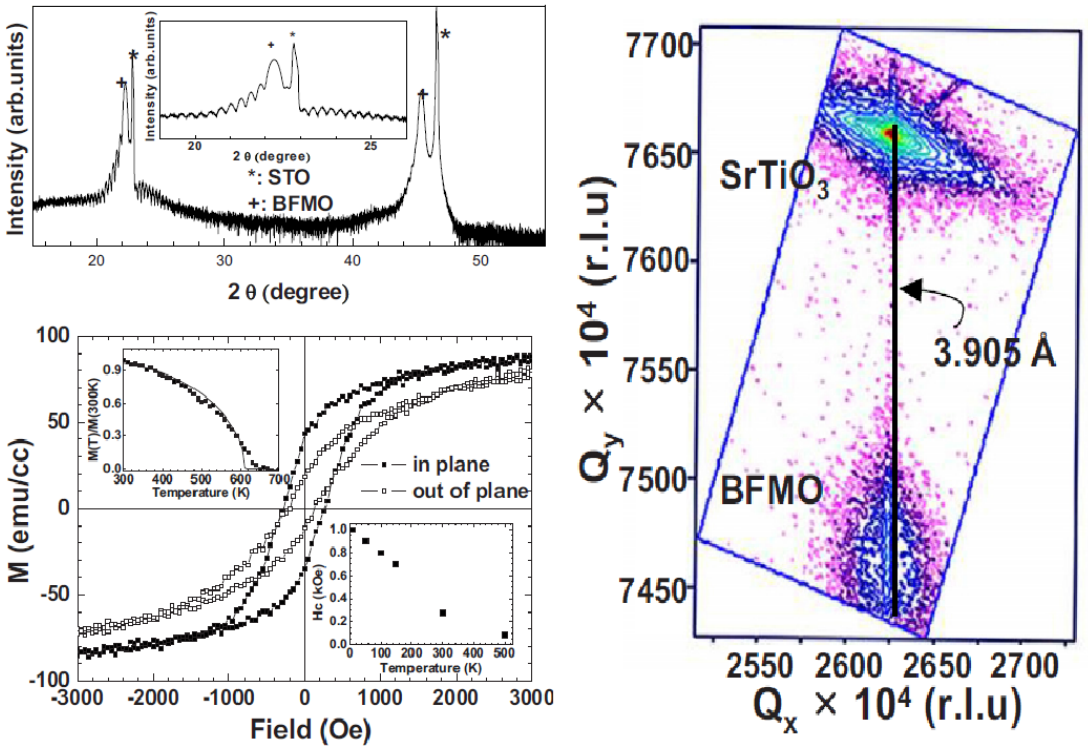

Figure 5.1: *Compiled results of highly strained BFMO/STO thin films reported by M-E Choi et al* [**22**] *Upper lest picture, shows 2theta scans, right panel shows reciprocal space maps and bottom left panel shows the M(H) measurements at room temperature.*

Electrical measurements performed on the $Bi(Mn_{0.5}Fe_{0.5})O_3$ (BFMO) thin films have been reported[**23**], finding a typical relaxor behaviour, in a film of 180 nm film. The lack of "strong" magnetism in their results seems to suggest that such behaviour is close related to the bulk composition [**24**] since is been already stated that the epitaxial strain of the substrate is responsible for the strong magnetism detected, this, such measurements are not compatible with the highly strained thin film scenario.

This chapter will be devoted to the dielectric properties of highly strained thin films deposited by pulsed laser deposition PLD. However, the strained nature and ferromagnetic properties of the films will be first demonstrated by XRD, SQUID and VNA.

5.1 Target Synthesis

Targets of $Bi(Fe_{0.5}Mn_{0.5})O_3$ have been synthesized by mixing stoichiometric powders of suitable oxides, summarized in **Table 4.1.** Oxides were place into an agate mortar. In order to synthesize the perovskite formula the B site ordered compound (Bi_2NiMnO_6) was considered, however in order to compensate the volatility of the Bi atom 10% more of the stoichiometric weight was added.

5.2 Thin Film Deposition

As shown before in this chapter, thin films of $Bi(Mn_{0.5}Fe_{0.5})O_3$ on STO(001) have been previously reported by E.-M. Choi *et al* [**22**], with an optimal substrate temperature of $820^{O}C$. However, previous experience of E. Langenberg in the growth of Bi based perovskites, such $Bi(Mn_{0.5}Fe_{0.5})O_3$, $BiMnO_3$ and $BiFeO_3$ [**21**], such high temperature of deposition can lead to several losses on Bi content on the films. Due to this fact, in this section a short study of epitaxial stabilization of BFMO is made a rather low temperature range of $500 - 650^{O}C$.

Samples were deposited under an oxygen pressure of 0.6 mbar, 5Hz repetition growth rate and a laser fluence of 1.7 J/cm^2. X-ray characterization of the samples is shown in **Figure 5.2**. All the samples shown a strong preferential growth of BFMO(0*k*0), indexed according to the powder diffraction table for $BiFeO_3$, (ICDD-PDF #01-072-2035). Low temperature samples, 500, 550 and $600^{O}C$ show small phase segregation, between Bi_2O_3 and Mn_3O_4, an effect also observed in Bi_2NiMnO_6 [**21**]. These phases progressively disappear with the increment of temperature. Finally, the

sample grown at 650^{O}C, show single out of plane crystalline domain, with no evident secondary phases.

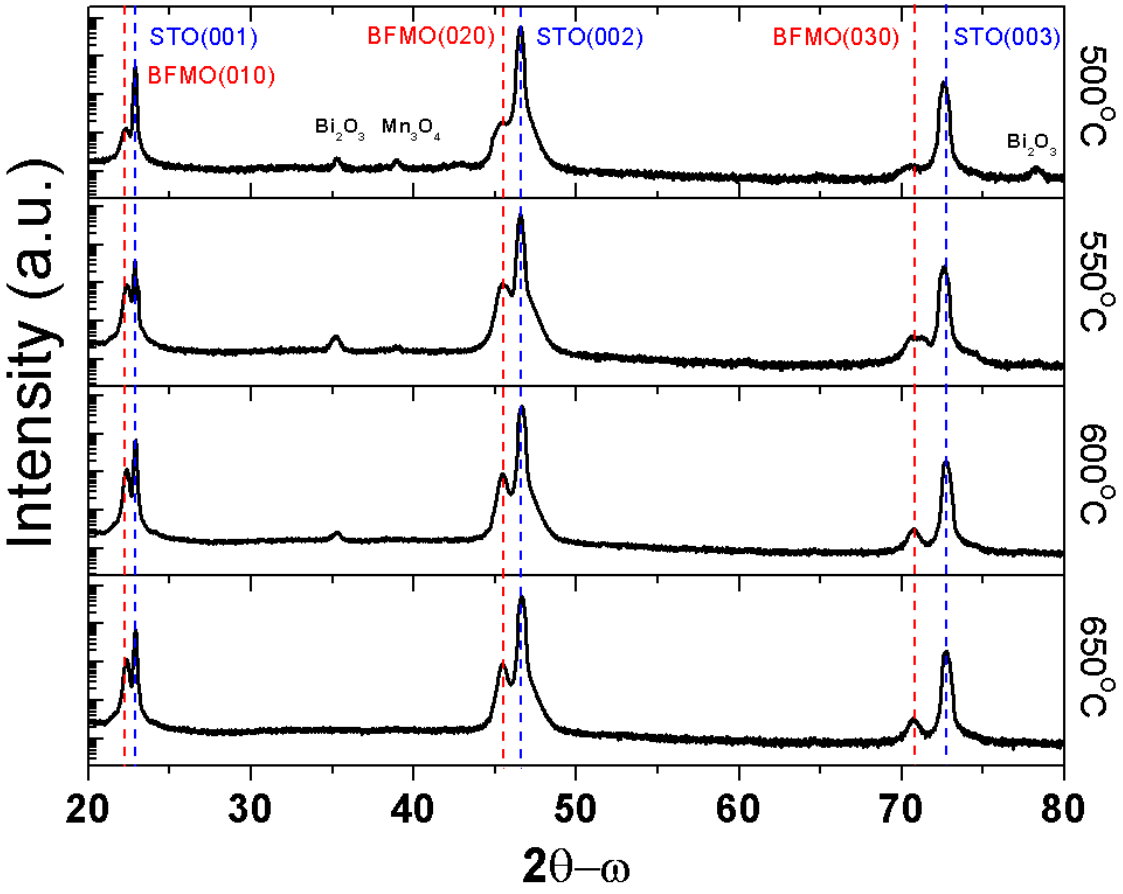

Figure 5.2: *2θ-ω scans of BFMO films deposited on STO(001) at different temperatures. Lines show the position of the (0k0) peaks on the plots*

Out of plane parameter remains rather constant in all the samples, using the methodology described in **Appendix 2**, the out of plane parameter of BFMO has a value of 3.99±0.2 Å. The in-plane ordering of the films are investigated by phi (φ) scans and reciprocal space maps, shown in **Figure 5.3**, reveal a highly epitaxial film with cube on cube epitaxial relationship. **Figure 5.3b)** shows the reciprocal space maps performed on the sample grown at 650^{O}C, the position of the BFMO(103) peak shows a highly strained film, very similar as the one reported by E-M *Choi et al* [**22**], Figure 5.1. The final lattice parameters are determined as a=c=3.92±0.2 Å with epitaxial relationship [100]BFMO(010)||[100]STO(001).

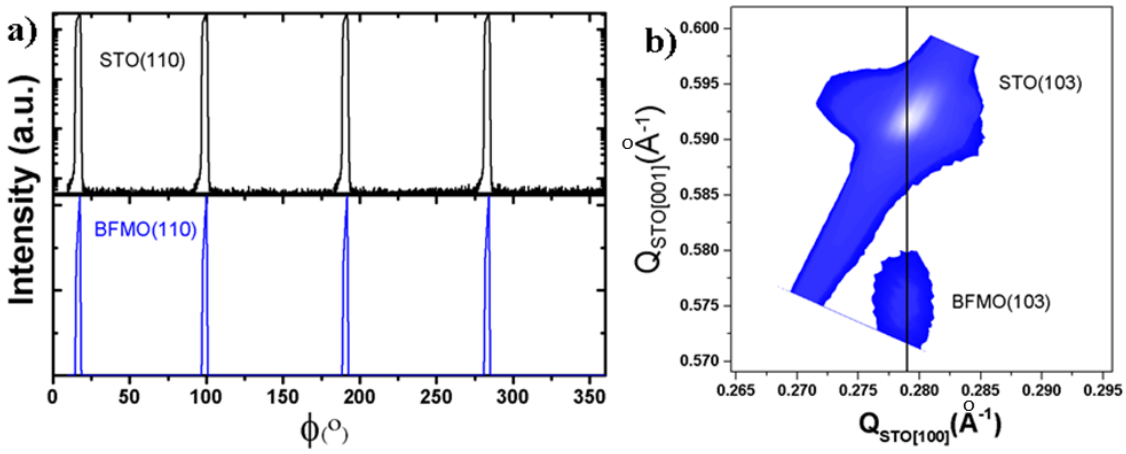

Figure 5.3: *Epitaxial relationship of BFMO/STO(001), a) shows φ-scans performed around the (110) directions. B) reciprocal space map performed around the STO(103).*

5.3 Chemical composition

In order to determine the appropriate stoichiometry of the film, XPS measurements are performed. As a result, the atomic ratio observed in the film is in fully agreement with the nominal stoichiometry (Bi 19.4%, Fe 11.2% and Mn 11%) **Figure 5.4 a)** of $Bi(Ni_{0.5}Mn_{0.5})O_3$ ruling out any possible off stoichiometric effect due to the deposition temperature. Additionally, the valences of Bi, Fe and Mn are investigated.

The extracted valences for Bi, Fe and Mn, are shown in **Figure 5.4 b,c,d)**, as it turns out, single valence is observed for both Bi^{3+} and Fe^{3+}, while the Mn shows a multiple valence between Mn^{4+} and Mn^{3+}. Therefore, by assuming the Goodenough–Kanamori rules for 180° superexchange couplings, **Chapter 1**, there are few possibilities for super exchange magnetism. First, the so called vibronic FM/AFM ordering of Mn^{3+}–O–Mn^{3+} with a theoretical 4 μB/B-site ion for ferromagnetic ordering and the second one, so called vibronic AFM/FM ordering of Fe^{3+}–O–Mn^{3+}, with a total magnetization of 1 μB/B-site, none of which are in agreement without results or reported data. However, the apparition of Mn^{4+} and no Fe^{+2} allows the Mn^{4+}-O-Fe^{3+} FM/ AFM, observed in other similar perovskites [**20**,**25**]. It is important to remark, that without B site ordering, Fe^{3+}-O-Fe^{3+}, Mn^{3+}-O-Mn^{3+} and Mn^{4+}-O-Mn^{3+} exchanges are also possible therefore the magnetic arrangement of the films is a rather complex issue that needs to be addressed. However, the existence of mixed valences can in principle

account for the low magnetization of the film, by having a strong magnetic areas and weak/nonmagnetic areas, showing nanopolar regions in the film.

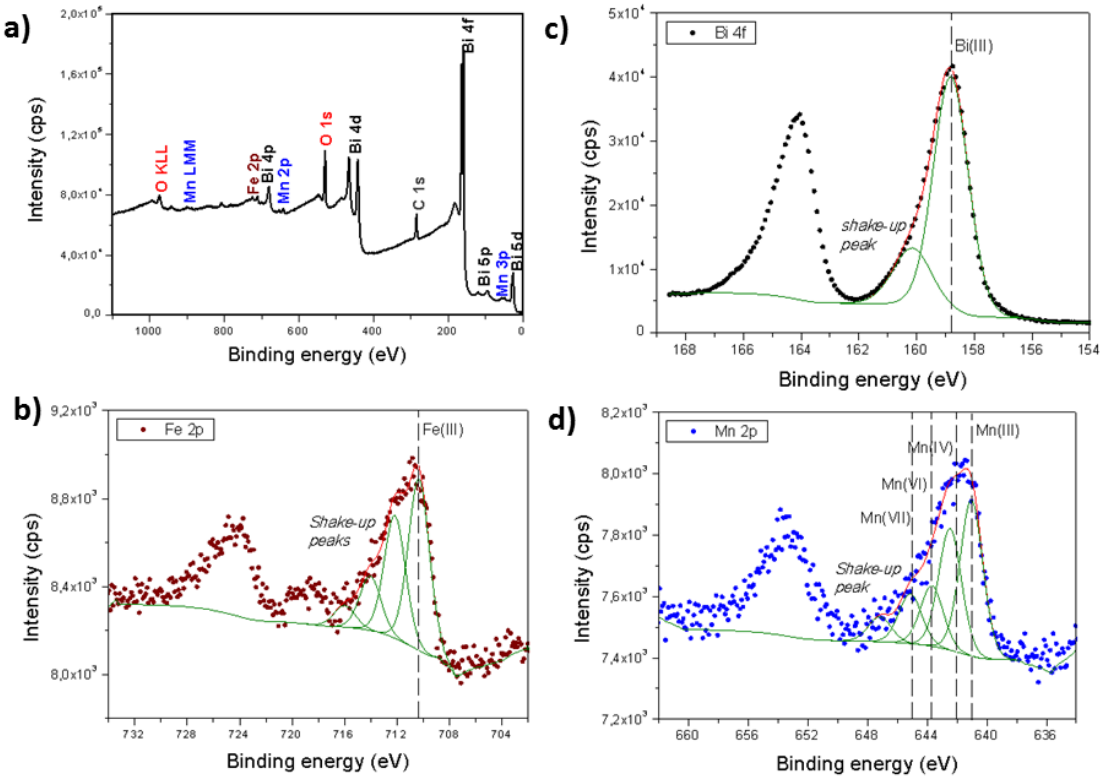

Figure 5.4: *XPS analysis of BFMO films, a) General survey of the film, b) Fe 2p fitting for the Fe3+, c)Bi 4f for Bi^{3+} and d) Mn 2p for Mn^{3+} and Mn^{4+}.*

5.4 Magnetic Measurements

In order to determine if the films produced in this thesis have the same functional properties of the reported in the literature, M(T), M(H) and VNA measurements are performed. **Figure 5.5** (a) shows the M(T) studies under a perpendicular applied field of at 1000 Oe and while M(H) loops are collected at room temperature, **Figure 5.5** b). In M(T) measurements temperature was swept from room temperature down to 5K. Previous studies by E.-M. Choi *et all* [**22**], have shown a high transition temperature of 600K for the highly strained BFMO films, in our case, temperatures above 300K were inaccessible, however, by carefully plotting the whole range of magnetization from 100K up to 300K and extrapolating the signal beyond 300K by a fitting of the Curie-Weiss formula, shown in the inset in **Figure 5.5a** , an estimation of the transition temperature can be obtained. In our case the estimated transition temperature is 730K much higher than the reported previously, but expected due to the model calculation.

Moreover, M(H) plots, confirm the ferromagnetic ordering of the film in the whole range of temperatures available, the total magnetization of the film was obtained after correcting the diamagnetic contribution of the substrate, **Appendix 3**, as 0.4 μB/f.u(Fe-Mn), a slightly lower value from the reported in the literature.[**22**].

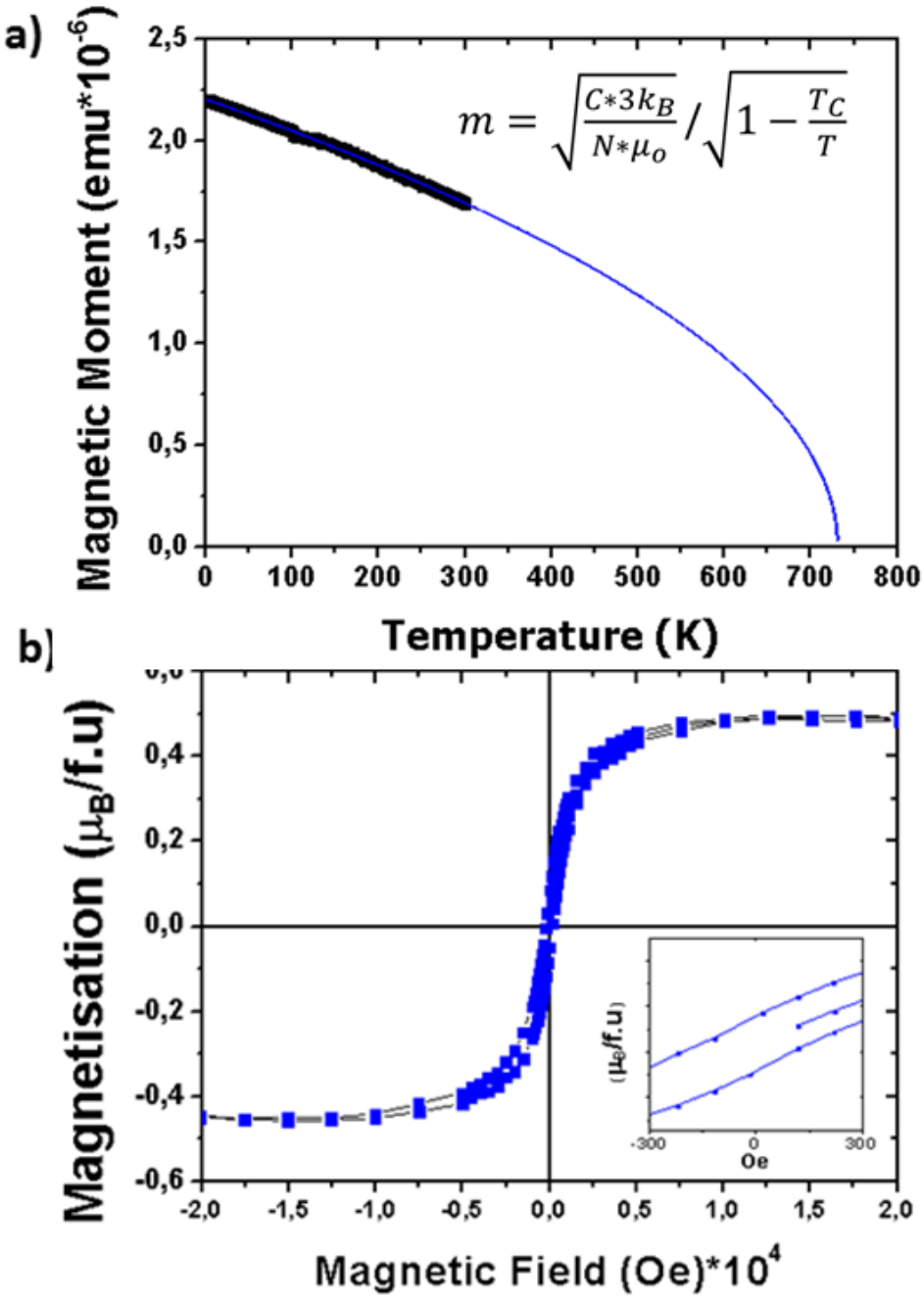

Figure 5.5: *Magnetic measurements performed on BFMO(010)/STO(001) samples. a) shows the FC measurement with the Curie Weiss fit and b) M(H) at 300K*

Magnetic moment at room temperature was found to be 57,42 emu/cm^3, this value was extracted using the Kittel equation, inscribed in **Figure 5.6**, fitted to the VNA-FMR results on the broad range of high frequencies, a similar methodology as the one shown in [**26**] in **Figure 5.6**. It is important to remark, that the origin of such magnetic response is still unknown, among some of the possible explanations are: valence recombination, small range ordered, check board like phases [**2**,**20**,**27**,**28**] and combinations among them, thus further complicating the elucidation of the origin of the magnetic response.

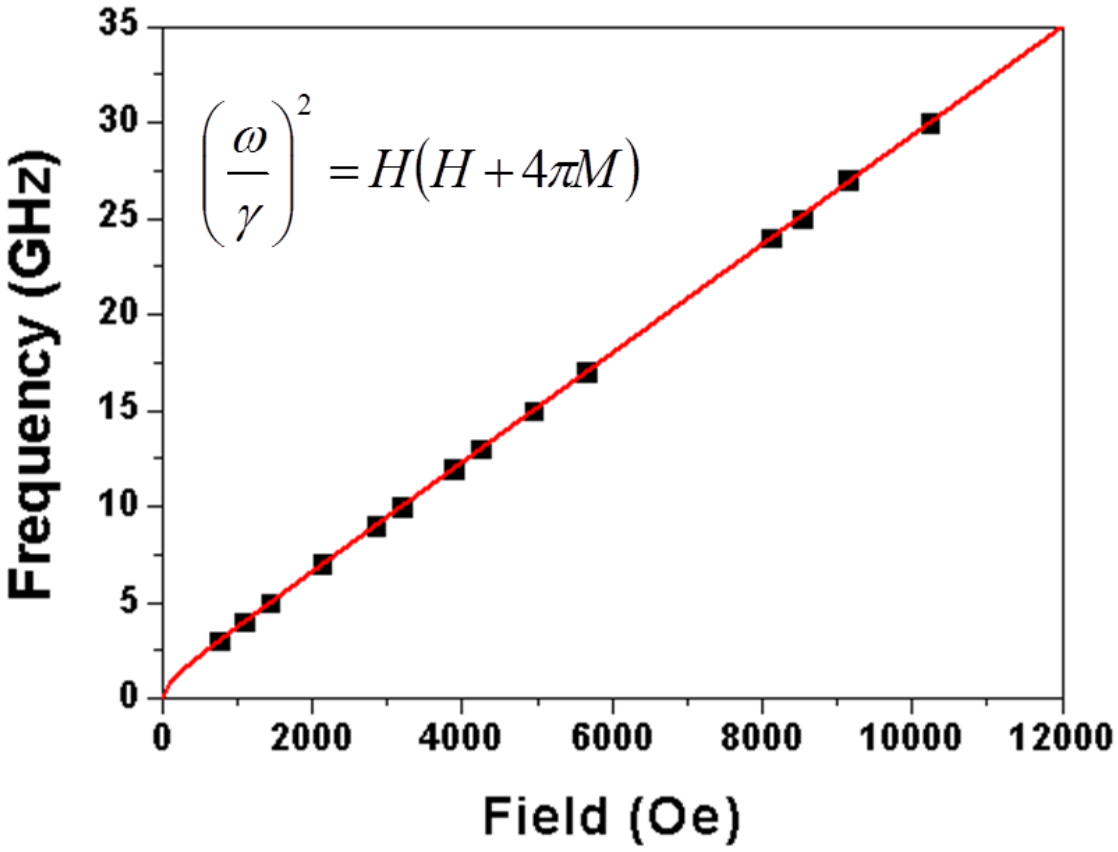

Figure 5.6: *VNA measurements performed at room temperature, red line shows the Kittel fitting.Where H is the external magnetic field, M is the magnetization and γ is the gyromagnetic ratio.*

5.5 Dielectric Measurements

This technique is used based on previous results of our group on similar perovskites like $BiFeO_3$, $BiMnO_3$ and Bi_2NiMnO_6, As described in the experimental section, samples were deposited on Nb-5%-STO(001), immediately after, platinum top

electrodes where deposited on using the sputtering technique and shadow masking method.

Samples were measured at the Department of Applied Physics of University of Barcelona using the multipurpose dielectric measurements system. Samples were measured in the range of 90K to 390K with a constant step of 10K, sweep frequency is 10Hz to 13 MHz. The typical measurement comprehends the permutation of several electrodes at room temperature in order of maximizing signal from the film.

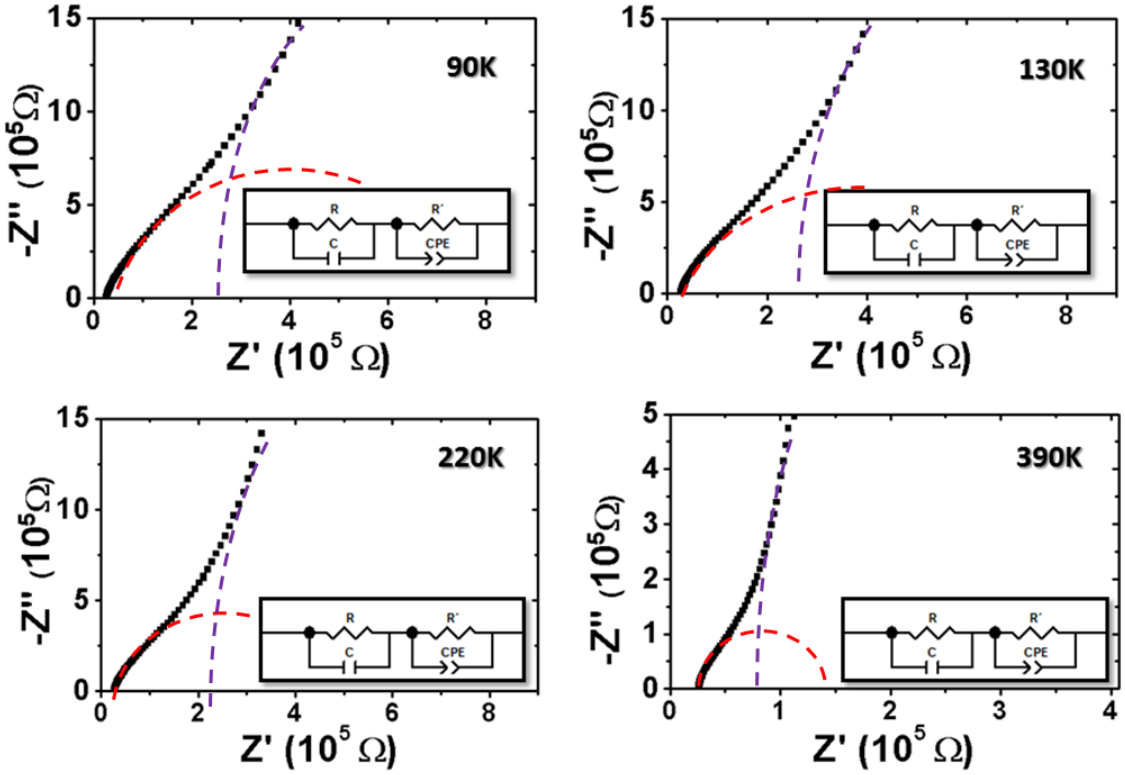

Figure 5.7: *Impedance spectroscopy measurements. showing the appearance of two independent mechanisms in the sample. High frequencies mechanisms, red dashed lines, are attributed to intrinsic properties of the film (R-CPE)*

Results are summarized in **Figure 5.7.** As mentioned in the experimental section, the Nyquist plot is very useful in the case of multiple mechanisms coexisting in the dielectric measurement. **Figure 5.7** shows the clear double contributions scenario, evidenced by the apparition of two semicircles in the Nyquist plot. As described in the literature [**29**–**31**], dielectric mechanism can be de convoluted by increasing the sweeping frequency. In this case, the high frequency contribution is clearly visible in

the whole range of temperature, thus allowing the analysis of the samples in a broader range of temperature.

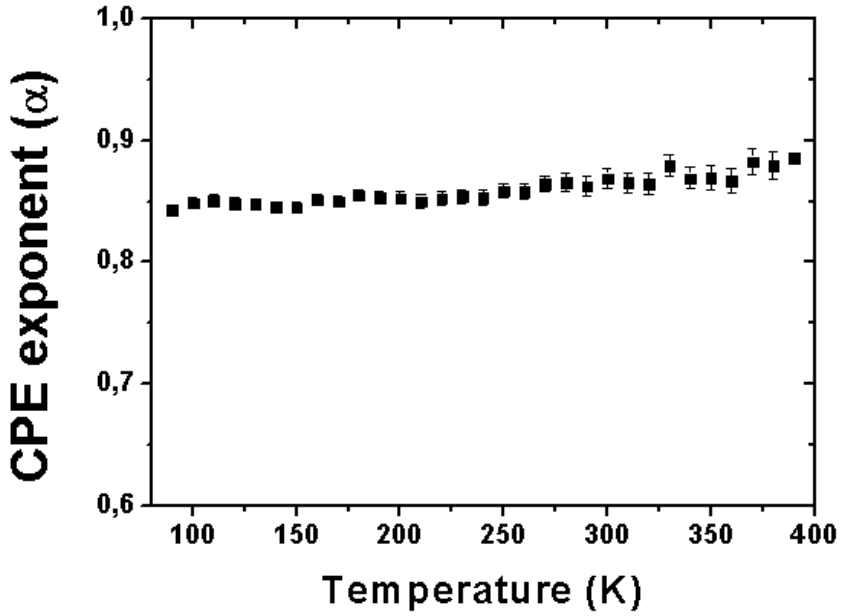

Figure 5.8: *Temperature dependence of the CPE exponent in the intrinsic mechanism.*

As described previously in the experimental section of this thesis, each of the semicircles corresponds to a resistor in parallel to a capacitor, R-C. However, as also described in this case the non-ideality of the thin film is better represented by the inclusion of a constant phase element, CPE. In **Equation 5.1,** where Q denotes the amplitude and α deals with the phase of the CPE, the typical values range from α ≤0,6-1, being α = 1 for an ideal capacitor, and in this case C=Q. Capacitance, *C*, and dielectric permittivity, ε, values can be obtained according to the relationship $C=(Q\cdot R)^{(1/\alpha)}/R$[**32**] , and C=εA/2t, where A accounts for the area of the electrode and t for the thickness of the sample.

$$Z^*_{R\text{-}CPE}=R/(1+RQ(iw)^{\alpha}) \qquad \textbf{Equation 5.1}$$

$$Z^* = R_I/(1+R_I.Q_I.(iw)^{\alpha}{}_I + R_E/(1+iw.R_E.C_E) \qquad \textbf{Equation 5.2}$$

Thus, the mentioned two contributions of the equivalent circuit have been fitted at each temperature, using expression in **Equation 5.2**. Where the first term correspond to the intrinsic ($_I$) contribution of BNMO and the second term deals with the extrinsic contributions ($_E$). The two contributions R-C and R-CPE of the equivalent circuit are

sketched in the insets of **Figure 5.7** where the line through data points corresponds to the performed fitting figuring out the goodness of the fit.

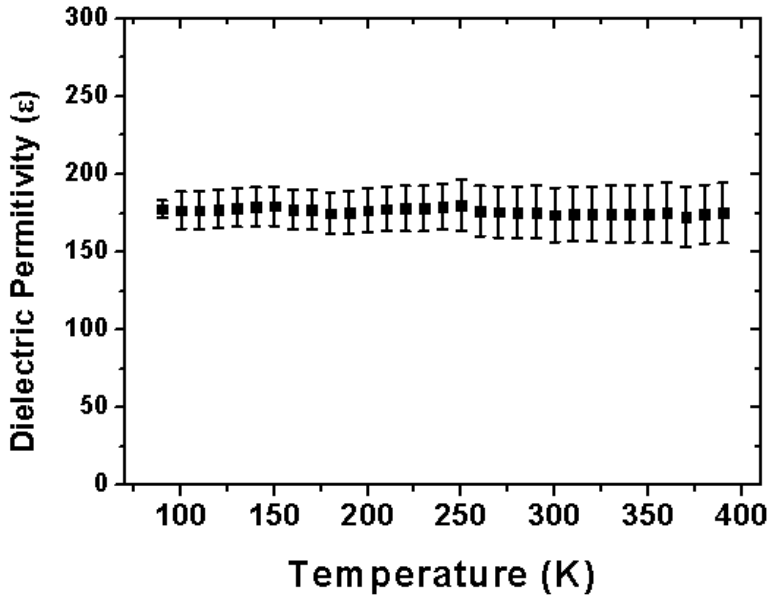

Figure 5.9: *Plot of the dielectric permittivity of BFMO(010) extracted from the complex impedance spectroscopy, as function of temperature.*

Fitted data corresponding to the intrinsic contribution of the film are shown in **Table 5.1**. The reliability of the results in the sample is corroborated by the low goodness-of-fit indicator $\chi 2$ which, in all temperature ranges, is $\sim 10^{-3}$, without any remarkable dispersion. A useful indicator of the behaviour of the film comes from plotting the exponent of the R-CPE element, which in fact tells about the non-ideality of the dielectric behaviour. The plot is shown **Figure 5.8**, the remarkable stability of the exponent shows a steady behaviour even at high temperatures.

The intrinsic dielectric permittivity of the film can then be plotted as function of temperature in the whole range. To extract the ε value for each temperature the set of equations described in **Equation 5.3** can be applied.

$$\varepsilon = C \cdot \left(\frac{2t}{\varepsilon_o A}\right)$$

$$C = \frac{(Q \cdot R)^{(1/\alpha)}}{R} \quad \textbf{Equation 5.3}$$

$$\rho = {A \cdot R}/{(2t)}$$

Where *A* accounts for the area of the electrode and *t* for the thickness of the sample, since the sample was measured on top-top configuration, this value is doubled. Dielectric permittivity is represented as function of temperature in **Figure 5.9**.

Fitting **R**esults BFMO(010)

T (K)	χ2	*Q* [$Fs^{\alpha-1}$]	Error *Q*	*α*	Error *α*	*R*(Ω)	Error R(Ω)
90	0,0021	3,40E-08	1,92E-09	0,842	0,0048	543,1	14,1
100	0,0018	3,18E-08	1,75E-09	0,848	0,0044	504,4	11,9
110	0,0017	3,11E-08	1,71E-09	0,850	0,0044	478,3	11,1
120	0,0016	3,26E-08	1,75E-09	0,847	0,0044	470,5	10,8
130	0,0017	3,29E-08	2,20E-09	0,847	0,0046	449,0	11,4
140	0,0015	3,43E-08	1,80E-09	0,845	0,0044	439,7	9,7
150	0,0015	3,48E-08	1,90E-09	0,844	0,0044	427,3	9,6
160	0,0015	3,19E-08	2,04E-09	0,851	0,0045	403,0	9,4
170	0,0016	3,26E-08	1,90E-09	0,849	0,0047	388,2	8,8
180	0,0016	3,04E-08	1,87E-09	0,854	0,0047	367,3	8,3
190	0,0016	3,14E-08	1,97E-09	0,853	0,0049	352,7	8,0
200	0,0015	3,21E-08	2,02E-09	0,852	0,0048	336,1	7,5
210	0,0015	3,37E-08	2,05E-09	0,849	0,0049	324,1	7,2
220	0,0017	3,28E-08	2,48E-09	0,852	0,0053	307,0	7,7
230	0,0016	3,24E-08	2,09E-09	0,854	0,0052	287,1	6,4
240	0,0017	3,32E-08	2,29E-09	0,852	0,0056	276,5	6,5
250	0,0016	3,16E-08	2,32E-09	0,858	0,0057	238,4	5,5
260	0,0017	3,15E-08	2,32E-09	0,858	0,0061	222,6	5,2
270	0,0017	2,91E-08	2,50E-09	0,864	0,0063	208,4	5
280	0,0017	2,89E-08	2,48E-09	0,865	0,0065	191,3	4,5
290	0,0019	3,06E-08	2,69E-09	0,862	0,0073	170,1	4,2
300	0,0020	2,81E-08	2,88E-09	0,868	0,0076	155,5	3,9
310	0,0019	2,99E-08	2,78E-09	0,865	0,0077	145,1	3,5
320	0,0020	3,06E-08	2,81E-09	0,864	0,0082	133,2	3,3
330	0,0020	2,50E-08	2,80E-09	0,879	0,0086	119,6	3,0
340	0,0019	2,94E-08	2,97E-09	0,868	0,0088	112,3	2,8
350	0,0019	2,95E-08	2,99E-09	0,869	0,0089	104,4	2,5
360	0,0020	3,12E-08	3,44E-09	0,866	0,0098	96,53	2,5
370	0,0020	2,46E-08	2,98E-09	0,88	0,01	85,91	2,2
380	0,0019	2,62E-08	3,24E-09	0,87	0,01	79,48	2
390	0,0018	2,44E-08	3,26E-09	0,88	0,01	70,98	1,8

Table 5.1: ***Fitting results of the high-frequency R-CPE element, sketched in Figure. 5.7.***

Having characterized the dielectric properties of the BFMO(010) film, a Neodymium Iron Boron permannet magnet, with maximum magnetization of 0.4 T is

placed under the sample holder. In this experiment, the same electrodes and conditions are used to measure the sample under the effect of external magnetic field.

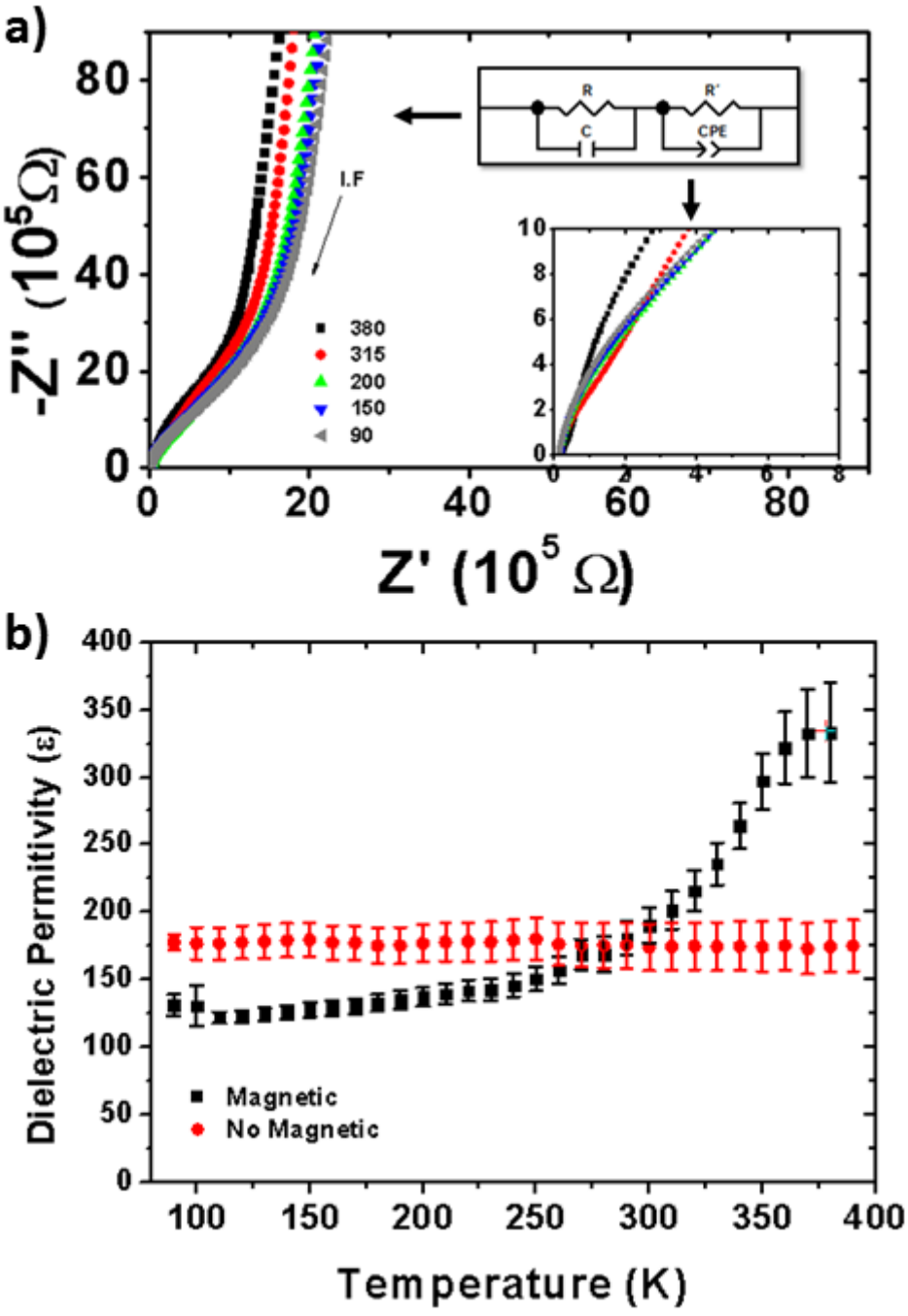

Figure 5.10: *a) Compilation of Nyquist plots collected under magnetic field b) Plot of the dielectric permittivity of BFMO(010) extracted from the complex impedance spectroscopy for both magnetic and without magnetic field measurements.*

Measurements performed under applied magnetic field show similar behaviour as the one shown in **Figure 5.10 a)**, with two mechanisms present, the intrinsic mechanism found at higher frequencies and the extrinsic one at lower frequencies. However, a clear effect of the magnetic field is observed in the dielectric measurements, as shown in **Figure 5.10b**, dielectric permittivity is extracted according to **Equation 5.3** using the data presented in **Table 5.2**.

Fitting **R**esults With Magnetic Field BFMO(010)

T (K)	χ2	*Q* [$Fs^{\alpha-1}$]	Error *Q*	α	Error α	*R*(Ω)	Error R(Ω)
90	0,0006	7,85E-09	2,87E-10	0,930	0,0034	1118	29,3
100	0,0053	7,84E-09	5,95E-10	0,930	0,0056	1073	36,6
110	0,0008	1,09E-08	2,59E-10	0,896	0,0017	1487	17,2
120	0,0008	1,12E-08	2,76E-10	0,895	0,0017	1473	17,6
130	0,0009	1,15E-08	2,96E-10	0,893	0,0018	1460	18,1
140	0,0009	1,22E-08	3,26E-10	0,890	0,0019	1445	18,5
150	0,0010	1,26E-08	3,55E-10	0,888	0,0020	1427	19,2
160	0,0011	1,30E-08	3,78E-10	0,886	0,0020	1410	19,6
170	0,0011	1,31E-08	3,94E-10	0,887	0,0021	1380	19,917
180	0,0012	1,41E-08	4,40E-10	0,882	0,0022	1364	20,6
190	0,0013	1,48E-08	4,84E-10	0,880	0,0023	1348	21,3
200	0,0014	1,57E-08	5,30E-10	0,876	0,0024	1349	22,3
210	0,0015	1,65E-08	5,79E-10	0,873	0,0025	1340	23,1
220	0,0016	1,74E-08	6,34E-10	0,870	0,0026	1334	24,0
230	0,0016	1,78E-08	6,48E-10	0,869	0,0026	1337	24,0
240	0,0017	1,91E-08	7,23E-10	0,865	0,0027	1319	25,2
250	0,0019	2,09E-08	8,30E-10	0,860	0,0028	1306	26,6
260	0,0021	2,37E-08	9,97E-10	0,852	0,003	1305	28,7
270	0,0020	3,00E-08	1,27E-09	0,837	0,003	1343	31,3
280	0,0028	3,11E-08	1,46E-09	0,834	0,003	1414	36,2
290	0,0023	3,90E-08	1,67E-09	0,819	0,003	1483	37,4
300	0,0023	4,42E-08	1,91E-09	0,812	0,003	1487	39,6
310	0,0024	5,12E-08	2,19E-09	0,803	0,003	1541	43,2
320	0,0023	6,05E-08	2,53E-09	0,793	0,003	1607	47,1
330	0,0022	7,31E-08	2,91E-09	0,781	0,002	1732	53,5
340	0,0021	8,90E-08	3,40E-09	0,770	0,002	1877	62,9
350	0,0025	1,02E-07	4,19E-09	0,764	0,002	2028	83,2
360	0,0036	1,01E-07	4,94E-09	0,770	0,003	2060	107,5
370	0,0053	8,15E-08	4,88E-09	0,793	0,004	1907	119,9
380	0,0064	5,77E-08	3,99E-09	0,827	0,005	1603	106,4
390	0,0006	7,85E-09	2,87E-10	0,930	0,003	1118	29,3

Table 5.1: ***Fitting results of the high-frequency R-CPE element, sketched in Figure. 5.10a .***

In the **Figure 5.10 b** change on the dielectric permittivity can be observed, for values below room temperature the dielectric permittivity decreases in 23% from the original value extracted from the sample without magnetic field. The dielectric permittivity continuously increases overpassing the previous values at around 300K where keeps rising to almost double its value around 390K, as shown in **Figure 5.11**.

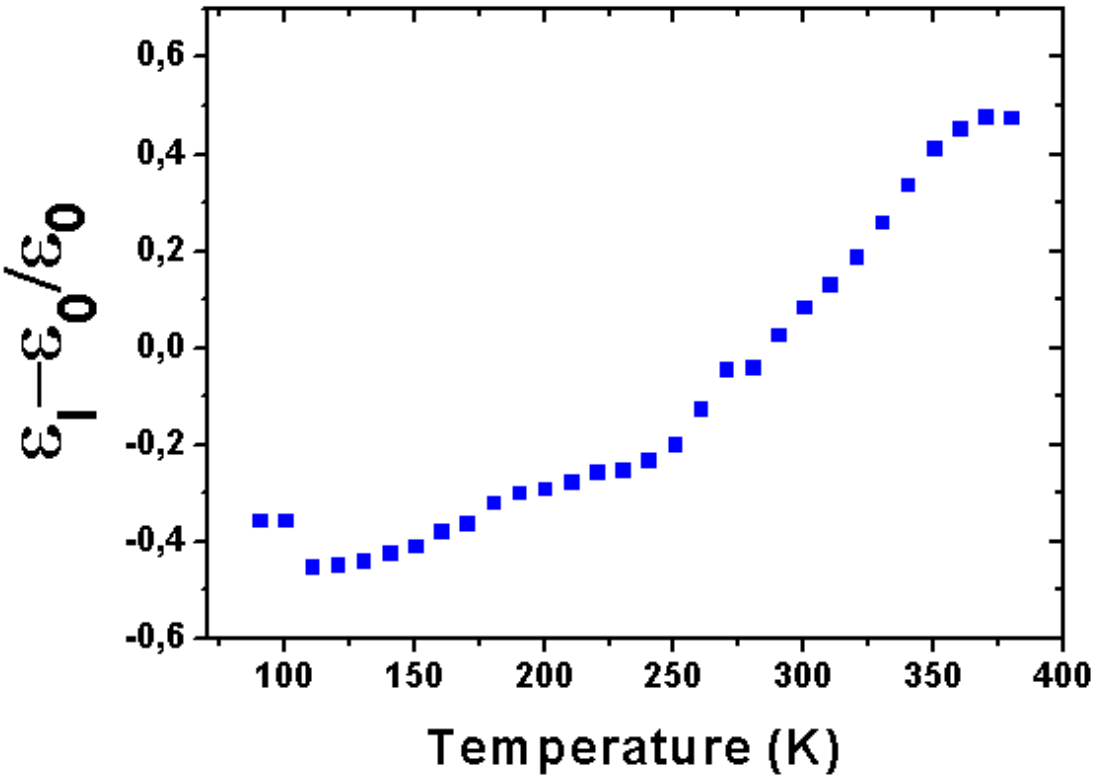

Figure 5.11: *Change on the dielectric permittivity in the sample measured under magnetic field.*

Although the origin of this anomalous behavior is uncertain, the possibility that it arouses from extrinsic effects is prevented by the model used. The behavior observed shows the intrinsic relationship between dielectric permittivity and magnetic field.

To conclude, is important to remark that no FE cycles were achieved on the sample at the prepared thickness, however the fact that all ferroelectric cycles shown in the literature of this material are shown for samples with almost 120 nm, suggest that the real ferroelectric nature of the strained BFMO is still disputable.

5.6 Conclusions of this chapter

- Highly strained $Bi(Mn_{0.5}Fe_{0.5)}O_3$ (BFMO) thin films were successfully stabilized on STO(001) substrates by PLD. Deposit conditions were adjusted in order to prevent losses in bismuth content.
- Films are highly strained and with the epitaxial an epitaxial relationship of [100]BFMO(010)||[100]STO(001).
- The ferromagnetic nature of the film was studied by VNA and SQUID techniques, revealing a room temperature ferromagnetism with a magnetic susceptibility of 57,42 emu and a magnetic moment of 0.4 μB/f.u(Fe-Mn). The origin of the ferromagnetism was attributed to the high mixture of valences of Mn. No long range B-site ordering was observed,
- Dielectric measurements performed from 100 to 400K show a well-defined decoupling between intrinsic and extrinsic mechanisms. The dielectric constant was found to be ε=175, in close agreement with the literature.
- Magneto impedance spectroscopy showed a direct effect influence of external magnetic field on the dielectric constant of the film, showing a maximum few degrees below 400K.
- The origin of this anomalous behavior is not well understood, although its origin is certainly intrinsic of the film, due to the observed features in the Nyquist plot.
- Further studies are needed in order to fully understand the role of external magnetic field on the dielectric properties of the highly strained BFMO thin films.

References

[1] Catalan, G. and Scott, J.F. (2009) **Physics and Applications of Bismuth Ferrite**. *Advanced Materials*, **21**, 2463–85. http://dx.doi.org/10.1002/adma.200802849

[2] Chen, A., Zhou, H., Bi, Z., Zhu, Y., Luo, Z., Bayraktaroglu, A. et al. (2013) **A new class of room-temperature multiferroic thin films with bismuth-based supercell structure.** *Advanced Materials (Deerfield Beach, Fla)*, **25**, 1028–32. http://dx.doi.org/10.1002/adma.201203051

[3] Kimura, T., Kawamoto, S., Yamada, I., Azuma, M., Takano, M. and Tokura, Y. (2003) **Magnetocapacitance effect in multiferroic BiMnO_{3}**. *Physical Review B*, **67**, 180401. http://dx.doi.org/10.1103/PhysRevB.67.180401

[4] Gajek, M., Bibes, M., Barthélémy, a., Bouzehouane, K., Fusil, S., Varela, M. et al. (2005) **Spin filtering through ferromagnetic BiMnO3 tunnel barriers**. *Physical Review B*, **72**, 020406. http://dx.doi.org/10.1103/PhysRevB.72.020406

[5] Belik, A. a. (2013) **Origin of magnetization reversal and exchange bias phenomena in solid solutions of BiFeO3-BiMnO3: intrinsic or extrinsic?** *Inorganic Chemistry*, **52**, 2015–21. http://dx.doi.org/10.1021/ic302384j

[6] Ederer, C. and Fennie, C.J. (2008) **Electric-field switchable magnetization via the Dzyaloshinskii–Moriya interaction: FeTiO 3 versus BiFeO 3**. *Journal of Physics: Condensed Matter*, **20**, 434219. http://dx.doi.org/10.1088/0953-8984/20/43/434219

[7] Jeong, J., Le, M.D., Bourges, P., Petit, S., Furukawa, S., Kim, S.-A. et al. (2014) **Temperature-Dependent Interplay of Dzyaloshinskii-Moriya Interaction and Single-Ion Anisotropy in Multiferroic BiFeO 3**. *Physical Review Letters*, American Physical Society. **113**, 107202. http://dx.doi.org/10.1103/PhysRevLett.113.107202

[8] Sergienko, I.A. and Dagotto, E. (2006) **Role of the Dzyaloshinskii-Moriya interaction in multiferroic perovskites**. *Physical Review B*, **73**, 094434. http://dx.doi.org/10.1103/PhysRevB.73.094434

[9] Park, J., Lee, S.-H., Lee, S., Gozzo, F., Kimura, H., Noda, Y. et al. (2011) **Magnetoelectric Feedback among Magnetic Order, Polarization, and Lattice in Multiferroic BiFeO 3**. *Journal of the Physical Society of Japan*, **80**, 114714. http://dx.doi.org/10.1143/JPSJ.80.114714

[10] Grizalez, M., Martinez, E., Caicedo, J., Heiras, J. and Prieto, P. (2008) **Occurrence of ferroelectricity in epitaxial BiMnO3 thin films**. *Microelectronics Journal*, **39**, 1308–10. http://dx.doi.org/10.1016/j.mejo.2008.01.023

[11] Chi, Z.H., Xiao, C.J., Feng, S.M., Li, F.Y., Jin, C.Q., Wang, X.H. et al. (2005) **Manifestation of ferroelectromagnetism in multiferroic BiMnO[sub 3]**. *Journal of Applied Physics*, **98**, 103519. http://dx.doi.org/10.1063/1.2131193

[12] Chi, Z.H., Yang, H., Feng, S.M., Li, F.Y., Yu, R.C. and Jin, C.Q. (2007) **Room-temperature ferroelectric polarization in multiferroic BiMnO3**. *Journal of Magnetism and Magnetic Materials*, **310**, e358–60. http://dx.doi.org/10.1016/j.jmmm.2006.10.335

[13] Padhan, P., LeClair, P., Gupta, A. and Srinivasan, G. (2008) **Magnetodielectric response in epitaxial thin films of multiferroic Bi 2 NiMnO 6**. *Journal of Physics: Condensed Matter*, **20**, 355003. http://dx.doi.org/10.1088/0953-8984/20/35/355003

[14] Langenberg, E., Varela, M., García-Cuenca, M. V., Ferrater, C., Polo, M.C., Fina, I. et al. (2009) **Epitaxial thin films of (Bi0.9La0.1)2NiMnO6 obtained by pulsed laser deposition**. *Journal of Magnetism and Magnetic Materials*, **321**, 1748–53. http://dx.doi.org/10.1016/j.jmmm.2009.02.005

[15] Langenberg, E., Fina, I., Gemeiner, P., Dkhil, B., Fàbrega, L., Varela, M. et al. (2012) **Ferroelectric phase transition in strained multiferroic (Bi0.9La0.1)2NiMnO6 thin films**. *Applied Physics Letters*, **100**, 022902. http://dx.doi.org/10.1063/1.3675869

[16] Luo, B.-C., Chen, C.-L., Xu, Z. and Xie, Q. (2010) **Effect of Cr substitution on the multiferroic properties of BiFe1−xCrxO3 compounds**. *Physics Letters A*, **374**, 4265–8. http://dx.doi.org/10.1016/j.physleta.2010.08.045

[17] Azuma, M., Takata, K., Saito, T., Ishiwata, S., Shimakawa, Y. and Takano, M. (2005) **Designed ferromagnetic, ferroelectric Bi2NiMnO6**. *Journal of the American Chemical Society*, **127**, 8889–92. http://dx.doi.org/10.1021/ja0512576

[18] Rajeevan, N.E., Kumar, R., Shukla, D.K., Thakur, P., Brookes, N.B., Chae, K.H. et al. (2009) **Bi-substitution-induced magnetic moment distribution in spinel Bi(x)Co(2-x)MnO(4) multiferroic.** *Journal of Physics Condensed Matter : An Institute of Physics Journal*, **21**, 406006. http://dx.doi.org/10.1088/0953-8984/21/40/406006

[19] Belik, A.A., Abakumov, A.M., Tsirlin, A.A., Hadermann, J., Kim, J., Tendeloo, G. Van et al. (2011) **Structure and Magnetic Properties of BiFe 0 . 75 Mn 0 . 25 O 3 Perovskite Prepared at Ambient and High Pressure**. 4505–14.

[20] Cortie, D.L., Stampfl, a. P.J., Klose, F., Du, Y., Wang, X.L., Zhao, H.Y. et al. (2012) **The magnetic structure of an epitaxial BiMn[sub 0.5]Fe[sub 0.5]O[sub 3] thin film on SrTiO[sub 3] (001) studied with neutron diffraction**. *Applied Physics Letters*, **101**, 172404. http://dx.doi.org/10.1063/1.4762818

[21] Langenberg Pérez, E. (2013) **Growth and characterisation of Bi-based multiferroic thin films** [Internet]. Universitat de Barcelona.

[22] Choi, E.-M., Patnaik, S., Weal, E., Sahonta, S.-L., Wang, H., Bi, Z. et al. (2011) **Strong room temperature magnetism in highly resistive strained thin films of BiFe[sub 0.5]Mn[sub 0.5]O[sub 3]**. *Applied Physics Letters*, AIP Publishing. **98**, 012509. http://dx.doi.org/10.1063/1.3540683

[23] Prokhorov, V.G., Kaminsky, G.G., Kim, J.M., Yoo, Y.J., Lee, Y.P., Svetchnikov, V.L. et al. (2012) **Evidence of the Griffiths phase in multiferroic BiMnO3 and BiFe0.5Mn0.5O3 films**. *Low Temperature Physics*, **38**, 413. http://dx.doi.org/10.1063/1.4709440

[24] Ianculescu, A., Gheorghiu, F.P., Postolache, P., Oprea, O. and Mitoseriu, L. (2010) **The role of doping on the structural and functional properties of BiFe1−xMnxO3 magnetoelectric ceramics**. *Journal of Alloys and Compounds*, **504**, 420–6. http://dx.doi.org/10.1016/j.jallcom.2010.05.135

[25] Bi, L., Taussig, A., Kim, H.-S., Wang, L., Dionne, G., Bono, D. et al. (2008) **Structural, magnetic, and optical properties of BiFeO3 and Bi2FeMnO6 epitaxial thin films: An experimental and first-principles study**. *Physical Review B*, **78**, 104106. http://dx.doi.org/10.1103/PhysRevB.78.104106

[26] Neudecker, I., Woltersdorf, G., Heinrich, B., Okuno, T., Gubbiotti, G. and Back, C.H. (2006) **Comparison of frequency, field, and time domain ferromagnetic resonance methods**. *Journal of Magnetism and Magnetic Materials*, **307**, 148–56. http://dx.doi.org/10.1016/j.jmmm.2006.03.060

[27] Kubota, M., Oka, K., Yabuta, H., Miura, K. and Azuma, M. (2013) **Structure and Magnetic Properties of BiFe 1 −**.

[28] Ablat, A., Muhemmed, E., Si, C., Wang, J., Qian, H., Wu, R. et al. (2012) **Electronic Structure of BiFe1−xMnxO3 Thin Films Investigated by X-Ray**

Absorption Spectroscopy. *Journal of Nanomaterials*, **2012**, 1–7. http://dx.doi.org/10.1155/2012/123438

[29] Schmidt, R., Ventura, J., Langenberg, E., Nemes, N.M., Munuera, C., Varela, M. et al. (2012) **Magnetoimpedance spectroscopy of epitaxial multiferroic thin films**. *Physical Review B*, **86**, 035113. http://dx.doi.org/10.1103/PhysRevB.86.035113

[30] Langenberg, E., Fina, I., Ventura, J., Noheda, B., Varela, M. and Fontcuberta, J. (2012) **Dielectric properties of (Bi0.9La0.1)2NiMnO6 thin films: Determining the intrinsic electric and magnetoelectric response**. *Physical Review B*, **86**, 085108. http://dx.doi.org/10.1103/PhysRevB.86.085108

[31] Kakarla, D.C., Jyothinagaram, K.M., Das, A.K. and Adyam, V. (2014) **Dielectric and Magnetodielectric Properties of R 2 NiMnO 6 (R = Nd,Eu,Gd,Dy, and Y)**. Viehland D, editor. *Journal of the American Ceramic Society*, Blackwell Publishing Inc. **97**, 2858–66. http://dx.doi.org/10.1111/jace.13039

[32] Berkemeier, F., Abouzari, M. and Schmitz, G. (2007) **Thickness-dependent dc conductivity of lithium borate glasses**. *Physical Review B*, **76**, 024205. http://dx.doi.org/10.1103/PhysRevB.76.024205

CONCLUSIONS

General Conclusions of the Thesis

- Ferromagnetic perovskites thin films of $Y(Ni_{0.5}Mn_{0.5})O_3$ were successfully deposited by PLD. The films shown epitaxial growth on STO(001), (110) and (111) single crystalline substrates. A clear influence of substrate temperature on the intensity of the YNMO(00l) peaks and the out–of-plane parameter was observed, while laser frequency showed only to take part at higher ablation frequencies. The epitaxial relationships and strain were quantified by means of reciprocal space maps images, tabulated and confronted with similar studies on $YMnO_3$. The partial substitution of Mn with Ni, was observed to reduce the unit cell volume thus reducing the mismatch between the substrate and the YNMO, however keeping a remarkably similarity to the growth observed in orthorhombic $YMnO_3$, contrary to the previously reported experimental data and moreover corroborating that absence of domains presenting in-plane stress of the same sign. Additionally, the pseudo cubic indexing relations were addressed in order to exploit the appearance of multiple in-plane domains in the samples for further applications and studies.
- YNMO growth mechanism was found to be a clear 3D columnar growth, where films with multiple in-plane orientations showed large single domain grains that maintain their epitaxial relationships along growing direction. Also, by correlating the two in-plane domains obtained by X-ray analysis on the YNMO(001)/STO(001) samples, with the morphology observed in the AFM images, using a simple numerical and geometrical approach, it was possible to

determine that the moulds observed by AFM were indeed single in-plane domains. This feature was previously observed in the literature in similar films, but the existence of the two-in plane domains was not reported, thus not showing a direct relationship with the inner structure of the film and the orthorhombic to pseudo cubic transformation. Moreover, the presence of small crystallites was observed in the samples with multiple in-plane domains, their origin is attributed to the higher surface ad atom mobility provided by the lower ablation rate and high substrate temperature, which allows the crystallites, to stop growing at the coalescence point of the film. Sharp interfaces and correct stoichiometric composition of the films are the norm for all the samples.

- Functional magnetic measurements corroborate the ferromagnetic nature of the films with a magnetic transition at 95K and a magnetic moment of 4,58 μ_B/f.u in concordance with previously reported data, although lower from the theoretical 5 μB/f.u expected.
- Temperature activated Ti diffusion was detected on samples of YNMO(101)/STO(111) the diffusion coefficient is found to be $1.2\pm0.9\ 10^{-15}$ cm^2/s at 750^0C. The diffusion can be controlled by increasing the deposition rate of the film from 2 to 10Hz.
- In this thesis the coexistence of both ferromagnetic and ferroelectric ordering in the YNMO perovskite has been experimentally proven, with a robust remanent polarization of $P_R \approx 3\ \mu C/cm^2$, (and $M_R \approx 4\ \mu_B$/ f.u comparable with the literature). The detection of a dielectric anomaly ≈100 K in both samples, very close to the ferromagnetic transition, indicates magnetoelectric coupling, signature of the correlation between the found ferroelectric nature of the material at low temperature and the magnetic ordering.
- Ferromagnetic perovskites thin films of $R(Ni_{0.5}Mn_{0.5})O_3$ R=Sm (SMNO), Nd (NMNO) & Pr (PRMNO), were successfully deposited by PLD. The films of $Sm(Ni_{0.5}Mn_{0.5})O_3$ shown epitaxial growth on STO(001) with two out of plane crystalline domains, SNMO(001) and SNMO(010), the epitaxial relationship was studied and determined as [100]SMNO(001) ‖ [011]STO(001), and [100]SMNO(010) ‖ [011]STO(001).
- Thin films of $R(Ni_{0.5}Mn_{0.5})O_3$ R=Sm (SMNO), Nd (NMNO) & Pr (PRMNO) show similar window of deposition parameters as the ones studied for YNMO thin films,

with an optimal deposition temperature of 750°C. The effect of deposition temperature on the crystalline structure of the films was discussed and described, as a rule the grain size distribution and intensity of the peaks would increase with temperature, while the FWHM decreases showing the increase of crystalline quality of the film.

- Thin films of $Pr(Ni_{0.5}Mn_{0.5})O_3$ and $Nd(Ni_{0.5}Mn_{0.5})O_3$ show a highly strained growth, fitting the substrate geometry rather closely, as compared with thin films of YNMO and SMNMO who present multiple in-plane and out plane domains. This observation allows to investigate both ionic radius and lattice b/a ratio as a function of the epitaxial relationship of the films on STO(001). Categorizing the b/c ratio as an important parameter for the fully epitaxial thin films of the RNMO family. The value for single domain thin films is found to be lower than b/c=1.03. It is assumed that b/c radius inferior to 0.97 would have similar effect in the thin films for a cube on cube epitaxial relationship.
- Functional magnetic measurements corroborate the ferromagnetic nature of the films with a magnetic transition close to the ones reported in bulk. SMNO 175K with a magnetic moment of 4,52 μ_B/f.u in concordance with previously reported data, although lower from the theoretical 6,6 μ_B/f.u expected. PNMO, 200K with a magnetic moment of 4,79 μ_B/f.u in concordance with previously reported data, although lower from the theoretical 11,6 μ_B/f.u expected and finally, NNMO, 190K with a magnetic moment of 5,15 μB/f.u in concordance with previously reported data, although lower from the theoretical 11,8 μ_B/f.u expected. The measured magnetization values suggest that the paramagnetic ions do not play any important part on the total magnetization of the unit cell, while the main magnetic response seems to remain close to the values reported for Ni-Mn.
- Highly strained $Bi(Mn_{0.5}Fe_{0.5})O_3$ (BFMO) thin films were successfully stabilized on STO(001) substrates by PLD.
- Films show similar crystalline features as the ones reported in the literature, with a highly strained BFMO an epitaxial relationship of [100]BFMO(010)||[100]STO(001).
- The ferromagnetic nature of the film was studied by VNA and SQUID techniques, revealing a room temperature ferromagnetism with a 57,42 emu/cm^3 and 0.4

μB/f.u(Fe-Mn). The origin of the ferromagnetism was attributed to the high mixture of valences of Mn. No long range B-site ordering was observed,

- Dielectric measurements performed from 100 to 400K show a well-defined decoupling between intrinsic and extrinsic mechanisms. The dielectric constant was found to be ε=175, in close agreement with the literature.
- Magneto impedance spectroscopy showed a direct influence of external magnetic field on the dielectric constant of the film, showing a maximum few degrees below 400K.

APPENDIX 1

Dimensions of the Sintered Target

Targets were made by a stoichiometric mixture according to the chemical composition described in **Table A.1.1**.

CHEMICAL STOICHIOMETRY

Rare Earth Oxide		Transition Metal Oxide			→	Re_2NiMnO_6
Y_2O_3	+	NiO	+	MnO_2	→	Y_2NiMnO_6
Pr_2O_3	+	NiO	+	MnO_2	→	Pr_2NiMnO_6
Nd_2O_3	+	NiO	+	MnO_2	→	Nd_2NiMnO_6
Sm_2O_3	+	NiO	+	MnO_2	→	Sm_2NiMnO_6

Table A.1.1: *Collective stoichiometric formulas of R_2NiMnO_3 targets.*

The following considerations, **Table A.2**, regarding weight and molecular mass were taken into account.

LATICCE CONSTANTS

R_2NiMnO_6	Lattice parameters	ρ (g/cm^3)
Y_2NiMnO_6	a = 5.2285(1) Å, b = 5.5518(1) Å, c = 7.4872(2) Å,β = 89.744(1)°, V = 217.337(1) Å^3	11,8408
Pr_2NiMnO_6	a = 5.4453(8) Å, b = 5.4701(7) Å, c = 7.6966(1) Å,β = 90.030(3)°, V = 229.257(7) Å^3	14,2386
Nd_2NiMnO_6	a = 5.4145(9) Å, b = 5.4842(1) Å, c = 7.6742(1) Å,β = 90.011(2)°, V = 227.883(9) Å^3	14,5188
Sm_2NiMnO_6	a = 5.3524(9) Å, b = 5.5119(1) Å, c = 7.6103(1) Å,β = 90.034(3)°, V = 224.522(1) Å^3	15,0983

Table A.1.2 *Lattice constants of RNMO bulk materials and their density ρ.*

Additionally the molecular weight for each oxide was taken into account, **Table A.1.3,** notice the oxygen atom is accounted with a molecular weight of 15,9994.

OXIDES WEIGHT & PURITY

Compound	Weight	Purity
NiO	58,69340	99,000%
MnO_2	54,93805	99,900%
Y_2O_3	88,90585	99,999%
Pr_2O_3	140,90766	99,900%
Nd_2O_3	144,24200	99,900%
Sm_2O_3	150,36000	99,900%

Table A.1.3 *Compendium of oxides, molecular weight and purity.*

Pellets were compressed in a cylindrical piston of 2.54 cm in diameter (1 inch), the weight of oxides was calculated according to the **Equation A.1.1**, & **Equation A.1.2** so the total density of each pellet was of 60%.

$$M = \frac{\rho * 60\% * T_H * \pi * T_R^2}{mol_{RNMO}} \quad \textbf{Equation A.1.1}$$

Where ρ is the density of the RNMO unit cell, T_H is the target high (standardized as 3 mm), T_R is the target radius and mol_{RNMO} is the molecular weight of 1 mol of R_2NiMnO_6. Having obtained the molecular mass (*M*), grams proportion for each oxide is easily obtained by:

$$M * mol_{Re} + M * mol_{NiO} + M * mol_{MnO} = g_{RNMO} \quad \textbf{Equation A.1.2}$$

Finally target oxide proportions as summarized in the **Table A.1.4**

SOLID SOLUTION

RNMO	Re_2O_3 (g)	NiO(g)	MnO_2(g)
Y_2NiMnO_6	6,280696	2,098497	2,420489
Pr_2NiMnO_6	8,703455	1,988989	2,294178
Nd_2NiMnO_6	8,930240	2,002371	2,309614
Sm_2NiMnO_6	9,394017	2,032429	2,344284

Table A.1.4 *Oxide proportions per pellet, values extracted from **Equation A.1.2**.*

APPENDIX 2

Lattice Parameters From XRD Data

Symmetric XRD scans

In Chapter 2 X-ray diffraction was carefully introduced and the Bragg`s law described. In highly textured thin films, such in the case of films described in this thesis, the family of plane parallel to the substrate are the only ones diffracting, i.e: YNMO(00*l*)/STO(00*l*), therefore one can easily extract the out of plane parameter using the aforementioned equation and solving it for d(00*l*) as shown in the **Equation A.2.1**:

$$d_{(00l)} = \frac{c}{l} = \frac{\lambda}{2\sin(\frac{2\theta_{(00l)}}{2})} \quad \textbf{Equation A.2.1}$$

Where λ is the X-Ray wavelength, d is the interplanar distance of the 00*l* planes and *c* is the out of plane parameter. This equation allows the extraction of such parameter for cubic, orthorhombic and tetragonal crystal systems. However, the extraction the c value can be affected by many experimental factors such as: i) misalignment of the instrument i.e center of the incident beam ii) curvature of the specimen iii) absorption of the sample. In order to address such experimental errors, and improve the accuracy of the measurement the Nelson-Riley extrapolation method can be used [**1**], shown in **Equation A.1.2**

$$F(\theta) = \frac{1}{2}\left(\frac{cos^2\theta}{\sin\theta} + \frac{cos^2\theta}{\theta}\right)$$ **Equation A.2.2**

Where θ is the Bragg angle, the successful extraction of the lattice constant value contemplates several 00*l* diffraction angles and is obtained when the equation is fitted for θ=0. However, it is important to also applied an experimental correction on the substrate, this is done by considering the substrate as a perfect crystal and therefore correcting the out of plane parameter accordingly to the a_{sto}=3.905 Å lattice value. In this case the experimental misalignment mentioned before can be further reduced by applying the **Equations A.2.3 and A.2.4**, and extracting the effective wavelength of the experiment.

$$\lambda_{eff} = \frac{a_{sto}}{l} * 2\sin(\frac{2\theta_{(00l)}}{2})$$ **Equation A.2.3**

Where λ_{eff} is the effective wavelength, a_{sto} is the lattice constant of STO and the angle θ corresponds to the 00*l* position of the substrate.

$$c_{film} = \frac{l * \lambda_{eff}}{2\sin(\frac{2\theta_{(00l)}}{2})}$$ **Equation A.2.4**

Therefore correcting the substrate position and increasing the results of the Nelson-Riley extrapolation method.

Reciprocal space maps

Angular corrections should be performed also for non-geometrical diffractions, since the same experimental errors are present in the measurements. In similar fashion as in the symmetric scans, the lattice constant of the known substrate are used to correct the position of the scan. The RSM plot should be both corrected for $\Delta\overrightarrow{q_{hkl}}$ where *hkl* corresponds to the crystalline direction of the named vector (parallel, q_x, or perpendicular q_y).

An important control parameter to keep in mind is that the out of plane lattice constant of the film, previously obtained in corrected in this section, can be also extracted from the RSM plots.

$$c_{film} = \frac{l_f}{\frac{l_s}{a_{STO}} + \Delta\overrightarrow{q_{hkl}}}$$ **Equation A.2.5**

Where l_f and l_s are the l miller index of the (*hkl*) reflection of the film and substrate, respectively. Similarly, the in-plane lattice parameter of the film, a_f, is assessed following:

$$a_f = \frac{\sqrt{h_f^2 + k_f^2}}{\frac{\sqrt{h_f^2 + k_f^2}}{a_{STO}} + \Delta\overrightarrow{q_{parallel}}}$$ **Equation A.2.6**

where h_f, k_f and h_s, k_s are the *h, k* index of the (*hkl*) XRD reflection of the film and substrate, respectively.

The general crystalline formulas for cubic, tetragonal and orthorhombic unit cells, are described in the following equations.

$$\frac{1}{d^2} = \frac{h^2 + k^2 + l^2}{a^2}$$ **Equation A.2.7**

$$\frac{1}{d^2} = \frac{h^2 + k^2}{a^2} + \frac{l^2}{c^2}$$ **Equation A.2.8**

$$\frac{1}{d^2} = \frac{h^2}{a^2} + \frac{k^2}{b^2} + \frac{l^2}{c^2}$$ **Equation A.2.9**

The *d* represents the interplanar distance, *h, k, l* the miller index of the (*hkl*) reflection and *a, b, c* the lattice constants for each crystal structure.

[1] Als-Nielsen, J. and McMorrow, D. (2011) **Elements of Modern X-ray Physics** [Internet]. Elem. Mod. X-ray Phys. Second Ed. John Wiley & Sons, Inc., Hoboken, NJ, USA. http://dx.doi.org/10.1002/9781119998365

APPENDIX 3

Diamagnetism of SrTiO3 substrates

Diamagnetic contribution of $SrTiO_3$ substrates were previously addressed in the PhD thesis of Dr. X. Marti[**1**], in his work, the magnetic susceptibility of commercially available substrates (Crystec GmbH) was meticulously study. In this thesis, the same type of substrate are used, thus the methods described in the aforementioned work are also implemented in this thesis. A general description, summarized in the thesis of Dr. E. Langenberg [**2**], of the methodology used is described.

The magnetic field dependence of the magnetization, M(H), of a set of as-received bare SrTiO3 substrates was measured at 35K and 300 K. As expected for the diamagnetic substrate $M = \chi STO \cdot H$, the negative slope of M(H) curves on increasing H allows obtaining the volume diamagnetic susceptibility of SrTiO3, $\chi_v STO$, for both temperatures, values are $-1.13 \cdot 10^{-6}$ $emu/(Oe \cdot cm^3)$ and $-1.22 \cdot 10^{-6}$ $emu/(Oe \cdot cm^3)$ at 35 K and 300 K, respectively. Note that the volume susceptibility was computed using the dimensions of SrTiO3 substrates: 5 x 5 x 0.5 mm^3.

In order to extract the diamagnetic contribution of the STO substrate, M(H) of samples with different thin film thickness were measured. The M(H) curves shown a behavior similar to $M = (\chi vSTO + \chi vfilm) \cdot H$. The diamagnetism can be described as: $\chi vfilm = K \cdot t$, where K and t are a constant and the film thickness, respectively. Then by differentiating M(H) a linear dependence is found as a function of thickness: $dM/dH = \chi vSTO + K \cdot t$. The extrapolation of t = 0 of the linear fitting allows extracting the volume diamagnetic susceptibility of SrTiO3, $\chi_v STO = (-1.11 \pm 0.05) \cdot 10^{-6}$ $emu/(Oe \cdot cm^3)$, in close agreement with the one extracted from bare SrTiO3

substrates. Is important to remark that determination of this value allows the correction of diamagnetic contributions of cut substrates by estimating the volume of the substrate, since the weight and density of STO is known.

[1] Marti, X. (2009) **Growth and characterization of magnetoelectric YMnO 3 epitaxial thin films**. Autonomus University of Barcelona.

[2] Langenberg Pérez, E. **Growth and characterisation of Bi-based multiferroic thin films**. Universitat de Barcelona.